Carl von Ossietzky

Universität Oldenburg

Ionic Liquids at Interfaces

– Structure and Potential-Driven Changes

(Ionische Flüssigkeiten an Grenzflächen

– Struktur und potentialgetriebene Veränderungen)

Von der Fakultät für Mathematik und Naturwissenschaften

der Carl von Ossietzky Universität Oldenburg

zur Erlangung des Grades und Titels eines

Doktors der Naturwissenschaften (Dr. rer. nat.)

angenommene Dissertation

von Herrn **Thorben Sieling**, M.Sc.

geboren am 03. November 1991 in Oldenburg (Oldb)

Oldenburg, Juni 2021

Gutachterin: PD Dr. Izabella Brand

Zweitgutachterin: Prof. Dr. Julia Kunze-Liebhäuser

Tag der Disputation: 28.07.2021

Für meine Eltern

„Die Wahrheit ist eben kein Kristall, den man in die Tasche stecken kann,

sondern eine unendliche Flüssigkeit, in die man hineinfällt.“

Robert Musil, *Der Mann ohne Eigenschaften*, Band 1, erschienen zuerst **1930** bei

Rowohlt in Berlin.

Translated from German:

"The truth is not a crystal one can put into a pocket,

but an endless liquid one falls into."

Abstract

Ionic liquids (ILs) are salts which melt at ambient temperatures. Their low volatility enables an environmentally friendly and safe use. Their interfacial properties are of interest for surface impregnation or electrochemical applications.

The Langmuir-Blodgett (LB) method can be used to transfer well-defined monolayers of amphiphilic ILs from aqueous subphases onto solid substrates. Subsequent characterization by X-ray photoelectron spectroscopy shows that the anion of the originally deposited IL exchanges with anions from the subphase solution. In addition, the heterocyclic ring head group of the cation interacts with the gold surface of the substrate. Polarization modulation infrared reflection absorption spectroscopy (PM IRRAS) enables the assessment of molecular order at the metal. Quantum chemical simulations facilitate the interpretation of the complex experimental spectra.

For surface impregnation, azolium-based ILs with short perfluorinated side chains are investigated after LB-transfer from H_2O and 1 M $NaCl_{(aq)}$ subphases onto Au(poly) substrates. In agreement with contact angle measurements, it is shown by PM IRRAS that the films transferred from 1 M $NaCl_{(aq)}$ subphase have higher order than those transferred from H_2O.

In order to explain the fundamental heterogeneous electron transfer and charge processes in electrochemical applications, the electrical double layer (EDL) of ILs at electrode interfaces must be understood. The IL-LB film serves as a model for the first layer on Au(111) surfaces. In situ PM IRRAS measurements show that ring groups remain unaffected by the potential, while the order of alkyl chains increases at negative potentials. They act as latent voids. Measurement of perdeuterated alkyl chains indicates nanosegregation of the cation into polar and apolar domains. Anomalous capacitance-potential curves show that the EDL of dilute ILs in aqueous solutions cannot be explained by the classical model of metal|compact layer|diffuse layer. The formation of an accumulation layer, in between of the compact and diffuse layers, is proposed.

Zusammenfassung

Ionische Flüssigkeiten (ionic liquids, ILs) sind Salze, die bei mäßigen Temperaturen schmelzen. Ihre geringe Flüchtigkeit ermöglicht einen umweltschonenden und sicheren Einsatz. Die Eigenschaften von ILs an Grenzflächen sind für die Oberflächenimprägnierung oder für elektrochemische Anwendungen von Interesse.

Mit der Langmuir-Blodgett (LB)-Methode können wohldefinierte Monolagen von amphiphilen ILs von wässrigen Subphasen auf feste Substrate übertragen werden. Die folgende Charakterisierung mittels Röntgen-Photoelektronenspektroskopie zeigt, dass das Anion der ursprünglich aufgetragenen IL mit Anionen aus der Subphasenlösung austauscht. Zudem wechselwirkt die heterocyclische Ringkopfgruppe des Kations mit der Goldoberfläche des Substrats. Mittels Polarisationsmodulierter Infrarot-reflexions-absorptions-spektroskopie (PM IRRAS) kann die molekulare Ordnung am Metall erfasst werden. Quantenchemische Simulationen ermöglichen die Interpretation der komplexen Spektren.

Für die Oberflächenimprägnierung werden Azolium-basierte ILs mit kurzen, perfluorierten Seitenketten untersucht, nachdem sie von H_2O und 1 M $NaCl_{(aq)}$-Subphasen mittels LB-Transfer auf Au(poly)-Substrate übertragen wurden. In Übereinstimmung mit Kontaktwinkelmessungen wird durch PM IRRAS gezeigt, dass die von der 1 M $NaCl_{(aq)}$-Subphase übertragenen Filme eine höhere Ordnung aufweisen als die von H_2O übertragenen.

Um in elektrochemischen Anwendungen die fundamentalen Elektronentransfer- und Ladungsprozesse zu erklären, muss die elektrische Doppelschicht von ILs an Elektrodengrenzflächen verstanden werden. Der IL-LB-Film dient dabei als Modell für die erste Schicht auf Au(111)-Oberflächen. In situ PM IRRAS Messungen zeigen, dass Ringgruppen unbeeinflusst vom Potential bleiben, während die Ordnung der Alkylketten bei negativen Potentialen ansteigt. Sie wirken wie latente freie Raumeinheiten. Die Messung von perdeuterierten Alkylketten deutet auf eine Nanoseggregation des Kations in polare und apolare Domänen hin. Anomale Kapazitäts-Potential-Kurven zeigen, dass die Doppelschicht von verdünnten ILs in wässrigen Lösungen nicht durch das klassische Modell, Metall|starre Schicht|diffuse Schicht, erklärt werden kann. Die Bildung einer Akkumulationsschicht zwischen starrer und diffuser Schicht wird vorgeschlagen.

x

Acknowledgement

Table of Contents

1 Introduction and Motivation

Liquids play in important role in everyday life and industry. Macroscopically, they can easily be deformed and adopt the form of their container, but they exhibit generally low compressibilities.[1] Microscopically, their molecules are bound by intermolecular forces, such as dispersive forces or hydrogen bonding interactions, which results in near order. In contrast to crystals, they do not exhibit long-range order and their molecules are mobile. Wetting is a unique phenomenon for them. Liquids are utilized in many fundamental applications, such as temperature control (heat transfer), lubrication, power transfer (hydraulics), chemical power storage and supply (fuel), solvation, or electric conductance.[1-3]

Solvents are of specific interest for chemistry. Often, they serve in more aspects than just for solubility; e.g. temperature control is equally important in many cases. Their use in separation and purification (extraction, flotation, rectification, precipitation or crystallization) is as crucial as in chemical reactions (diffusion medium, homogeneity, dilution and activity control, impact partner, chemical interaction) or analytics (absorption medium, mobile phase).[2-4]

The history of solvents was outlined by Reichardt and Welton, and is briefly summarized below:[5] In ancient times, Greek alchemists regarded all chemically active liquids as "Divine water". Aristotle (384-322 BC) allocated reactivity predominantly to the liquid phase, which is outdated considering many solid-solid reactions known today. In the 15th to 18th centuries, emphasis was given to solvents and the process of dissolution. It is reflected by the alchemist's quest for a universal solvent, which was also called "Alkahest" or "Menstruum universale" by Paracelsus (1493-1541). Water, the oldest and most important solvent, cannot fulfill all demands. When van Helmont (1577-1644) claimed to have prepared this "Alkahest", contemporaries mocked at him, asking in which vessel he had contained the universal solvent. In this era, numerous new solvents, reactions, and compounds were uncovered, leading to the earliest chemical rule "similia similibus solvuntur" – like dissolves like. However, physical and chemical dissolution were not distinguished yet, and it was assumed that the nature of a substance vanishes upon dissolution. This was opposed by van Helmont, but the process of dissolution and forces acting on molecules

remained obscure. Major progress leading to modern solution theory was made in the 19th to 20th centuries by Raoult (1830-1901), van't Hoff (1852-1911), and Arrhenius (1859-1927). The latter introduced the theory of incomplete and complete dissociation of ionic electrolytes into dissolved cations and anions. Crucial contributions to the physical chemistry of solutions arose from Ostwald (1853-1932), Nernst (1864-1941), Lewis (1875-1946), Debye (1884-1966), Hückel (1896-1980), and Bjerrum (1879-1958). At the same time, the influence of solvents on reaction rates, chemical equilibria, or absorption spectra was noted. Emphasis on environmental protection, sustainability, and health[6] have lead to a new wave of research in solvents and liquids. Safer and cleaner technologies are favorable in industry and academia, but many classic solvents are volatile and used in huge amounts. Out of this quest, new "neoteric solvents" emerged, e.g. supercritical fluids, perfluorohydrocarbons, deep eutectic solvents,[7] switchable solvents,[7] or ionic liquids (ILs).

Ionic liquids are salts which are liquid at ambient temperatures. Large organic cations are paired with inorganic or organic anions, leading to versatility in structures as well as desirable properties, such as non-volatility, non-flammability, electric conductivity, or thermal and chemical stability.[8] However, in comparison to the classical solvents already running in processes, the industrial implementation of ILs is rather slow and hesitant.[9] Their environmental impact, health issues and bioaccumulation have to be accounted for, too, as awareness and standards in these domains have risen in the last decades. Yet, ILs are applied in all types of the fundamental liquid applications today, except for the use as a fuel.[9] A more detailed description of the structures, properties, and applications of ILs is given in chapter 2.

Interesting properties of ILs and polyfluorinated organic compounds (PFCs) are combined in fluorinated ionic liquids (FILs). A review by Lindstrom et al. elucidates the state of PFCs:[6] F-C bonds rank among the strongest bonds in nature, yielding stability at high temperatures and resistance toward oxidation, hydrolysis, and photolysis. Furthermore, they are excellent water and oil repellants, leading to application in surface coatings of papers and textiles. PFCs dispersants and surfactants are used in paints, lubricants, fire-extinguishing foams, or as emulsifiers in production of fluoropolymers. Their resistance toward physical, chemical, and biological degradation is as advantageous as hazardous. Some PFCs are toxic or mutagenic. In the 2000s, the broad distribution of PFCs in the environment became evident and they were found almost all human blood samples. The

uptake via food may be a major route in bioaccumulation of PFCs. As long-chain PFCs ($\geq C_8$) were found to be significantly more bioaccumulative than shorter ones, the first are likely to be banned, soon. New compounds are required which preserve desired properties of PFCs while consisting of shorter perfluorocarbon segments. Recently, Alpers et al. developed new partially perfluorinated pyridinium-, imidazolium-, 1,2,3-triazolium-, and 1,2,4-triazolium-based ILs with perfluorohexyl chains for surface impregnation.[10-11] These FILs are an example of $R^1–(CF_2)_n(CH_2)_m–R^2$ diblock compounds, which are a promising solution for applicable semifluorinated surfactants.[12] Amphiphilic, amphidynamic, and amphisteric properties make them interesting for interfacial applications.[12] One topic of this work is to analyze the behavior of FILs at different interfaces, which is elaborated in chapter 5.

The microscopic structure at interfaces results in macroscopic properties. Besides wetting phenomena, e.g. repellency of water, a physicochemical understanding of interfaces is important. Usually, interfaces are charged to some extent. Electrostatic and chemical interactions cause adjacent molecules to accumulate, deplete, or orient at the interface. In electrolyte solutions, this phenomenon is called "electrical double layer" (EDL).[3] Along with the formation of the EDL, the electric field of the surface is sharply screened, affects the behavior of charge carriers. Consequently, a potential drop occurs at the interface, which is crucial for interfacial applications. As the potential is directly related to the free energy of the system, it controls the rate of charge transfer as well as its direction. Both electric field and potential vary as a function of distance with respect to the electrode surface. Therefore, knowledge about the structure of the EDL is essential, as it determines how close a reactant may approach the electrode. For example, a potential-driven transition of the surface structure formed by an IL-water mixture on a metal electrode was found to determine the onset of the CO_2 reduction reaction.[13-15] Also, the selectivity of this reaction is enhanced. Unwanted reaction sites are blocked by the IL and thus the concurring hydrogen evolution reaction is suppressed.

The EDL has been studied in classical diluted electrolytes,[16-17] high-temperature molten salts,[18-19] and in ILs,[20] which is reflected in chapter 3. Generally, liquids are harder to grasp by theory than crystals or gases. In the quotation in the beginning of this thesis, Musil related the complicated concept of "truth" not simply to "a crystal that can be put into a pocket, but

[to] an endless liquid one falls into."[*] The truth behind ILs is certainly drowning. To assess the EDL experimentally, capacitance-potential curves are measured. A theory is regarded as correct when it accurately predicts the capacitive behavior of the system. As elaborated in chapter 3.3.3, the investigations on the EDL of ILs are complex and lead to contradictory results. Molecular reorientations and generally slow kinetics are not considered in current equilibrium models and may play an important role.[20]

Amphiphilic and surface-active ILs are also of interest for electrochemical applications. Besides polar regimes formed by their ionic headgroups, they exhibit large apolar domains consisting of alkyl chains.[21-23] This spatial segregation in polarity leads to unusual ion distributions, shortening the EDL and thus enhancing the charge storage performance at electrified interfaces for supercapacitors.[24] Therefore, the second topic of this thesis was to investigate the EDL, especially the first layer, of a more simple, aliphatic and amphiphilic IL at a well-characterized metal electrode surface. This is described in chapters 6 and 7 for an amphiphilic IL with a perhydro- or perdeutero-alkyl chain, respectively.

In order to study structural changes in the EDL, surface sensitive techniques must be applied. For the investigates of amphiphilic ILs at interfaces, an *experimental modelling* methodology was used. An overview of the applied experimental techniques is given in chapter 4 and partially in sections 3.1 and 3.2. Filipe at al. showed that an imidazolium-based IL behaves similarly to classic amphiphilic molecules in Langmuir films.[25] Polar headgroups are directed toward the aqueous subphase, whereas apolar tailgroups are oriented toward air. An analogical orientation was found for ILs evaporated onto metal surfaces in vacuo.[26] The Langmuir-Blodgett (LB) technique offers to fabricate well-ordered monolayers of amphiphiles. Utilizing this technique for the goals of this thesis yielded systems, whose initial state was known to some extent. X-ray photoelectron spectroscopy (XPS) was used to further characterize these substrates with respect to elemental composition and chemical nature. Vibrational spectroscopy methods are particularly suitable for studying the EDL of polyatomic molecules. According spectra contain valuable information, e.g. molecular constitution, conformation, order, or orientation. Vibrational modes of different functional groups resonate at different frequencies, which

---

[*] Translated from German. Robert Musil, *Der Mann ohne Eigenschaften*, Band 1, first published in **1933** by Rowohlt, Berlin, Germany.

allows for the simultaneous submolecular characterization of distinguishable cations and anions. Polarization modulation infrared reflection absorption spectroscopy (PM IRRAS) was employed because it can be applied at flat and single-crystalline surfaces, ex situ in air as well as in situ under electrochemical potential control. Additionally, quantum chemical frequency calculations were used to facilitate band assignment and analysis of complex vibrational spectra. Results from vibrational spectroscopy could be correlated with complementary contact angle measurements or potential-dependent capacitance measurements by electrochemical impedance spectroscopy (EIS), which yielded information on the supramolecular behavior of the studied system. Finally, molecular scale pictures were constructed to elucidate structure-property relationships.

After examination of the modelled first layer in the EDL, interactions of IL molecules in solution close to the interface were studied. 1-Ethyl-3-methylimidazolium triflate is a model IL[27-31] and was chosen for this task. For the analysis, aliphatic CH stretching infrared absorption bands needed to be assigned. However, this assignment was neither straightforward nor conclusive from literature reports.[32-37] Therefore, an anharmonic frequency calculation was conducted and discussed with literature in chapter 8. Results of this study were required for the following analysis of interactions in aqueous IL solutions in chapter 9.

2 Ionic Liquids

Ionic liquids are composed of cations and anions. To distinguish them from high temperature molten salts (HTMS), e.g. alkali halides and their eutectic melts, ILs are defined to melt below a certain temperature T_m. Varying melting points are taken as upper limits, for example

(i)   room temperature ILs melting below T_m = 100-150 °C,[20]

(ii)   ILs melting below T_m = 100 °C,[8]

(iii)   or room temperature ILs being liquid at room temperature.[38]

The second definition is most common and was introduced already in 1914 by Walden. He was one of the first to study physicochemical properties of what is today defined as ILs.[8, 39] Walden characterized different organic ammonium salts, of which some melted below 100 °C and one was liquid at room temperature.

An overview of the IL history in research is given in the reviews of Wasserscheid,[40] and Plechkova and Seddon:[8] Briefly, the research on ILs was initiated with Walden's work published in 1914.[39] First, ILs remained unrecognized for many years. Scarce applications are found in 1948-51 and 1976-78 in electrochemistry. Predominantly pyridinium chloroaluminates were investigated as electrolytes for electroplating of aluminum and batteries. However, the liquid range with respect to the composition of these IL-AlCl$_3$ mixtures was narrow and the cation was prone to reduction, which lead to the application of imidazolium-based salts. Another obstacle is that chloroaluminates are sensitive to moisture and must be handled under protective conditions. In 1992, Wilkes and Zawarotko synthesized ILs with air- and water-stable anions, such as tetrafluoroborates,[41] and gave an impulse for further developments in academia and industry. Due to extraordinary properties arising from the structural diversity of cations and anions, ILs expand the spectrum of available liquids and their applicability.

2.1 Structure

ILs are usually formed of organic cations and inorganic or organic anions (Fig. 2.1).[8] Large, asymmetrical, and low-coordinating ionic structures

reduce lattice energy and thus lower the melting point. Ionic charge densities are low and often delocalized among several atoms. By variation of cations, anions, and substituents, one million ILs may possibly be created, as estimated by Seddon.[8]

A feature, which sets ILs fundamentally apart from conventional molten salts, is their microstructure: For salts substituted with medium or long alkyl chains, the formation of heterogeneous domains is observed experimentally and supported by theory.[21-23] Apolar segments are formed by alkyl chains and separated from polar segments of charge-carrying headgroups. Both form a dynamic, intertwined, and three-dimensional network. As this agglomeration phenomenon acts on molecular scales, it is called "nano-segregation", "nanostructuring" or "microheterogeneity".[23]
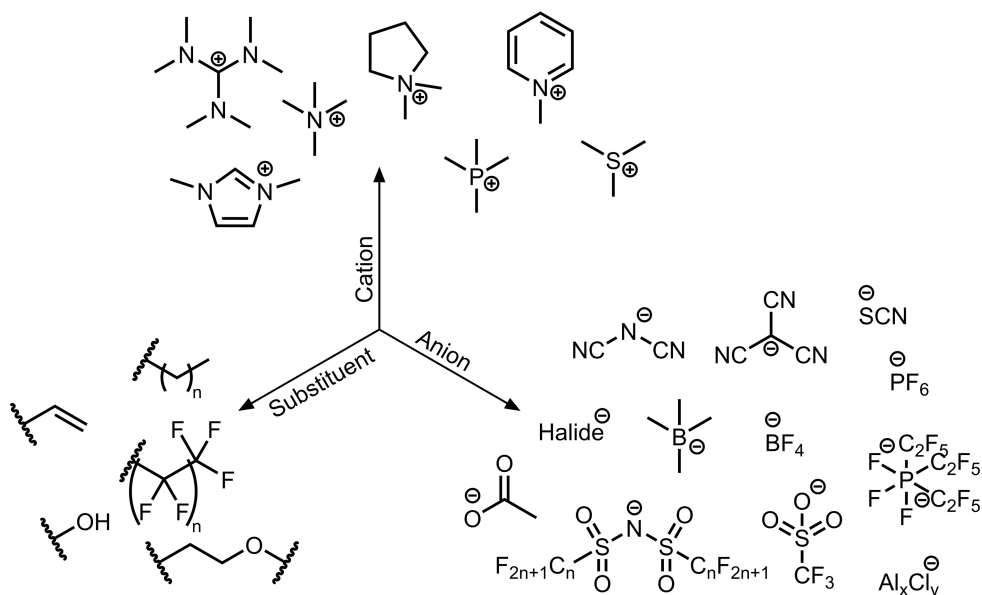
Figure 2.1: Common ionic base structures and substituents used to form ILs. Note that not all possible combinations lead to salts with melting points satisfying strict IL definitions. Figure design inspired by Fedorov and Kornyshev.[20]

Already in 1914, Walden emphasized the degree of association and dissociation of cations and anions in liquid salts.[39] This topic is still relevant.[8, 23] Ion pairs are found in the gas phase.[8] The polar domain in the liquid phase is less well understood, as reviewed by Kirchner et al.[23] Major arguments of this review are presented below: Experimentalists ascribe deviations from a linear behavior of logarithmic conductivity as a function of logarithmic inverse viscosity (Walden plot) to the formation of neutral ion pairs, because the amount of effective charge carriers is less than expected

from the bulk concentration of the IL. The measured Debye-length (Section 3.3) at an interface leads to similar conclusions.[42] On the other hand, the nucleophilic substitution mechanism in ILs or polarity measurements indicate a complete dissociation of ILs. Generally, the definition of an ion pair is difficult per se, as a central ion in a melt is always surrounded by associating counterions and thus never completely cleaved. The simulated lifetimes of ions in the closest approach are shorter than a picosecond, and the distances diffused together as pairs are less than their interionic distances. Theoreticians criticize the assumption of (formal) unity charges during evaluation of experimental results. In the dynamic liquid, a significant and varying charge transfer is proposed to occur between anions and cations due to the formation of weak bonds, such as H-bonds, or associates. As a consequence, a part of their charges shall be neutralized, causing the apparently lower concentration of free charge carriers.

2.2 Properties

"Some ionic liquids are toxic, some can be eaten, and others may be used as pharmaceuticals or explosives."[9] This statement given by Schubert shows that ILs exhibit versatile properties and can hardly be generalized. The only discrete property common to all ILs may be ionic conductivity.[23] Table 2.1 provides an overview of selected properties of ILs. Ranges from minimum to maximum values reflect the versatility of ILs as well as their approximate limits. Medians and arithmetic means show their most common properties. However, corresponding standard deviations are high in some cases, which supports that ILs cannot be generalized.

It must be noted that impurities may have a severe impact on IL properties, but also low purity ILs may preserve desired properties.[9] ILs will likely be applied in ternary systems, where the first IL determines the chemistry, the second one is used for fine tuning of physical properties, and the third IL for cost reduction.[8] Accordingly, Seddon and Plechkova estimated a trillion of possible combinations.[8] Due to the huge structural diversity in cations and anions leading to versatile physico-chemical properties, ILs can be legitimately called "designer solvents".[8]

Table 2.1: Selected properties of ILs extracted from tables of Marcus.[43] The average was taken in case of multiple values for a single compound. Note that the number of listed ILs per property strongly deviates which limits the validity of generalization. Also, organic salts sharing the structures of ILs were taken into consideration which do not belong to the most common IL definition of melting below 100 °C. Given values may be exceeded by non-listed ILs. Min. – Minimum Value, Max. – Maximum Value, Lg. – Logarithmic, Coef. – Coefficient.

Property / Unit (Number of Listed ILs)	Min. – Max.	Median	Mean
Molar Mass / g mol^{-1} (235)	146.6 – 764.0	299.4	329 ± 120
Melting Point / °C (190)	-88 – 230	23	36 ± 62
Decomposition Temperature / °C (104)	136 – 444	302	308 ± 66
Density / g cm^{-3} (194)	0.89 – 1.69	1.21	1.2 ± 0.2
Surface Tension / mN m^{-1} (97)	23.6 – 65.1	36.5	39.9 ± 8.9
Dynamic Viscosity / mPa s (153)	15 – 18920	170.75	767 ± 2320
Molar Conductivity / S cm^2 mol^{-1} (91)	0.0028 – 4.72	0.5035	0.7 ± 0.8
Refractive Index (125)	1.369 – 1.569	1.447	1.46 ± 0.04
Relative Permittivity (36)	6.5 – 35	14	14 ± 5
Lg. 1-Octanol/Water Partition Coef. (54)	-3.55 – 1.38	-1.47	-1.3 ± 1.2

A strong advantage of ILs is their low volatility at ambient conditions:[8-9]

(i) High acquisition cost can be compensated by recycling, reuse, or resale.

(ii) Despite toxicity, they can be handled without major constraints.

(iii) They do not evaporate from even poorly sealed vessels and thus minimize atmospheric contamination.

In addition to the aforementioned features, non-flammability makes ILs interesting for safer electrochemical devices.[9] Another advantage is their inertness, which leads to wide electrochemical potential windows, typically spanning 4.5-5 V, up to 8-9 V.[44-46] On the other hand, their low conductivity (Tab. 2.1), which is likely to be caused by slow self-diffusion coefficients due to high viscosity, is their major drawback for electrochemical applications.[23]

Most ILs are hydrophilic, whereas some are hydrophobic, which can be characterized by their 1-octanol/water partition coefficient (Tab. 2.1). This behavior is mostly determined by anions and alkyl chain length, and influences their solvation properties.[43] Furthermore, some ILs show a marked ability to dissolve gases.[8, 43]

2.3 Applications

ILs were often perceived as a "lab curiosity" and their impact on industry was barely recognized.[9] This perception is partially caused by non-disclosure of IL-involving processes.[9] Actually, "parallel developments between academic research and industrial developments" have proceeded since ILs became known to a greater community, as elucidated by Plechkova and Seddon.[8] For example, a catalyzed isomerization process had been operated in a phosphonium-based IL, and it was already terminated (1669-2004).[8] Further interesting applications were summarized by Wasserscheid,[40] Plechkova and Seddon,[8] or Schubert,[9] and are described below.

Toxicity is a disadvantage when dealing with certain ILs. Nevertheless, they can be used to make certain processes safer: Their ability to absorb gases is used for the production and storage of hazardous compounds, such as AsH_3 or BF_3.[8] Also, imidazolium-based ILs have replaced more perilous phosgene in chlorination as well as hydrofluoric and sulfuric acids in alkylation processes, which is the largest scale application of ILs so far.[8-9] Further commercialized applications comprise ILs as the stationary phase in gas chromatography columns, hydraulic fluid, antistatic additives or as conductive coatings in electron microscopy.[9] In future, IL/oxidizer combinations may replace hydrazine-based hypergolic fuels, which are volatile as well as environmentally toxic, and used in rocket engines.[47]

Biphasic systems are of great interest:[8, 40] In several catalytic processes homogeneous cationic transition metal catalysts are retained in an IL phase, which makes them reusable. Products can easily be separated with molecular solvents. Implemented processes comprise for example alkene dimerization, hydrosilylation, and reactions for pharmaceutical inter-mediates.[8] Moreover, ILs can be loaded on porous supports or catalysts to increase the available surface area and make use of bifunctional catalysts, as summarized by Haumann and Wasserscheid:[48] Either a non-leaching homogeneous catalyst is immobilized in this way or the reactivity of nanoparticulate metal on the solid support is tuned by coadsorption of the IL. The first principle is used in industry for the removal of mercury from natural gas. Interfacial properties of ILs matter in both cases: To prevent pores from being blocked, low IL loadings leading to thin films must be used. However, a complete coverage can only be achieved, if the wetting on the support is sufficient. Otherwise, the IL forms islands and does not penetrate

the pores. More commercialized interfacial applications encompass synthesis and stabilization of nanomaterials, or lubrication.[9]

Future perspectives are seen in application of ILs for dissolution of biopolymers (an early patent for the dissolution of cellulose was filed in 1934)[49] to access biomass as renewable feedstock, emulsion polymerization, stabilization of biomolecules, current and heat conducting fluids in vacuo, sorption cooling, delivery of pharmaceutical agents, or in composite materials.[8-9]

The large electrochemical window (Section 2.2) of ILs enables high polarizations and access to extreme potentials, which leads to the development of several applications:[8-9] Many metals are reactive and cannot be processed in water. ILs may offer a possibility for electroplating of some reactive metals, such as aluminum or chromium. Electropolishing and recycling of noble or rare earth metals are also investigated. Driven by the urge for renewable energy usage, electrochemical energy storage devices receive much attention. Supercapacitors offer high power densities and fast charging utilizing electrical double layer adsorption in porous electrodes. Research on batteries with IL electrolytes may lead to the production of different systems, e.g. metal-air or lithium-sulfur batteries.

3 Thermodynamics of Interfaces

In comparison to their bulk analogues, species present at the interface are exposed to different forces (such as electrostatic or dispersive ones) due to the adjacent species of the contacting phase or its absence.[50] Thus, they persist in energetically different states, and a governing quantity for the thermodynamics of interfaces is the creation or depletion of the interfacial area A. The amount of energy, in the form of free enthalpy G under constant temperature T and pressure p, which is required to reversibly form a unit section of interfacial area, is called surface tension γ (Eq. 3.1).

$$\left(\frac{\partial G}{\partial A}\right)_{T,p} = \gamma \tag{3.1}$$

3.1 Wetting

Experimental assessment of surface tensions mostly involves a third phase.[50] When three phases are in contact, three surface tensions between each of the phases equilibrate. The exposed area of a liquid (L) on a solid substrate (S) in gaseous atmosphere (G) is adjusted by variation of the contact angle ϑ according to Young's equation (Eq. 3.2, Fig. 3.1). Wetting properties are equally affected in other systems, e.g. for two immiscible liquids in a solid capillary.

$$\gamma_{S|G} = \gamma_{S|L} + \gamma_{L|G} \cos \vartheta \tag{3.2}$$
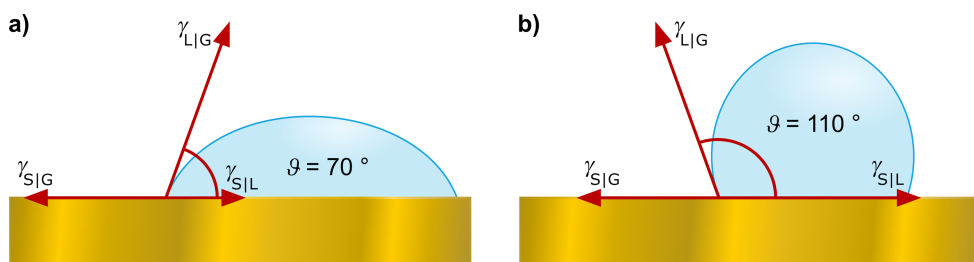
Figure 3.1: Droplets (light blue) placed on a solid (golden). Varying surface tensions (red arrows indicate corresponding forces) at the L|S interface result in a) wetting ($\vartheta < 90\,°$) or b) dewetting ($\vartheta > 90\,°$).

Energetically favorable interactions of the L|S interface can be observed by spreading of a droplet on the substrate and thus, a low contact angle

(Fig. 3.1a). In contrast, a contracting droplet exhibits a high contact angle and shows repelling interactions (Fig. 3.1b).

3.2 Surface Excess

In a multi-component system containing immiscible phases, species i dispersed in the bulk phases may adsorb at the phase boundary.[50] The surface tension changes under constant temperature and pressure according to the Gibbs adsorption equation (Eq. 3.3). It depends on the surface concentrations Γ_i (Eq. 3.4) and chemical potentials μ_i of the species i. In case of variable T and p, excess entropy and excess volume would additionally influence γ.

$$\mathrm{d}\gamma = -\sum \Gamma_i \, \mathrm{d}\mu_i \, \Big|_{T,p} \tag{3.3}$$

$$\Gamma_i = \frac{n_i}{A} \tag{3.4}$$

For soluble species, the surface concentration yields a relative excess or depletion with respect to a chosen species in the bulk phase. Insoluble species accumulate at the interface, e.g. amphiphilic molecules at the air | water interface. In this case, Γ_i is known from the amount of substance n_i deposited at the interface and the interfacial area. At low surface concentrations, the distances between single molecules provide a large mean molecular area A_{molec} (Eq. 3.5). Interactions of individual species are negligible and the system behaves like a two-dimensional, ideal gas (Eq. 3.6).

$$A_{\mathrm{molec}} = \frac{A}{\mathcal{N}} \tag{3.5}$$

$$\Pi A_{\mathrm{molec}} = k_{\mathrm{B}} T \tag{3.6}$$

Upon compression of interfacial area for a fixed number of molecules $\mathcal{N}$ at constant temperature, the surface pressure Π will rise in relation to the Boltzmann constant k_{B}. The surface pressure is given by the difference of the uncovered and the covered interfaces' surface tensions (γ_0 and γ, respectively; Eq. 3.7).

$$\Pi = \gamma_0 - \gamma \tag{3.7}$$

Similarly to three-dimensional systems, a phase transition will take place upon sufficient compression at $\mathrm{d}T = \mathrm{d}p = \mathrm{d}n_i = 0$. When two phases are present simultaneously, Π is constant for a range of A_{molec}, until the transition of the whole molecular layer is completed. The phases can be

characterized by the two-dimensional inverse compressibility modulus (compressibility) K^{-1} (Eq. 3.8).

$$K^{-1} = \left[-\frac{1}{A_{\mathrm{molec}}} \left(\frac{\partial A_{\mathrm{molec}}}{\partial \Pi} \right)_{T,p,n_i} \right]^{-1} \tag{3.8}$$

3.3 Adsorption at Electrified Interfaces

Adsorption of ions and neutral compounds changes the surface potential at the interface.[3, 50] Thermodynamic considerations require a proper description of the potential changes between adjacent phases, because the potential is directly related to the free enthalpy of the system. Therefore, the amount of charge, the orientation of molecules and ions, and their distances with respect to the electrode surface must be known. The interfacial potential drop is preferably studied in electrochemical systems containing an ideally polarizable metal electrode, because its potential versus a reference electrode U can be controlled externally and the interfacial potential drop within a metal is negligible. Accordingly, the Gibbs adsorption equation (Eq. 3.3) must be modified with a polarization term, which describes the change of the surface charge density per unit area σ. As a result, the electrocapillary equation is formed (Eq. 3.9).

$$\mathrm{d}\gamma = -\sigma \, \mathrm{d}U - \sum \Gamma_i \, \mathrm{d}\mu_i \, \Big|_{T,p} \tag{3.9}$$

This equation neglects changes in some junction potentials. Under constant composition, temperature, and pressure, the Lippman equation (Eq. 3.10) yields the negative surface charge density.

$$\left(\frac{\partial \gamma}{\partial U} \right)_{T,p,\mu} = -\sigma \tag{3.10}$$

The potential of zero charge (PZC) equals the electrocapillary maximum $\partial\gamma/\partial U = -\sigma = 0 \, \mathrm{C \, cm^{-2}}$ and is approximately determined by the work function of the metal. As the PZC is only well defined for a uniform face, mostly liquid or single-crystalline electrodes were studied.[3, 16] Surface reconstruction phenomena on the latter may complicate investigations.[51]

Further derivation of equation 3.10 gives the charge density which is stored at the interface for a given potential, yielding the differential capacitance C (Eq. 3.11).

$$-\left(\frac{\partial^2 \gamma}{\partial U^2}\right)_{T,p,\mu} = \left(\frac{\partial \sigma}{\partial U}\right)_{T,p,\mu} = C \qquad (3.11)$$

The capacitance reflects the structure of the interface and can be measured to test models. For practical reasons, the capacitance is mostly evaluated as a function of the potential applied rather than the electrode polarization (surface charge). Helmholtz described the electrode interface as a plate capacitor, in which two planes of opposite charge are separated along the screening length d by a dielectric of a given permittivity, which consists of the vacuum and relative permittivities (material-specific), ε_0 and ε_r, respectively.[52] Often, $C(U)$ curves are discussed qualitatively in terms of a plate capacitor. In Helmholtz' model for electrolyte solutions, the counter-ions are supposed to fully screen the electrode charge in a single layer which is separated from the surface by the solvation shell (d_{sol}). Consequently, the capacitance of this so-called "electrical double layer" is given by equation 3.12 for $d = d_{sol}$ and the potential drops linearly across the adsorbed layer. In more complex models this approach is often used to describe the first layer and is then referred to as the "Helmholtz", "inner" or "compact" layer.

$$C_{inner} = \frac{\varepsilon_r \varepsilon_0}{d} \qquad (3.12)$$

3.3.1 Electrolyte Solutions

Traditionally, the EDL of ionic solutions was studied in aqueous solutions of simple and common compounds, e.g. alkali halides or acids.[3, 16] Helmholtz' early model cannot accurately describe the EDL capacitance: Firstly, thermal movement counteracts the alignment of equally charged species in one plane. Secondly, the capacitance is predicted to be constant. This objects experimental results, as $C(U)$ curves are usually camel-shaped for low concentrations or bell-shaped for high concentrations (Fig. 3.2).[53-54] Thus, either the permittivity, the screening length or both must depend on the electrode polarization.
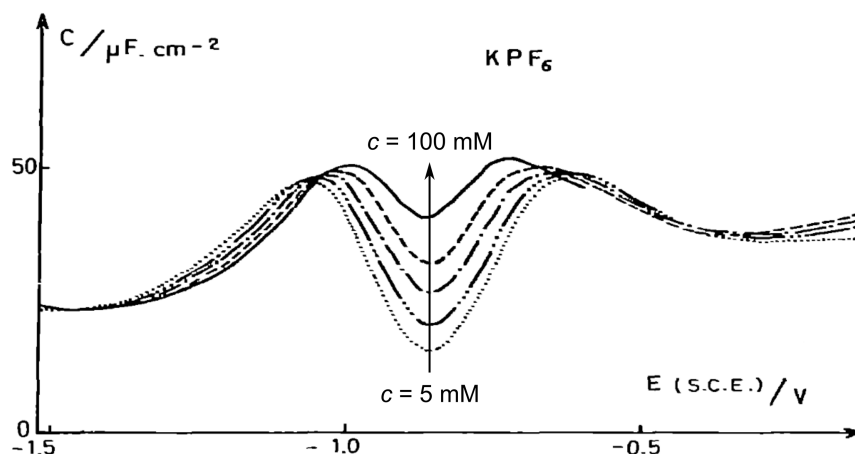
Figure 3.2: Experimental capacitance (C) - potential (E) curves of KPF$_6$ solutions at the Ag(100) surface measured versus a saturated calomel electrode (S.C.E.) by Valette.[55] Copied with permission from Elsevier.

Gouy and Chapman independently derived a model from Boltzmann statistics in which electrostatic attraction acts versus thermally driven randomization (eq. 3.13).[56-57]

$$\tilde{c} = \tilde{c}_0 \exp\left(\frac{W}{k_B T}\right)$$ (3.13)

Physical properties of ions are included through their bulk number density $\tilde{c}$ and their charge q, and the solvent is modeled as a dielectric continuum similarly to the Debye-Hückel theory. Upon polarization of the electrode, ions are predicted to migrate from the bulk along the surface normal coordinate z (Fig. 3.3, right section). Enrichment of ions at the interface requires electrical work W for the transfer of ions along with solvent molecules being replaced and filling left gaps. Due to thermal movement, ions adsorb at different distances with respect to the electrode surface and form a "diffuse" layer. The space charge density ρ is obtained from the ion concentration and gives the potential drop ψ via the electrostatic Poisson equation (eq. 3.14). $\psi = f(z)$ denotes the potential of a plane within the double layer with respect to the electrode potential. Poisson-Boltzmann (PB) models are often used to describe the EDL.

$$\vec{\nabla}^2 \psi(z \to \infty) = -\frac{\rho}{\varepsilon_r \varepsilon_0}$$ (3.14)

As a result, a potential dependent cosh term is yielded, predicting a U-shaped capacitance which describes the valley between camel humps (Eq. 3.15).

$$C_{\text{diffuse,GC}} = \varepsilon_r \varepsilon_0 \kappa \cosh\left(\frac{q\psi}{2k_B T}\right) \qquad \text{(3.15)}$$

$$\kappa^{-1} = \sqrt{\frac{\varepsilon_r \varepsilon_0 k_B T}{2q^2 \tilde{c}_0}} \qquad \text{(3.16)}$$

κ^{-1} denotes the Debye length (Eq. 3.16) and describes the exponential attenuation of a local ionic excess charge. In the original Gouy-Chapman theory, $\psi(z)$ is set to the surface potential of the metal $\psi(z = 0)$, and the model leads to an exponential potential drop across the interface. For nonspecifically adsorbing electrolytes, the minimum coincides with the PZC. The capacitance at the PZC (C_{PZC}) is given by equation 3.17 and is also called the "Debye capacitance". In general, high electrode polarizations and/or ionic bulk concentrations lead to shorter screening lengths and higher capacitances.

$$C_{\text{PZC}} = \varepsilon_r \varepsilon_0 \kappa \qquad \text{(3.17)}$$

However, this model is only applicable within small electrode polarizations because gaseous osmotic pressure laws must be valid, which is the case for low concentrations only. Moreover, ions are taken as point charges in this model, which results in charge residing closer to the electrode surface than an ionic radius, leading to quantitative discrepancies. To overcome this physically unreasonable obstacle, Stern combined Helmholtz' with Gouy's and Chapman's models in series (Eq. 3.18).[58] Consequently, the plane of closest approach to the electrode surface is set to the radius of a solvated ion. A part of the compensating ions is adsorbed at this Helmholtz plane, whereas the remaining charge is distributed diffusely and screens the potential starting at $\psi(z = d_{\text{sol}})$. This leads to a linear potential drop in the beginning (between $z = 0$ and $z = d_{\text{sol}}$) and is followed by an exponential decay (at $z > d_{\text{sol}}$).

$$\frac{1}{C} = \frac{1}{C_{\text{inner}}} + \frac{1}{C_{\text{diffuse}}} \qquad \text{(3.18)}$$

The capacitance at the PZC is then given by equation 3.19:

$$C_{\text{PZC}} = \frac{\varepsilon_r \varepsilon_0}{d_{\text{sol}} + \kappa^{-1}} \qquad \text{(3.19)}$$

Grahame stressed that some ions are found to adsorb while their charge and the surface charge of the metal electrode exhibit the same polarity.[16] In this case, energy is required to overcome electrostatic repulsion, which is given by the formation of a chemical bond. This interaction is short-ranged and thus, these so-called specifically adsorbed or chemisorbed ions are

tightly bound to the electrode surface with shed solvation shells. They are located at the inner Helmholtz plane (IHP) in contrast to nonspecifically adsorbed counterions in the outer Helmholtz plane (OHP), resulting in two sections of linear potential drops at the electrode|electrolyte interface (Fig. 3.3, left section). In the presence of specific adsorption, the point of zero total charge (PZTC) is defined and corresponds to the electrocapillary maximum.

Further improvements toward quantitative accuracy are the involvement of solvent dipoles orienting along the electric field close to the electrode surface and their deviant permittivity.[59] Altogether, these features lead to a model of the EDL as depicted in figure 3.3.
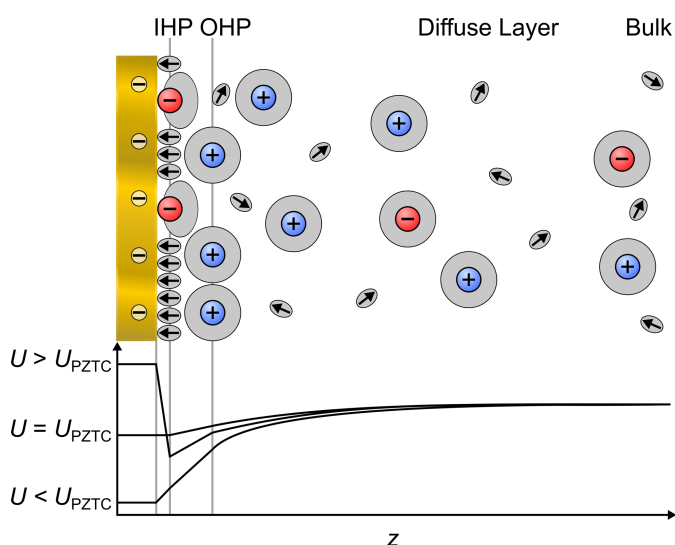
Figure 3.3: Schematic EDL model in a diluted dipolar electrolyte according to Bockris, Müller, and Devanathan.[59] Neutral solvent molecules (grey) with dipole moments are uniformly oriented on the electrode surface (golden), whereas they are randomly oriented in the solution phase. Their orientation in solvation shells is omitted for clarity. Anions (red) with a partially shed solvation shell are specifically adsorbed on the electrode surface, forming the inner Helmholtz plane (IHP). In the outer Helmholtz plane (OHP), cations (blue) are fully solvated and screen charge. Excess concentrations decay into the bulk along the surface normal coordinate z. The lower panel shows different potential drops across the interface. In the case of the model depicted above, the potential drop for $U < U_{PZTC}$ is valid.

In absence of specific adsorption, the inner layer capacitance does not depend on the ion concentration.[60] Using Stern's model (Eq. 3.18), C_{inner} can be extrapolated from measuring C at different ion concentrations and plotting it versus calculated $C_{diffuse}$ (Parsons-Zobel plot). $C_{inner}(U)$ curves are bell-shaped with a maximum at the PZC. Due to the reciprocal addition of capacitances in series, the lowest capacitance governs the total

capacitance. Thus, the inner layer capacitance causes the camel-shaped total capacitance to decrease at more extreme electrode polarizations, where C_{diffuse} is very high. Henderson and Schmickler used a crude jellium model to describe the impact of the metal on the inner layer capacitance, which was reviewed by the latter:[60] Solvent molecules and ions are taken as hard spheres with a finite size and exhibit a permanent dipole moment or a net charge, respectively. Depending on the metal-specific bulk electron density, the electrons exceed to some extent the edge formed by the outer most atomic cores. This electron spillover is counteracted by an oscillating electron density decaying into the metal bulk, and a surface dipole moment directed toward the metal is formed. It is increased upon negative polarizations and decreased upon positive polarizations. The bell-shaped decrease in C_{compact} upon polarization is attributed to the dielectric saturation of solvent molecules orienting on the surface. Pseudopotentials are used to account for different faces of solid metals.

More sophisticated descriptions of the EDL involve consideration of finite ion and solvent sizes via mean spherical approximations, modified PB, or lattice gas models, and yield a camel-shaped $C(U)$ dependence.[17, 61]

3.3.2 High-Temperature Molten Salts

The EDL at the metal|molten salt interface was often studied in eutectic alkali halide melts at $T_{\text{m}} = 350\text{-}800\ °\text{C}$.[19, 62] $C(U)$ curves usually exhibit a parabolical shape with the minimum at the PZC (electrocapillary maximum).[19, 62] Similarly to diluted electrolytes, the potential dependence of the capacitance contradicts the complete compensation of the electrode charge by counter-ions in a single layer, as assumed in the Helmholtz model. Despite that the Gouy-Chapman model yields the correct shape of the $C(U)$ curve, it cannot be applied due to the high ionic strength and the generally high capacitance at the PZC.

Dogonadze and Chizmadzhev calculated the ionic structure at a planar wall with binary distribution functions.[63] As a result of strong correlation forces, several ionic layers in z-direction are predicted. Their excess charges are of alternating sign, oscillate and are damped into the bulk. A relationship for the minimum capacitance was derived, and it depends on the ions' Debye radius, correlation radius λ^{-1} and the distance d_1 of the first excess

concentration maximum with respect to the electrode surface (Eq. 3.20)[†]. Despite several approximations and lacking consideration of differently sized ions, the model yields an increase in the capacitance with rising temperature. This was found experimentally and accounted to the decreasing correlation radius, i.e. the thermal disruption of ionic near-order.

$$C_{\text{PZC}} = \frac{\kappa^2 \lambda d_1^2}{8\pi^4}$$

(3.20)

A PB model was derived by Sotnikov and Esin.[64] They assumed that the electrode charge is completely screened by ion vacancies. In the melt, a local kind of crystalline structure is preserved and ions are coordinated by an effective number ξ of counter-ions. Due to the electric field, a dipole may be induced by displacement of the central ion with respect to the center of its coordination shell. The displacement depends on the polarizability α. The formation of a vacancy at the interface requires work to

(i) reverse the formation of the induced dipole,

(ii) transport of the central ion into a suitable bulk vacancy, and

(iii) sorption of $\xi - 1$ countercharges into the bulk (e.g. by ion exchange),

which leaves one net unit charge in the coordination shell. The excess charge and potential distribution oscillate sign-altering in distances of $\pi\delta$, which are comparable to the lattice constant of the salt and are damped into the bulk (Fig. 3.4). Similarly to Stern's model (Eq. 3.18), the first layer is described by the Helmholtz-capacitance in series with a second term, given in equation 3.21.[‡] In the diffuse term, β and δ incorporate the above-mentioned features of the melt (Eqs 3.22 and 3.23). C_{PZC} is given by equation 3.24.

$$\frac{1}{C} = \frac{4\pi d_1}{\varepsilon_{\text{r}}} - \frac{4\pi\delta}{1 - 4\pi\delta\beta|\sigma|}$$

(3.21)

$$\beta = \frac{8\pi q \tilde{c}_0 \alpha(\xi - 1)}{k_{\text{B}}T} = \frac{\kappa^2 \alpha(\xi - 1)}{q}$$

(3.22)

[†] This equation is given in electrostatic units. The Debye length was defined without consideration of the relative permittivity, i.e. $\varepsilon_{\text{r}} = 1$.

[‡] These equations are given in electrostatic units. Electrode polarization is incorporated via the variation of surface charge density $\sigma(U)$ instead of potential. Apart from the first layer, $\varepsilon_{\text{r}} = 1$.

$$\delta = \sqrt{\frac{k_B T}{8\pi q^2 \tilde{c}_0 (\xi - 2)}} = \frac{1}{\kappa \sqrt{\xi - 2}} \qquad (3.23)$$

$$C_{PZC} = \frac{\varepsilon_r}{4\pi (d_1 - \delta \varepsilon_r)} \qquad (3.24)$$

In the first layer, the relative permittivity deviates from 1 and thus is explicitly considered. The number of vacancies and the effective co-ordination number can be estimated from densities of the solid and liquid at a given temperature and the coordination number in the solid for the latter. This model describes the temperature dependence as well as the parabolic potential course well for ions of similar radii and approximately for salts containing small cations.
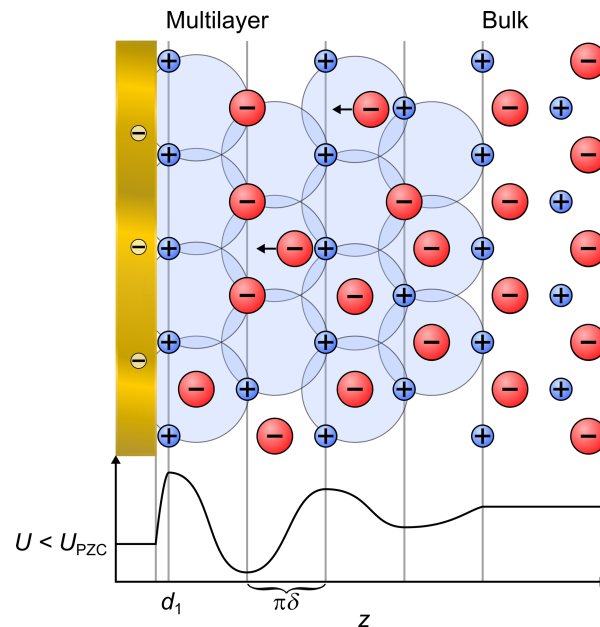
Figure 3.4: Schematic EDL model in high temperature molten salts at negative potentials $U < U_{PZC}$ according to Sotnikov and Esin.[64] The crystalline structure of the solid salt is preserved to some extent in the melt (ordering and free space are exaggerated for clarity). In the first layer at the metal surface (golden), the electrode charge is overscreened by cations (blue). Anions (red) are effectively coordinated by $\xi = 3$ cations (light blue circle). Central anions get shifted with respect to their cationic solvation shell in response to the electric field and thus, a dipole is induced (black arrows). To form a positive vacancy (solvation sheath without a central ion), an anion is transferred into the bulk and one cation of the sheath is replaced by an anion. The second layer overscreens the first layer slightly less with negative charge. Excess charges (excess concentrations) decay oscillating into the bulk along the surface normal coordinate z. The lower panel shows the oscillating potential drop across the interface.

At high temperatures, the capacitance increases more rapidly upon polarization. Graves and Inman account reversible redox reactions for this:[19] On the negative branch of the parabola alkali cations deposit onto the electrode whereas on the positive branch ions from the metal electrode dissolve into the bulk. However, this would restrict capacitive theories as the corresponding equations 3.9-3.11 are valid only for a constant composition. Both the minimal capacitance and the slope of the parabolic branches are determined by the ratio of the ionic radii: For small cations the melt structure is dominated by mutual repulsion of the anions and $C_{\min}$ is comparatively high. In the case of equally sized ion pairs anions cannot pack closely and $C_{\min}$ is lowered due to increasing influence of the cations.

According to a review by Parsons, "there has been no convincing demonstration of the correctness" of the models mentioned above.[17] Kisza criticized the measurement of capacitances by single frequency impedance methods and demands an evaluation by impedance spectra of a broad frequency range. Accordingly, the mentioned temperature-dependence may be an artifact due to a capacitive process which could not be separated from EDL charging. He proposed an alternative PB model based upon Stern's approach (Eq. 3.18): The inner layer overscreens the electrode charge and is followed by a diffuse layer screening the first layer's excess charge. Due to the quasi-crystalline structure in molten salts, electrostatic forces dominate over thermal energy. However, these forces are more equal in voids ("holes") of the molten structure and allow for the placement of ions, which are co-ions with respect to the electrode charge and counter-ions with respect to the inner layer. The number of voids can be assessed through the free volume of the melt and the average hole volume, which can be estimated by the surface tension and thermal energy. The resulting diffuse capacitance (Eq. 3.25) yields a U-shaped potential dependence, which is hyperbolically sharp at very low polarizations.

$$C_{\text{diffuse}} = \mp\, \varepsilon_{\text{r}} \varepsilon_0 \kappa \, \frac{\exp\left\{-\dfrac{q\psi}{k_{\text{B}}T}\right\} - 1}{2\sqrt{\exp\left\{-\dfrac{q\psi}{k_{\text{B}}T}\right\} - 1 + \dfrac{q\psi}{k_{\text{B}}T}}} \tag{3.25}$$

The minus sign is valid for $\psi > 0$ and the plus sign for $\psi < 0$. In absence of specific adsorption, C_{PZC} is given by the inner layer capacitance (Eq. 3.26).

$$\lim_{\psi \to 0} C_{\text{diffuse}} = 0 \tag{3.26}$$

3.3.3 Ionic Liquids

Ionic liquids are solely composed of anions and cations. In contrast to classical aqueous electrolyte solutions, they do not contain a neutral, dipolar solvent molecule. Consequently, the Gouy-Chapman theory cannot be applied to describe their EDL. In comparison to high temperature molten salts, the thermal energy in (room temperature-) ILs is much lower. To melt at lower temperatures, ILs must consist of voluminous and asymmetrical ions. Often, the charge is delocalized and distributed highly inhomogeneously along the molecular structure. Polar, charged segments form domains separated from apolar alkyl chains, resulting in nanosegregation of ILs. All these features impede the application of simple models assuming point charges or charged spheres to describe the EDL of ILs.

In 2006, Kisza applied his model for the EDL of HTMS (Section 3.3.2) also to ILs.[65] This model yields a U-shaped $C(U)$ curve, which is broader than the Gouy-Chapman curve due to lower permittivities of ILs. However, he refrained from a comparison to experimental IL systems. His model is seldomly considered for interpretation of IL capacitances.

In contrast, Kornyshev's model proposed in 2007 received a lot of attention.[20, 45] He derived a PB lattice gas model for charged spheres of equal size. The amount of free space ("voids") is incorporated via the packing parameter η (Fig. 3.5). The potential drops monotonously and is steeper for lower η.
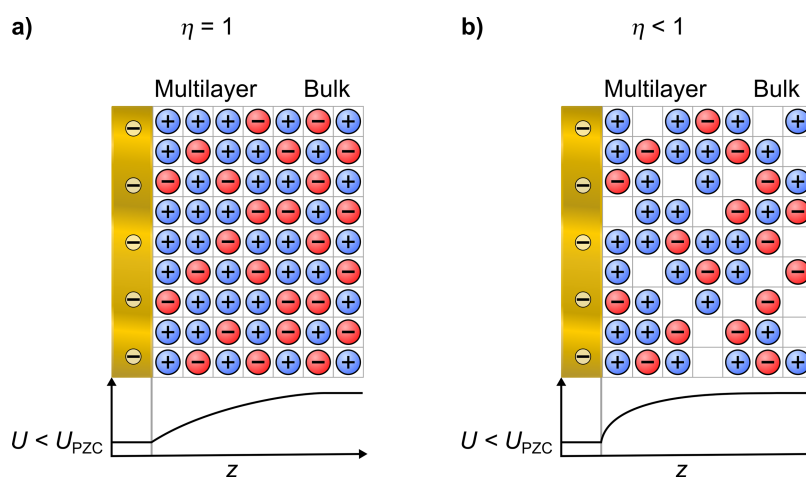
Figure 3.5: Schematic PB lattice gas model to describe the EDL of ILs according to Kornyshev.[45, 66] In the upper panel, the number of adsorption sites (grey lattice) at the electrode (golden) is limited by the size of anions (red) and cations (blue). The melt is either most densely packed ($\eta = 1$, a) or voids (white space) occupy lattice sites ($\eta < 1$, b). The lower panel shows the monotonous potential drop, which is steeper for higher amounts of voids.

According to equation 3.27, the $C(U)$ curves are bell-shaped for $\eta > 1/3$ and camel-shaped for $\eta < 1/3$. The PZC is located at the central extremum (Fig. 3.6). For isolated ions, i.e. $\eta \to 0$, this model converges with the Gouy-Chapman theory (Eq. 3.15).

$$C_{\text{diffuse}} = \varepsilon_r \varepsilon_0 \kappa \frac{\cosh\left(\frac{q\psi}{2k_BT}\right)}{1 + 2\eta \sinh^2\left(\frac{q\psi}{2k_BT}\right)} \sqrt{\frac{2\eta \sinh^2\left(\frac{q\psi}{2k_BT}\right)}{\ln\left[1 + 2\eta \sinh^2\left(\frac{q\psi}{2k_BT}\right)\right]}}$$

$$= C_{\text{diffuse,GC}} \frac{1}{1 + 2\eta \sinh^2\left(\frac{q\psi}{2k_BT}\right)} \sqrt{\frac{2\eta \sinh^2\left(\frac{q\psi}{2k_BT}\right)}{\ln\left[1 + 2\eta \sinh^2\left(\frac{q\psi}{2k_BT}\right)\right]}}$$

(3.27)

$$\lim_{\psi \to 0} C_{\text{diffuse}} = \varepsilon_r \varepsilon_0 \kappa$$

(3.28)

At the PZC, the Debye capacitance is yielded (Eq. 3.28). Different ion sizes can be parametrized by modifying η. In this case, the PZC deviates from extreme points and cannot be easily extracted from the asymmetric $C(U)$ curve.
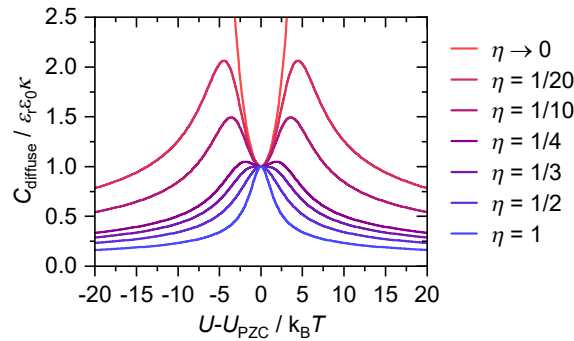
Figure 3.6: Capacitance-potential curves at different packing parameters for a 1:1 electrolyte with ions of equal size according to Kornyshev[45]. Note that the curve for $\eta \to 0$ corresponds to the Gouy-Chapman theory. The capacitance is normalized to the Debye capacitance and the potential to the thermal energy.

When this theory was published, not many experiments were available for comparison. The matching bell-shaped $C(U)$ curves measured by Nanjundiah et al.[67] were reasonably judged to be "most pertinent",[45] while incompatible curves (for example by Gale and Osteryoung,[68] or Baldelli[69]) were neglected. Parabolic $C(U)$ curves found for HTMS (Section 3.3.2) may be described by Kornshev's model, too.[45] Upon melting, a large amount of free volume is acquired, growing with increasing temperature. This leads to substantially smaller η. Along with high thermal energies, the proposed

camel shape may appear parabolic within potential window of measurement. Generally, Kornyshev's model may also be applied for the diffuse layer of aqueous electrolytes when the finite ion size cannot be neglected.[70-72]

Shortly after Kornyshev, Oldham created a PB model based on Stern's approach (Eq. 3.18).[73] The compact layer is filled with spherical counter- and co-ions of equal size, approaching the interface to the distance d_{ion}. The Boltzmannian term in the diffuse layer was changed for the electrical work of counter-ions approaching the interface: Whereas in solutions a solvent molecule can be replaced and fill the ion vacancy created by a charge-compensating ion, counter- and co-ions need to be exchanged in solventless ILs. Overall, this modification leads, in contrast to the parabolic shape in electrolyte solutions, to a bell-shaped $C(U)$ curve (Eq. 3.29). This term is equivalent to Kornyshev's theory for a densely packed electrolyte ($\eta = 1$, Fig. 3.6). C_{PZC} also results in the Debye capacitance (Eq. 3.28).

$$C_{\text{diffuse}} = \varepsilon_{\text{r}}\varepsilon_0 \kappa \frac{\tanh\left|\frac{q\psi}{k_{\text{B}}T}\right|}{\sqrt{2\ln\left\{\cosh\left(\frac{q\psi}{k_{\text{B}}T}\right)\right\}}} \tag{3.29}$$

The difference between U- and bell-shape is phenomenologically explained by Oldham in the following way:[73] "With an electrolyte solution, there are solvent molecules that can easily be displaced to make room for new arrivals [of counter-ions]. For an ionic liquid, however, half of the prime sites along the interface are already occupied at zero charge and the others are soon taken by immigrating counterions. Later arrivals must take up residence 'in the suburbs', where they are farther from the interface and hence contribute less to the capacitance." This phenomenon is called lattice saturation and an independent result of Kornyshev's model. The capacitance is supposed to attenuate at large polarizations (Eq. 3.30).[45]

$$C \approx \varepsilon_{\text{r}}\varepsilon_0 \kappa \sqrt{\left(2\eta\left|\frac{q\psi}{k_{\text{B}}T}\right|\right)^{-1}} \tag{3.30}$$

However, charge oscillations should also be present in ILs, as calculated for HTMS by Dogonadze and Chizmadzhev.[63] Kornyshev acknowledged that his theory fails to predict them.[45] Both Kornyshev and Oldman noted that ILs are neither hard nor spherical and considered their models as a first approach to understand the EDL of ILs.[45, 73] Simulations of charged and hard Lennard-Jones-spheres at an ideally conducting wall result in a $C(U)$ curve

of peaked shape and lower capacitance with increasing polarizations.[74-75] Moreover, they show overscreening of the electrode charge in the first layer and following charge oscillations as found for HTMS. Experimentally, these oscillations are indirectly found due to the appearance of ordered layers at interfaces. In 1988, Horn et al. discovered oscillating rupture forces in the range of molecular diameters with a surface force apparatus while approaching two mica surfaces in pure ethylammonium nitrate and its aqueous solutions.[76] However, they proposed that the ethylammonium cations fully screen (not overscreen) the charge of the mica surfaces and form an ordered Stern layer (first layer), where ethyl chains are directed toward the bulk. Size effects were accounted for the oscillations, primarily. Atomic force microscopy approach curves published by Atkin, Endres, or Mao groups confirm the pronounced layering of ILs at solid interfaces.[27, 77-81] Furthermore, the number and strength of oscillations was found to increase with electrode polarization.[27, 79] Perkin et al. observed that layering changes crucially when increasing the alkyl chain length of the 1-butly-3-methylimidazolium cation by two methylene units.[82] Whereas oscillatory forces typical for lamellar and repeating cation-anion layering were found for the butyl-derivative, the hexyl-derivative exhibited larger distances within the oscillations, leading to the proposal of a bilayer arrangement. Very recently, Mao et al. have shown that surface active ILs exhibit significantly less charge oscillations, and demonstrated its impact on electrochemical applications.[24] Due to the presence of long alkyl chains in inherently amphiphilic ILs, distinct polar and apolar domains form. Resulting bilayers align along the electrode surface upon polarization. Ionic headgroups are confined in polar domains, but less associated as in short-chain ILs, which leads to a higher density of free ions. In contrast to commonly used non-amphiphilic ILs, overscreening of the Helmholtz layer is compensated in the following layer, but not overcompensated. Bulk-like electroneutrality is reached sooner. Consequently, shorter Debye lengths as well as EDLs, and therefore higher capacitance are yielded.

The asymmetry in structure and charge distribution of IL ions, partially caused by the presence of alkyl chains, fundamentally distinguishes ILs from HTMS. To account for alkyl chains, neutral "tail" spheres were attached to charged spheres in Monte Carlo simulations.[83] $C(U)$ curves with a pronounced camel shape were obtained, supporting Kornyshev's theory for a low packing parameter. Interestingly, the neutral spheres were shown to act as latent voids: By translational movement or rotation they can be replaced by

charged groups (Fig. 3.7), which leads to the rising capacitance branches starting from the central minimum. Capacitance maxima (camel humps) mark the onset of lattice saturation due to maximal charge density. The chain length – curve shape relation agrees with experimental results. Short alkyl chains lead to a bell shape and long chains give a camel shape (Nishi et al. as shown below).[83-84]
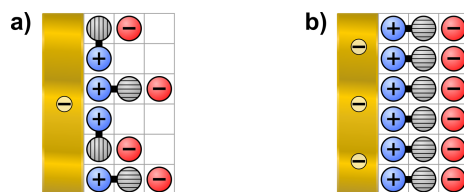
Figure 3.7: Schematic model to describe the role of alkyl chains in ILs according to Fedorov, Georgi and Kornyshev.[83] The number of adsorption sites (grey lattice) at the electrode (golden) is limited by the size of anions (red) and cations (blue). Besides charged groups, real voids (white space) and neutral substituents (grey, striped) of cationic spheres occupy lattice sites. a) At slightly negatively surfaces charges, cationic headgroups are oriented toward the electrode or the whole molecules lies flat on the electrode. b) At more negatively surface charges, the neutral tails are repelled from the electrode surface and replaced by cationic headgroups. The maximal amount of space charge density is limited.

Numerous $C(U)$ curves were measured with different techniques for a variety of systems: Mostly Hg(l)[67-68, 84-85], poly or single crystalline Au[86-98], Pt[69, 88, 96-97, 99-100], or glassy carbon (GC),[24, 67, 86, 97, 101] working electrodes (WEs) were employed.[20] Imidazolium[24, 69, 84-91, 94-99, 101-102]- and pyrrolidinium[96-97, 100]-based ILs were studied predominantly.[20] Despite the large electrochemical potential window of ILs (Section 2.2), capacitances are often determined within narrow potential ranges only, to ensure the absence of faradaic processes.[94] The measured curves exhibit a variety of shapes, which can be classified as bell-, camel-, U-shaped, constant within some microfarads or other (Fig. 3.8). Table 3.1 shows literature examples for various shapes found for exemplarily chosen n-alkyl-methyl-imidazolium ($C_n Im^+$) ILs with similar or different anions.

Nishi et al. provide $C(U)$ curves of [C_2Im][BF_4] and [C_8Im][BF_4] at the Hg(l) surface as shown in figure 3.8 a) in upper and lower panels, respectively.[84] Capacitance values measured via the pendant drop method yield a bell- and a camel-shaped curve, respectively, and thus, support Kornyshev's theory (filled symbols). When employing EIS, the capacitance values change dramatically, and the curve shape cannot be easily classified (open symbols). Pajkossy et al. analyzed the interfaces of different ILs and

solid Au(100) electrodes with EIS (Fig. 3.8 b).[93] Within the potential range measured, the capacitance values are almost constant or change little. These results do not support the Kornyshev model. Other EIS experiments provide a large variety of data, which do or do not agree with his theory (Tab. 3.1). Even for similar ILs, electrode materials, and analytical methods, contradictory results have been reported in literature (e.g. $C_4C_1ImBF_4$|Au, EIS).[86-88, 91, 94] Values extracted from EIS measurements highly depend on several factors, e.g. cell alignment and geometry, equilibration time prior measurement, start potential and direction of the scan, applied frequencies, or equivalent circuit employed for data interpretation.[90, 98, 101-104]
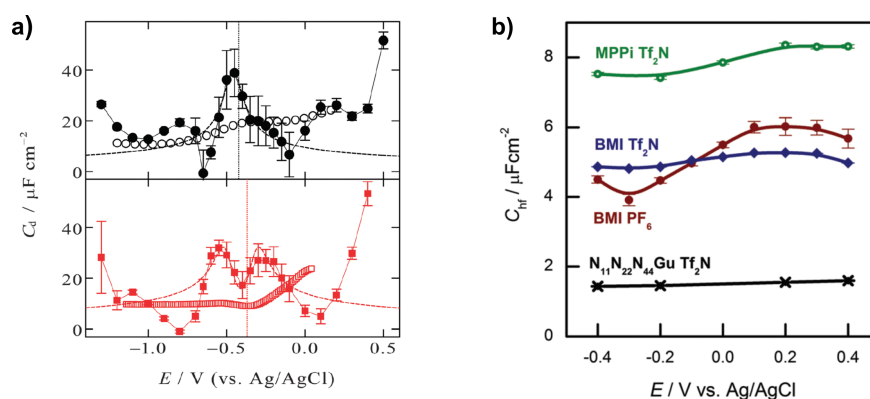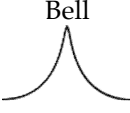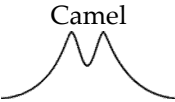
Figure 3.8: Selected experimental capacitance (C) – potential (E) curves of ILs at different metal electrodes. a) Capacitances measured by Nishi et al. at the IL|Hg(l) interface via EIS (open symbols) or the pendant drop method (filled symbols).[84] Vertical lines indicate the PZC. Dashed lines show a fit of Kornyshev's theory to central values around the PZC. Upper panel (black circles) – [C_2Im][BF_4], lower panel (red squares) – [C_8Im][BF_4]. b) Capacitances measured by Pajkossy et al. at the IL|Au(100) interface via EIS.[93] MPPi Tf$_2$N (green) – N-propyl-N-methyl-piperidinium Tf$_2$N, BMI Tf$_2$N (blue) – $C_4C_1ImTf_2N$, BMI PF$_6$ (red) – [C_4Im][PF_6], $N_{11}N_{22}N_{44}Gu$ Tf$_2$N (black) – N,N-dibutyl-N',N'-diethyl-N'',N''dimethyl-guanidinium Tf$_2$N. Copied with permission from [84] - Published by the PCCP Owner Societies and [93] - Published by the PCCP Owner Societies.

Oldham stressed that measuring an IL under equilibrium conditions is difficult because they generally exhibit slow dynamics due to their high viscosity.[73] However, high perturbation frequencies in EIS are required to measure the EDL capacitance apart from pseudocapacitive features (Section 4.4). Theoreticians Kornyshev and Fedorov also account the divergence between experiment and theory to difficulties in measuring under equilibrium conditions.[20] Intrinsic limitations of EIS are debated.[70-72] On the other side, experimentalists, Roling, or Pajkossy and Jacob, desire a theory which includes the frequency or time dependence.[93, 100, 102, 105]

Table 3.1: Differently shaped capacitance potential curves of C_nIm^+ ILs at electrode surfaces measured in literature. Sorting refers to the general shape. Smaller humps may be imposed on these curves. ACV – alternating current voltammetry. AOT – 1,4-bis(2-ethylhexoxy)-1,4-dioxobutane-2-sulfonate. HOPG – highly oriented pyrolytic graphite.

$C(U)$ curve shape	Nonionic Conductor	Chain length	Anion	Method	Reference
Bell	Au(111)	2, 4, 8	BF_4^-	EIS (single f_{AC})	Alam[87]
	Au(poly)	4	BF_4^-	EIS	Gomes[88]
	Au(poly)	4	TfO^-	ACV, EIS	Gore[89]
	GC	4	BF_4^-	EIS	Mao[24]*
	Hg(l)	2	BF_4^-	Drop time	Nanjundiah[67]
	Hg(l)	2	BF_4^-	Pedant drop	Nishi[84]
	Hg(l)	2	Tf_2N^-	Pedant drop	Nishi[85]
Camel	Au(poly)	4	TfO^-	ACV, EIS	Gore[89]
	GC	2, 4, 6	Cl^-	EIS	Lockett[101]
	GC	4	BF_4^-	EIS	Mao[24]*
	GC	4	AOT^-	EIS	Mao[24]
	Hg(l)	8	BF_4^-	Pedant drop	Nishi[84]
	Pt(poly)	4	BF_4^-	EIS	Islam[96]
U / Parabolic	Au(poly)	2	Tf_2N^-	EIS	Alam[86]
	Au(poly)	2, 4, 8	BF_4^-	EIS	Alam[86]
	GC	4, 8	BF_4^-	EIS	Alam[86]
	HOPG	4	BF_4^-	EIS	Alam[86]
	Pt(poly)	4	BF_4^-	EIS	Baldelli[69]
	Pt(poly)	4	$C(CN)_2^-$	EIS	Aliaga[99]
Almost constant (within 3 µF)	Au(100)	4	BF_4^-	EIS	Gnahm[91]
	Au(100)	4	Tf_2N^-	EIS	Pajkossy[93]
	Au(111)	4	PF_6^-	EIS	Gnahm[90]
	Au(poly)	4	BF_4^-	FT-ACV	Lucio[94]**
	Au(poly)	4	PF_6^-	EIS	Vargas-Barbosa[95]
	Au(poly)	4	PF_6^-	EIS	Gomes[88]
	Au(poly)	4	Tf_2N^-	EIS	Gomes[88]
	HOPG	4	BF_4^-	EIS	Müller[106]

* Mao et al. generally classified the shape to be bell-like.[24] At T = 25 °C and 70 °C, humps are imposed on the bell. At T = 130 °C and 200 °C, two distinct maxima are seen.

** Lucio et al. classified the shape of their curve to be U-shaped.[94] However, changes in their $C(U)$ curve barely exceed 1 µF cm^{-2}.

Slow dynamics of ILs at interfaces manifest in multiple experiments. Makino et al. demonstrated "ultraslow relaxations" (up to 0.4 s) in charging currents upon potential steps of ILs at a Pt electrode.[107] During the electrocapillary measurements of Nishi et al., equilibration times in the order of minutes were needed to reach a steady state surface tension.[84] When stopping a rotating disc covered with an IL, molecular ordering may take minutes to hours, as shown by Anaredy and Shaw.[108] They found that thick, anisotropic layers of up to 2 μm in length are formed, where thickness and ordering time highly depend on the composition of the studied IL. The rotational freedom of a probe dye was measured by Wang et al. as a function of the distance normal to the electrode surface.[38] By reasonably assuming that an impeded rotation is caused by complexation with anions, they concluded that the free charge density of the studied IL changes over 100 μm. Despite debates about ion pairing (Section 2.2), this still gives a proof of long-ranging structures formed in ILs at interfaces. Lindner et al. determined entropy changes during EDL charging.[109] Upon potential steps, steady states of heat are reached slowly after 200 ms. The measured entropies of EDL formation are much larger than expected from purely configurational entropies of a two-dimensional lattice gas model. They concluded that the mobility of ions adsorbed at the interface depends on the electric field strength and is strongly restricted in comparison to bulk ions.

Restricted ion mobility at charged interfaces is supported by findings of Motobayashi et al.:[110] By application of surface enhanced attenuated total reflection infrared spectroscopy they monitored orientation- and concentration-dependent signals of [C_4Im][Tf_2N] at the Au(poly) electrode. A hysteresis in several band intensities was found while changing the direction of electrode polarization and accounted to the slow response of the IL upon potential changes. They explained their findings in with a model of lamellar layers consisting predominantly of either cations or anions. The hysteresis is caused by an activation barrier which is required to break these layers and given by overpotentials. Steric hinderance of larger ions leads to higher activation barriers.[111] Ring moieties of short *n*-alkyl-methyl-imidazolium cations often adopt a flat orientation on Pt or Au surfaces at negative electrode polarizations and erect at positive potentials, as shown by first spectroelectrochemical studies of the Baldelli group, or later by Motobayashi et al.[99, 110, 112] However, for longer alkyl chains the ring moiety stays more rigid.[111]

The behavior of electrode material exposed to the IL is also hard to understand at the interface. Recent in situ scanning tunneling microscopy studies by Rudnev et al. show that the interaction of the Au(111) surface with imidazolium- and pyrrolidinium-based ILs is hard to generalize:[113] A comparison among different ILs with equal or different cations or anions reveals that the nature of the anion affects the interface even in negatively polarized regions, where a predominant covering of cations is expected, and vice versa. At highly negative polarizations, the typical herringbone reconstruction is present, whereas etching takes place at moderately negative potentials. Onset potentials depend on both the scan direction and the IL composition. Wen et al. observed changing adsorbate structures on Au(111) at moderately negative potentials.[114] These temporal fluctuations may suggest that the thermodynamically most favorable adsorption state is either kinetically hindered and other states are occupied instead, or the energetical minimum is not clearly distinct from adjacent states, complicating studies in this potential range.

Clearly, the findings mentioned above show that there is a need for in-depth studies of the IL∣electrode interface to understand its EDL, especially at solid electrode materials.

4 Characterization Methods

Various techniques are used to investigate interfaces. In this work, the following experimental techniques were applied:

(i) The Langmuir trough is used to characterize ILs at the air|water interface as well as to deposit IL films on gold surfaces via the LB method.

(ii) Insight into the IL film composition and its state of adsorption on the substrate are gained from XPS.

(iii) Contact angle measurements (Section 3.1) provide a macroscopic characterization.

(iv) EIS is applied measure the capacitive behavior at the solution|electrode interface, yielding coarse and supramolecular information of the interface as a whole system.

(v) More detailed information, i.e. submolecular changes in the structure and orientation of molecules present at the air|metal and electrolyte|metal interfaces, can be obtained by means of PM IRRAS.

Within the scope of this chapter, physical fundamentals of the applied methods and their results' interpretation are explained.

4.1 Langmuir-Blodgett Method

The Langmuir-Blodgett method offers a possibility for the fabrication of well-ordered films with thicknesses in the range of single monolayers up to multilayers.[115] First, a small amount of molecules is placed in form of a crystal or solved in a volatile solvent at the vapor|liquid interface in a Langmuir trough. The molecules must be insoluble in the used subphase. With suitable barriers, the interfacial area available per molecules can be controlled, and the state of compression (expansion) determines the properties of the two-dimensional system (Fig. 4.1) Often amphiphilic molecules are used because their usually polar headgroups orient toward an aqueous subphase, whereas their hydrophobic tails are directed toward air. The interfacial behavior is monitored by measuring the surface pressure with a Wilhelmy balance. For a strongly wetting subphase, the surface pressure is

given by the force ΔF pulling the balance into the subphase normalized to the circumference l of the plate after calibration (Eq. 4.1).

$$\Pi = \frac{\Delta F}{l}$$

(4.1)

After formation of a suitable monolayer, it may be transferred onto solid substrates. A constant $\Pi(A_{\text{molec}})$ is maintained throughout the transfer by continously adjusting the position of the barriers. Hydrophobic substrates can be immersed from air into the film-covered subphase, yielding a monolayer with tails oriented toward the surface (X-type). A monolayer oriented with their headgroups toward the subtrates may be deposited by withdrawing the substrate from the film-covered subphase (Z-type). Consecutive immersion and withdrawal yield Y-type multilayers, in which groups of similar polarity (heads or tails) are directed toward each other.
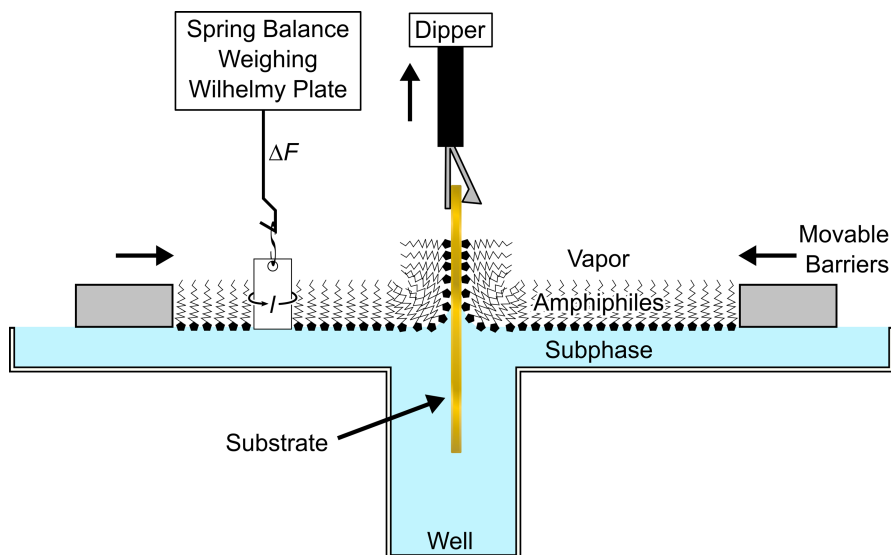
Figure 4.1: Scheme of a Langmuir trough performing a Langmuir-Blodgett transfer. Amphiphiles (black, size exaggerated) are deposited on a liquid subphase (blue). A solid substrate (golden) is withdrawn from the subphase to fabricate a Z-type monolayer. Barriers (grey) compress the interfacial area to maintain the surface pressure, which is measured via the Wilhelmy plate (white).

4.2   X-Ray Photoelectron Spectroscopy

X-ray photoelectron spectroscopy is used to analyze the composition and chemical state of elements in suitable samples.[116] This technique is based on the external photoelectric effect: A photon interacts with an orbital and its

whole energy $h\nu_{\text{photon}}$ gets absorbed (h – Planck constant, ν_{photon} – photon frequency). If the energy is sufficiently high to overcome the electron's binding energy, it will be emitted. The resulting photoelectron contains the spare energy of the photon as kinetic energy, which is analyzed. From the known photon energy the binding energies are calculated (Eq. 4.2). Additionally, the work function ϕ of the instrument must be overcome.

$$h\nu_{\text{photon}} = E_{\text{b}} + E_{\text{kin}} + \phi \qquad \textbf{(4.2)}$$

A set of core electron binding energies is specific for each element and used to identify them (except for hydrogen and helium, which contain valence electrons only). Small shifts in E_{b} indicate different chemical environments and oxidation states. The intensity of a photoelectron line is proportional to the element concentration and allows for quantification.

After photoemission (Fig. 4.2 a), the hole relaxes to outer electron orbitals via emission of Auger electrons or X-ray fluorescence (Fig. 4.2b,c). Outer holes are then filled by charge compensation via contact to the ground or an electron gun.
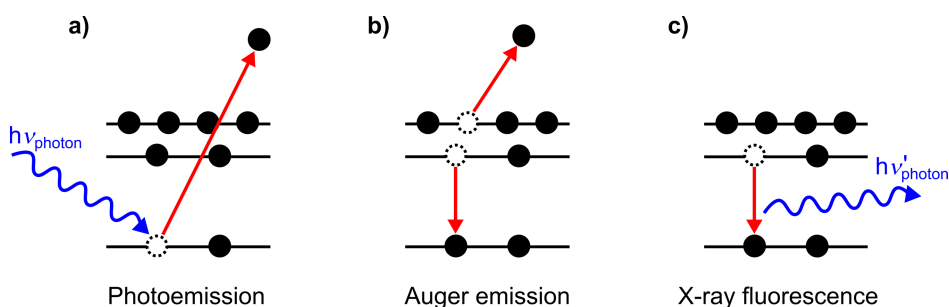
Figure 4.2: Schematic photoelectron emission a) and secondary processes: b) Auger effect and c) X-ray fluorescence. Electrons are represented by black spheres horizontal lined energy levels. Holes left are shown by white circles with a dotted circumference. X-ray photons with the energy $h\nu$ are depicted as blue waves.

4.2.1   Binding Energy and Chemical Shift

The binding energy is specific for a given element and its chemical environment. It can be described as the difference in energies of the final state with $N - 1$ electrons and the N-electron initial state during photoemission (Eq. 4.3).[117]

$$E_{\text{b}} = E_{N-1} - E_N \qquad \textbf{(4.3)}$$

Essentially, the measured E_{b} is an ionization energy. With Koopmans' theorem, it is interpreted as the negative orbital energy. However, this

interpretation is valid only for an electron shell which stays frozen after emission. Generally, the electron shell is in an unfavorable state with a core hole, and in order to minimize energy, it relaxes. Furthermore, electron correlation and relativistic effects contribute to E_b. In the case of electrons emitted from outer levels, correlation and relaxation energies may compensate each other. For core levels however, relaxation dominates.

Different chemical environments affect the initial and final state energies, and thus the binding energy of a given photoelectron line may vary. This effect is called "chemical shift". For example, electronegative substituents withdraw electron density. As a result, the atomic core charge is less screened, and the attraction to the remaining electrons rises along with the energy required to remove them. Often, shell relaxation affects the final states similarly and the chemical shift is in line with the state of oxidation, i.e. E_N changes most significantly. Nevertheless, final state effects may also affect the binding energy, leading to counter-intuitive chemical shifts. Atomic relaxation originates primarily from the rearrangement of outer orbitals. Extra atomic relaxation depends strongly on the investigated material and may induce charge transfers or polarizations with neighboring atoms.

4.2.2 Intensity and Surface Sensitivity

The measured photoelectron intensity I depends on several factors.[117] The photoionization cross section is specific for a given photon energy and element line. Instrumental factors influence the measured intensities through the angle of incidence, angle of detection, photon flux, or spot size. Generally, the element concentration is proportional to the intensity for a homogeneously distributed element. Inside the sample, emitted electrons may collide inelastically and lose a part of their kinetic energy. This is described by the attenuation length of the electrons, which depends on the matrix as well as the electron's kinetic energy. The attenuation lengths lie usually within some nanometers and this leads to two severe effects: Firstly, only photoelectrons of outer atomic layers retain enough energy to leave the sample. Low attenuation lengths lead to the surface sensitivity of this technique. Consequently, low pressures are needed to minimize the collisions between electrons and molecules in the gas phase, maximizing the number of detected electrons. Secondly, the inelastically scattered electrons may still leave the sample and become detected, forming a background

which must be corrected. Besides matrix collisions, the kinetic energy also affects the electron transmission to the detector.

4.3 Vibrational Infrared Spectroscopy

Molecular vibrations are sensitive to the molecular structure and environment, which makes vibrational spectroscopy an attractive analytical technique.[118] Information about the composition, constitution, conformation, as well as important intra- and intermolecular interactions are contained in vibrational spectra, complicating their interpretation. Vibrations can be probed by various methods, such as infrared spectroscopy (IRS), Raman spectroscopy, sum frequency generation, or electron energy loss spectroscopy. In the case of infrared spectroscopy, vibrations are excited by direct absorption of light.

4.3.1 Resonance Frequencies and Intensities

The excitation of normal modes can be described by the quantum harmonic oscillator, whose potential energy is classically based on Hooke's law. The resulting energies are quantized (v – vibrational quantum number) and equidistantly distributed (Eq. 4.4, Fig. 4.3).[50]

$$E_{\text{vib}} = \left(v + \frac{1}{2}\right)h\cdot\nu_{\text{osc}} = \left(v + \frac{1}{2}\right)h\cdot\frac{1}{2\pi}\sqrt{\frac{k}{m}} \tag{4.4}$$
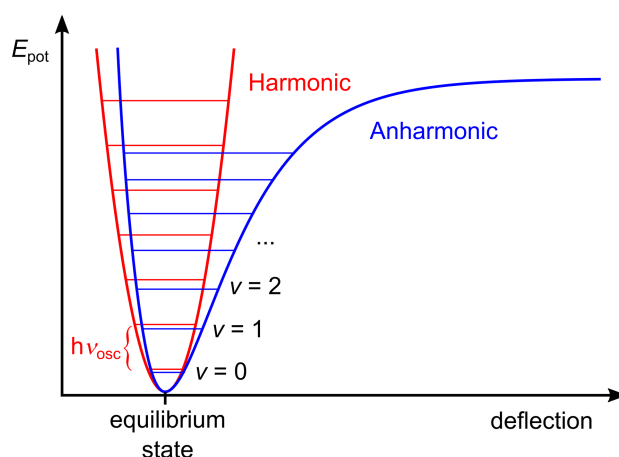
Figure 4.3: Potential energy E_{pot} curves as a function of deflection (separation of nuclei or change of a bond angles) and vibrational energy states of the harmonic (red) and anharmonic (blue) oscillator.

The resonance frequency ν_{osc} is proportional to the force constant k of the involved bond and the reduced mass m. Consequently, the energetic position of a vibrational state is determined by bond strength and participating nuclei.

In order to excite a state by absorption of light, the photon's energy must be approximately equal the energy difference of the states involved (Eq. 4.5). Furthermore, the probability for a transition, and thus the extinction coefficient ϵ, depends on the overlap and strengths of the electric field $\vec{E}$ and transition dipole moment $\vec{M}$ (Eq. 4.6). The whole electric dipole moment of the molecule must change during deflection, leading to nonzero $\vec{M}$. For equal $\vec{E}$, equal concentrations, and appropriate $h\nu_{photon}$, the relative intensities of vibrational lines depend on the polarity of their deflected groups, which determine the molecular dipole change and therefore $\vec{M}$.

$$h\nu_{photon} \cong E_{vib}(v) - E_{vib}(v \pm 1) = h \cdot \nu_{osc} \tag{4.5}$$

$$\int \epsilon \, d\tilde{\nu} \propto \left| \vec{E} \cdot \vec{M} \right|^2 \tag{4.6}$$

Transitions are permitted for $\Delta v = \pm 1$, and due to equidistant energy states only one absorption line is expected per vibration. However, the model of the harmonic oscillator does neither consider bond dissociation at high internuclear distances nor strong coulombic repulsion of close nuclei. As implemented with the Morse potential, the anharmonic oscillator yields a more realistic approximation (Fig. 4.3). Anharmonicity enables transitions to overtones $\Delta v = \pm 2, \pm 3, \ldots$, which are forbidden in the harmonic approximation. Non-equidistant energy states explain differing frequencies of e.g. hot bands. First overtones are expected to resonate at slightly lower wavenumbers $\tilde{\nu}$ than twice their fundamentals ($\tilde{\nu}_{v=2} \lesssim 2\tilde{\nu}_{v=1}$).

Overtones or combination bands are usually less populated and weak. However, their intensity may be enhanced by Fermi resonance (FR). For this, two conditions must be fulfilled: (i) The vibrations must resonate at approximately equal frequencies (i.e. they are accidentally degenerated), and (ii) have the same symmetry. As a result of the FR, intensity is transferred from the generally stronger fundamental mode to the resonating state and both drift apart in frequency.

Energies required to excite vibrations are also sufficient to excite rotations. Both excitations overlap and form a band, whose central position is dominated by vibrational energies. In the case of condensed matter, molecular interactions are strong and impede free rotations, which leads to

broad and overlapping bands. On the other hand, moments of inertia are high for bigger molecules, and thus their rotation constant becomes small, leading to an overall lower frequency range of populated rotation states.

4.3.2 Infrared Reflection Absorption Spectroscopy

Techniques in both internal and external reflection configuration can be applied to probe vibrational modes on surfaces.[119] To investigate metal surfaces via attenuated total reflection (ATR, internal) IR spectroscopy, a thin but rough metal film needs to be deposited onto an IR transparent prism made of e.g. diamond or silicon. Metal surfaces of smooth single crystals can be probed externally by infrared reflection absorption spectroscopy (IRRAS). Spectra depend on the polarization of the irradiating light, its angle of incidence, as well as thicknesses and optical constants, i.e. the refractive index n and the attenuation coefficient k, of matter within the beam path. These systems can be accurately described by the Maxwell- and Fresnel-equations.

In general, metals exhibit high values of k in comparison to common molecular matter. At high angles of incidence with respect to the surface normal, e.g. 80 °, the phase of p-polarized light shifts by $\pi/2$ upon reflection, causing the electric field vectors of incident and reflected beams to overlap. As a result of this constructive interference, an ellipsoid standing wave is formed at the interface in z- and x-direction (Fig. 4.4 a). Under the same circumstances, the phase of s-polarized light is shifted by π, which leads to a destructive interference at the interface in y-direction (Fig. 4.4 b).
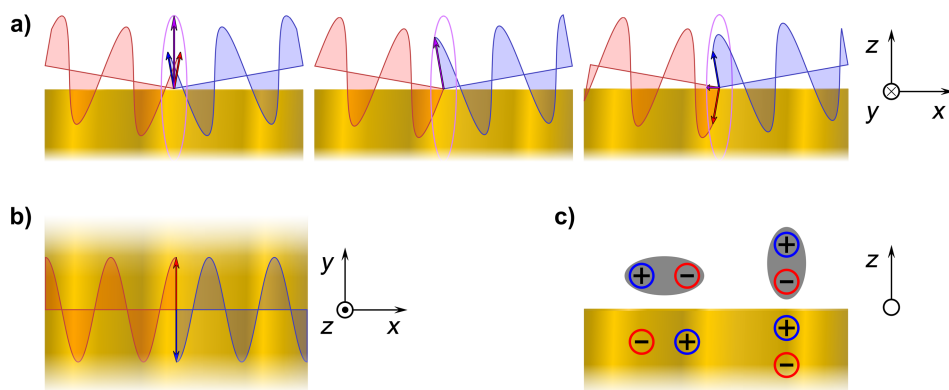
Figure 4.4: a) At the metal (golden)|air/vacuum interface at grazing incidence, p-polarized light is shown at different states of propagation. Incident (red) and reflected (blue) waves overlap and form an ellipsoid standing wave (pink). b) s-polarized light cancelling at the interface upon reflection under the same conditions. c) Creation of image charges and surface dipoles on a metal surface. z-components are enhanced, whereas x- and y-components are counteracted.

Moreover, metal electrons are mobile and polarizable, which leads to image charges at the interface and the formation of surface dipoles. Consequently, dipoles being excited in parallel to the surface are counteracted, whereas dipoles in z-direction become enhanced (Fig. 4.4 c). Due to this "metal surface selection rule" (MSSR), only z-components of molecular vibrations are probed.

4.3.3   Polarization Modulation

If low surface concentrations are to be probed by IRRAS, long acquisition times are needed in order to achieve a sufficient signal to noise ratio. However, water vapor, carbon dioxide, and hydrocarbons are present in air. Electrochemical measurements demand an ionic conductor which usually is a liquid electrolyte. Species present in the latter cover spectral regions of interest. Concentrations of airborne and electrolyte species fluctuate significantly over measurement time in comparison to the usually small total absorbance of sample species, which complicates their measurement and impedes the use of separately recorded background spectra. This obstacle may be overcome by modulating the incident light between s- and p-polarizations with a photoelastic modulator (PEM, Fig. 4.5):[120] Both beams contain information about the molecules within the beam path, but upon reflection from a metal surface only p-polarized light probes interfacial molecules due to the MSSR.
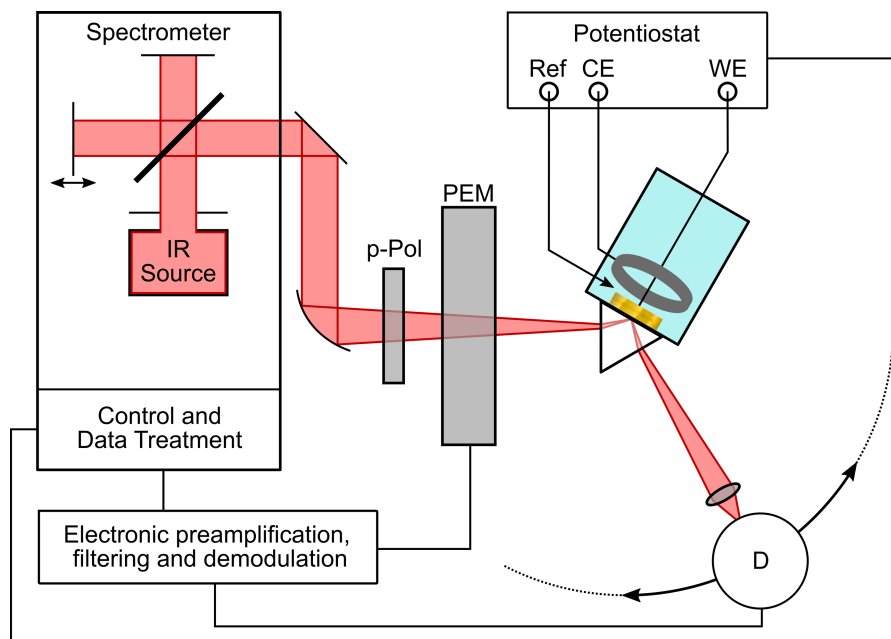
Figure 4.5: Scheme of an electrochemical in situ PM IRRAS setup: Originating from an IR source (e.g. a globar) the light (red) is modulated firstly in the interferometer. After linear polarization (p-Pol), the light is modulated by the photoelastic modulator (PEM). Next, the beam is focused through a prism (white, e.g. an equilateral CaF_2 crystal) to the spectroelectrochemical cell, consisting of the working electrode (golden disk), counterelectrode (CE, grey ring), reference electrode (Ref, black arrow), and electrolyte (blue). The electrolyte cavity between the prism and the WE is small and usually set to a few micrometers. The electric potential at the WE is controlled by the potentiostat, which is controlled by the spectrometer. Upon reflection, the light is focused on the detector (D), and followingly electronically preamplified, split and filtered. A lock-in amplifier receives information about the frequency of the voltage which is applied to the PEM. After dual-channel acquisition, the interferograms are converted to spectra.

The polarization modulation (PM) is caused by a half-wave retardation (HWR) of light passing through an IR transparent, birefringent single crystal (ZnSe), which is mechanically deformed by a piezoelectric under alternating voltage. The detected reflectivity R_D then consists of the polarized reflectivities (R_s, R_p), and their fractions vary with time t. Equation 4.7 yields the detected reflectivity for p-polarized light entering the PEM, whose strain axis is tilted by 45 ° with respect to the orthogonal polarization planes.

$$R_D(t) = \frac{R_p + R_s}{2} + \frac{R_p - R_s}{2} \cos\left[\frac{\tilde{v}}{\tilde{v}_{HWR}} \pi \cos(\omega_m t)\right]$$ (4.7)

Table 4.1 elucidates scenarios for the detected reflectivity depending on different $\omega_m t$. The inciding polarization is not changed at zeros of the modulation (no deformation). Between the zeros and extrema, the PEM

yields elliptically polarized light. At most extreme stresses the polarization shifts by 90°. However, the complete shift only occurs for single wavenumbers $\tilde{\nu}_{\text{HWR}}$, to which the HWR has been set, and whole multiples of them. Deviant wavenumbers are retarded insufficiently, which leads to two consequences:

(i) Maximum signal intensity is gained at $\tilde{\nu}_{\text{HWR}}$ and approximately some tens to hundreds of wavenumbers around. $\tilde{\nu}_{\text{HWR}}$ depends on the voltage applied to the piezoelectric and must be set to the spectral region of interest for maximum phase shift and intensity.

(ii) An additional background in the form of Bessel functions $J_\tau(\tilde{\nu}/\tilde{\nu}_{\text{HWR}} \cdot \pi)$ of integer order τ is introduced into the spectrum, which originates from a Fourier expansion of the twofold cosine relationship.

Table 4.1: Detected reflectivities for different modulation times. ζ_ω and $\zeta_{\tilde{\nu}}$ denote possibly different natural numbers (0, 1, 2, …).

$\omega_{\text{m}} t$	$\dfrac{\tilde{\nu}}{\tilde{\nu}_{\text{HWR}}} \pi \cos(\omega_{\text{m}} t)$	$R_{\text{D}}(t),$ $\tilde{\nu} \neq \tilde{\nu}_{\text{HWR}} + \zeta_{\tilde{\nu}} \cdot \tilde{\nu}_{\text{HWR}}$	$R_{\text{D}}(t),$ $\tilde{\nu} = \tilde{\nu}_{\text{HWR}} + \zeta_{\tilde{\nu}} \cdot \tilde{\nu}_{\text{HWR}}$
$\dfrac{\pi}{2} \pm \zeta_\omega \pi$	0	R_{p}	R_{p}
$\dfrac{\pi}{3} \pm \zeta_\omega \pi$	$\dfrac{\tilde{\nu}}{\tilde{\nu}_{\text{HWR}}} \dfrac{\pi}{2}$	$\dfrac{R_{\text{p}} + R_{\text{s}}}{2} + \dfrac{R_{\text{p}} - R_{\text{s}}}{2} \cos\left[\dfrac{\tilde{\nu}}{\tilde{\nu}_{\text{HWR}}} \dfrac{\pi}{2}\right]$	$\dfrac{R_{\text{p}} + R_{\text{s}}}{2}$
$0 \pm \zeta_\omega \pi$	$\dfrac{\tilde{\nu}}{\tilde{\nu}_{\text{HWR}}} \pi$	$\dfrac{R_{\text{p}} + R_{\text{s}}}{2} + \dfrac{R_{\text{p}} - R_{\text{s}}}{2} \cos\left[\dfrac{\tilde{\nu}}{\tilde{\nu}_{\text{HWR}}} \pi\right]$	R_{s}

Experimentally, one signal S_{raw} is built from two simultaneously acquired spectra:

(i) The differential signal ΔR in the numerator of equation 4.8 is separated from the twofold modulated interferogram after high pass filtering and application of a lock-in amplifier detecting the second harmonic $R_{\text{D}}(2\omega_{\text{m}})$.

(ii) Low pass filtering yields the average signal $\langle R \rangle$ shown in the according denominator.

A gain factor g is required to account for different electronic treatments in the two channels. In order to separate the signals, ω_{m} is much higher than the modulation frequency of the interferometer. Both signals contain absorptions from species within the beam path and isotropically oriented molecules close to the surface, and their ratio compensates these.

$$S_{\text{raw}} = \left(\frac{\Delta R}{\langle R \rangle}\right)_{\text{exp}} = g \frac{\left|R_{\text{p}} - R_{\text{s}}\right| \cdot J_2}{\dfrac{R_{\text{p}} + R_{\text{s}}}{2} + \dfrac{R_{\text{p}} - R_{\text{s}}}{2} \cdot J_0} \qquad \text{(4.8)}$$

On highly reflecting metals, the second term in the denominator can be neglected (Eq. 4.9), because $R_{\text{s}} \approx R_{\text{p}} \Rightarrow (R_{\text{s}} + R_{\text{p}}) \gg (R_{\text{s}} - R_{\text{p}})$ and $J_0 < 1$.

$$S_{\text{raw}} = \left(\frac{\Delta R}{\langle R \rangle}\right)_{\text{exp}} \approx g \frac{\left|R_{\text{p}} - R_{\text{s}}\right| \cdot J_2}{(R_{\text{p}} + R_{\text{s}})/2} \qquad \text{(4.9)}$$

The background can be corrected by subtraction of an uncovered surface's spectrum $S_{\text{background}}$ from the spectrum of a surface covered with the sample. Due to the high spectral impact of changes in the cell geometry and beam path, a sufficiently precise reproduction of a second experiment under equal conditions is hardly achievable in case of in situ experiments, and the background must be estimated instead, for example with a polynomial function. After background subtraction the measured signal ΔS adopts the form of the theoretical PM IRRAS signal (Eqs 4.10 and 4.11). It is proportional to the absorbance $\mathcal{A}$ for small absorptions, which is usually valid when PM IRRAS is applied.

$$\Delta S = S_{\text{raw}} - S_{\text{background}} \qquad \text{(4.10)}$$

$$\left(\frac{\Delta R}{\langle R \rangle}\right)_{\text{theo}} = \frac{\left|R_{\text{p}} - R_{\text{s}}\right|}{(R_{\text{p}} + R_{\text{s}})/2} \approx 2.3 \, \mathcal{A} \qquad \text{(4.11)}$$

In certain cases, the background is hard to correct by manual spline-interpolation. Difference spectra can be used to track intensity changes. Spectra at variable electrode potentials $S_{\text{raw}}(U)$ can be referenced to the spectrum of a selected potential $S_{\text{raw}}(U_{\text{ref}})$ (Eq. 4.12).

$$\Delta S_{\text{raw},U} = S_{\text{raw}}(U) - S_{\text{raw}}(U_{\text{ref}}) \qquad \text{(4.12)}$$

Due to relaxation of strained in situ cell components, the thin cavity between the prism and the electrode may change its thickness over time. As a result, the water background of the spectrum changes. This can be partially compensated by a vertical offset of the spectra to averaged values in non-adsorbing spectral regions.

4.3.4 Determination of Molecular Orientation and Order

The measured absorbance of a (PM) IRRAS sample on a metal surface depends on its surface concentration and the overlap of the electric field vector with the transition dipole moment vectors of the excited modes (Eqs 4.6 and 4.13).[120]

$$\int \mathcal{A}\,d\tilde{v} = \Gamma \int \epsilon\,d\tilde{v} \;\propto\; \Gamma \left| \vec{E}_z \cdot \vec{M} \right|^2 = \Gamma \langle \vec{E}_z^{\,2} \rangle \vec{M}^2 \cos^2\theta \qquad\text{(4.13)}$$

Additionally, it is influenced by the optical constants of the media in the beam path. Due to the MSSR, molecular absorbance depends on the overlap of a certain modes' $\vec{M}$ with the mean square electric field strength in z-direction. An isotropically distributed vector contributes $|M|/3$ to each space coordinate and is tilted by the so-called magic angle of ca 54.7 ° (Fig. 4.6 a).
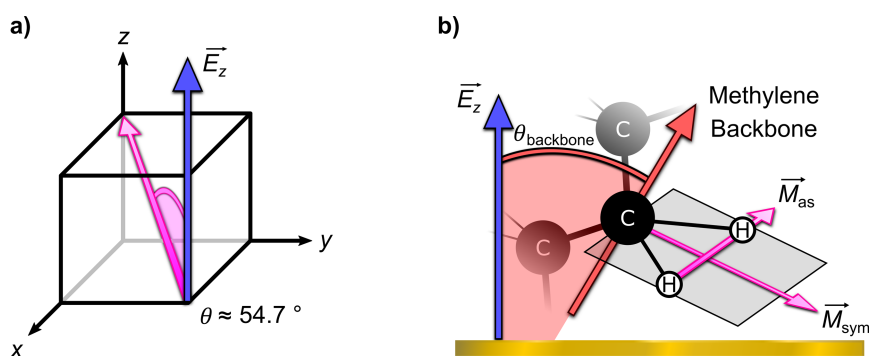
Figure 4.6: a) Isotropic orientation of a vector (pink) in a space cube. The vector's tilt angle with respect to the z-directed electric field vector $\vec{E}_z$ (blue) corresponds to the magic angle. b) Scheme of a methylene group (C – black, H – white) within an alkyl chain on a metal surface (golden). The transition dipole moment vectors of the symmetric and asymmetric CH$_2$ stretching vibrations ($\vec{M}_{sym}$ and $\vec{M}_{as}$, respectively; pink) are orthogonal to each other and the methylene backbone (red).

Experimental intensity enhancements or attenuations in comparison to an isotropic spectrum reflect changes of the overlap angle θ, and thus the tilt vs the surface normal which is parallel to $\vec{E}_z$. With knowledge of the optical constants and thicknesses of all layers in the stratified system, an isotropic (PM) IRRA spectrum consisting of reflectivities (Eq. 4.11) can be simulated using Maxwell and Fresnel equations. Next, the tilt angle for a mode's $\vec{M}$ is evaluated from a comparison of the simulated spectrum under experimental conditions and measured intensities (Eq. 4.14). The tilt of the transition dipole moment vector can be related to (sub-) molecular axes and deliver information about molecular orientation. Therefore, the orientation of $\vec{M}$ with respect to the molecular structure must be known, which can be

estimated by considering the partial charges in deflection or by quantum chemical calculations.

$$\cos^2 \theta = \frac{1}{3} \frac{\int \mathcal{A}_{\text{experimental}} \, d\tilde{\nu}}{\int \mathcal{A}_{\text{simulated}}^{\text{(isotropic)}} \, d\tilde{\nu}} \tag{4.14}$$

However, a molecular axis cannot always be defined, e.g. for alkyl chains in liquid state with multiple gauche conformations, where different conformers are present at the same time and an averaged structure is unknown. In these cases, a discrete tilt angle cannot be reasonably determined, but the principles above are still valid and allow to assess the average orientation of molecules. The segmental order parameter $\mathcal{S}$ is based on the averaged tilt $\langle \theta \rangle$ of individual molecular parts (Eq. 4.15).

$$\mathcal{S} = \frac{1}{2} (3 \cos^2\langle\theta\rangle - 1) \tag{4.15}$$

In the case of methylene groups, their backbones are defined as a set of submolecular axes. From geometric considerations, the tilt θ_{backbone} is equal to an as-if all-trans chain tilt, and can be calculated from the tilt angles of symmetric and asymmetric methylene stretching modes, θ_{sym} and θ_{as}, respectively, because all vectors are orthogonal to each other (Eq. 4.16, Fig. 4.6 b).

$$\cos^2 \theta_{\text{as}} + \cos^2 \theta_{\text{sym}} + \cos^2 \theta_{\text{backbone}} = 1 \tag{4.16}$$

Accordingly, the segmental methylene order parameter reflects the order between three limiting cases:

(i) For $\mathcal{S} = 0$, the methylene groups are completely disordered with an average tilt corresponding to the magic angle $\theta_{\text{backbone}} \approx 54.7\,°$.

(ii) At $\mathcal{S} = -0.5$, the methylene groups are ordered in the all-trans conformation while the alkyl chain is oriented in parallel to the surface ($\theta_{\text{backbone}} = 90\,°$).

(iii) The methylene groups persist also in the all-trans conformation for $\mathcal{S} = 1$, but the alkyl chain is oriented perpendicular to the surface ($\theta_{\text{backbone}} = 0\,°$).

4.4 Electrochemical Impedance Spectroscopy

With electrochemical impedance spectroscopy elements of electro-chemical cells can be interpreted in terms of classic electric circuit components.[121] By Ohm's law, the complex impedance Z is defined as the fraction of potential by current i (Eqs 4.17 and 4.18, with the imaginary unit $j = \sqrt{-1}$). Under potentiostatic conditions, a direct voltage is applied and perturbed by an alternating voltage of a given frequency $f = \omega_{AC}/2\pi$. The resulting alternating current i and its phase shift φ with respect to the voltage are measured to give the complex impedance.

$$Z = \frac{U(f)}{i(f)} = \frac{U_0 \cdot \exp(-j\omega_{AC}t)}{i_0 \cdot \exp(-j\omega_{AC}t + \varphi)} = |Z| \exp(-j\varphi) \qquad (4.17)$$

$$Z = |Z| \cos \varphi - j|Z| \sin \varphi = Z' - jZ'' \qquad (4.18)$$

Practically, four criteria must be met for a successful measurement:

(i) The voltage-current relation must be linear. Thus, low amplitudes U_0 in the range of a few millivolts are applied to invoke small and quasi-linear current responses i_0.

(ii) The relation between perturbation and response function must be causal, so currents measured must not originate from other sources despite the voltage applied.

(iii) The system must be stationary, i.e. stable over time.

(iv) Real and imaginary parts of the impedance must be finite over the whole frequency range, which can be tested via Kramers-Kronig relations.

For evaluation, the measured data need to be interpreted with a model circuit. In the case of single frequency measurements, the results are directly calculated from the measured set. For varying frequencies, two-dimensional plots of the phase angle, absolute, real, or imaginary impedances are evaluated graphically or by fitting. However, the selection of a proper equivalent circuit may be difficult. Multiple physically different circuits can lead to equal or differing functions describing a set of data similarly well.

4.4.1 Determination of the Double Layer Capacitance

The simplest model for an electrochemical half cell comprises a resistor, which describes the electrolyte resistance, in series with a capacitor, which accounts for the EDL capacitance.[121] Ideal resistors and capacitors exhibit completely real and completely imaginary impedances, respectively. Thus, the EDL capacitance can by determined from the imaginary impedance by equation 4.19:

$$C = \frac{1}{\omega_{AC} Z''} \tag{4.19}$$

However, pseudocapacitive effects and frequency dependence of the capacitance, "capacitance dispersion", complicate the application of simple models. Pseudocapacitive effects originate from species which transfer charge to the electrode and simultaneously adsorb in the inner layer. Molecular reorientations are also of such nature. On the other hand, surface heterogeneity and roughness (single crystals should not be affected by these), slow ion diffusion and adsorption, reorientation of molecules, faradaic processes, or surface reconstruction may cause capacitance dispersion. Pseudocapacitive features are equilibrated at $f \rightarrow 0$ Hz and their capacitance should correspond to a slow cyclic voltammogram divided by its scan rate. Higher frequencies cause these features to be perturbed and vanish, and thus pure EDL capacitances are theoretically received by extrapolating $C(f \rightarrow \infty)$. For a better visualization of capacitive processes taking place at different time scales, impedance spectra in absence of faradaic currents may be converted to capacitance spectra by equation 4.20:

$$C_{\text{complex}} = \frac{1}{j\omega_{AC} Z} = C + jC'' \tag{4.20}$$

Pajkossy stressed that the solution resistance must be subtracted from the complex impedance before conversion whereas others neglected or objected to this.[90, 103-104] Without subtraction, the ending of the first semi-circle should show the real equilibrium capacitance of the EDL charging process.

5 Interfacial Structure of Partially Fluorinated Ionic Liquids Based on Azolium Cations

Due to persistence in the environment, accumulation in food chains, and toxicity, fluoroorganic compounds with perfluorinated chains longer than seven carbon atoms are likely to be banned soon.[6] New pyridinium- and azolium-based ILs by Alpers et al. were developed with perfluorohexyl chains.[10-11] Despite the short perfluorinated segments, these FILs possess desired interfacial properties of PFCs. For applications in surface impregnation, the hydrophobicity of these compounds in macroscopically thick films was tested. In this chapter, interfacial properties of selected azolium FILs from Alpers et al. are studied: FIL monolayers were fabricated and characterized at the air|aqueous subphase and air|metal interfaces. An in-detail investigation of microscopic properties, i.e. composition, conformation, order, orientation, or interaction was correlated with macroscopic contact angle measurements. Major results of these investigations are published and adapted with permission from T. Sieling, J. Christoffers, I. Brand, *ACS Sustainable Chem. Eng.* **2019**, *7*, 11593-11602.[P1] Copyright 2019 American Chemical Society.

Structures of the studied FILs are shown in figure 5.1. The side chains of the cations consist of two methylene units connected to perfluorohexyl groups. They are attached to the azolium nitrogen atoms, which are linked in β-positions to each other. The azolium head groups deviate in numbers and positions of nitrogen atoms within the azolium ring, forming bis($1H,1H,2H,2H$-perfluorooctyl)-imidazolium (Im^{F+}), -1,2,3-triazolium (1,2,3-Tria$^+$), and -1,2,4-triazolium (1,2,4-Tria$^+$) triflates (TfO$^-$). The FILs, along with the imidazolium iodide derivative [Im^F][I], were synthesized and provided by Torben Alpers from the working group of Jens Christoffers, University of Oldenburg.[10-11]
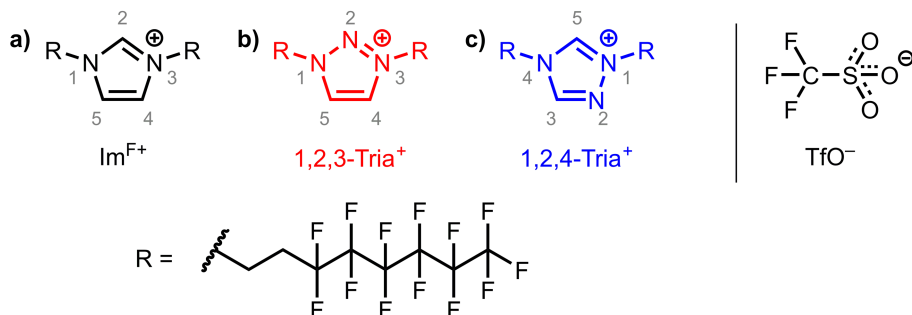
Figure 5.1: Ion structures of the FILs investigated in this study; the anion is always triflate (trifluoromethanesulfonate, TfO⁻); a) [Im^F][TfO] [1,3-bis(1*H*,1*H*,2*H*,2*H*-perfluoro-octyl)imidazolium triflate]; b) [1,2,3-Tria][TfO] [1,3-bis(1*H*,1*H*,2*H*,2*H*-perfluoro-octyl)-1,2,3-triazolium triflate] and c) [1,2,4-Tria][TfO] [1,4-bis(1*H*,1*H*,2*H*,2*H*-perfluorooctyl)-1,2,4-triazolium triflate]. Numbers at the cations denote the numbering system of the respective azolium rings.

All used azolium compounds share typical IL structures. Their melting points are high: [Im^F][TfO] – T_m = 163 °C, [1,2,3-Tria][TfO] – T_m = 99 °C, and [1,2,4-Tria][TfO] – T_m = 196 °C.[10-11] Strictly, [1,2,3-Tria][TfO] is the only FIL used which adheres to the most common definition of ILs (Section 2). However, in the following section will be shown that the behavior of the selected FILs at the air|subphase interface is in accordance with the definition in most cases.

5.1 Characterization of the Fluorinated Ionic Liquids at the Air|Liquid Interface

The amphiphilic FILs form monolayers at the liquid|air interface.[p1] Compression isotherms on pure water and 1 M NaCl(aq) subphases are shown in figure 5.2. Quality and reproducibility of compression isotherms depend on the subphase.

On the pure water subphase, the studied FILs give compression isotherms of poor reproducibility. Characteristic points and shapes of the isotherms vary significantly in independent experiments (Fig. 5.2a). The lift-off area depends on the amount of FIL placed at the interface and is in the range of 1.15 nm² to 0.9 nm². Upon compression, the surface pressure increases to 35-60 mN m⁻¹, but the collapses of the monolayers are ill-defined. Clearly, the studied compounds are surface active at the air|water interface. However, the results indicate that ill-defined, aggregated structures are formed at this

interface. Parallels can be drawn to results by Filipe et al., who first investigated an imidazolium-based IL at the air|water interface in detail.[25] They have shown that the long chain amphiphilic compound [C18Im][Tf2N] forms stable monolayers at low surface pressures only. Further compression to higher surface pressures leads to the formation of a multilayered film.
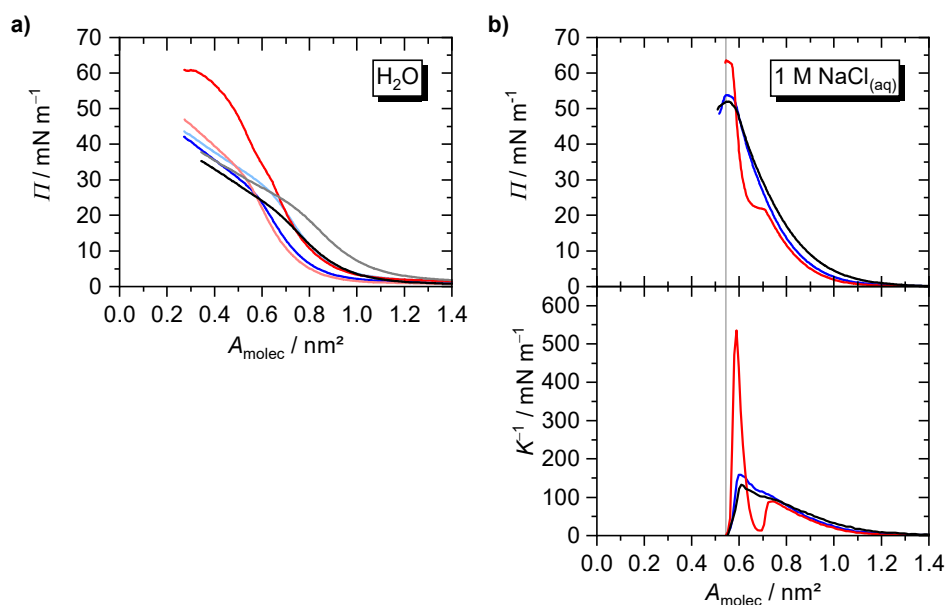
Figure 5.2: Compression of FILs at the air|liquid interface. Gray and black – [Im^F][TfO], red – [1,2,3-Tria][TfO] and blue – [1,2,4-Tria][TfO]. a) Surface pressure vs mean molecular area isotherms of FILs on pure water. Different shades indicate repeated experiments. b) Compression isotherm (upper panel) and corresponding compressibility moduli (lower panel) of the FILs on the 1 M NaCl$_{(aq)}$ subphase. The limiting mean molecular area is indicated with a vertical line.

Langmuir films can be stabilized by addition of salt to the subphase.[122] The amphiphilic FIL cations Im^{F+}, 1,2,3-Tria$^+$, and 1,2,4-Tria$^+$ may interact electrostatically with anions from the subphase. In effect, reproducibility of compression isotherms and stability of the FIL films increase drastically when formed on the 1 M NaCl$_{(aq)}$ subphase (Fig. 5.2b, upper panel). The studied FILs share a common lift-off area of ca 1.1 nm². Upon compression of [Im^F][TfO] and [1,2,4-Tria][TfO], Π increases monotonously and finally, the monolayers collapse at a limiting area of $A_{\text{molec,lim}} = 0.55$ nm². The corresponding surface pressures at monolayer collapse are $\Pi_{\text{coll}} = 51.9$ mN m^{-1} and 53.7 mN m^{-1}, respectively. In contrast to the other azolium ILs, the compression isotherm of [1,2,3-Tria][TfO] displays a phase transition and the appearance of a two-phase region (constant Π) starting at $A_{\text{molec}} = 0.69$ nm²

and $\Pi = 21.6$ mN m^{-1}. The collapse of this monolayer occurs at $A_{molec,lim} = 0.54$ nm^2 and $\Pi_{coll} = 63.4$ mN m^{-1}.

Packing of such two-dimensional films is determined by the actual geometry of present species. As expected from their similar structure, the three azolium FILs share almost equal lift-off areas and limiting areas. Based on the crystal structure of 1,3-dimethyl-imidazolium perchlorate[123] and van der Waals radii,[124] the in-plane cross-sectional area of a 1,3-dialkyl-imidazolium ring with erected substituents is estimated to be in the range of 0.50-0.53 nm^2. This is slightly less than the limiting area of the studied FILs, $A_{molec,lim} = (0.55 \pm 0.02)$ nm^2. Fluorocarbon chains exhibit a cross-sectional area of 0.26-0.30 nm^2,[122, 125] and consequently, for the studied FILs containing two fluorocarbon chains, $A_{molec,lim}$ is expected to be 0.52-0.60 nm^2. This range matches better with the measured $A_{molec,lim}$ and indicates that the packing of the monolayers is determined by the arrangement of the cations' fluorocarbon chains rather than by the ring headgroups.

In contrast to monolayers of [Im^F][TfO] and [1,2,4-Tria][TfO], the [1,2,3-Tria][TfO] film exhibits a phase transition and collapses at significantly higher surface pressures (Fig. 5.2b, upper panel). For further discussion of their physical states, the inverse compressibility moduli were calculated for the films according to equation 3.8 and are shown in the lower panel of figure 5.2b. Maximal values of $K^{-1} = 150$ mN m^{-1} or 180 mN m^{-1} are reached in monolayers of [Im^F][TfO] and [1,2,4-Tria][TfO], respectively. This indicates a two-dimensional liquid-like state after lift-off, which is expected for ILs. Due to the phase transition, the inverse compressibility modulus of the [1,2,3-Tria][TfO] film shows a valley between two maxima. One maximum appears at $A_{molec,1} = 0.74$ nm^2 ($K_1^{-1} = 86$ mN m^{-1}) and, similarly to the other azolium derivatives, indicates a liquid-like region for higher A_{molec}. The second maximum exhibits significantly less compressibility ($K_2^{-1} = 540$ mN m^{-1}) and appears prior to the collapse ($A_{molec,2} = 0.59$ nm^2). The high values of K_2^{-1} indicates a solidification of the monolayer.

The markedly different interfacial behavior of the 1,2,3-Tria$^+$ cation, in comparison with Im^{F+} and 1,2,4-Tria$^+$ cations, may be explained by hydrogen-bonding interactions. Whereas a nitrogen atom is present at position 2 in the 1,2,3-triazolium ion (Fig. 5.1b), the α-position between two nitrogen atoms is occupied by a CH group in imidazolium and 1,2,4-triazolium ions (Fig. 5.1a,c). This group has been shown to interact via H-bonds with anions in ILs.[126] Due to this donating H-bond, ion pairs may be

formed in the films by association with anions (TfO⁻, Cl⁻, maybe HO⁻). Consequently, the mean molecular area is not determined by the sole cation but increased due to anion being present in-plane. Indeed, at surface pressures below the phase transition of the [1,2,3-Tria][TfO] monolayer ($\Pi < 21.6$ mN m^{-1}), the compression isotherms of Im^{F+} and 1,2,4-Tria$^+$ cations show larger A_{molec} at the same Π (Fig. 5.2b, upper panel). This trend increases drastically after the phase transition ($\Pi > 21.6$ mN m^{-1}). This interaction is not possible for the 1,2,3-Tria$^+$ cation. Its electron lone pair situated at N(2) may accept H-bonds, which is impeded by the positive charge located at the ring moiety. In effect, anions must pack differently to interact with the amphiphilic cations, which may be responsible for the phase transition. Interestingly, the $K^{-1}(A_{molec})$ curves of the Im^{F+} and 1,2,4-Tria$^+$ films exhibit a small dip between 0.74 nm² $< A_{molec} <$ 0.59 nm², where the 1,2,3-Tria$^+$ film gives a pronounced minimum due to the appearance of its two-phase region (Fig. 5.2b, lower panel). This may indicate that also for those azolium ions a phase transition could be possible, which is likely due to their structural similarity. However, it seems to be somehow impeded, most probably by H-bonding.

For further investigations of the composition, conformation and orientation, the films were deposited onto polycrystalline gold substrates at surface pressures of transfer, $\Pi_t = 15$ mN m^{-1} and 30 mN m^{-1} by LB vertical withdrawing. The transfer ratios of 1.03 ± 0.07 indicate that the monolayers present at the air|liquid interfaces were quantitatively transferred onto the gold surfaces. Therefore, surface coverages calculated from transfer conditions can be used for simulation of isotropic PM IRRA spectra under experimental conditions. Table 5.1 shows $A_{molec,lim}$ and mean molecular areas at transfer $A_{molec,t}$ as well as corresponding surface concentrations, Γ_{lim} and Γ_t , respectively. Surface coverages Θ of transferred films were calculated by taking Γ_{lim} as maximum packing density (or $A_{molec,lim}$ as minimal area per molecule).

Table 5.1: Mean molecular areas and corresponding surface concentrations at surface pressures of the monolayer transfer and collapses used to calculate surface coverages on the 1 M NaCl$_{(aq)}$ subphase.

FIL	Π_t / mN m^{-1}	$A_{molec,t}$ / nm^2	$A_{molec,lim}$ / nm^2	Γ_t / 10^{-10} mol cm^{-2}	Γ_{lim} / 10^{-10} mol cm^{-2}	Θ
[Im^F][TfO]	15	0.82	0.55	2.0	3.0	0.68
[1,2,4-Tria][TfO]	15	0.79	0.55	2.1	3.0	0.69
[1,2,3-Tria][TfO]	15	0.77	0.54	2.2	3.0	0.71
[Im^F][TfO]	30	0.70	0.55	2.4	3.0	0.80
[1,2,4-Tria][TfO]	30	0.68	0.55	2.4	3.0	0.80
[1,2,3-Tria][TfO]	30	0.62	0.54	2.7	3.0	0.89

Due to the irreproducibility of the compression isotherms on the water subphase, the parameters listed above were only calculated for the 1 M NaCl$_{(aq)}$ subphase. The simulation of spectra (Section 5.4) will show that errors caused by neglecting differing $A_{molec,t}$ on the purely aqueous subphase are negligible in the range of used packing densities.

5.2 Composition of the Imidazolium-Based Fluorinated Ionic Liquid Langmuir-Blodgett Films on the Au(poly) Surface

For the analysis of the film composition on Au(poly) via XPS, the [Im^F][TfO] monolayer was selected as an example.[p1] Literature data of imidazolium ions at gold and nickel interfaces are available,[127-129] and this system is also of interest for the upcoming chapter. The survey XP spectrum shown in figure 5.3a reveals the presence of Au, C, Cl, F, N, and O for the [Im^F][TfO] monolayer deposited from the 1 M NaCl$_{(aq)}$ subphase. A more detailed analysis requires fitted high-resolution XP spectra (Figs 5.3 and 5.4).

As expected for the fluorinated imidazolium cation, C 1s, F 1s, and N 1s photoelectron lines for the cations are detected (Fig. 5.3). The N 1s signal of the monolayer transferred from the 1 M NaCl$_{(aq)}$ subphase exhibits one broad signal with a full width at half maximum (fwhm) of 2.5 eV at E_b = 400.5 eV (Fig. 5.3b). In case of the monolayer transferred from the pure water subphase, the N 1s line appears at E_b = 400.1 eV and is much broader (fwhm = 3.3 eV, Fig. 5.5b). For bulk imidazolium compounds and macroscopic films, a binding energy close to 402.0 eV is expected.[127, 130] Cremer et al. have shown that this binding energy is downshifted by up to -1.4 eV for sub-monolayer coverages of imidazolium-based Ils evaporated

onto Au(111) and Ni(111) surfaces.[127-128] Similar effects were observed by Beattie et al. during self assembly of an imidazolium IL on Au(poly) substrates.[129] Direct interaction of the imidazolium ring with the metallic surfaces is assumed to be responsible for this large downshift.[127] The measured binding energies of the transferred FIL monolayers indicate that the ring headgroups are in direct contact with the Au(poly) surface in both cases. Large fwhms of the N 1s signals may reflect differences in the chemical environment of the cations.
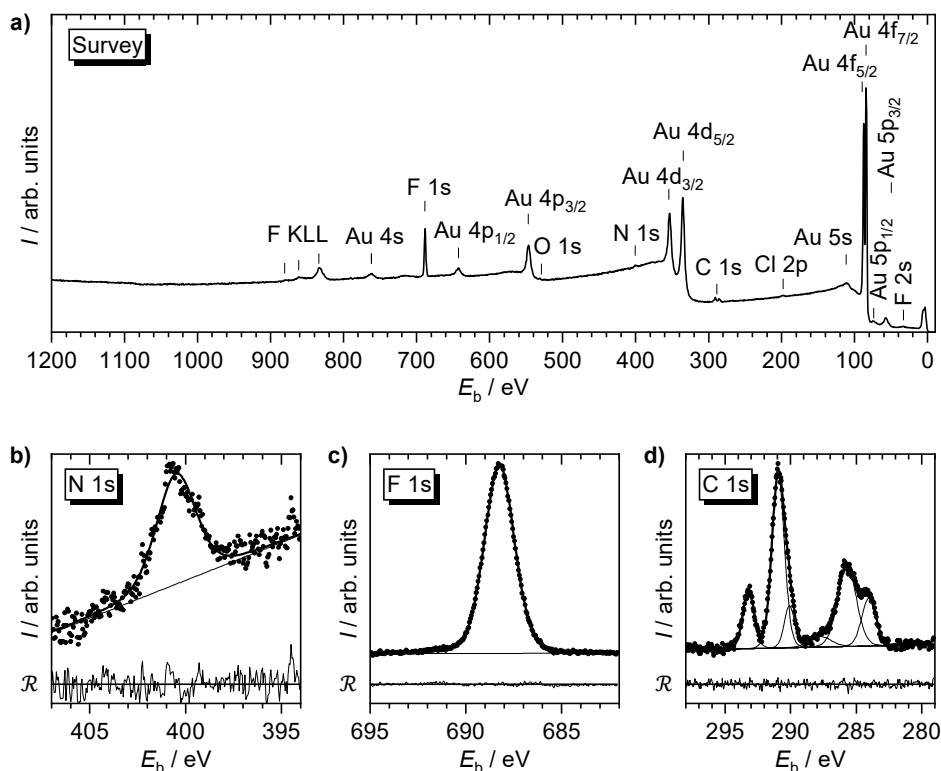
Figure 5.3: XP spectra of the Im^{F+}-based LB monolayer transferred at Π_t = 30 mN m^{-1} from the 1 M NaCl$_{(aq)}$ subphase onto an Au(poly) substrate: a) survey spectrum; high resolution spectra b) N 1s, c) F 1s and d) C 1s. Residuals ($\mathcal{R}$) are shown below fitted spectra.

The F 1s line originates from the side chains of the Im^{F+} cation, whereas C 1s lines arise from both carbon atoms in the side chains and the head group. As shown in figure 5.3b, one F 1s photoelectron line is found for the fluorocarbons of the FIL at E_b = 688.3 eV, which is in agreement with binding energies of partially fluorinated SAMs on Au and Ag surfaces.[131-134] Whereas individual components of CF$_2$ or CF$_3$ moieties are not resolved in the F 1s line, they can be distinguished in the C 1s spectrum (Fig. 5.3c). In accordance with literature,[131-134] the different CF$_n$ groups (n = 2 or 3) can be assigned in

the following way (Tab. 5.2): $\underline{C}F_3$ – E_b = 293.2 eV, CF_n–$\underline{C}F_2$–CF_n – E_b = 291.0 eV, and CF_2–$\underline{C}F_2$–CH_2 – E_b = 290.1 eV. The remaining carbon atoms are adjacent to electron-withdrawing groups, either CF_2 groups or a nitrogen atom incorporated into the positively charged aromatic ring. Thus, they give a joint signal at E_b = 285.7 eV.[127, 131-134] The signals at E_b = 287.7 eV and E_b = 284.1 eV are ascribed to adventitious carbon.[133]

Table 5.2: Binding energies, full widths at half maxima, and assignments of C 1s, Cl 2p, F 1s, N 1s, and O 1s photoemission lines in the LB monolayer of Im^{F+} transferred at Π_t = 30 mN m^{-1} from the 1 M NaCl$_{(aq)}$ subphase onto a Au(poly) substrate.

XPS Line	E_b / eV	fwhm / eV	Assignment
C 1s	284.1	1.3	$\underline{C}_{adventitious}$
C 1s	285.7	1.7	$\underline{C}$-N, $\underline{C}H_2$–CF_2
C 1s	287.7	1.9	$\underline{C}_{adventitious}$
C 1s	290.1	0.9	CF_2–$\underline{C}F_2$–CH_2
C 1s	291.0	1.1	CF_n–$\underline{C}F_2$–CF_n (n = 2 or 3)
C 1s	293.2	1.0	$\underline{C}F_3$
Cl 2p$_{(3/2, 1/2)}$	197.2, 198.8	1.2*, 1.2*	[$\underline{Cl}$]$^-$ on Au
Cl 2p$_{(3/2, 1/2)}$	199.7, 201.2	1.2*, 1.2*	[$\underline{Cl}$]$^-$ in adlayer
F 1s	688.3	1.9	C$\underline{F}_2$ and C$\underline{F}_3$
N 1s	400.5	2.5	$\underline{N}$
O 1s	530.8	3.4	[O$\underline{H}$]$^-$, H$_2$$\underline{O}$, Au oxide, or contamination

*The fwhms of all Cl 2p signals were constrained to be variable but equal during fitting.

Due to the triflate anion present in the originally synthesized compound, photoelectron lines of C, F, S, and O are to be expected. Whereas C-F groups are also present in the cation and therefore are not suitable for the analysis of the anion, S-O species are unique for the latter. However, neither the survey (Fig. 5.3a) spectrum nor the S 2p spectrum (Fig. 5.4a) show intensity in the region of 168 eV < E_b < 171 eV, where S 2p photoemission lines of the sulfonyl group are expected.[130] Corresponding O 1s lines should appear at E_b = 532.0 eV.[130] The recorded O 1s spectrum reveals one broad (fwhm = 3.4 eV) photoemission line at E_b = 530.8 eV (Fig. 5.4b), which is downshifted by -1.2 eV from the expected signal. Thus, this signal may tentatively be assigned to hydroxide anions, which were transferred along with the organic monolayer from the aqueous subphase onto the gold surface. Other sources for this signal could be adventitious contaminations or water, whose evaporation was hindered in vacuo, e.g. due to coordination or encapsulation. Downard et al. crystallized [$C_{18}Im$][Cl]·H_2O from 1,2-dichloroethane,[135] which indicates that a sort of crystal water may also be

deposited in LB films. Furthermore, this binding energy matches well with surface oxides of Au,[136-138] being produced by treatment in the UV/ozone chamber.[139] The absence of O 1s and S 2p lines characteristic for the sulfonyl group indicates that, within the limits of XPS sensitivity, the triflate anions were not transferred from the 1 M NaCl$_{(aq)}$ subphase onto the Au(poly) surface.
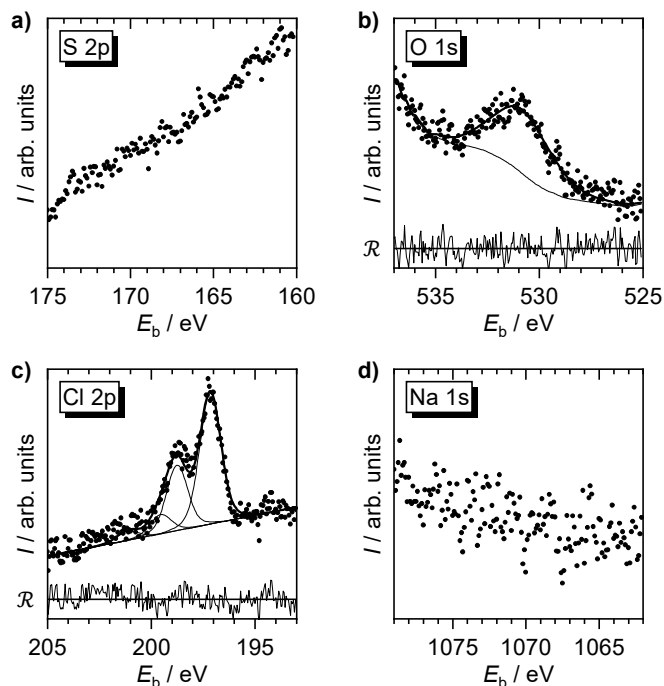
Figure 5.4: High resolution XP spectra of the Im^{F+}-based LB monolayer transferred at $\Pi_t = 30$ mN m^{-1} from the 1 M NaCl$_{(aq)}$ subphase onto an Au(poly) substrate: a) S 2p, b) O 1s, c) Cl 2p. Residuals ($\mathcal{R}$) are shown below fitted spectra.

Although not present in the original imidazolium FIL, two doublets of Cl species are detected (Fig.5.4 c). The first, well-resolved doublet is located at $E_b = 197.2$ eV (Cl 2p$_{3/2}$) and $E_b = 198.4$ eV (Cl 2p$_{1/2}$). This doublet is ascribed to chloride anions adsorbed directly on the gold surface.[140-141] The second doublet is weak and shifted toward higher binding energies at $E_b = 199.7$ eV (Cl 2p$_{3/2}$) and $E_b = 201.2$ eV (Cl 2p$_{1/2}$). It is assigned to chloride ions present in an adlayer,[140-141] providing a source of counter-ions for the Im^{F+} cations. XPS results show clearly, that the triflate anions, which were present in the original FIL, are absent in the monolayer after transfer from the 1 M NaCl$_{(aq)}$ subphase. Instead, chloride and probably hydroxide ions, too, are found on the gold surface. Despite the marked transfer of chloride ions, sodium ions are absent within XPS sensitivity (Figs 5.3a and 5.4d). Note that due to its more than eightfold higher photoionization cross section when using Al K$_\alpha$

radiation, Na would be much more easily detected than C species of similar amount.[142] This indicates that only the film is transferred, validating the surface sensitivity of the LB method.

In the case of the pure water subphase, the anion content after transfer of the imidazolium-based film onto Au(poly) is different. The corresponding survey spectrum reveals Au, C, F, N, and O species (Fig. 5.5a). Traces of S are not evident from the survey spectrum, but the high-resolution S 2p spectrum (Fig. 5.5c) shows a weak doublet at $E_b = 167.6$ eV (S 2p$_{3/2}$) and $E_b = 168.9$ eV (S 2p$_{1/2}$). These binding energies correspond to sulfonyl species.[143-144] Small downshifts in comparison to bulk spectra[130] may be explained by direct interaction with the Au(poly) surface, as seen above for chloride anions.
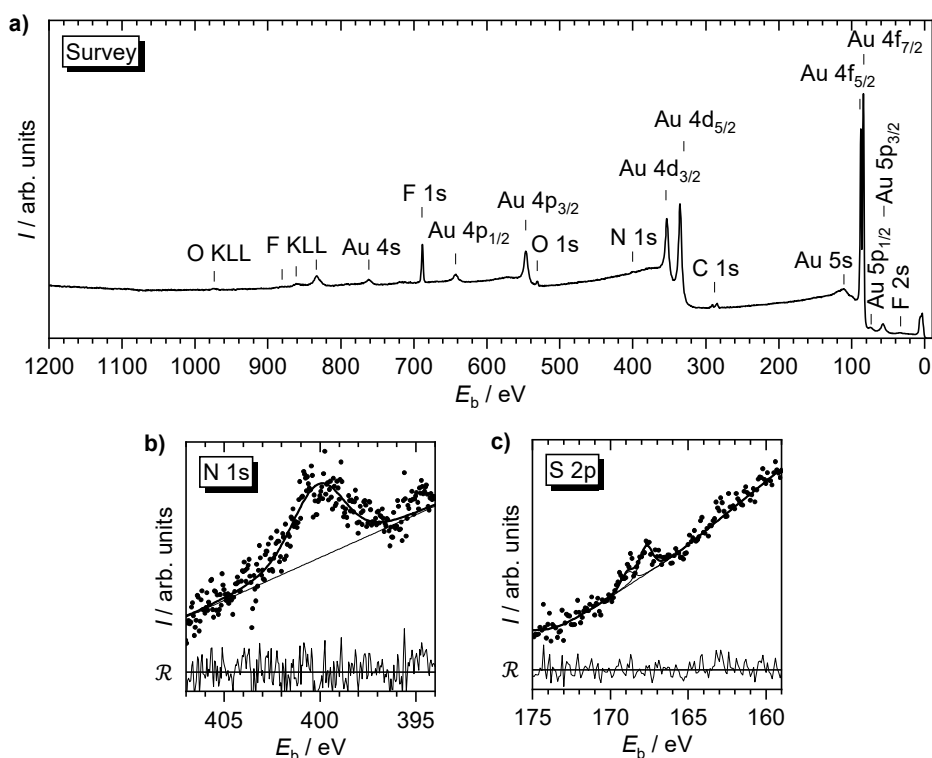
Figure 5.5: XP spectra of the Im^{F+}-based LB monolayer transferred at $\Pi_t = 15$ mN m^{-1} from the water subphase onto an Au(poly) substrate: a) survey spectrum; high resolution b) N 1s, c) S 2p. Residuals ($\mathcal{R}$) are shown below fitted spectra.

In conclusion, the amphiphilic cations were transferred successfully onto the gold substrates and the cationic headgroups are directed toward the metal surface. The LB technique on electrolyte subphases provides new experimental approach for exchange of water-soluble ions. As a result, the

composition of the deposited FILs changes. Thus, for the following investigations the FILs in LB monolayers will be named [Im^F][X], [1,2,4-Tria][X], and [1,2,3-Tria][X], where X$^-$ corresponds to Cl$^-$, HO$^-$, and/or TfO$^-$ anions.

5.3 Wetting Properties of the Fluorinated Ionic Liquid Monolayers on the Au(poly) Surface

After LB transfer, the FIL monolayers will determine the surface properties of the polycrystalline gold substrates. Contact angle measurements can provide a fast and macroscopic assessment of interfacial differences. As alkyl chain segments are hydrophobic and perfluoroalkyl segments are lipophobic and hydrophobic, water was chosen as contact liquid.[p1]

Figure 5.6 shows exemplary images of the [Im^F][X] under different transfer conditions. The contact angle of the film transferred from the water subphase at Π_t = 15 mN m^{-1} is ϑ = (95 ± 2) ° and thus shows slightly hydrophobic behavior (Fig. 5.6a). When transferring the film from the 1 M NaCl$_{(aq)}$subphase at Π_t = 30 mN m^{-1}, it increases significantly to ϑ = (111 ± 1) ° (Fig. 5.6b).
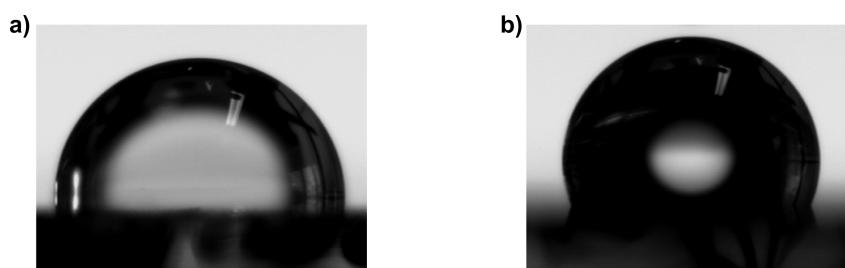
Figure 5.6: Water contact angle images of [Im^F][X] monolayers on Au(poly) surfaces transferred from a) water (Π_t = 15 mN m^{-1}) and b) 1 M NaCl$_{aq}$ (Π_t = 30 mN m^{-1}) subphases.

For both triazolium films, the contact angles are similar to the imidazolium film, as listed in table 5.3. They depend crucially on the transfer conditions, but the chemical structure of the cation has less impact. Averaged contact angles amount to ϑ = (94 ± 2) ° for transfers from aqueous subphases and ϑ = (109 ± 2) ° for transfers 1 M NaCl subphases.

Table 5.3: Water contact angles of FILs transferred from water (Π_t = 15 mN m^{-1}) and 1 M NaCl$_{(aq)}$ (Π_t = 30 mN m^{-1}) subphases.

FIL	Π_t / mN m^{-1}	Subphase	ϑ / °
[Im^F][X]	15	water	95 ± 2
[1,2,4-Tria][X]	15	water	93 ± 1
[1,2,3-Tria][X]	15	water	94 ± 1
[Im^F][X]	30	1 M NaCl$_{(aq)}$	111 ± 1
[1,2,4-Tria][X]	30	1 M NaCl$_{(aq)}$	109 ± 1
[1,2,3-Tria][X]	30	1 M NaCl$_{(aq)}$	106 ± 1

The difference of ca 15 ° in contact angles from the two subphases may be attributed to various causes, e.g. the film composition and anion content, density (surface concentration) of the molecules, or orientation and packing of the azolium cations. XPS investigations showed that the CF$_3$ group containing triflate anion is replaced by a certainly more hydrophilic chloride ion. Still, these layers exhibit more hydrophobic properties, which indicates that the film composition is unlikely to be responsible for higher contact angles. Interestingly, the contact angle equals (70 ± 1) ° on a thick film of [Im^F][TfO] smeared onto glass,[10] which is $\Delta\vartheta$ = -25 ° or -41 ° lower than measured for the [Im^F][X] LB monolayers of this work. This result indicates that the packing and conformational order of the amphiphilic cations in the monolayer severely influence the surface properties of the LB-modified Au(poly) substrate.

5.4 Orientation of the Fluorinated Ionic Liquid Monolayers on the Au(poly) Surface

Information about conformation and orientation of the azolium FIL monolayers on the solid substrate can be extracted from PM IRRA spectra by utilizing the MSSR.[p1] Ring headgroups and fluorinated tails give rise to several IR absorption modes, of which some are separated and suitable for analysis.

A variety of modes appear in the $\tilde{\nu}$ = 1700-900 cm^{-1} spectral region of the isotropic optical constants determined from [Im^F][I] (Fig. 5.7). Iodide anions were chosen because they not absorb IR light and thus, all IR absorption modes originate exclusively from the cation in the investigated region. They facilitate mode assessment and qualitative analysis (composition,

conformation). For quantitative analysis (orientation), isotropic intensities of suitable modes are required.
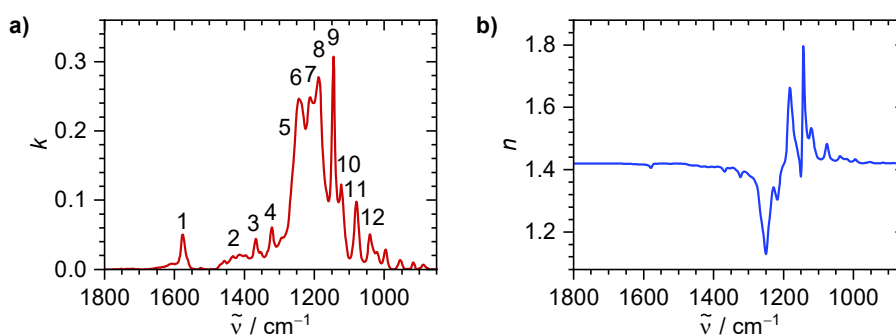
Figure 5.7: Isotropic optical constants of [Im^F][I] in KBr: a) attenuation coefficient and b) refractive index.

Vibrational modes of perfluorinated n-alkanes are well known.[132-134, 145-146] However, substituents may perturb them and lead to changes in their nature and position. To aid the assignment of bands, the IR spectrum of the isolated Im^{F+} cation in vacuo was calculated with quantum chemical methods. First, geometry optimizations were carried out with the conformers depicted in figure 5.8.

As shown in table 5.4, various density functional theory (DFT) and correlation methods with different basis sets have a severe impact on the actual single point energies of the individual conformers. Nevertheless, all calculations indicate that conformer V has the minimum energy and thus, it represents the most stable structure. Most of the energy difference to the other conformers is attributed to the basis set superposition error (BSSE). The fluorinated chains, and therefore the basis sets on their nuclei, approach, overlap, and thus describe the electron density in their proximity better. An error of few kJ per moles may be expected, due to this effectively higher-level basis set for close atoms. However, the correction of the BSSE is difficult. For intermolecular systems, the BSSE can be estimated and corrected by calculation of the individual molecules in their interaction geometry with the additional basis set at ghost atoms of interacting partner. For intramolecular interactions there is no pleasing method.[147] On the other hand, dispersive interactions cannot be described by non-correlation methods as Hartree-Fock (HF) or DFT (empirically parametrized corrections are available for the latter).[148] In the case studied here, a convenient error compensation is achieved by an energetically favorable BSSE, which mimics the fluorophillic chain-chain interactions.
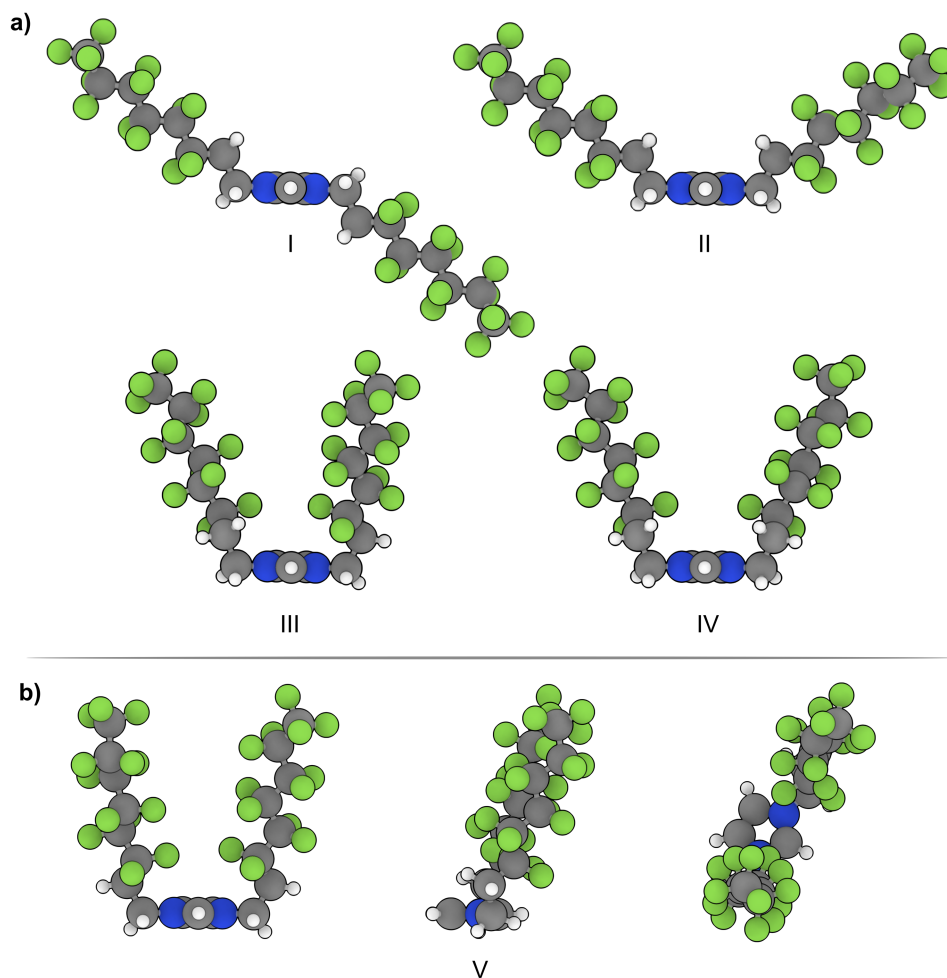
Figure 5.8: Geometry optimized conformers of the Im^{F+} cation. Chain directions out of the figure plane are indicated by the rotational state of methylene groups. I – all trans chains anti to the ring plane, II-V – chains syn to the ring plane, II – all trans chains, III-V gauche methylene groups, III – chains pointing in opposite directions, IV – chains directed to the C(4)-C(5) facing side, V – chains directed to the C(2) facing side, a) More unstable conformers I-IV. b) Minimum energy conformer V (B3LYP/def2-TZVP) from different perspectives. Note the helical arrangement of the CF_2 groups in the right structure. Color code: H – white, C – grey, N – blue, F – green.

Conformer V is depicted from different perspectives in figure 5.8b. The tail chains are placed in syn-conformation with respect to the ring plane. Gauche-aligned methylene groups allow for a close contact between the tail chains, which are directed toward the C(2) atom facing side of the imidazolium ring. This structure corresponds to a conformation that can be expected in organized LB films. The final geometry optimization (cartesian coordinates are listed in the appendix, table 12.1) and frequency calculation

of V were conducted with the def2-TZVP triple-ζ basis set and the B3LYP functional.

Table 5.4: Single point energies relative to the minimum energy (conformer V) of the conformers depicted in figure 5.8a. n.c. – not calculated.

	$E_{sp} - E_{sp,min}$ / kJ mol^{-1}		
Conformer	B3LYP/ 6-31+G*	B3LYP/ def2-TZVPD	RI-MP2/ def2-TZVPD
I	13.4	10.2	n.c.
II	16.3	10.4	n.c.
III	0.3	3.3	2.7
IV	6.7	6.1	10.2
V	0.0	0.0	0.0

Modes of the Im^{F+} cation were assigned based on literature and the frequency calculation (Fig. 5.7a, Tab. 5.5). In general, vibrational modes are abbreviated with symbols according to Schrader[149] (Tab. 13.4, Abbreviations and Symbols). The IR absorption modes 1 at $\tilde{\nu} = 1576$ cm^{-1} and $\tilde{\nu} = 1560$ cm^{-1} are ascribed to the in-plane stretching modes R$_1$ and R$_2$ of the imidazolium ring, for which the nomenclature of Grondin et al. is used.[32, 150-151] The scissoring modes (modes 2) of the methylene groups δ(CH$_2$) are located at $\tilde{\nu} = 1457$ cm^{-1} and $\tilde{\nu} = 1433$ cm^{-1}. Stretching and deformation modes involving fluorocarbon chains dominate the $\tilde{\nu} = 1380\text{-}900$ cm^{-1} spectral region (Fig. 5.7a).[145] Strongest IR absorption modes appear at 1280 cm$^{-1} < \tilde{\nu} < 1200$ cm^{-1} and consist of ν_{as}(CF$_3$) and ν_{as}(CF$_2$) asymmetric stretching, CC stretching ν(CC)$_{helix}$, and CF$_2$ deformation modes ω(CF$_2$). These modes are complex in nature because of the helical structure of the perfluorocarbon chain and reduced mass of the C-F bond. Since fluorine atoms are larger than hydrogen atoms (van der Waals diameters equal 294 pm and 220 pm, respectively),[124] the staggered conformation found in methylene groups is energetically unfavorable. Instead, repulsive 1,3 F-F interactions induce a twist of 12 ° on the average in the C-C-C-C axis, which results in the formation of 15/7 or 13/6 helices (Fig. 5.8b).[12, 134] In the spectral region of $\tilde{\nu} = 1150\text{-}800$ cm^{-1}, progression modes involving symmetric CF$_2$ stretching modes appear.[145] The number and frequency of these modes depend on the chain length and its conformation. In amorphous films, their intensities decrease and the number of these modes increases. Symmetric CF$_2$ stretching modes ν_s(CF$_2$) combined with ν(CC)$_{helix}$ stretching modes are observed at $\tilde{\nu} = 1400\text{-}1300$ cm^{-1}. For a fluorocarbon chain of high conformational order, two strong modes are expected at $\tilde{\nu} = 1380\text{-}1360$ cm^{-1}

and $\tilde{v}$ = 1330-1320 cm⁻¹. In contrast, disorder leads to a decrease in intensity and increases in number of modes in this region.[145]

Table 5.5: Wavenumber, assignment, and direction of the transition dipole moment vector of the IR absorption modes of the amphiphilic, partially fluorinated imidazolium cation in the 1700-900 cm⁻¹ spectral region. The following spectra are compared: isotropic [Im^F][I] in KBr (Figs 5.7 and 5.9a), anisotropic [Im^F][X] LB monolayers transferred from 1 M NaCl$_{(aq)}$ (Π_t = 30 mN m⁻¹) and water (Π_t = 15 mN m⁻¹) subphases (Fig. 5.9b). n.o. – not observed

| | $\tilde{v}$/ cm⁻¹ | | | | Direction of $\vec{M}$ |
| | Isotropic | LB monolayers | | | (based on calculation |
#		Π_t = 30 mN m⁻¹	Π_t = 15 mN m⁻¹	Mode assignment	results)
1	1576, 1560 sh	n.o.	n.o.	R₁, R₂	plane of the ring
2	1457, 1431	1444	1444	$\delta(CH_2)$	bisector of the methylene group
3	1366, 1352 sh	1365, 1355 sh	1365, 1355 sh	$\nu_s(CF_2)_{progression}$, $\nu(CC)_{helix}$	∥ to the helix axis
4	1322, 1302 sh	1322, 1302 sh	1322, 1302 sh	$\nu_s(CF_2)_{progression}$, $\nu(CC)_{helix}$, $\tau(CH_2)$	a small tilt from the helix axis
5	1266 sh	1269 sh	1268 sh	$\nu_{as}(CF_3)$, $\omega(CF_2)$, $\nu(CC)$, $\tau(CH_2)$	almost ⊥ to the helix axis
6	1247, 1233 sh	1249, 1230 sh	1249, 1230 sh	$\nu_{as}(CF_3)$, $\nu_{as}(CF_2)$, $\nu(CC)$, $\omega(CF_2)$, $\tau(CH_2)$	almost ⊥ to the helix axis
7	1216	1213	1213	$\nu_{as}(CF_3)$, $\nu_{as}(CF_2)$, $\nu(CC)$, $\tau(CH_2)$	roughly in the direction of the helix axis
8	1187	1188	1188	$\nu_{as}(CF_2)$, $\omega(CH_2)$	⊥ to the helix axis
9	1147	1147	1148, 1138 sh	$\nu_s(CF_2)_{progression}$, $\delta(CF_2)$	⊥ to the helix axis
10	1124	1124	1124	$\nu_s(CF_2)$, $\omega(CH_2)$	almost ⊥ to the helix axis
11	1079	1072	1072	$\nu_s(CF_2)$, $\nu_s(CF_3)$, $\omega(CH_2)$	in the direction of the helix axis
12	1039	1046	1030	$\nu_s(CF_2)$, $\nu_s(CF_3)$, $\omega(CH_2)$	in the direction of the helix axis
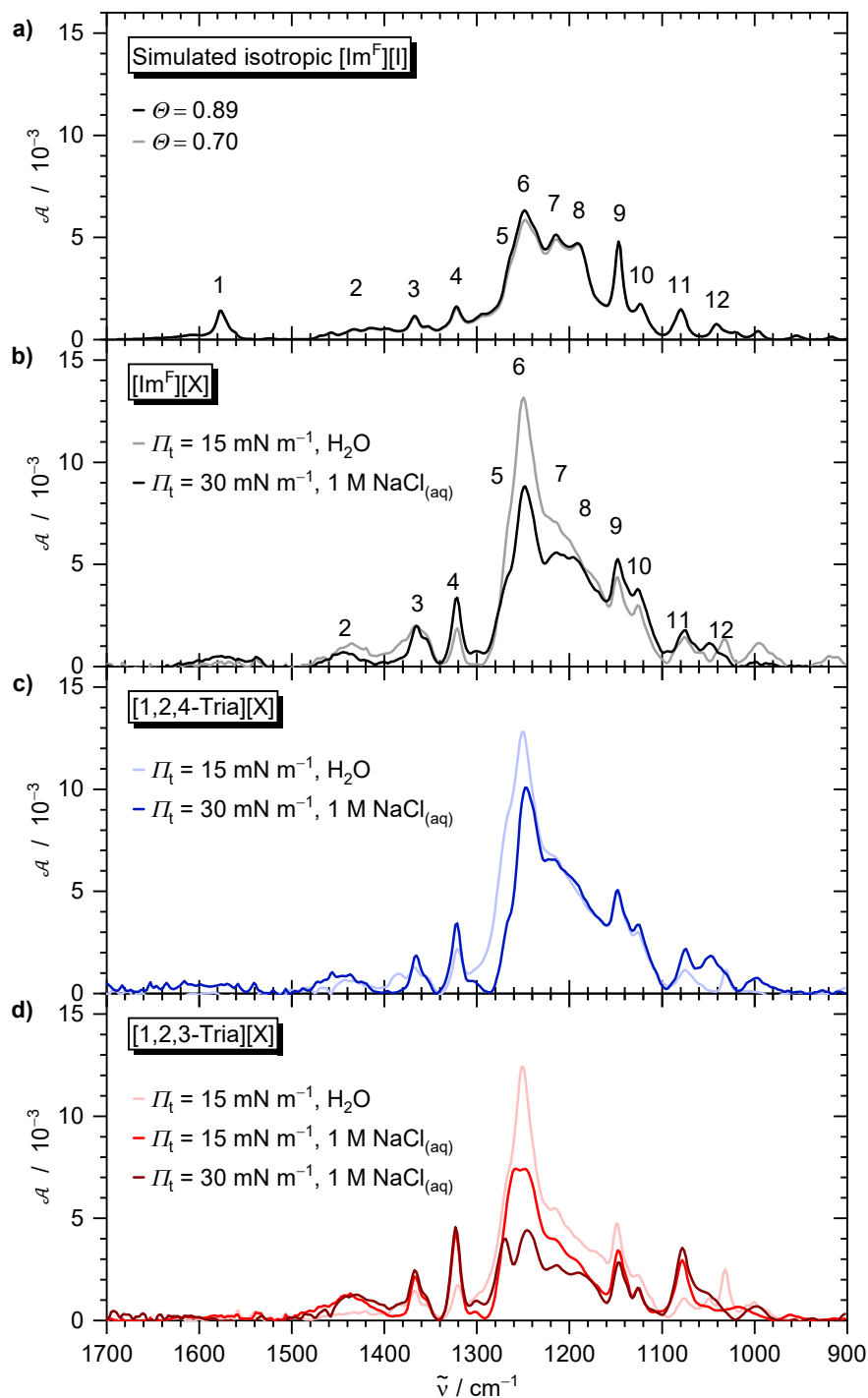
Figure 5.9: PM IRRA spectra in the 1700-900 cm⁻¹ spectral region of a) randomly distributed [Im^F][I] in a monolayer thick film (1.6 nm) at the surface coverages marked in the figure; b-d) in LB monolayers on the gold surface of b) [Im^F][X] c) [1,2,4-Tria][X] and d) [1,2,3-Tria][X]. Monolayer transfer conditions are given in the figure.

The experimental spectrum in figure 5.7a shows two sets of modes located at $\tilde{\nu} = 1366\ \text{cm}^{-1}$ (mode 3) and $\tilde{\nu} = 1322\ \text{cm}^{-1}$ (mode 4). Both exhibit shoulders on the lower wavenumber sides. The presence and positions of modes 3, 4, and 9 indicate a helical conformation of the fluorocarbon chain.

Figure 5.9 displays spectra of the [Im^F][X], [1,2,4-Tria][X], and [1,2,3-Tria][X] LB monolayers transferred from water and 1 M NaCl$_{(aq)}$ subphases at different surface pressures onto Au(poly) substrates as well as a monolayer thick film of the isotropically distributed Im^{F+} cation, simulated under experimental conditions from optical constants. For the latter, different surface coverages according to table 5.1 were simulated (Fig. 5.9a). The film thickness was estimated based on the quantum chemical geometry optimization of the Im^{F+} cation. An interatomic length of 1.1 nm was found along the long axis of the molecule and van der Waals radii[124] were added. Additionally, 0.2 nm were given for uneven distributions of the amphiphilic cation within the monolayer,[25] resulting in a final thickness of 1.6 nm. The simulations show that the difference in intensities between $\theta = 0.89$ and $\theta = 0.70$ is negligible, as the surface concentrations stay in the same order of magnitude. Literature spectra of partially fluorinated thiolate and selenolate SAMs indicate that the modes of fluorocarbons are very strong and their intensity dominates over modes of methylene bridges and azolium rings.[132-134, 146, 152] Thus, simulated spectra of Im^{F+} cations are suitable for the analysis of fluorocarbon chains in [1,2,4-Tria][X] and [1,2,3-Tria][X] spectra as well.

All three compounds share similar features in LB films. For comparison with the simulated spectrum, table 5.5 also shows the modes of the Im^{F+} film. As in imidazolium compounds, 1,2,3-triazolium and 1,2,4-triazolium ions exhibit ring stretching modes (1) located between $\tilde{\nu} = 1590\ \text{cm}^{-1}$ and $\tilde{\nu} = 1520\ \text{cm}^{-1}$.[10-11] In the experimental LB film spectra (Fig. 5.9b-d), the in-plane stretching modes of the azolium rings are strongly attenuated. Experimental intensities of $\delta(\text{CH}_2)$ modes (2, around $\tilde{\nu} \approx 1450\ \text{cm}^{-1}$) in the films are increased in comparison to the isotropic spectrum (Fig. 5.9a), but they are broad and poorly defined. The presence and positions of modes 3 ($\tilde{\nu} \approx 1322\ \text{cm}^{-1}$), 4 ($\tilde{\nu} \approx 1366\ \text{cm}^{-1}$), and 9 ($\tilde{\nu} \approx 1147\ \text{cm}^{-1}$) indicate that the six carbon atoms long perfluorocarbon chains adopt a helical conformation in all transferred LB films. Weak shoulders suggest a non-perfect conformational order.

In general, LB monolayers transferred from water subphases exhibit comparably higher absorbances than monolayers transferred from 1 M

NaCl$_{(aq)}$ subphases. However, surface concentrations during transfers from water subphases (Γ_t = 2.0-2.2 ·10^{-10} mol cm^{-2}) were lower than during transfers from 1 M NaCl$_{(aq)}$ subphases (Γ_t = 2.4-2.7 ·10^{-10} mol cm^{-2}, Tab. 5.1). According to equation 4.13, the absorbance is proportional to the surface concentration and overlap of transition dipole moment vectors with electric field vectors. Despite a concentration-determined attenuation being expected for films transferred from water subphases in comparison to films transferred from 1 M NaCl$_{(aq)}$ subphases, they exhibit higher absorbances. This indicates that the average orientation of the transition dipole moment vectors with respect to the electric field vector (surface normal, MSSR) is different for both sets of monolayers. Due to the LB transfer, the monolayers are likely to be distributed anisotropically on the Au(poly) surfaces.

For orientational analysis, modes with appropriate transition dipole moment vectors with respect to a sub-molecular axis have to be selected. The absence of ring stretching vibrations indicates that the azolium rings are oriented parallel to the surface. Strongest absorptions are given by modes of the fluorocarbon chains in the $\tilde{\nu} \approx$ 1270-1220 cm^{-1} spectral region. The difference in absorbances between water and 1 M NaCl$_{(aq)}$ subphases is most pronounced there. However, their transition dipole moment vector are ill-defined, i.e. they are slightly tilted from the normal to the helix axes (Tab. 5.5). Moreover, in some cases these modes are hardly separable by fitting. The triflate anion, present in traces only for LB monolayers transferred from water subphases, gives ν_{as}(SO$_3$) modes at $\tilde{\nu} \approx$ 1270-1220 cm^{-1},[30] which complicates quantitative evaluation in this region. Modes 3, 4, and 9 originate from the fluorocarbon chains, and they are separated from other modes. The error margin during fitting is expected to be less for those modes in comparison to more entangled, super positioned modes. Figure 5.10 shows the orientations of the transition dipole moment vectors of these modes with respect to the fluorocarbon chains from the quantum chemical frequency calculation of the Im^{F+} cation. From literature, modes 3 ($\tilde{\nu}$ = 1366 cm^{-1}) and 4 ($\tilde{\nu}$ = 1322 cm^{-1}) are expected to be oriented in parallel to the helix axis.[134, 146] However, figure 5.10b shows that this is not the case. The methylene and imidazolium moieties significantly influence this mode, resulting in a small tilt from the helix axis for mode 4. In agreement with literature, the transition dipole moment vectors of mode 3 orient parallel and mode 9 ($\tilde{\nu}$ = 1147 cm^{-1}) perpendicular with respect to the helix axis.[134, 146]
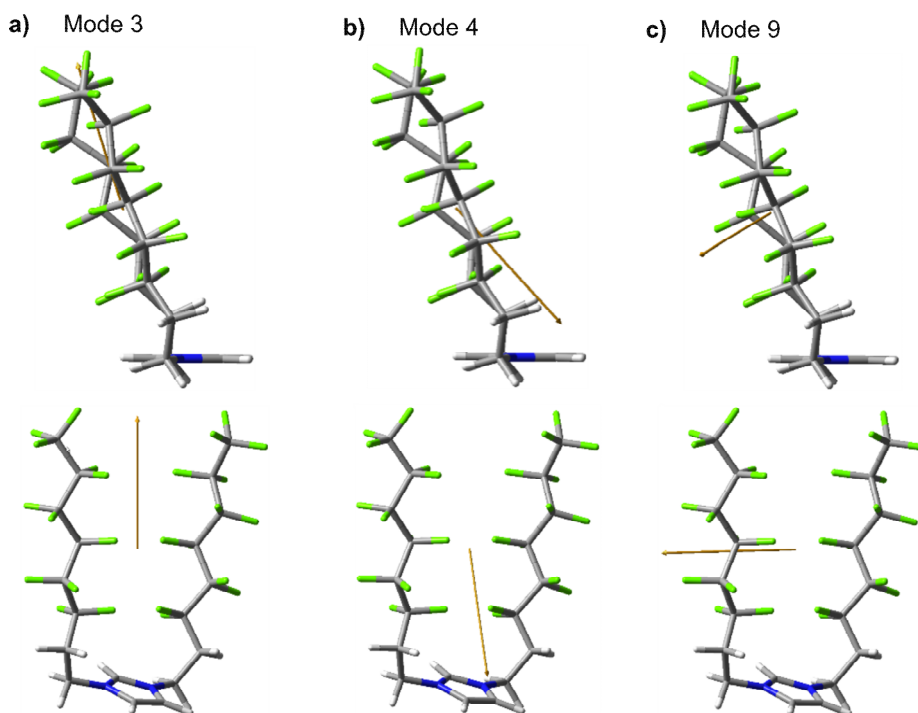
Figure 5.10: Wired structure of the amphiphilic imidazolium cation (conformer V) with marked direction of the transition dipole moment vector (orange) for the IR vibrations at mode 9, mode 4, and mode 3 from two perspectives (top and bottom). Wavenumbers displayed give the unscaled result of the DFT calculation. Color code: H – white, C – grey, N – blue, F – green.

Further analysis requires fitting of the spectra (Fig. 5.11) to extract the intensities of individual IR absorption modes. Integrated absorbances of the selected modes can be compared with simulated spectra to extract tilt angles of the transition dipole moment vectors using equation 4.14. As mode 3 is directly in line with the helix axis, the tilt of the fluorocarbon chains can be directly evaluated.
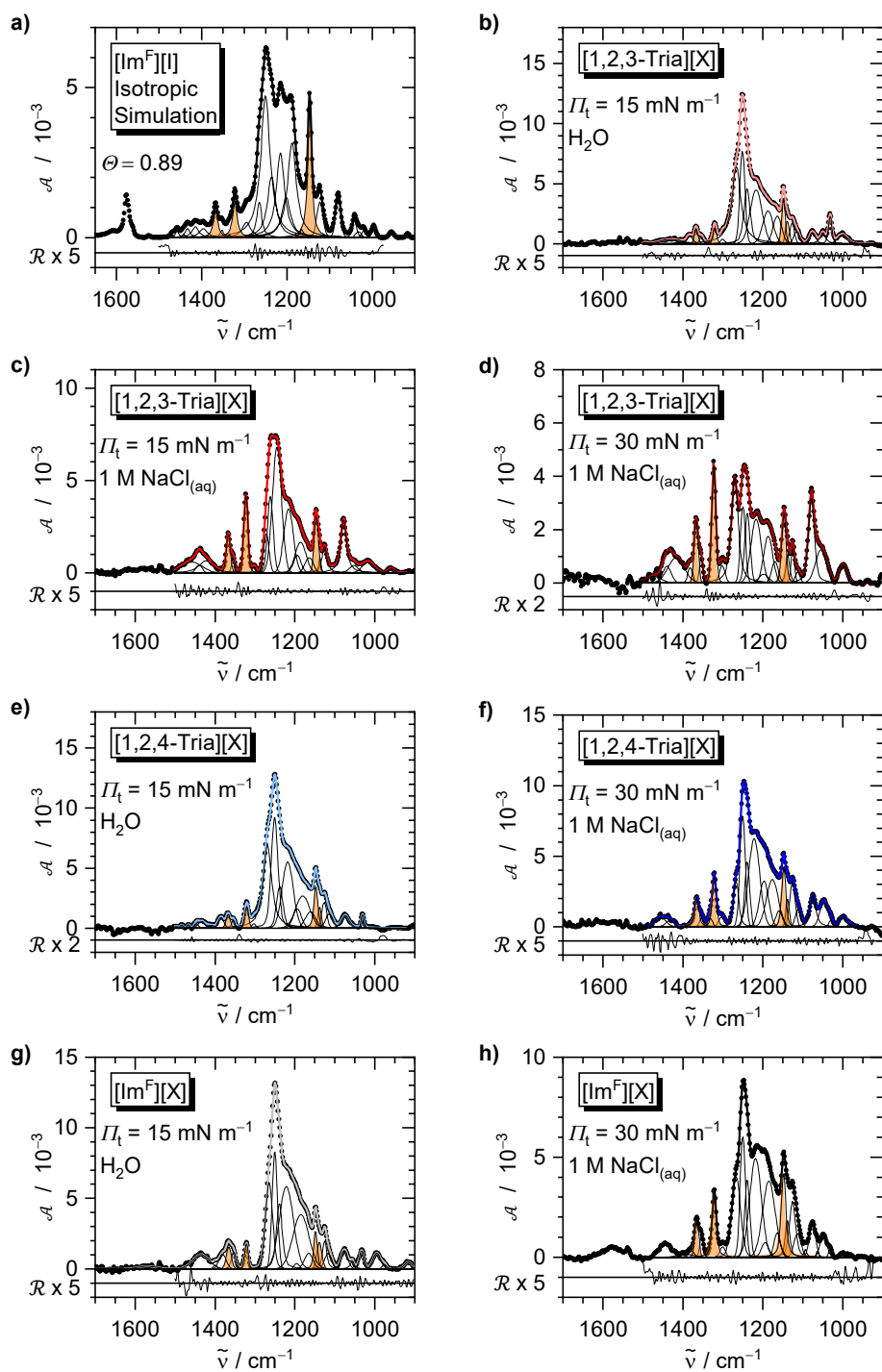
Figure 5.11: Deconvoluted PM IRRA spectra of FILs: a) simulated spectrum, b)-h) FIL-LB-films with compound and transfer conditions given in insets. Residuals *R* shown with magnification below. Bands used for tilt angle determination were colored orange.

Results of the tilt angle analysis are summarized in table 5.6. In case of the FIL monolayers transferred from the purely aqueous subphases, the selected transition dipole moment vectors of modes 3, 4, and 9 yield an average tilt angle of $\theta = (55 \pm 4)$ °. This value is very close to the magic angle of 54.7 ° and, as three modes with different transition dipole moment vectors are affected, the fluorocarbon chains are therefore randomly distributed in the transferred films, indicating the absence of long-range orientational order. On the contrary, long-range orientational order is observed for FIL monolayers transferred from the 1 M NaCl$_{(aq)}$ subphase. The tilt angle of mode 3 directly gives the helix tilt, yielding $\theta = (43 \pm 3)$ ° on the average. In accordance with the DFT calculation, the tilt angle of mode 4 deviates by ca 10-15 ° from the one of mode 3.

Table 5.6: Calculated tilt angles between the transition dipole vector of the analyzed IR absorption modes and the surface normal in LB monolayers of FILs on the Au(poly) surface. The orientation of the transition dipole vector with respect to the helix axis is marked.

FIL	Π_t / mN m^{-1}	Subphase	θ / °		
			Mode 3 ‖	Mode 4	Mode 9 ⊥
[Im][X]	15	H$_2$O	45	57	57
[1,2,4-Tria][X]	15	H$_2$O	57	51	54
[1,2,3-Tria][X]	15	H$_2$O	58	63	56
[Im][X]	30	1 M NaCl$_{(aq)}$	48	29	45
[1,2,4-Tria][X]	30	1 M NaCl$_{(aq)}$	42	42	55
[1,2,3-Tria][X]	15	1 M NaCl$_{(aq)}$	41	23	62
[1,2,3-Tria][X]	30	1 M NaCl$_{(aq)}$	42	27	60

Clearly, the order of the fluorinated alkyl chains depends on subphase for LB transfer. Higher order is found for FIL monolayers transferred from the 1 M NaCl$_{(aq)}$ subphase, which is in accordance with measured water contact angles.

5.5 Molecular Scale Picture of the Fluorinated Ionic Liquid Monolayers on the Au(poly) Surface

Detailed information on the composition, conformation, and orientation of the FIL films transferred onto Au(poly) surfaces are provided by XPS as well as PM IRRAS studies and outlined in figure 5.12. [p1]

FIL monolayers transferred from the pure water subphase exhibit a complex composition (Fig. 5.12a). Probably hydroxide and trace amounts of triflate anions are deposited as counter-ions for the amphiphilic cation. The aromatic azolium rings are oriented preferentially parallel to the gold surface and interact with it. The fluorocarbon chains adopt a helical conformation; however, their orientational order with respect to the surface normal is ill-defined.
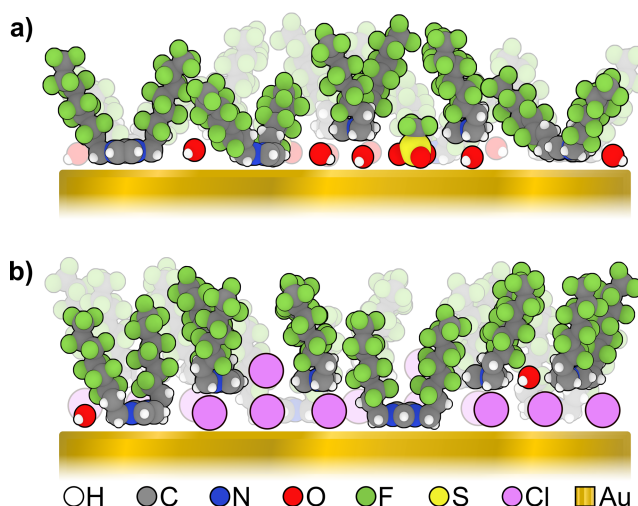
Figure 5.12: Schematic representation of the packing and orientation of [Im^F][X] in LB monolayer transferred onto gold surfaces from a) water, b) 1 M NaCl$_{(aq)}$ subphases. Copied from own publication.[p1]

Chloride and probably hydroxide anions are found in FIL films transferred from the 1 M NaCl$_{(aq)}$ subphase (Fig. 5.12b). Different chloride species found in XPS indicate specific adsorption on the gold surface and the presence of an adlayer. The rings are in contact with the gold surface and adopt an orientation parallel to it. The fluorocarbon chains exhibit a helical conformation and are directed toward air with a defined orientation.

As shown in section 5.3, FIL monolayers exhibit different water contact angles depending on the conditions of transfer rather than on imidazolium,

1,2,3-, or 1,2,4-triazolium structures. Similarly, their molecular orientation is affected hardly by the conditions of transfer in contrast to the individual azolium ion nature. Indeed, this indicates that microscopic packing and orientation properties severely influence the macroscopic contact angle. More uniformly directed fluorocarbon chains, as found in films transferred from the 1 M $NaCl_{(aq)}$ subphase, may lead to increased hydrophobicity of the surfaces. On the other hand, fluorocarbon chains in films transferred from the pure water subphase are of random orientation and thus, yield lower contact angles. However, the latter surfaces are still hydrophobic, too, indicating that fluorocarbon chains are coarsely directed toward air.

6 Interfacial Structure of an Aliphatic Imidazolium-Based Ionic Liquid

Understanding the electrical double layer at the molecular level is fundamental for interface science and electrochemistry. Whereas the EDL of diluted solutions is well understood, the unification of theory and experiments aiming at IL interfaces remains insufficient (Section 3.3.3). The Langmuir-Blodgett method enables the fabrication of well-ordered monolayers of amphiphilic ILs. This gives the opportunity to study a well-defined system, whose preliminary state is known to some extent. To gain more information about its composition and structure, it can be characterized ex situ prior to electrochemical studies. In situ studies under electrochemical control elucidate the capacitive behavior of IL monolayer, which can be correlated with potential-dependent sub-molecular changes in the structure of the film. Major results of these investigations are published with open access in T. Sieling, I. Brand, *ChemElectroChem* **2020**, *7*, 3233-3243.[P2]

Imidazolium-based ILs are widely used in research on the EDL of IL|metal interfaces (Section 3.3.3). Therefore, 1-methyl-3-octadecylimidazolium chloride [$C_{18}Im$][Cl] was chosen as a simple, aliphatic and amphiphilic model compound. Due to $T_m = 210\ °C$,[153] this compound is not a strict IL. However, similarly as described in the previous chapter, the composition changes. The ex situ investigation of FILs at the air|aqueous subphase and air|Au(poly) interfaces in chapter 5 yielded interesting results for this study:[P1]

(i)   An electrolyte subphase stabilizes the IL monolayers at the air|aqueous solution subphase interface.

(ii) While amphiphilic cations stay at the air|electrolyte subphase interface, the water-soluble anion can be exchanged with anions from the subphase.

(iii) Interaction of the cationic, aromatic headgroup with the gold substrate is observed via XPS. This specific interaction may play an important role in the EDL and is observed in literature.[97, 101, 127]

However, chloride anions were shown to adsorb specifically from aqueous alkali chloride solutions on Au electrode surfaces,[154-155] which may complicate studies. Moreover, [$C_{18}Im$][Cl] is soluble in pure water and does not form stable LB monolayers.[156] The hydrophilicity of chloride anions serves to form commercially unavailable compounds. An electrolyte be ue to weak adsorption of perchlorate anions on gold,[51, 157] 0.1 M KClO$_{4(aq)}$ subphases were used in order to form a [$C_{18}Im$][ClO$_4$] film.

6.1   Characterization of the Aliphatic Ionic Liquid at the Air|Liquid Interface

At the air|0.1 M KClO$_{4(aq)}$ interface, [$C_{18}Im$][Cl] forms stable mono-layers.[P2] Due to solubility of the ions in water, a [$C_{18}Im$][Cl] monolayer is unstable on the pure water subphase.[156] Interestingly, Filipe et al. have shown that [$C_{18}Im$][Tf$_2$N] forms stable monolayers at the air|water interface.[25] Therefore, the hydrophobic character of both, the cation and the anion, determines the ability of ILs to from stable monolayers at liquid interfaces. The Langmuir isotherm of the [$C_{18}Im$][Cl] IL is shown in figure 6.1a. Electrostatic interactions between perchlorate anions from the subphase and amphiphilic cations stabilize the monolayer at the air|electrolyte interface.

After starting at the lift-off area of 0.68 nm², the surface pressure of the [$C_{18}Im$][Cl] monolayer increases progressively until the film collapses at $A_{molec,lim}$ = 0.30 nm² and Π_{coll} = 36.2 mN m⁻¹ (Fig. 6.1a, left axis).
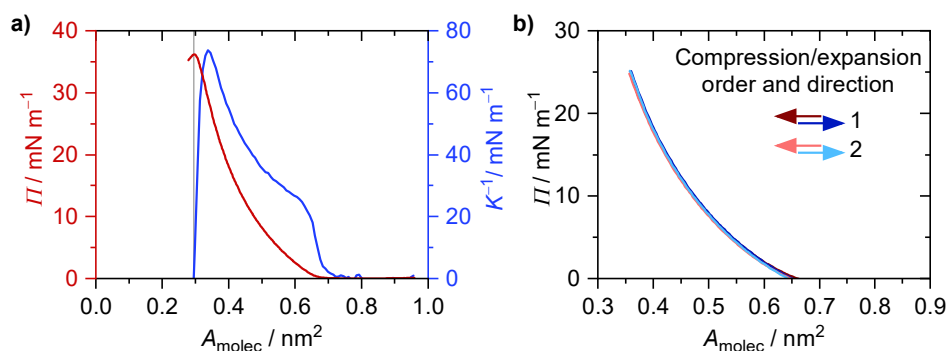
Figure 6.1: a) Surface pressure versus mean molecular area compression isotherm of [C₁₈Im][Cl] on the 0.1 M KClO₄(aq) subphase (red, left axis) and corresponding compressibility modulus (blue, right axis). The limiting mean molecular area is indicated with a vertical line. b) Compression (red) and expansion (blue) of the [C₁₈Im][Cl] monolayer on a 0.1 M KClO₄(aq) subphase. The duration was ca 30 min.

Considering molecular packing, a saturated hydrocarbon chain spans a cross sectional area of 0.26 nm²,[158] which is not reached before monolayer collapse at $A_{molec,lim}$ = 0.30 nm². Thus, the compression is limited by the imidazolium ring. As described in section 5.1, the cross sectional area of a flat imidazolium ring including methylene anchors is close to 0.50-0.52 nm², and much wider than $A_{molec,lim}$. For a vertically arranged imidazolium ring with some degree of unhindered rotation, the area is approximately 0.3 nm². This suggests that the rings are erected or slightly tilted prior to the monolayer collapse. However, the value of $A_{molec,lim}$ is comparably small and indicates monolayer instability. Results of Felipe et al. indicate that [C₁₈Im][Tf₂N] forms a trilayer at A_{molec} < 0.33 nm² on a water subphase.[25] After formation of this trilayer, the isotherm of the [C₁₈Im][Tf₂N] IL exhibits a large hysteresis between compression and expansion. Moreover, the solubility of [C₁₈Im][Cl] in pure water may suggest that the ionic strength or nature of the electrolyte solution is not sufficient to suppress dissolution of single molecules. To verify the stability and packing of the film, compression-expansion cycles were conducted to the surface pressure of the monolayer transfer (Π_t = 25 mN m⁻¹, Fig. 6.1b). The compression and expansion isotherms of two cycles overlap almost perfectly. Particularly, the absence of a hysteresis indicates that neither dissolution nor multilayer-aggregation phenomena take place at these mean molecular areas.

The 2D liquid-like state is a key property when transferring the film onto the gold electrode. The liquid character of ILs must be preserved for further studies, as the C₁₈Im⁺ cations need space and flexibility to react on electrode potential changes. The compressibility modulus (Fig. 6.1a, right axis) was

calculated using equation 3.8 and reaches a maximum value of 72 mN m^{-1}. Followingly, the hydrocarbon chains persist in a 2D liquid-like between lift-off and monolayer collapse, as expected for ILs. Next, the [C$_{18}$Im][Cl] monolayers were transferred onto Au substrates at $\Pi_t = 25$ mN m^{-1} and $A_{molec,t} = 0.36$ nm^2 ($\Gamma_t = 4.6 \cdot 10^{-10}$ mol cm^{-2}), where a densely packed monolayer is formed at the air|electrolyte interface. The transfer ratio was 1.00 ± 0.07.

6.2   Composition of the Aliphatic Ionic Liquid Monolayer on Gold

To study the composition of the [C$_{18}$Im][Cl] monolayer via XPS, it was transferred from the 0.1 M KClO$_{4(aq)}$ subphase onto an Au(poly) substrate, which could be mounted easily onto an XPS sample holder.[P2] The survey XP spectrum of the film shown in figure 6.2 exhibits photoemission lines of Au, C, N, O. Weak signals of Cl and N can be found in high-resolution XP spectra (Fig. 6.3b,c).
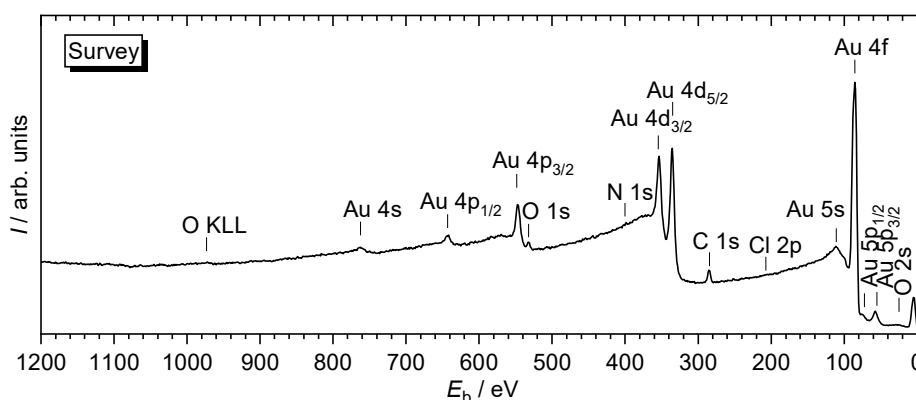
Figure 6.2: XP survey spectrum of the C$_{18}$Im$^+$-based LB-film transferred from 0.1 M KClO$_{4(aq)}$ onto an Au(poly) substrate.

C 1s and N 1s photoemission lines originate from the C$_{18}$Im$^+$ cation.[127] The C 1s spectrum shows two components (Fig. 6.3a). The main signal at $E_b = 284$ eV is ascribed to carbon atoms in the aliphatic chain. The neighboring, weaker signal at $E_b = 286$ eV arises from carbon atoms bound to nitrogen atoms in the C$_{18}$Im$^+$ cation. As the subphase contained 0.1 M KClO$_{4(aq)}$, potassium ions could have been transferred onto the Au(poly) surface. The K 2p photoemission doublet is expected in the vicinity of the C 1s lines, at 292 eV $< E_b < 298$ eV.[143] Within XPS sensitivity, no K 2p signal

is detected in this region, showing the absence of potassium ions in the transferred monolayer. Note that the photoionization cross section of the K $2p_{3/2}$ line is almost one and a half time larger than for the N 1s line when using Al K_α radiation, and thus it should be more easily detected when present in similar amounts.[142] Similarly, no Na 1s signal was detected in the FIL monolayer transferred from the 1 M NaCl(aq) subphase (Section 5.2).[p1]

As discussed in section 5.2, the downshifted binding energy of the N 1s line at $E_b \approx 401$ eV (Fig. 6.3b) indicates interaction of the imidazolium ring with the Au(poly) substrate.[127, 129],[p1] Fine differences in the chemical environment of the imidazolium headgroup are proposed to lead to the breadth of this signal.
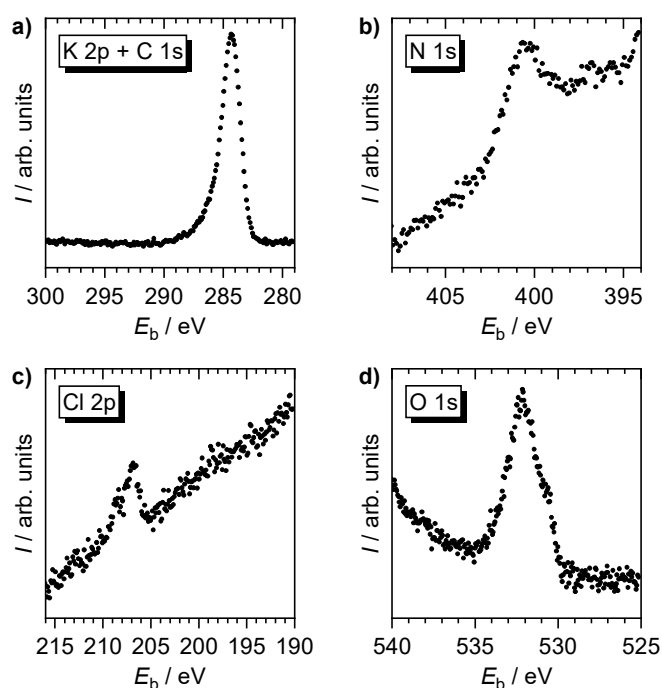
Figure 6.3: High resolution X-ray photoelectron spectra of the C18Im+-based LB monolayer transferred from 0.1 M KClO4(aq) onto a Au(poly) surface: a) C 1s, b) N 1s, c) Cl 2p and d) O 1s.

The Cl 2p spectrum in figure 6.3c shows a doublet at $E_b = 207$ eV (Cl $2p_{3/2}$) and $E_b = 209$ eV (Cl $2p_{1/2}$). The binding energy of Cl $2p_{3/2}$ matches excellently with perchlorate ions present on Al[159] and Au(111)[160] surfaces as well as perchlorate ions in salts[161] paired with organic cations. Chloride anions, present in the compound placed on the LB originally, are within XPS sensitivity absent in the LB monolayer on the Au surface, because no intensity is observed in the region of 197 eV < E_b < 201 eV.[140-141].

Two signals are found in the O 1s spectrum (Fig. 6.3d). The strong line at E_b = 533 eV is ascribed to the perchlorate adsorbed on Au(111) with –0.5 eV difference to literature.[160] The weaker line at E_b = 531 eV is tentatively ascribed to hydroxide ions, encapsulated water,[135] or Au surface oxide.[136-139] Note that this XPS study was conducted on an UV/ozone-cleaned Au(poly) slide, whereas the following electrochemical studies were realized with flame annealed Au(111) single crystals. As observed in the previous study of FILs, water-soluble anions were exchanged by out-numbering anions of the subphase.[p1] Thus, the transferred IL monolayer will be called [C_{18}Im][X], where $X^- = ClO_4^-$ and possibly HO^-.

6.3 Electrochemical Characterization of the Aliphatic Ionic Liquid on Au(111) in an Aqueous Electrolyte

The ionic liquid|metal electrode interface is analyzed in terms of a well-defined model:[p2] The composition and rough orientation of the [C_{18}Im] [X] monolayer on gold was studied in section 6.2. Next, the capacitance of this system and its potential-dependent changes must be measured to elucidate the first layer of the EDL. An aqueous 0.1 M $KClO_{4(aq)}$ electrolyte was chosen for the several reasons:

(i) Slow kinetics in viscous ILs having comparatively high self-diffusion coefficients and low conductivities (Section 2.2) influence potential-driven changes and have been shown to impede successful correlations between capacitance measurements and theory (Section 3.3.3). With an aqueous electrolyte in this system, the diffuse part of the EDL is known, and, most probably, slower rate constants in the LB film will determine the capacitance-potential curve.

(ii) The 0.1 M $KClO_{4(aq)}$|Au(111) interface is well characterized in literature.[157, 162-163] Weak adsorption of perchlorate ions on Au(111) should not perturb studies of the [C_{18}Im][X] monolayer.

(iii) For the following submolecular PM IRRAS studies, it is clear that the measured signals only originate from this very-first layer because other organic species are absent.

Conveniently, characterization in an aqueous electrolyte does not require elaborate and expensive experimental approaches to exclude moisture.[92, 101] Similar measures would additionally be required to be adopted for the PM IRRAS investigation.[110, 112] Due to the impact of a neutral and diluting solvent, this system cannot represent a real IL. Still, results of this model may help to understand the IL|metal interface and potential-driven changes, especially in aqueous solutions of ILs. These kinds of approaches may facilitate the filling of gaps between experiments and theory.

Figure 6.4a shows $C(U)$ curves of the flame annealed, bare Au(111) electrode in 0.1 M KClO$_{4(aq)}$. These curves match excellently with those of Pajkossy et al.,[157] indicating a sufficiently clean and proper setup. The studied potential window is limited to negative potentials by the hydrogen evolution reaction at $U < -0.7$ V and to positive potentials by gold oxidation at $U > 0.6$ V.[164] All potentials in this thesis are referenced vs Ag|AgCl|sat. KCl (abbreviated as Ag|AgCl). Capacitive peaks around $U \approx 0.3\text{-}0.4$ V originate from anion (perchlorate/hydroxide) adsorption/ desorption in combination with lifting or partial recovery of surface reconstruction for positive or negative scans, respectively.[157, 164-165]

Clearly, the capacitances of this film-less system deviate entirely from the 0.1 M KClO$_{4(aq)}$|[C$_{18}$Im][X]|Au(111) system (Fig. 6.4b). This shows that

(i)   the $C(U)$ curve, and thus the interface itself in this system, is dominated by the [C$_{18}$Im][X] monolayer and

(ii) this monolayer stays adsorbed over a wide potential range.

In the potential range of measurement, the capacitance at the 0.1 M KClO$_{4(aq)}$|Au(111) interface greatly exceeds the capacitance at the 0.1 M KClO$_{4(aq)}$|[C$_{18}$Im][X] |Au(111) interface.
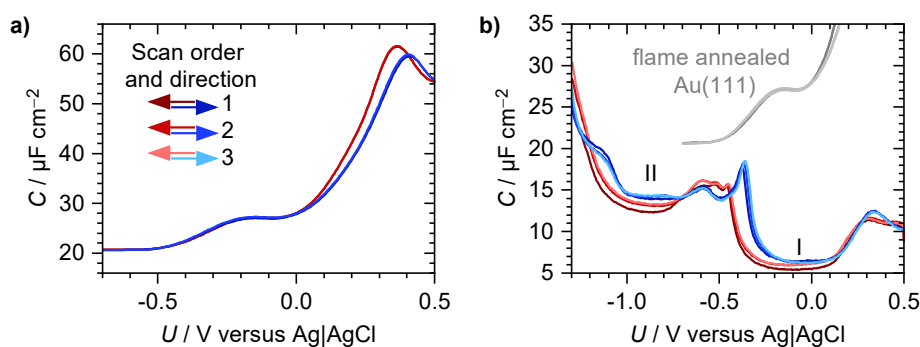
Figure 6.4: Differential capacitance versus potential plots of 0.1 M KClO$_{4(aq)}$ on the Au(111) electrode surface. a) Flame annealed Au(111) electrode. b) Au(111) covered with

the [C$_{18}$Im][X] LB monolayer. Negatively (red lines) and positively (blue lines) going potential scans in a) two and b) three consecutive potential scans, as marked in the figure.

The measured capacitance may depend on the frequency applied (Section 4.4.1). For determination of the DL capacitance at the [C$_{18}$Im][X]-covered Au(111) interface in 0.1 M KClO$_{4(aq)}$ (Fig. 6.4b), a low frequency (f = 20 Hz) was chosen. Frequencies in this order of magnitude were used for the capacitance measurements of more simple aqueous electrolyte (e.g. alkali halides) at metal electrodes.[51, 53, 154, 157] Also, metal electrodes covered by organic molecules were studied in this range of frequencies.[166] Possible molecular reorientations shall be elucidated in this study and, due to usually slow kinetics, must be detected with a low frequency. The resulting curves do not show equilibrium capacitances, but they are useful for qualitative interpretation.[166]

Two plateau-like regions are visible in the $C(U)$ curves of the 0.1 M KClO$_{4(aq)}$|[C$_{18}$Im][X]|Au(111) system. These are marked in figure 6.4b as states I and II. State I is in the potential region of -0.3 V < U < 0.1 V and exhibits a low capacitance of 6-7 µF cm^{-2}. Pseudocapacitive peaks present on both sides of state I, which is the capacitance minimum, indicate rearrangements or reorientations in the film. Following these peaks on the negative polarization branch, state II forms in the potential region of -1.0 V < U < -0.7 V. Its capacitance is higher and increased to 13-15 µF cm^{-2}. For more negative potentials (U < -1.1 V), the onset of hydrogen evolution reaction and desorption of the [C$_{18}$Im][X] monolayer is proposed. Note that on a bare Au(111) electrode in 0.1 M KClO$_{4(aq)}$, the onset of the hydrogen evolution reaction occurs at $U \approx$ -0.7 V.[164-165] Upon reversal of the potential scan, the film is reconstituted with a hysteresis at -1.2 V < U < -1.0 V on the Au(111) surface. Furthermore, the presence of a ca 100 mV hysteresis of the positive and negative potential scan between states I and II (-0.4 V < U < -0.3 V) indicates that the transition between these states is a slow process.

Further insight is given by electrochemical impedance spectroscopy in a wide frequency range (Fig. 6.5). The 0.1 M KClO$_{4(aq)}$|[C$_{18}$Im][X]|Au(111) system was studied at four selected potentials: U = 0.4 V (transition peaks), 0.0 V (state I), -0.4 V (transition peaks), and -0.8 V (state II). Instead of fitting vague model circuits, these results are examined diagnostically.

The potential changes affect the total impedance little (Fig. 6.5a). For wide frequency ranges ($2 \cdot 10^{-1}$ Hz $< f < 2 \cdot 10^2$ Hz and $1 \cdot 10^4$ Hz $< f < 1 \cdot 10^5$ Hz), the slope of the $|Z|(f)$ curves is independent of the potential. Highest impedances are reached at $U = 0.0$ V. When shifting to more positive or more negative potentials, the absolute impedance decreases, concurring with the capacitance changes described above.
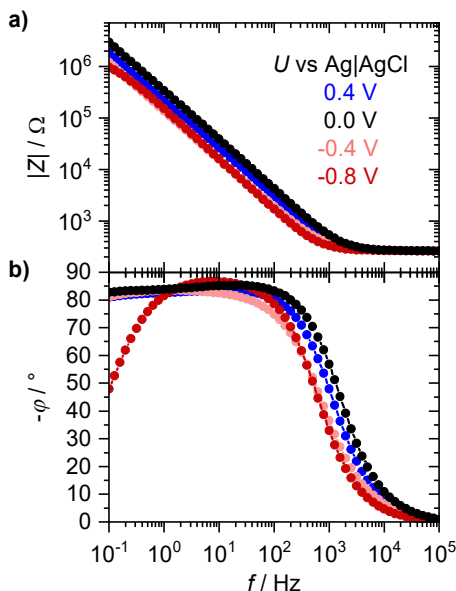
Figure 6.5: EI spectra of the [C$_{18}$Im][X] LB monolayer on the Au(111) in 0.1 M KClO$_{4(aq)}$. a) Impedance and b) phase angle versus frequency at the following potentials: blue – $U = 0.4$ V, black – $U = 0$ V, light red – $U = -0.4$ V, and dark red – $U = -0.8$ V versus Ag|AgCl. The measured values are connected by splines.

The phase angle shows more pronounced difference in the potential-dependence (Fig. 6.5b), particularly in the region of 10^{-1} Hz $< f < 10^0$ Hz. Whereas $-\varphi$ is close to 85 ° for $U = 0.4$ V, 0.0 V, and -0.4 V, it decreases for $U = -0.8$ V to $-\varphi \approx 50$ ° at $f = 0.1$ Hz. Minima following such decreases are ascribed to the formation of pores and channels in films adsorbed on electrode surfaces.[167-169] Although no minimum is observed (yet), the decrease in the phase angle suggests a permeability or sensitivity for ion transport through the [C$_{18}$Im][X] film.

Additionally, a representation of the EIS results in the complex capacitance plane (Eq. 4.20) is given in figure 6.6. The double layer capacitance can be extracted from the real part at the ending of the first semicircle and matches quite well with the single frequency curve measured in figure 6.4a.
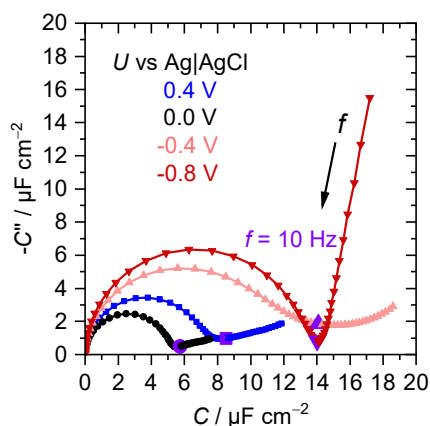
Figure 6.6: EI spectra of the [C₁₈Im][X] LB monolayer on the Au(111) in 0.1 M KClO₄(aq) in the complex capacitance plane at the following potentials: blue – U = 0.4 V, black – U = 0 V, light red – U = -0.4 V, and dark red – U = -0.8 V versus Ag|AgCl. Values at f = 10 Hz are highlighted in purple and by size. The measured values are connected by splines.

Electrochemical studies suggest that alterations in the structure and/or composition of the [C₁₈Im][X] monolayer on the Au(111) surface are caused by electric potentials.

6.4 Potential-Driven Changes in the Langmuir-Blodgett Film

In order to investigate (sub-)molecular potential-driven changes in the [C₁₈Im][X] monolayer on the Au(111) surface, in situ PM IRRAS under electrochemical control is employed.[P2] The C₁₈Im⁺ cation consists of an imidazolium headgroup and an aliphatic tail. Both give rise to IR absorption modes in different regions.[32, 170-173] Therefore, PM IRRA spectra provide information on orientation and conformation of molecules in the studied film.

6.4.1 Potential-Dependent Behavior of the Ring Moieties

Raw in situ PM IRRA spectra of the 0.1 M KClO₄(aq)|[C₁₈Im][X] |Au(111) system are depicted in figure 6.7 and were measured with the half-wave retardation of the PEM set to $\tilde{v}_{\mathrm{HWR}}$ = 1600 cm⁻¹.[P2] The in-plane ring stretching vibrations R₁ and R₂ are located at $\tilde{v}$ = 1575 cm⁻¹ and $\tilde{v}$ = 1561 cm⁻¹, respectively.[170] Figure 6.7a shows that all spectra overlap, independently of the applied electrode potentials. The enlargement shown in the inset of figure 6.7a reveals humps at $\tilde{v}$ = 1570 cm⁻¹, 1540 cm⁻¹, and 1506 cm⁻¹, which

likely arise from not fully compensated water vapor as shown by matching dips in figure 6.7b.
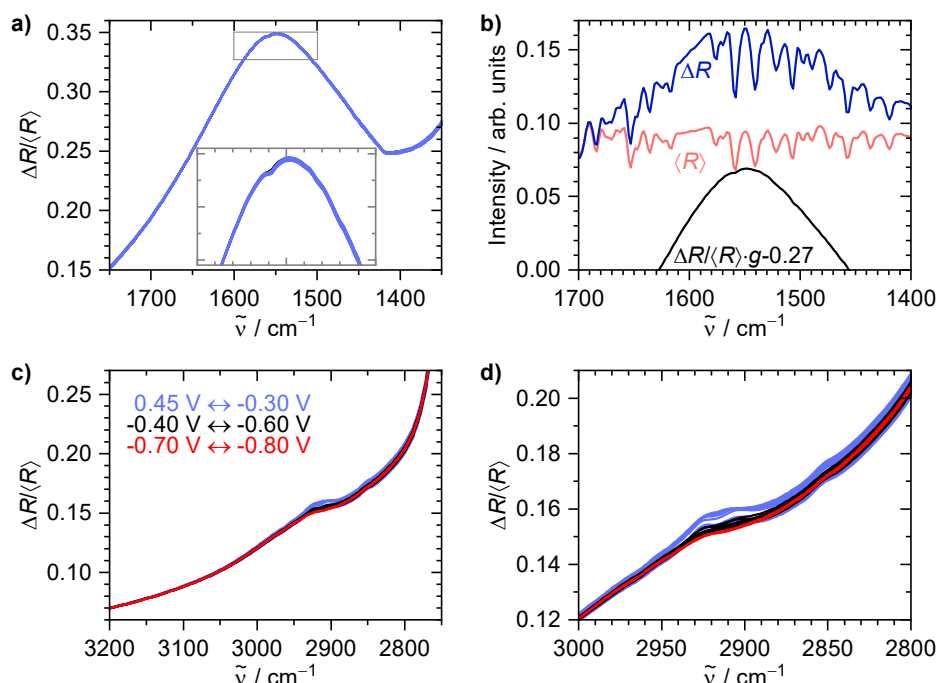
Figure 6.7: Raw in situ PM IRRA spectra of the [C18Im][X] monolayer on Au(111) in 0.1 M KClO4 (D2O) measured at $\tilde{v}_{HWR}$ = 1600 cm^{-1}. a) Ring stretching region. b) Differential and averaged signals as well as the raw PM IRRA spectrum of a single potential scan (U = -0.05 V) in the ring stretching region. c) CH stretching region 2770 cm^{-1} < $\tilde{v}$ < 3200 cm^{-1}. d) Enlargement of c. Different colors in a), c), and d) represent potential ranges applied to the Au(111) electrode as indicated in c). Note that spectra in a and c are displayed in the same intensity scale, $\Delta R/\langle R\rangle$ spans 0.21.

After background correction, a very weak signal in the order of 10^{-4} absorption units appears around $\tilde{v} \approx 1570$ cm^{-1} in the ring region (Fig. 6.8a, purple line). However, it is not suitable for quantitative analysis due to the insufficient signal to noise ratio and very low intensity. The transition dipole moment vectors of the ring modes are in the plane of the imidazolium ring.[32, 170] The presence of intensity indicates that the rings are not completely flat on the electrode surface, although interaction with gold is shown by XPS (Section 6.2). With optical constants of the in-plane ring modes (Fig. 6.8b), different intensity enhancements (Section 4.3.4) due to varying tilt angles of the ring were simulated under experimental conditions and shown for comparison together with the experimental spectrum (Fig. 6.8a). The film thickness was set to 2.7 nm and the surface coverage (θ = 0.94) estimated from the LB transfer as described in section 5.1. Low intensities indicate that the ring is tilted toward the gold surface, and vice versa. From comparison

to the simulated spectra, an average tilt of $\theta \approx 50\text{-}60\,°$ is estimated tentatively. Whereas the mean molecular area for a flat imidazolium ring is calculated to be close to $0.50\text{-}0.52\ \text{nm}^2$ (Section 5.1), the available area at LB transfer conditions is much less ($A_{\text{molec,t}} = 0.36\ \text{nm}^2$ at $\Pi_{\text{t}} = 25\ \text{mN m}^{-1}$, section 6.1). Roughly, a ring tilt of $\theta \approx 53\,°$ vs the surface normal is estimated under these conditions, which corresponds well to the tilt angle determined from PM IRRAS experiments. Apparently, the orientation of the imidazolium moiety is dominated by the LB transfer conditions and rigid with respect to potential changes. Motobayashi et al. have shown that octyl- or dodecyl- methyl-imidazolium cations adopt a flat orientation on the Au(poly) surface.[111] Over a broad potential range they stay rigid in contrast to short chain methyl-imidazolium cations (Section 3.3.3), which is in accordance with this experiment.
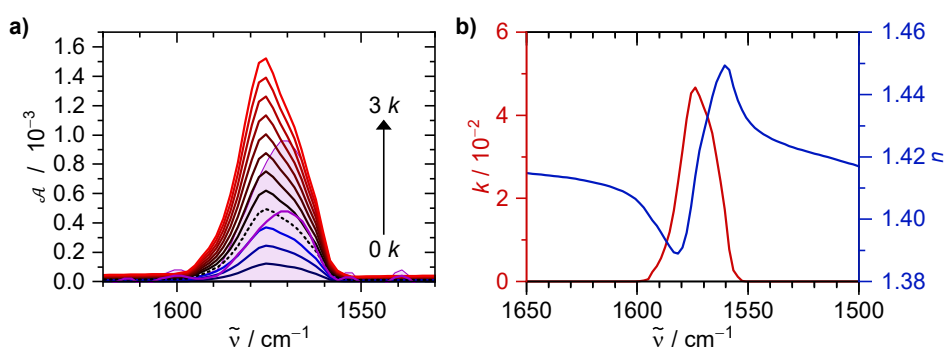
Figure 6.8: a) Averaged and background corrected PM IRRA spectrum (purple line) of the [C18Im][X] monolayer on Au(111) in 0.1 M KClO4 (D2O); the shadowed area shows the estimated intensity uncertainty due to background correction. Simulated PM IRRA spectra of the in-plane ring stretching modes from optical constants under experimental conditions are shown behind. Different intensity attenuations and enhancements of the absorption coefficient in steps of $0.25\,k$ correspond to the overlap of the transition dipole moment vectors of the ring stretching modes and the electric field vector: attenuation ($0\text{-}0.75\,k$, blue lines), random distribution ($1\,k$, black dotted line), and enhancement ($1.25\text{-}3\,k$, red lines) of the absorption modes. b) Absorption coefficient and refractive index of [C18Im][Cl] in methanol-d_4 in the in-plane ring stretching region.

CH stretching vibrations of aromatic carbon atoms in the imidazolium ring appear between $\tilde{\nu} = 3200$ and $3000\ \text{cm}^{-1}$. Overtones and combinations of ring modes enhanced by Fermi resonances may also appear in this region, too.[174-177] Their transition dipole moment vectors are also located in the ring plane. Similarly to the in-plane ring stretching modes, the aromatic $\nu(\text{CH})$ modes do not change with the applied potential and cannot be distinguished from the background spectrum (Fig. 6.7c).

6.4.2 Potential-Dependent Behavior of the Alkyl Chains

Potential dependent changes are clearly visible in the $\tilde{v} = 3000\text{-}2800$ cm^{-1} spectral region, even without background correction (Fig. 6.7d).[P2] These modes are ascribed to methyl- and methylene groups from the aliphatic chain of the $C_{18}Im^+$ cation on the Au(111) surface.[171-173] Their optical constants are required for the quantitative analysis and are shown in figure 6.9.
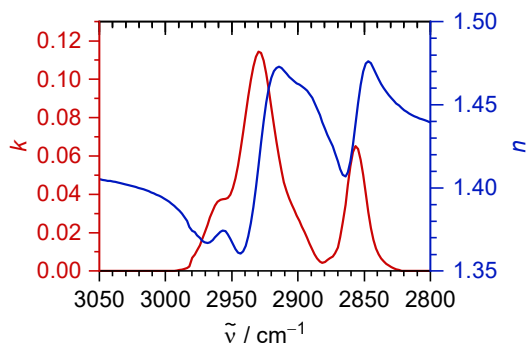
Figure 6.9: Absorption coefficient and refractive index of [$C_{18}Im$][Cl] in methanol-d_4 in the aliphatic CH stretching region.

An isotropic simulation of a monolayer thick film of [$C_{18}Im$][Cl] under experimental conditions is shown in figure 6.10a and plotted in the same scale as potential-dependent in situ PM IRRAS experiments underneath (Fig. 6.10b). The asymmetric CH stretching vibrations of methyl group bonded to the hydrocarbon chain $v_{as}(C\text{-}CH_3)$ appears at $\tilde{v} = (2949 \pm 2)$ cm^{-1}.[174] It is overlapped with overtones or combinations of methylene scissoring modes $\delta(CH_2)$ enhanced by Fermi resonance (FR1).[171-173, 178] The IR absorption mode of the symmetric methyl stretching $v_s(C\text{-}CH_3)$ is centered at $\tilde{v} = (2877 \pm 2)$ cm^{-1}. In the simulated spectrum (Fig. 6.10a), the asymmetric $v_{as}(CH_2)$ and symmetric $v_s(CH_2)$ methylene stretching modes appear at $\tilde{v} = 2932$ cm^{-1} and $\tilde{v} = 2856$ cm^{-1}, respectively. These modes are redshifted in the experimental spectrum (Fig. 6.10b), yielding $\tilde{v} = (2926 \pm 1)$ cm^{-1} for $v_s(CH_2)$ and $\tilde{v} = (2852 \pm 1)$ cm^{-1} for $v_s(CH_2)$. The lower wavenumbers indicate that less gauche configurations are present in the [$C_{18}Im$][X] LB film on the Au(111) surface than for [$C_{18}Im$][Cl] which probably forms micelles in methanol solution. Still, the methylene band positions in both samples are characteristic for liquid and mobile alkanes.[172] This is compatible with a preservation of the LB transfer conditions, at which the compressibility modulus indicates a 2D liquid-like state (Section 6.1).
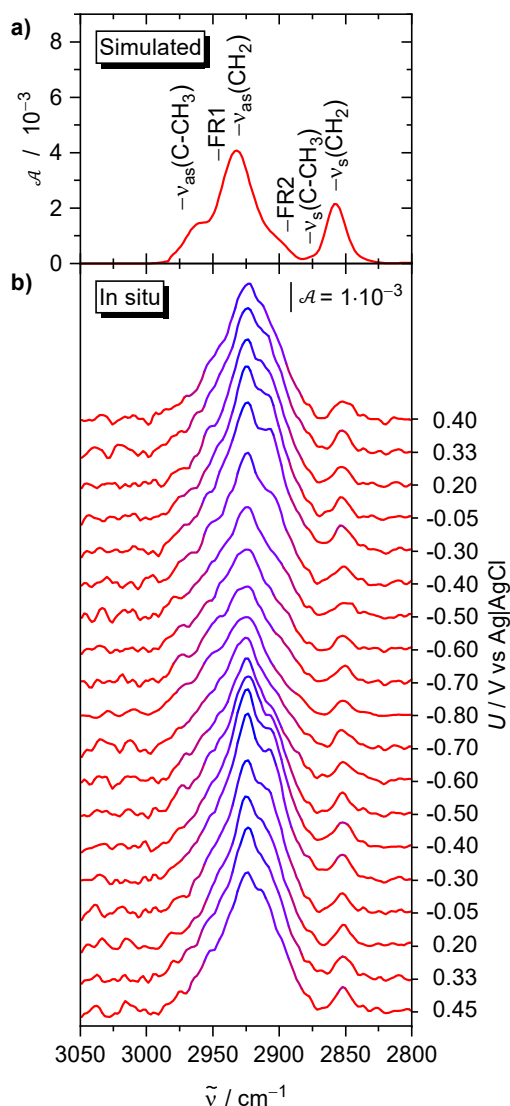
Figure 6.10: a) PM IRRA spectrum simulated from isotropic optical constants of the of [C$_{18}$Im][Cl] IL for a monolayer thick film (2.7 nm) under experimental conditions. b) Background corrected PM IRRA spectra ($\tilde{\nu}_{HWR}$ = 2900 cm^{-1}) of the [C$_{18}$Im][X] LB monolayer on Au(111) in 0.1 M KClO$_4$ (D$_2$O) at potentials marked in the figure. Colors correspond to higher (blue) or lower (red) absorbance.

Two bands originating from overtone or combination of δ(CH$_2$) vibrations are enhanced by Fermi resonance interaction with ν$_s$(CH$_2$) vibrations: FR1 around $\tilde{\nu} \approx 2949$ cm^{-1} and FR2 around $\tilde{\nu} \approx 2900$ cm^{-1} (Fig. 6.10). The latter mode is related to lateral interchain interactions und thus influenced by neighboring methylene groups and their packing.[171, 178-179] In comparison to the simulated spectrum originating from C$_{18}$Im$^+$ molecules in the solution phase (Fig. 6.10a), this mode is enhanced in the in situ spectra of the [C$_{18}$Im][Cl] monolayer in the Au(111) surface (Fig. 6.10b). Followingly,

intermolecular interaction are significantly stronger in the film. On the other hand, the FR1 mode is influenced by intrachain interactions and sensitive to the ratio of gauche and trans conformations in a hydrocarbon chain. In addition to the unchanging wavenumber positions mentioned above, the FR1 mode's independence of the electrode potential indicates no variations in the average conformation of the hydrocarbon chain. According to quantum chemical simulations, ca 30 % of gauche conformations are present in a liquid hydrocarbon chain.[180]

Interesting potential-dependent changes are observed in the intensities of the fundamental methylene stretching modes (Fig. 6.10b), most pronounced for the $\nu_{as}(CH_2)$ band. According to equation 4.13, intensity variations can be ascribed to different factors:

(i) Change of the surface concentration. This is not the case, as subsequent $C(U)$ curves show no desorption and the minimal capacitance stays at similar values (Section 6.3).

(ii) Change of the electric field strength of the radiation on the surface. If this was the case, all bands were affected similarly.[181] However, intensity changes are unique for different bands in this experiment.

(iii) Change of the transition dipole moment. In the case of methylene groups, this term does not depend on the electrode potential.[181] The dipole moment (and therefore the transition dipole moment) increases with increasing polarizability and electric field strength of the electrode.[182] As evident from equation 4.13, the increase in intensity is proportional to the square of the transition dipole moment and thus to the square of the electric field. Upon polarization of the electrode, a parabolic intensity increase centered around the PZC is expected,[183] which is not the case. Also, this effect should affect all bands, though to different extents.

(iv) Change in the overlap angle θ of $\vec{E}_z$ and $\vec{M}(CH_2)$. This cause is most likely, as other factors were excluded. It indicates potential-driven reorientations, which are subject to this study.

To quantify orientational changes, integral intensities must be extracted from the spectra and compared (Section 4.3.4). Two methods have been applied: Curve fitting and raw integration within fixed boarders. Both methods have severe advantages and disadvantages. Curve fitting is difficult, but capable of giving accurate and more results. As described above, at least seven bands contribute to the spectrum. Each band is

characterized by a unique wavenumber position, fwhm, intensity, and Gaussian-Lorentzian shape. Without constraints, physically unreasonable results are achieved, mostly due to the broad and featureless flanks of the in situ spectra (Fig. 6.10b), which lead to unrealistically large and low fwhms. With constraints, an operator-given bias is imposed into the procedure. Fourier self-deconvolution and the second derivative can aid for constraining band positions or setting initial bands. Zero to two bands were constrained during deconvolution, and a fully Gaussian line shape was assumed (Fig. 6.11a).
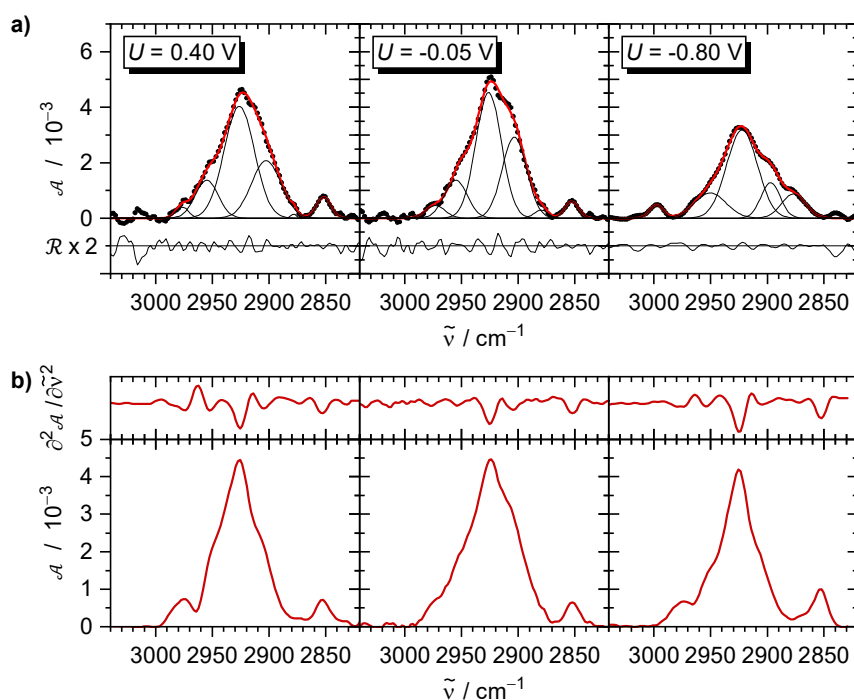
Figure 6.11: Analysis of the PM IRRA spectra of the [C_{18}Im][X] LB monolayer on Au(111) in 0.1 M KClO$_4$ (D$_2$O) in the aliphatic CH stretching region. a) Exemplary deconvolution of the spectra measured at three different potentials vs Ag|AgCl. b) Spectra of three different experiments averaged over all potentials within one set int the lower panels. Maxima of the second derivative shown in the upper panels were used as integration boarders.

On the other hand, raw integration is an easy procedure and solely yields the integrated area. To set the bounds of integration, maxima in the second derivative were used (Fig. 6.11b). The operator bias is kept to a minimum. A fixed set of bounds for the whole potential scan is only valid, if the band positions and their fwhms do not change.

The resulting integrals of both procedures overlap well (Fig. 6.12). Fitting led to band positions and fwhms, which do not change much depending on

the applied potential. Thus, the crude and simple raw integration can be used. The overlap with the latter procedure shows that operator-based errors by presetting fitting parameters in the deconvolution procedure is small. Concluding, both methods can be used and co-control each other after careful analysis of the IR spectra.
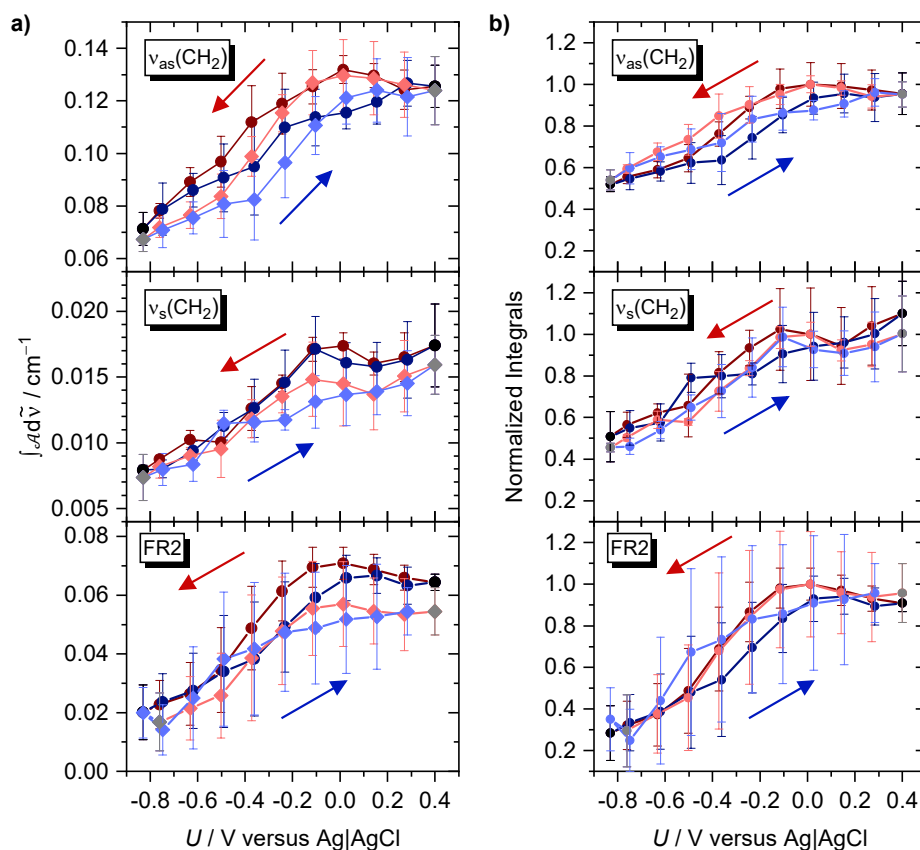
Figure 6.12: a) Integrated absorbances of $\nu_{as}(CH_2)$, b) $\nu_s(CH_2)$, and FR2 bands as a function of electrode potential in the $0.1\,M$ $KClO_4$ $(D_2O)\,|\,[C_{18}Im][X]\,|\,Au(111)$ system. b) Results normalized to the integrals at a shared reference potential close to the capacitance minimum. blue – positive sweeps, red – negative sweeps, circles in darker shades – results of the raw integration, rhombuses in lighter shades – results of the band deconvolution.

Generally, highest integrated absorbances of methylene stretching modes in the $[C_{18}Im][X]$ monolayer on Au(111) are found in in adsorption state I at moderately negative potentials (Fig. 6.12, cf. Fig. 6.4a). The transition into state II at more negative potentials leads to an intensity decrease for all depicted bands.

The FR2 mode reflects interchain interaction, which is a crucial film property considering effects such as nanosegregation in ILs. The transition

dipole moment vector of overtones or binary combinations of $\delta(CH_2)$ modes are located in the same plane and direction as for the resonating $\nu_s(CH_2)$ mode. For a single, decoupled mode, it lies in the bisector of the methylene group. Both absorbances must be affected if the methylene groups reorient. It is to distinguish whether the FR2 mode loses intensity upon going to negative polarizations due to either change in the tilt angle or reduced interchain interaction. A change in the latter would cause a dissimilar behavior, as FR is a process of intensity redistribution and energy must be preserved. If both modes lose intensity in the same manner, the change in the tilt angle of the methylene groups is responsible. However, in this case the extent of intensity change can still be different due to unequal transition dipole moment strengths. Thus, the integrated absorbances were normalized to the value at $U = $ -0.05 V, close to the capacitance minimum and maximum absorption (Fig. 6.12b). Whereas the integral intensities of both $\nu_{as}(CH_2)$ and $\nu_s(CH_2)$ modes decrease to approximate 50 % of the reference value, the FR2 intensity decreases even more to 30-40 % of the reference value. This indicates that interchain interaction indeed decreases with decreasing potentials. However, this result should be taken tentatively when considering the standard errors of the mean.

As discussed above, changes in the orientation of methylene groups are accounted for the intensity changes. The alkyl chain is in a liquid state with multiple gauche conformations and no discrete conformation. Therefore, orientational changes cannot be calculated explicitly, but they can be assessed with the segmental order parameter (Section 4.3.4). According to intensity changes of the methylene stretching modes, the order depends on the applied electrode potential (Fig. 6.13). In the adsorption state I at rather positive potentials (-0.3 V < U < 0.1 V), low order is found ($S = 0.25 \pm 0.1$). It corresponds to a large average tilt of methylene segments with respect to the surface normal. The potential-driven transition of the film into state II (-1.0 V < U < -0.7 V) results in an intensity decrease in $\nu_{as}(CH_2)$ and $\nu_s(CH_2)$ modes (Fig. 6.12b,c), and consequently in an increase in order. S equals 0.60 ± 0.05 at $U = $ -0.8 V, indicating increasing order in packing and orientation of the hydrocarbon chains.
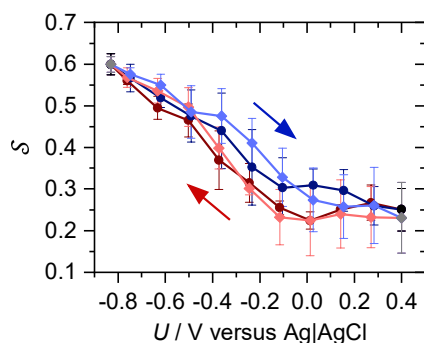
Figure 6.13: Segmental order parameter of the hydrocarbon chain in the [C₁₈Im][X] LB monolayer on the Au(111) electrode surface in 0.1 M KClO₄ (D₂O) as a function of potential in the negative (red) and positive (blue) going potential scans.

The decrease in intensity of $\nu_{as}(CH_2)$ and $\nu_s(CH_2)$ modes, and therefore positive values of $\mathcal{S}$, indicate an overlap of the methylene backbone with the electric field vector normal to the surface (Section 4.3.4), i.e. the hydrocarbon chain erects. The results described above show that significant changes in the hydrocarbon chains of the amphiphilic cation accompany the phase transition of the [C₁₈Im][X] monolayer adsorbed on the Au(111) surface and show that this transition is of supramolecular nature.

6.5   Molecular Scale Picture of the Aliphatic Ionic Liquid at the Electrolyte|Electrode Interface

The results obtained by complementary probing techniques yield a consistent molecular scale picture of electric potential-driven changes in the studied system.[p2] First, LB transfer was used to deposit a 2D-liquid [C₁₈Im]⁺-based monolayer on gold. The following XPS analysis confirms the successful transfer and shows that chloride anions present in the original compound were replaced by perchlorate anions of the subphase. N 1s spectra indicate a contact between the imidazolium ring and the gold surface. Accordingly, alky chains must be directed toward vacuum. Perchlorate ions may either be located in the ring plane, due to H-bonding with ring CH atoms, or be positioned above the ring, interacting with it via dispersive and electrostatic forces.[184-186] The tetrafluoroborate anion is similar in structure, size, and net charge to the perchlorate ion. According to IRS, nuclear magnetic resonance spectroscopy, and quantum chemical calculations, it should be located above the ring in 1-ethyl-3-methy-

imidazolium IL water mixtures, independently of the water concentration.[187] Rare crystal structures of imidazolium perchlorates reveal hydrogen bonds between cations and anions,[123, 184] or perchlorate ClO_4^- ions being located above the ring.[185-186] According to Downard et al, rectangular $[(H_2O)_2Cl_2]^{2-}$ dimers are formed in the crystal structure of $[C_{18}Im][Cl] \cdot H_2O$.[135] For the amphiphilic cation, two conformers are found, in which the headgroup is either bent or linear with respect to the interdigitated alkyl chains. Whereas the anionic $[(H_2O)_2Cl_2]^{2-}$ dimers interact above the imidazolium plane with all aromatic CH groups in the linear conformer, these H-bonding interactions take place in the ring plane of the bent conformers. Concluding, anions may be located in the ring plane as well as above in the $[C_{18}Im][X]|Au(111)$ system. Due to the interaction of the imidazolium ring with the Au surface and the packing density of the cation, space in the plane of the ring for H-bonding is limited, and thus the position above the ring is more likely.

The correlation of results obtained from different electrochemically controlled techniques, provides a complex behavior for the 0.1 M $KClO_{4(aq)}$ $|[C_{18}Im][X]|Au(111)$ system. In situ PM IRRAS indicates an attenuation of the in-plane ring signals in the monolayer, suggesting that the imidazolium ring is inclined toward the Au(111) surface. The orientation of the ring is determined by LB transfer conditions and does not respond to potential changes. On the contrary, the liquid hydrocarbon chain in the $C_{18}Im^+$ cation adapts to electric potentials. The chain order in states I and II are illustrated schematically in figure 6.14.

State I refers to moderate potentials (-0.3 V $< U < 0.1$ V) and low capacitances (6-7 μF cm^{-2}). According to Su et. al, the PZC of an unmodified Au(111) electrode in 0.1 M $KClO_{4(aq)}$ is close to 0.3 V vs Ag|AgCl,[188] from which can be concluded that a low negative charge density is accumulated on the Au(111) electrode in adsorption state I. In this case, perchlorate anions may be located close to the ring headgroup, in order to (partially) compensate the positive excess charge given by the cations. Different experimental[76, 81, 110] and theoretical[75, 189-190] results indicate a stratified cation-anion structure of ILs subjected to moderate electrode potentials (Section 3.3.3). This structure is also preserved to some extent in the presence of water.[27, 76, 81] The low capacitance can be ascribed to the low permittivity of the film. To a substantial part, the film consists of apolar hydrocarbon chains, whose permeability is low ($\varepsilon_r \approx 2$). Perchlorate ions are classified as chaotropic and affect the packing, conformation, and mobility of aliphatic

chains.[191] A low order and large average tilt of methylene groups can be explained by aggregation of the alkyl chains, which is driven by van der Waals interactions (Fig. 6.14a).
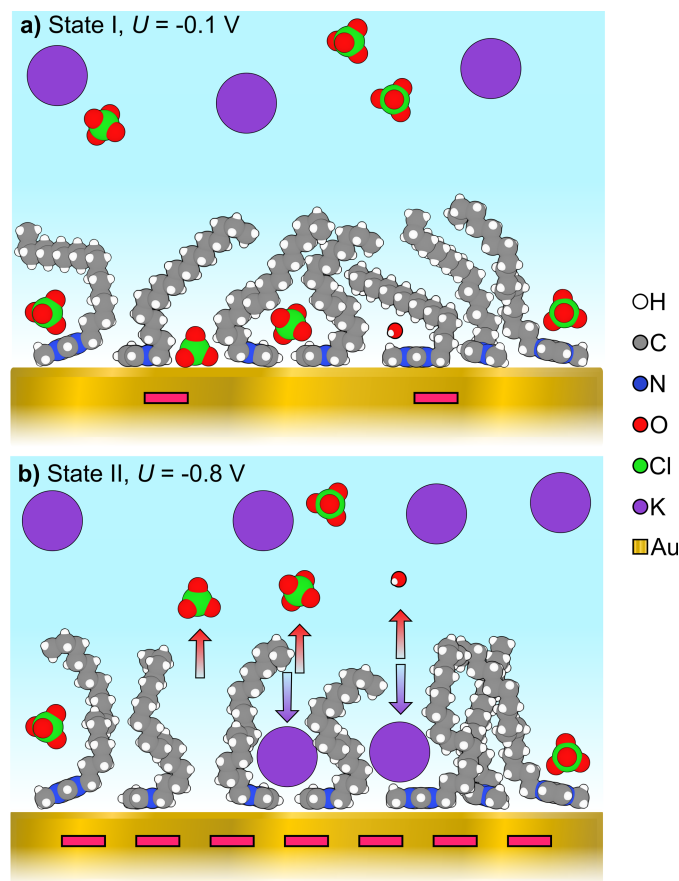
Figure 6.14: Scheme illustrating the molecular scale-order in the [C$_{18}$Im][X] ionic liquid film on the Au(111) surface in 0.1 M KClO$_{4(aq)}$ in adsorption states a) I and b) II. Note that van der Waals radii are used for the different atoms. The use of ionic radii would imply that no solvation shell is present, whereas hydrodynamic radii suggest a complete hydration shell. However, the hydration number of ions close to the electrode and in the organic film is unknown.

Upon polarization to more negative potentials (-1.0 V < U < -0.7 V), a transition into the high capacitance (13-15 μF cm^{-2}) state II occurs. The decreased surface charge density should lead to an increase in attraction between the Au(111) surface and imidazolium cations. The change of the ion-electrode interaction may also lead to a change in ion-ion interactions at the phase boundary, which could be responsible for the phase transition. A change of the phase angle in the EIS experiment indicates an increased ion permeability through the monolayer due to the formation of defects. Perchlorate anions may leave the monolayer, to compensate the change in

surface charge density. Instead, potassium cations and water may penetrate the film. The formation of defects for transport of different species may cause a supramolecular rearrangement in the film. As the imidazolium rings stay rigid, the transition only affects a fragment of the film. The disentanglement of partially aggregated structures, as proposed in figure 6.14a, may lead to an erection of the alkyl chains, which is observed via increased order in PM IRRAS experiments and necessary for ion penetration (Fig. 6.14b). Moreover, the tentatively proposed decrease in interchain interaction supports a disentanglement of alkyl chains. Due to the flow of electrolyte into the film, the permittivity becomes increased and the screening length reduced. This is consistent with higher capacitances in adsorption state II.

The hysteresis between positive and negative potential scans in the $C(U)$ curves is reflected in the potential-dependent alterations of the methylene stretching intensities and chain order, although less significantly in these cases. It may be related to an activation barrier which is required to lift the structure present in the state prior to phase transition. Such phenomena have been observed or proposed in literature.[110-111, 113] In the proposed process for the [C_{18}Im][X] monolayer, alkyl chains my be aggregated in state I. To form defects, which are required for ion permeability, the energy gain of van der Waals interactions in this aggregate must be overcome and is given by an overpotential.

Interestingly, the reorientation of alkyl chains matches well with coarse-grained IL simulations of Fedorov et al. mentioned in section 3.3.3.[83] Indeed, the neutral tails in this IL film may act as latent voids. When the driving force is given by the need for charge compensation, they may create space close to the phase boundary by reorientation (cf. Fig. 3.7).

7 Infrared Spectroscopic Features in Perdeuterated Alkyl Chains of Ionic Liquids and Anion Effects

In the previous chapter, the aliphatic chains in the amphiphilic imidazolium-based IL LB monolayer were shown to give interesting responses to the applied potential. The IR spectroscopic analysis was based on methyl and methylene groups in the saturated alkyl chain, which give rise to symmetric and asymmetric stretching modes in the $2970\ cm^{-1} > \tilde{v} > 2840\ cm^{-1}$ spectral region.[172-173] However, the $v_s(CH_2)$ and $v_s(CH_3)$ modes are perturbed by overtones and binary combination bands of deformation modes due to Fermi resonance (Fig. 6.10, FR1 and FR2).[172-173, 178] The resulting overlap with fundamental modes of interest hampered the analysis of individual components in the supramolecular assembly in both ways qualitatively, for the accurate determination of resonance frequencies and the physical state of the alkyl chain, and quantitatively, for its order or tilt. This overlap can be partially unraveled by isotopic substitution of hydrogen atoms by deuterium atoms in the alkyl chain. The $v(CD_2)$ and $v(CD_2)$ modes are bathochromically shifted by $\Delta\tilde{v} \approx -750\ cm^{-1}$ in comparison to their perhydro-analogues.[192-193] They absorb in the $\tilde{v} \approx 2220\text{-}2060\ cm^{-1}$ spectral region, which does not interfere with IR absorption modes of other functional groups present in this system or in airborne contaminations. In perdeuterated alkyls, asymmetric and symmetric stretching modes are separated by ca $\Delta\tilde{v} \approx 100\ cm^{-1}$, in contrast to ca $\Delta\tilde{v} \approx 75\ cm^{-1}$ in perhydro-alkyls. Furthermore, modes enhanced by FR resonance are less intense and not or only barely overlapped with asymmetric stretching modes.[173, 194] Conveniently, the substitution of the H by D atoms perturbs the chemical and physical properties of the alkyl chain fragment only to a little extend.[193] Most importantly, they allow for the analysis of a molecule or molecular fragment in a system containing other, non-deuterated alkyl group, which is required for the analysis of interactions between different molecules in chapter 9. Drawbacks for the use of deuterated molecules are their availability, or costs.

To study the behavior of side chain apart from ν(N-CH₃) modes of the methyl at the imidazolium ring, 1-methyl-3-(octadecyl-d_{37})-imidazolium triflate [C₁₈Im-d_{37}][TfO] was used. It was synthesized and provided by Torben Alpers from the working group of Jens Christoffers, University of Oldenburg. With T_m = 66 °C,[195] it is an IL per definition, in contrast to its chloride derivative used in chapter 6. To study the impact of the anion, C₁₈Im-d_{37}^+-based LB monolayers were transferred from 0.1 M KClO₄(aq) and 0.1 M KCl(aq) subphases for anion exchange, according to the previous chapters 5 and 6.[P1,P2] The [C₁₈Im-d_{37}][X] LB films were transferred under the same transfer conditions as of their perhydro-derivative (Section 6.1) onto gold surfaces. The results of this study are subject to a forthcoming publication, which is currently under review.[P3]

7.1 Composition of the Aliphatic Ionic Liquid Monolayer after Langmuir-Blodgett Transfer from a Chloride-Containing Subphase

The composition of the [C₁₈Im-d_{37}][X] film transferred from the 0.1 M KClO₄(aq) subphase should not differ markedly from its perhydro-analogue, which was analyzed in section 6.2. After transfer from a chloride-containing subphase, anion exchange of TfO⁻ to Cl⁻ is expected, as described in the FIL study.[P1,P2] The former XPS studies also showed that the cation of the subphase is not transferred with an amphiphilic imidazolium cation into the LB film. Originally, the transfer of the C₁₈Im⁺-based LB film was studied together with the transfer of the [Im^F][X] FIL, and thus a NaCl(aq) subphase was used. Later, to keep the study consistent with previous (spectro-)electrochemical studies in KClO₄(aq), KCl was employed. XP spectra of the C₁₈Im⁺-based LB film transferred from 0.1 M NaCl(aq) onto Au(poly) are shown in figures 7.1 and 7.2.

The survey spectrum shown in figure 7.1 indicates the presence of Au, C, Cl, N, and O species. Sodium ions are found neither in the survey nor in the high-resolution XP spectra (Figs 7.1 and 7.2a). Due to its more than eightfold higher photoionization cross section when using Al K$_α$ radiation, Na would be much more easily detected than C species of similar amount.[142]
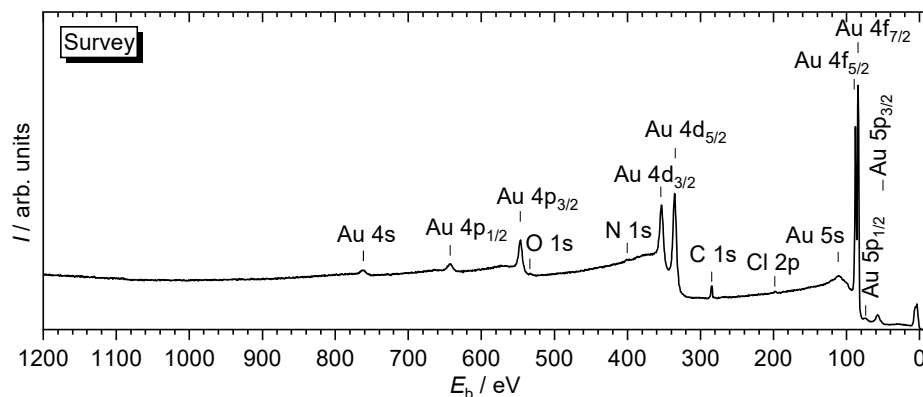
Figure 7.1: XP survey spectrum of the C₁₈Im⁺-based LB-film transferred from 0.1 M NaCl(aq) onto Au(poly).

The C 1s spectrum gives a strong line at E_b = 285 eV with a shoulder at slightly higher binding energies $E_b \approx 286$ eV (Fig. 7.2b), which are assigned to the C-C and C-N groups in the amphiphilic C₁₈Im⁺ cation, respectively.[127] The N 1s spectrum exhibits one line at E_b = 400 eV and is ascribed to the nitrogen atoms of the imidazolium ring (Fig. 7.2c). In the LB monolayer, its binding energy is downshifted with respect to IL bulk surfaces, indicating interactions of the aromatic ring with the Au(poly) surface.[127-129]
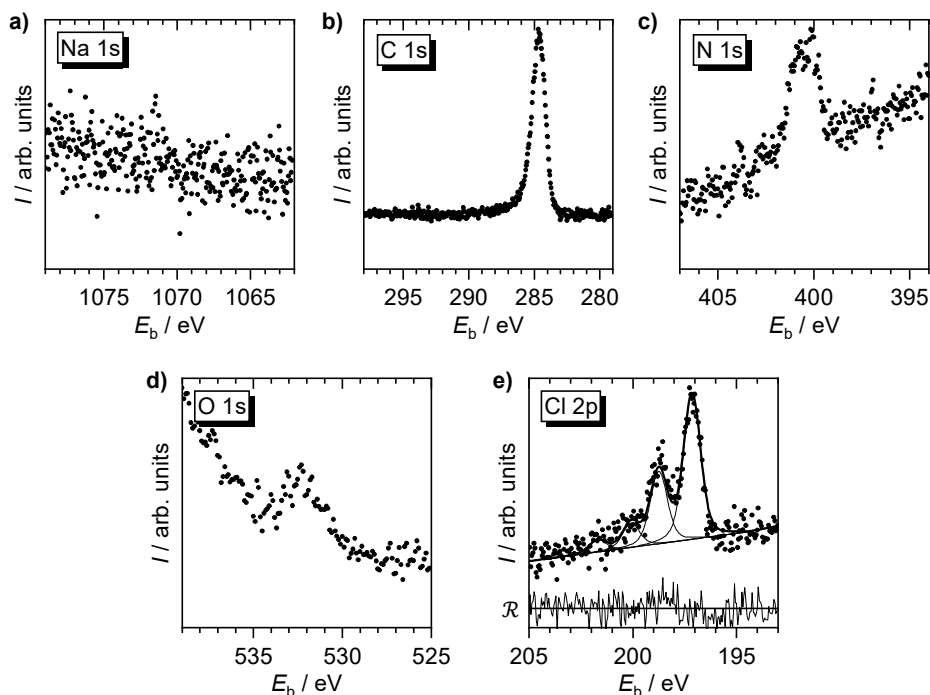
Figure 7.2: High resolution X-ray photoelectron spectra of the C₁₈Im⁺-based LB monolayer transferred from 0.1 M NaCl(aq) onto a Au(poly) surface: a) Na 1s, b) C 1s, c) N 1s, d) O 1s and e) Cl 2p.

7.1 Composition of the Aliphatic Ionic Liquid Monolayer after Langmuir-Blodgett Transfer from a Chloride-Containing Subphase

97

As for the other samples in sections 5.2 and 6.2, an O 1s line at $E_b = 532$ eV is found (Fig. 7.2d) and assigned tentatively to hydroxide ion, encapsulated water, or surface oxide.[136-139] Please, note that this XPS study was conducted on an UV/ozone-cleaned Au(poly) slide, whereas the following spectroscopic studies were conducted with flame annealed Au(111) single crystals. The Cl 2p spectrum reveals two Cl 2p doublets (Fig. 7.2e), of which the strong one at $E_b = 197.1$ eV (Cl 2p$_{3/2}$) and $E_b = 198.7$ eV (Cl 2p$_{1/2}$) is assigned to chloride specifically adsorbed on the Au(poly) surface.[140-141] The other weak doublet at $E_b = 200.1$ eV (Cl 2p$_{3/2}$) and $E_b = 200.7$ eV (Cl 2p$_{1/2}$) may reflect chloride species within the imidazolium film. Due to the nature of the LB film, it is called [C$_{18}$Im][X], where X represents chloride and possibly hydroxide ions. Generally, the XPS results agree with previous studies of [Im^F][X]|Au(poly) and [C$_{18}$Im][X]|Au(poly) LB monolayers transferred from NaCl$_{(aq)}$ and KClO$_{4(aq)}$ electrolyte subphases, respectively.[p1,p2]

Considering the surface concentration and geometry of the C$_{18}$Im$^+$ molecules (Section 6.1), a side-by-side arrangement of chloride and imidazolium rings is not reasonable. However, binding energies of both imidazolium nitrogen and chloride species indicate interaction with the gold surface. Specific adsorption is known for chloride[140-141, 154-155] and proposed for imidazolium[97, 101, 127] cations. Apart from the Au(poly) surface, other impacts of chemical environments may influence their binding energies. For chloride anions only two positions are reasonable, i.e. on the Au surface below the film and within the [C$_{18}$Im][X] film close to the cationic ring moiety.[135] As two different chlorine species are found in the XP spectra, both positions are possible. In this case, the downshift of the N 1s binding energy with respect to the bulk IL surface might be explained by a deviant effective coordination number at the surface and thus a different chemical environment in comparison to the bulk.

7.2 Infrared Spectra of the Ionic Liquid with the Perdeuterated Aliphatic Chain at the Air|Au(111) Interface

For reference, an ATR IR spectrum of the starting compound [C$_{18}$Im-d_{37}][TfO] is shown in figure 7.3a. This spectrum is typical for perdeuterated alkyl substituents.[192-194] Asymmetric stretching modes give rise to

absorptions at $\tilde{v} \approx 2214$ cm^{-1} for CD$_3$ and at $\tilde{v} = 2195$ cm^{-1} for CD$_2$ groups.[192-194] In contrast to the H-substituted alkanes, the v_s(CD$_3$) mode absorbs at lower wavenumbers, at $\tilde{v} \approx 2072$ cm^{-1}, than the v_s(CD$_2$) band at $\tilde{v} = 2091$ cm^{-1}.[192-194] Both symmetric modes are subject to FR with overtones or binary combinations of methyl or methylene bending modes.[194] The weak FR3 mode at $\tilde{v} = 2158$ cm^{-1} interacts with the v_s(CD$_2$) mode. In some cases, this mode was assigned to belong to the v_s(CD$_3$) FR couple.[196-198] However, results by MacPhail et al. indicate no absorption close to this position in an alkane with selectively deuterated methyl groups.[173] They observe a weak FR mode close to $\tilde{v} \approx 2120$ cm^{-1}, which is associated to v_s(CD$_3$) and not visible in the ATR spectrum of figure 7.3a.
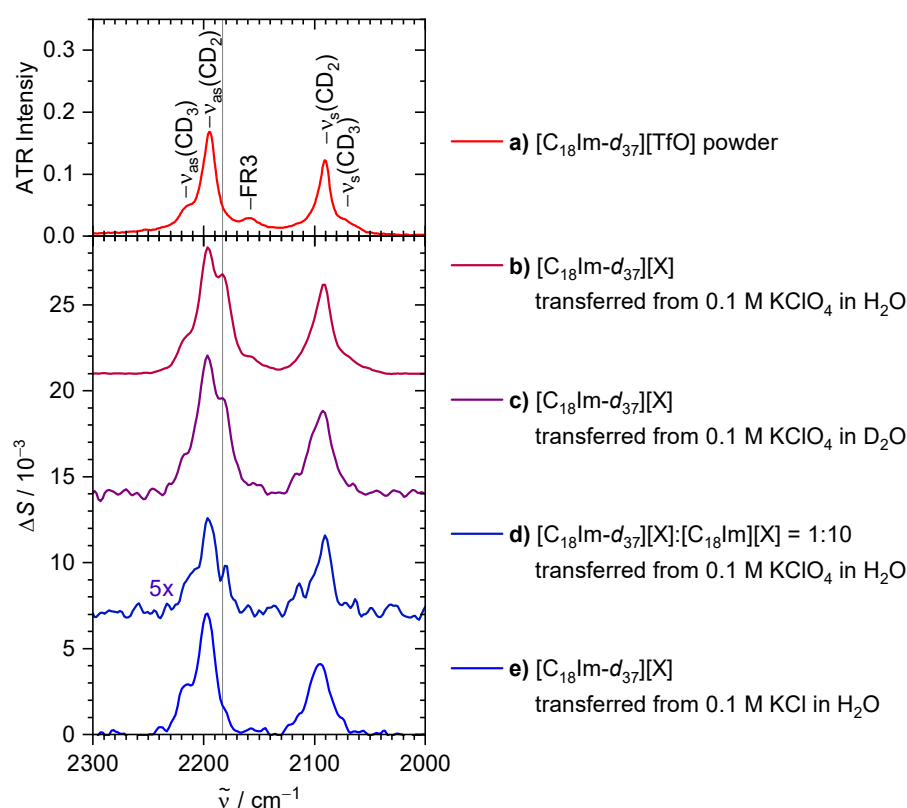
Figure 7.3: Spectra of C$_{18}$Im-$d_{37}{}^+$-based samples. a) ATR spectrum of the [C$_{18}$Im-d_{37}][TfO] powder. b-e) Ex situ PM IRRA spectra ($\tilde{v}_{HWR} = 2200$ cm^{-1}) in air after LB transfer of [C$_{18}$Im-d_{37}][X] onto Au(111) under conditions denoted on the right side of the figure; b) usual transfer conditions as in chapter 6, c) transfer with deuterated solvents to exclude possible D/H-exchange, d) isotopic dilution, and e) fabrication of a chloride containing film. The vertical line serves as a guide to mark the position of the unusual band at $\tilde{v} \approx 2183$ cm^{-1}.

PM IRRA spectra shown in figure 7.3b-d were recorded from [C$_{18}$Im][X] monolayers transferred from the 0.1 M KClO$_{4(aq)}$ subphase onto on Au(111).

The positions of $\nu_{as}(CD_3)$, FR3, $\nu_s(CD_2)$, and $\nu_s(CD_3)$ modes in the LB monolayer (Fig. 7.3b) match well with the ATR powder spectrum of [C_{18}Im][TfO] (Fig. 7.3a). A striking distinction is drawn by the appearance of two comparatively strong modes at $\tilde{\nu} \approx 2197$ cm^{-1} and $\tilde{\nu} \approx 2183$ cm^{-1}, which are not typical for a long alkyl chain in both, bulk phase and interfaces.[192, 196-202] Both signals are tentatively assigned to asymmetric methylene stretching modes.[202]

Prior to deposition of [C_{18}Im-d_{37}][TfO] onto the electrolyte subphase, it was dissolved in CHCl$_3$. D/H-exchange may cause the appearance of an additional band, for example if CHD groups were present. However, the exchange is improbable due to the lacking basicity of the solvent and subphase. To rule this out, [C_{18}Im-d_{37}][TfO] was dissolved in CDCl$_3$ and transferred from a subphase consisting of 0.1 M KClO$_4$ in D$_2$O. The corresponding spectrum (Fig. 7.3c) is similar to the spectrum of the H-containing solvent and subphase (Fig. 7.3a), which confirms that the H/D exchange is not responsible for the appearance of two distinct bands in the $\nu_{as}(CD_2)$ spectral region.

Hsi et al. investigated spectra of single selectively deuterated methylene groups in palmitic and stearic acids.[203] Whereas CD$_2$ groups close to the carboxyl group as well as in the middle of the alkyl chain gave rise to single $\nu_{as}(CD_2)$ and $\nu_s(CD_2)$ bands only, a splitting of both bands was observed at methylene groups close to the terminal methyl group. The split $\nu_{as}(CD_2)$ bands appeared close to $\tilde{\nu} \approx 2180$ cm^{-1} and 2165 cm^{-1}. Hsi et al. wondered whether the splitting may be induced by crystal field splitting due to intermolecular interactions with neighboring molecules. Isotopic dilution of the deuterated compound in an excess of the perhydro-compound prevents intermolecular CD$_2$ interactions while preserving packing properties of the target compound. However, the spectra were not differing significantly apart from intensity, and thus crystal field interactions were not accountable for the splitting. As described in section 6.4.2, the H-substituted chains of C_{18}Im$^+$ cations are in a liquid state.[P1] This makes crystal field splitting unlikely, as it requires high order and well-defined packing. Nevertheless, the effect of isotopic dilution was tested for the C_{18}Im-d_{37}^+-based monolayer on Au(111). In a single solution of CHCl$_3$, both [C_{18}Im-d_{37}][TfO] and [C_{18}Im][Cl] substances were dissolved in a molar ratio of 1:10. The corresponding spectrum after LB transfer onto Au(111) is shown in figure 7.3d. Due to the low surface concentration of the C_{18}Im-d_{37}^+ cation, absorptions are overall weak. However, a signal appears close to

$\tilde{\nu} \approx 2183$ cm^{-1}, showing that interchain CD interactions are not responsible for the origin of this absorption.

Finally, the [C$_{18}$Im-d_{37}][X] was transferred from an 0.1 M KCl$_{(aq)}$ subphase (Fig. 7.3e), yielding a monolayer with chloride as dominating counter-ion to the amphiphilic cation. A very weak absorption band appears at $\tilde{\nu} \approx 2183$ cm^{-1}, while the band at $\tilde{\nu} \approx 2197$ cm^{-1} remains strong. This indicates, that the high-wavenumber band originates "commonly" from ν_{as}(CD$_2$) modes, whereas the lower wavenumber band is "special". Obviously, the anion has a great impact on interactions or packing of the alkyl chains.

As it is the case for ν(CH$_2$) resonance frequencies,[172-173] also ν(CD$_2$) resonance frequencies are influenced by the physical state of the alkyl chain.[192, 194, 204] In solid structures, methylene units are arranged in all-trans conformation, whereas liquid structures exhibit multiple gauche units. However, for ν(CD$_2$) modes, this effect is less pronounced. For example, in lipids the melting of alkyl chains results in a hypsochromic shift of barely $\Delta\tilde{\nu} \approx 4$ cm^{-1} or less for ν_{as}(CD$_2$).[192, 194] This is far too less to only account an alkyl chain solidification for the band at $\tilde{\nu} \approx 2183$ cm^{-1}, which is separated by $\Delta\tilde{\nu} \approx -14$ cm^{-1} from the other ν_{as}(CD$_2$) band.

Comparing the shape of the alkyl chain spectra of the [C$_{18}$Im][X] (Fig. 6.10b) and [C$_{18}$Im-d_{37}][X] (Fig. 7.3b) LB films on the Au(111) surfaces reveals a striking similarity. In both cases, a band assigned to asymmetric methylene stretching modes, ν_{as}(CH$_2$) at $\tilde{\nu} \approx 2926$ cm^{-1} and ν_{as}(CD$_2$) at $\tilde{\nu} \approx 2197$ cm^{-1}, is followed by an intense mode on the lower wavenumber side. In the perhydro-film, this mode is located $\tilde{\nu} \approx 2900$ cm^{-1} ($\Delta\tilde{\nu} \approx -26$ cm^{-1}). Based on literature, it was assigned to the overtone or binary combination modes FR2, which originate from lateral interchain interactions of methylene groups and are enhanced due to FR with ν_s(CH$_2$) modes.[171, 178-179] In the [C$_{18}$Im-d_{37}][X] film, the mode of similar behavior appears at $\tilde{\nu} \approx 2183$ cm^{-1} ($\Delta\tilde{\nu} \approx -14$ cm^{-1}). It cannot be excluded that this mode originates from FR interactions. However, a FR interaction band has not been described in literature at wavenumbers this high in IR absorption.[192-194, 202, 205] Furthermore, the FR3 mode is in resonance with ν_s(CD$_2$) modes and appears at lower wavenumbers, $\tilde{\nu} \approx 2159$ cm^{-1} ($\Delta\tilde{\nu} \approx -38$ cm^{-1}) in both ATR bulk and PM IRRA surface spectra (Fig. 7.3a,b). If the mode at $\tilde{\nu} \approx 2183$ cm^{-1} is of similar origin as the FR2 mode at $\tilde{\nu} \approx 2900$ cm^{-1} in the perhydro-analogues, it should be severely quenched to the bulk-level when no lateral interchain interactions of CD$_2$ groups are possible. Nevertheless, the isotopic dilution

experiment described above still proves the presence of this band (Fig. 7.3d). Therefore, it is unlikely that the band at $\tilde{\nu} \approx 2183$ cm^{-1} originates from FR interactions similar to the perhydro-film.

7.3 Influence of the Local Chemical Environment

One possible explanation for the nature of the band at $\tilde{\nu} \approx 2183$ cm^{-1} may be the chemical environment. Both polarity and polarizability of solvents significantly influence the resonance frequency and intensity of IR absorption modes.[5] For example, Fawcett et al. have shown that $\nu_{as}(CD_3)$ and $\nu_s(CD_3)$ bands of acetonitrile-d_3 shift monotonously with increasing polarity of the solvent.[206] The resonance frequency shifts bathochromically for both modes, though to greater extent for $\nu_{as}(CD_3)$ by up to $\Delta\tilde{\nu} \approx$ -25 cm^{-1} in comparison to $\nu_s(CD_3)$ by up to $\Delta\tilde{\nu} \approx$ -9 cm^{-1}. Kleeberg et al. have investigated CDCl$_3$ in solvents interacting by van der Waals forces only as well as in H-bond acceptor solvents. For the latter, bathochromic shifts of up to $\Delta\tilde{\nu} \approx$ -85.7 cm^{-1} for the $\nu(CD)$ mode were observed, whereas in van der Waals solvents the shift spans up to $\Delta\tilde{\nu} \approx$ -27.7 cm^{-1} with increasing polarity. Both CDCl$_3$ and acetonitrile-d_3 are small molecules and their CD$_n$ groups are attached to electron-withdrawing groups. Similarly, the perdeuterated octadecyl chain of the C$_{18}$Im-d_{37}^+ amphiphile is attached to an electron-withdrawing and cationic imidazolium substituent. However, apart from carbon atoms in α- and β-positions, the electron-withdrawing effect is negligible for the long alkyl chain, hampering the comparison to the literature examples mentioned above.

In an interesting study, Cameron et al. shed new light on this issue.[194] They have analyzed the amphiphilic phospholipid dipalmitoyl-phosphatidylcholine (DPPC), in which different positions of the palmitate chain were selectively deuterated (Fig. 7.4). Different resonant frequencies are found along the alkyl chain. Due to the electron-withdrawing ester group, $\nu_{as}(CD_2)$ modes close to it resonate at high wavenumbers, $\tilde{\nu} \approx 2215$ cm^{-1} and $\tilde{\nu} \approx 2198$ cm^{-1} for α- and β-positions, respectively. In the middle section of the alkyl chain, $\nu_{as}(CD_2)$ modes are found to decrease to $\tilde{\nu} \approx 2182$ cm^{-1}, and the resonance frequency decreases further to $\tilde{\nu} \approx 2171$ cm^{-1} when approaching the terminal methyl group. The frequency shift of $\nu_s(CD_2)$ modes is not monotonous.
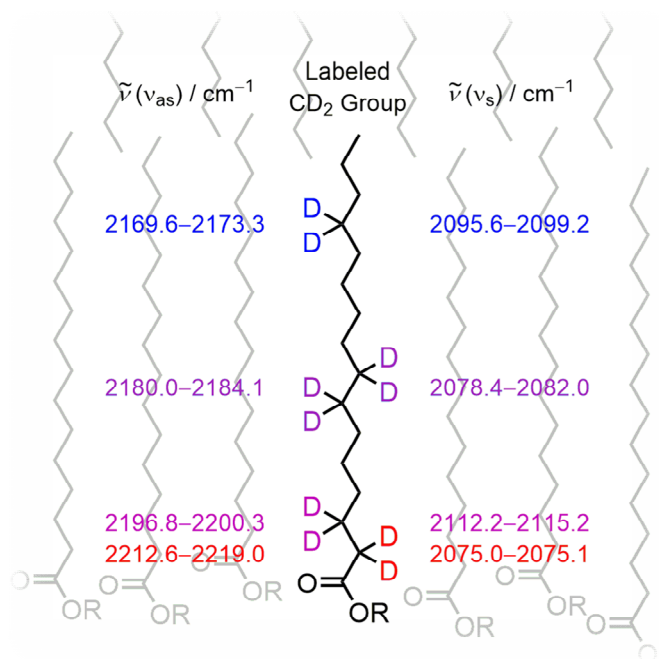
Figure 7.4: Illustration of results obtained by Cameron et al.[194] for the palmitoyl chain of DPPC in lipid bilayer assemblies, selectively deuterated at different positions. Only the palmate substituent is shown, R = phosphatidylglycerylcholine. The wavenumber spans denoted in the figure comprise anhydrous and hydrated DPPC as well as different temperatures. These conditions affect the spectra to less extent than the position of selective deuteration does. Increasing temperatures lead to disorder in the alkyl chain, which cause the appearance of gauche conformations and raises the overall resonance frequency of the convoluted band.

Certainly, inductive effects of the carbonyl group do not affect the modes of the middle and terminal sections significantly. However, the chemical environment may have an impact on the resonance frequencies and intensities of these modes. The middle section is much closer to the hydrophilic and zwitterionic phosphatidylcholine part of the lipid than the terminal section. Lipids are known to pack in lamellar bilayers, in which hydrophobic tailgroups are directed toward each other and hydrophilic headgroups to themselves.[207] In effect, the ending section of the palmitate is exposed to a far more apolar environment than the section close to the ester group. This phenomenon is closely related to the nanosegregation of polar and apolar segments found in the bulk of ILs (cf. Section 2.2).[21-22] Similar to the solvents effects described above, the polarity and polarizability of the local environment may influence the resonance frequencies of $\nu_{as}(CD_2)$ modes. In the study of Cameron et al., the apolar segments exhibit lower frequencies and the polar segments higher ones, which is in fundamental contrast to the solvent effects as mentioned above. It may be proposed that

the appearance of two $\nu_{as}(CD_2)$ modes in the [C_{18}Im-d_{37}][X] monolayer on Au(111) (Fig. 7.3b-d) reflects a strong segregation of two lateral segments within the film. In the segment directed toward air, an apolar domain consisting of hydrocarbon chain fragments only is formed. In the segment adjacent to the Au(111) surface, hydrocarbon chain fragments are present along with the cationic headgroup and anions. This arrangement is typical for LB films and in accordance with molecular dynamics simulations of [C_{18}Im][Tf_2N] on water.[25] However, if the whole palmitate substituents of DPPC are perdeuterated, individual $\nu_{as}(CD_2)$ modes will couple and give rise to a convoluted band located at $\tilde{\nu} \approx 2193$ cm^{-1}.[192] Therefore, a single band is found in the ATR spectrum of the bulk compound before LB transfer (Fig. 7.3a). On the other hand, the ordering and packing is not bulk-like in a monolayer on the Au(111) surface.

To estimate the impact of different chemical environments, harmonic vibrational spectra of a [C_{18}Im-d_{37}][ClO_4] ion pair were calculated in vacuo and under the impact of solvents with the Polarizable Continuum Model (PCM).[208] Dielectric continua of water and heptane were employed to simulate polar and apolar environments, respectively. The DFT calculations were carried out by Thorben Petersen from working group of Thorsten Klüner, University of Oldenburg. We constructed an input geometry in which the alkyl chain exhibits four gauche conformations, as roughly 30 % of gauche conformations are found in liquid alkyl chains.[180] Gauche conformations often appear at methyl endings.[207, 209] As the ring group is inclined toward the Au surface and the alkyl chain is oriented upward, gauche conformations are also likely to be close to the headgroup.[P2] As discussed in section 6.5, the perchlorate anion was positioned above the ring. Besides this geometry and ion arrangement, others may exist on the surface. However, the solvent or environment effect should affect the most reasonable input geometries similarly, and a single conformer may serve to study the effect of interest. The geometry-optimized structures in vacuo is shown in figure 7.5. For the solvent models, the same conformation was optimized. Cartesian coordinates for all structures are listed in the appendix (Tabs 12.2-12.4).
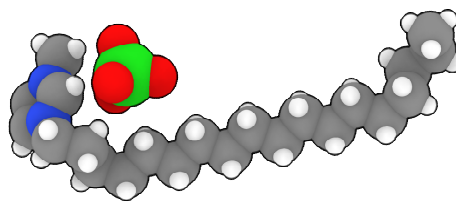
Figure 7.5: Optimized geometry of the [C$_{18}$Im-*d$_{37}$*][ClO$_4$] ion pair in vacuo (PBE0-D3BJ/def2-TZVP). H – white, C – grey, N – blue, O – red, Cl – green.

IR absorption spectra of the [C$_{18}$Im-*d$_{37}$*][ClO$_4$] ion pair in different environments are compared in figure 7.6. The calculated ν(CD) modes described by resonance frequencies, integral intensities I_{IR}, and relative weights of individually displaced methyl and methylene groups in the alkyl chain are listed in the appendix (Tabs 12.5-12.7).
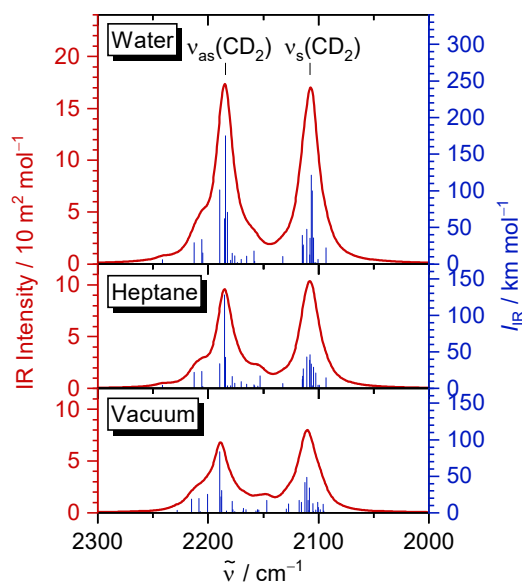
Figure 7.6: Calculated spectra of the [C$_{18}$Im-*d$_{37}$*][ClO$_4$] ion pair in vacuo, as well as in heptane and water solvent simulations (PBE0-D3BJ/def2-TZVP). The left axes correspond to the wavenumber-dependent extinctions (red), which are the result of convoluted Lorentzian modes with a fwhm = 15 cm^{-1}. Absolute intensities of individual modes are given in the from of the blue line spectra and reflected by the right axes. The resonance frequencies were scaled by a factor of 0.9575.[210]

It is evident, that the influence of the solvent model is rather subtle. Intensity-weighted averages of ν_{as}(CD$_2$) and ν_s(CD$_2$) modes differ slightly (Tab. 7.1). In line with the experimental solvent effects mentioned above, both methylene stretching bands are bathochromically shifted in water compared to hexane and vacuum. However, the difference in polarity is huge, whereas the difference in resonance frequencies span only

$\Delta \tilde{v}$ = -2 cm^{-1}. Interestingly, the IR intensity depends on solvent and is much higher in water than in heptane, in which it is little higher than vacuum.

Moreover, the simulated spectra show features between the dominant $\nu_s(CD_2)$ and $\nu_{as}(CD_2)$ band convolutions (Fig. 7.6). Distinct humps are seen at $\tilde{v}$ / cm^{-1} = 2147, 2151, and 2158 for vacuum, heptane, and water environments, respectively, and their intensity is given by $\nu_s(CD_2)$ modes in α-position to the imidazolium ring. Due to the electron-withdrawing effect of the cationic imidazolium moiety, the alkyl chain modes $\nu_s(CD_2)$ and $\nu_{as}(CD_2)$ at α- and β-positions are hypsochromically shifted (Tab. 7.2) in contrast to other modes in the alkyl chain.

Table 7.1: Intensity-weighted averages and standard deviations of the calculated spectra of the [C$_{18}$Im-d_{37}][ClO$_4$] ion pair in vacuo, as well as in heptane and water solvent simulations (PBE0-D3BJ/def2-TZVP). The wavenumbers were scaled by a factor of 0.9575.[210]

Modes	$\tilde{v}$ / cm^{-1}		
	Vacuum	Heptane	Water
$\nu_s(CD_2)$	2112 ± 11	2112 ± 11	2110 ± 11
$\nu_{as}(CD_2)$	2190 ± 14	2190 ± 14	2188 ± 11

This indicates that not all experimental features in between the major $\nu_s(CD_2)$ and $\nu_{as}(CD_2)$ bands ($\tilde{v} \approx$ 2170-2120 cm^{-1}, Fig. 7.3) must be assigned to FR interaction bands.

Table 7.2: Resonance frequencies $\nu(CD_2)$ modes in α- and β-positions to the imidazolium ring in the calculated spectra of the [C$_{18}$Im-d_{37}][ClO$_4$] ion pair in vacuo, as well as in heptane and water solvent simulations (PBE0-D3BJ/def2-TZVP). The wavenumbers were scaled by a factor of 0.9575.[210] Please, note that the $\nu_s(\beta$-CD$_2$) mode is mixed with the $\nu_s(\varepsilon$-CD$_2$) mode in vacuo and heptane, and thus two modes are given.

Mode	$\tilde{v}$ / cm^{-1} (I_{IR} / km mol^{-1})		
	Vacuum	Heptane	Water
$\nu_s(\beta$-CD$_2$)	2127 (12.6), 2129 (5.3)	2129 (12.7), 2131 (6.8)	2132 (10.4)
$\nu_s(\alpha$-CD$_2$)	2147 (17.3)	2151 (17.1)	2158 (17.8)
$\nu_{as}(\beta$-CD$_2$)	2207 (1.6)	2207 (2.9)	2205 (14.9)
$\nu_{as}(\alpha$-CD$_2$)	2228 (3.6)	2233 (4.4)	2341 (6.0)

The harmonic frequencies calculation cannot show band perturbations by resonance effects nor overtones or combination bands. For this, an anharmonic frequency calculation is required. As the ATR bulk spectrum does not show the special band, a two-dimensional film of packing according to LB transfer parameters would be needed to be simulated on an Au(111) surface. This is complex and not straight-forward but may yield insight into

the nature of the band at $\tilde{v} = 2183$ cm^{-1} and rule out or confirm environmental or FR contributions.

7.4 Infrared Spectra of the Ionic Liquid with the Perdeuterated Aliphatic Chain at the Electrolyte|Au(111) Interface

In situ spectra of the [C$_{18}$Im-d_{37}][X] monolayer on Au(111) in 0.1 M KClO$_{4(aq)}$ were recorded under similar conditions as for its perhydro-derivative described in section 6.4. Raw spectra are shown in figure 7.7a and exhibit only subtle differences for the ν(CD) modes. Due to generally low absorbances of the perdeuterated chains, the background correction was challenging. Therefore, the corrected results (Fig. 7.7b) are interpreted qualitatively only. Difference spectra are not subject to any operator bias and are shown for control in figure 7.7c.

Clearly, two ν$_{as}$(CD$_2$) bands appear at $\tilde{v} = 2197$ cm^{-1} and $\tilde{v} = 2183$ cm^{-1}, and a weak ν$_s$(CD$_2$) band is seen at $\tilde{v} \approx 2091$ cm^{-1} (Fig. 7.7b). The same resonance frequencies as observed in the ex situ spectra (Section 7.1). Due to the low signal-to-noise ratio, possible small changes in the resonance frequency as a function of the electric potential cannot be tracked. As for the perhydro-derivative (Section 6.4), predominantly the ν$_{as}$(CD$_2$) bands decrease in intensity upon polarization to negative potentials. In agreement with that, the intensities of both modes, at $\tilde{v} \approx 2900$ cm^{-1} (FR2) in the [C$_{18}$Im][X] monolayer and at $\tilde{v} = 2183$ cm^{-1} for the [C$_{18}$Im-d_{37}][X] monolayer, decrease with decreasing potentials. However, whereas the FR2 mode in the perhydro-film decreases more strongly in comparison to the ν$_{as}$(CH$_2$) mode (Fig. 6.12b), the mode at $\tilde{v} = 2183$ cm^{-1} decreases parallelly with the mode at $\tilde{v} = 2198$ cm^{-1} (Fig. 7.7c). This indicates that both modes do not behave similarly and are not of analogous origin, despite their analogue resonance frequency as a band in between symmetric and asymmetric methylene stretching modes. The ν$_s$(CD$_2$) band follows this behavior, but to significantly less extent. At $U = -0.80$ V, the intensities of the ν(CD$_2$) modes seem to vanish completely, suggesting a fully erected all-trans chain ($S = 1$, $\theta = 0$ °). In comparison, an upward orientation ($S \approx 0.6$) was observed in the perhydro-derivative (Section 6.4.2).[P2] Thus, a vertical orientation of perdeuterated chains is not reasonable, but may result from an inaccuracy in the difficult

background correction or an insufficient signal-to-noise ratio. Importantly, the band positions do not vary with the potential, showing that the physical state of the alkyl chain is preserved.
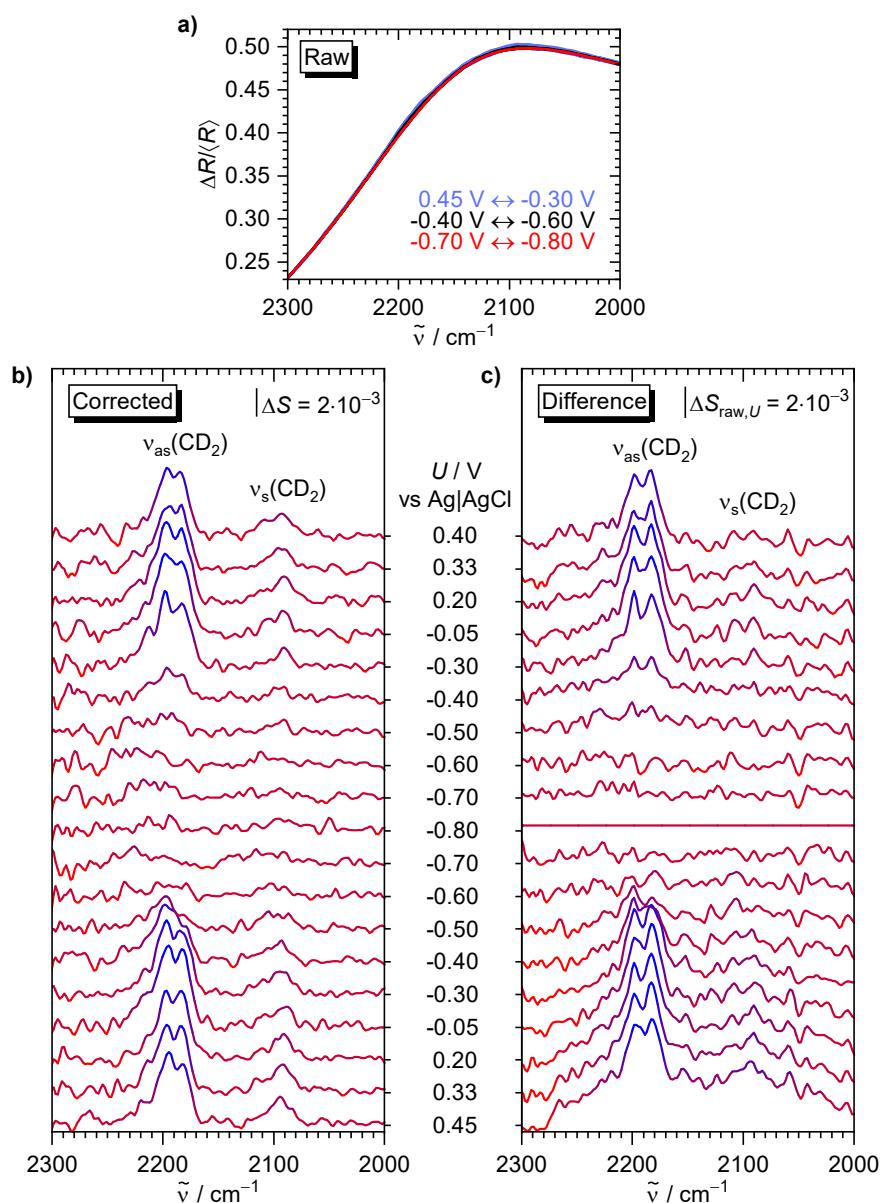
Figure 7.7: In situ PM IRRA spectra of the [C$_{18}$Im-d_{37}][X] monolayer transferred from 0.1 M KClO$_4$ (H$_2$O) on Au(111) in 0.1 M KClO$_4$ (H$_2$O) measured at $\tilde{\nu}_{HWR}$ = 2200 cm^{-1}. a) Raw spectra with potential ranges applied to the Au(111) electrode as indicated in the figure. b) Background corrected spectra in absorbance units. c) Difference spectra of raw signals in differential reflection units. Colors in b) and c) correspond to higher (blue) or lower (red) intensities.

As expected from the ex situ spectra (Section 7.1), the behavior of the [C₁₈Im-*d₃₇*][X] monolayer on Au(111) changes when transferred and studied from/in the 0.1 M KCl(aq) solution. Raw situ spectra, under equal conditions apart from the electrolyte composition, show only slight potential-dependent changes (Fig. 7.8a).
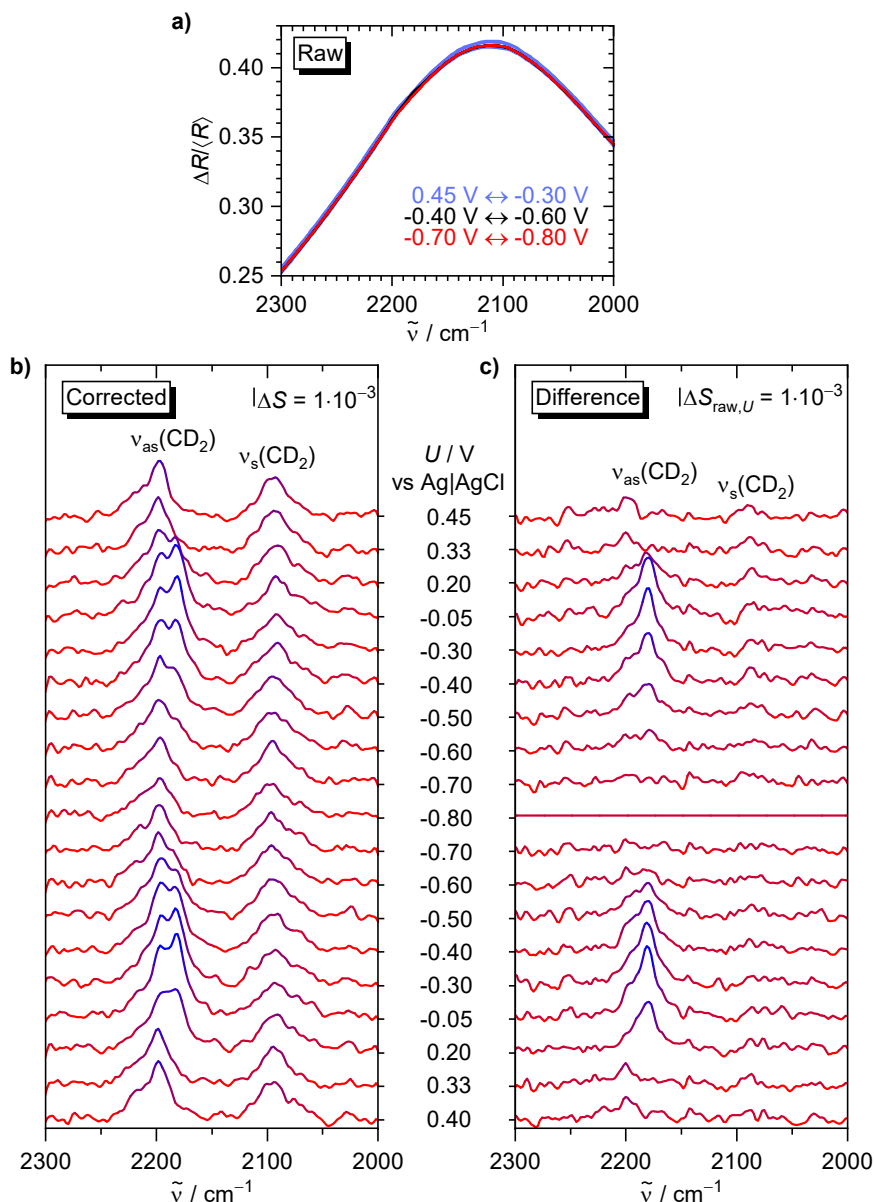
Figure 7.8: In situ PM IRRA spectra of the [C₁₈Im-*d₃₇*][X] monolayer transferred from 0.1 M KCl (H₂O) on Au(111) in 0.1 M KCl (H₂O) measured at $\tilde{\nu}_{HWR} = 2200$ cm⁻¹. a) Raw spectra with potential ranges applied to the Au(111) electrode as indicated in the figure. a) Background corrected spectra in differential reflectivity units. c) Difference spectra of raw signals in differential reflection units. Colors in b) and c) correspond to higher (blue) or lower (red) intensities.

7.4 Infrared Spectra of the Ionic Liquid with the Perdeuterated Aliphatic Chain at the Electrolyte|Au(111) Interface

109

In background-corrected spectra, two $\nu_{as}(CD_2)$ bands at $\tilde{\nu} = 2198$ cm^{-1} and $\tilde{\nu} = 2181$ cm^{-1}, as well as a $\nu_s(CD_2)$ band at $\tilde{\nu} \approx 2093$ cm^{-1} (Fig. 7.8b). Difference spectra highlight that main changes occur for the $\nu_{as}(CD_2)$ band at $\tilde{\nu} = 2180$ cm^{-1}, and to way less extent for the band $\tilde{\nu} = 2198$ cm^{-1} (Fig. 7.8c). Both $\nu_{as}(CD_2)$ bands are most intense at $U = -0.05$ V. When sweeping to both more positive ($U = 0.45$ V) and more negative potentials ($U = -0.80$ V), the band at $\tilde{\nu} = 2180$ cm^{-1} almost vanishes. On the other hand, the band $\tilde{\nu} = 2198$ cm^{-1} seems to retain its intensity upon sweeping to positive potentials, whereas it loses intensity during negative polarizations. The almost independent behavior of both $\nu_{as}(CD_2)$ bands supports that different chain segments may be involved. Interestingly, symmetric bands are only slightly affected by potential changes.

7.5 Refinement in the Molecular Scale Picture for the Aliphatic Ionic Liquid

The molecular scale picture deduced from investigations of the perhydro-analogous 0.1 M KClO$_{4(aq)}$ | [C$_{18}$Im][X] | Au(111) system shall be advanced by results gained from the [C$_{18}$Im-d_{37}][X] film. As described above, both the modes at $\tilde{\nu} \approx 2197$ cm^{-1} and at $\tilde{\nu} \approx 2183$ cm^{-1} are ascribed to asymmetrical CD$_2$ stretching vibrations in different environments. Following the trend of the DFT calculation in solvent models and experimental findings in solvents, the lower wavenumber mode at $\tilde{\nu} \approx 2183$ cm^{-1} is ascribed to the polar environment, leaving the apolar environment for the mode at $\tilde{\nu} \approx 2197$ cm^{-1}. Intensity changes of these modes may result from two causes:

(i) The average tilt of a chain fragment in one of the domains may change, leading to intensity enhancements or attenuations according to the MSSR.

(ii) The number of methylene groups present in one domain may vary.

Both causes may depend on the applied electrode potential and counteract each other, leading to changes which may be invisible in the PM IRRA spectra. A quantitative study with ascription of a specific number of methylene units to one phase is not straight-forward, as the chemical environment influences the extinction coefficient (Fig. 7.6). In the simplest assumption, the film is laterally homogeneous. The content of water and ions within the segregated domains must be considered. Polar domains are likely

to be close to the cationic headgroup and richer in water and anions, whereas apolar domains must lack water and ions. Moreover, the nature of the anions strongly influences the supramolecular behavior of the film. Fundamentally different properties distinguish the chloride and perchlorate ions:

(i) Chloride anions are solvated by a primary hydration shell. They are more kosmotropic than perchlorate ions and stabilize hydrogen bonds.[211]

(ii) In contrast, perchlorate ions are chaotropic and weaken H-bond structures.[211] They are less solvated and adhere to organic matter.

(iii) Chloride anions are known to specifically adsorb on Au(111),[154-155] which may have a severe impact on the behavior of the $[C_{18}Im\text{-}d_{37}][X]$ on the Au(111) surface.

(iv) On the other hand, perchlorate ions only weakly adsorb,[51, 157] leaving dominating electrode interactions to the imidazolium headgroup.[97, 101, 127]

In the following, three limiting states will be considered, which are summarized in table 7.3 together with in situ PM IRRA observations for both electrolytes. Please, note that $U = 0.05$ V corresponds to the capacitance minimum of the 0.1 M $KClO_{4(aq)}|[C_{18}Im][X]|Au(111)$ system (Section 6.3). As no $\nu_{as}(CD_2)$ band increases while the other one decreases in intensity and vice versa (Figs 7.7 and 7.8), spectral changes are likely to originate from changes in the average tilt angle of a chain segment, in contrast to redistribution of methylene segments among polar and apolar domains. Considering the MSSR, strong bands indicate alkyl chains inclined toward the Au surface and weak bands suggest erected chains.

Table 7.3: Observations concerning the two $\nu_{as}(CD_2)$ bands in in situ PM IRRA experiments of the $[C_{18}Im\text{-}d_{37}][X]$ film on Au(111) in different electrolytes at three potentials of limiting behavior (Figs 7.7 and 7.8).

U / V	0.1 M $KClO_{4(aq)}$	0.1 M $KCl_{(aq)}$
0.45	Both bands are strong.	The apolar band is strong. The polar band is not visible.
-0.05	Both bands are most intense.	Both bands are most intense.
-0.80	Both bands are not visible.	The apolar band is strong. The polar band is not visible.

First, the 0.1 M $KClO_{4(aq)}$ electrolyte system is interpreted. Bands corresponding to both polar and apolar domains in the [C₁₈Im-

d_{37}][X]|Au(111) are strong at $U = 0.45$ V and $U = -0.05$ V. As proposed for the perhydro-system (Section 6.5), an aggregated structure is likely and methylene groups in both domains are tilted (Fig. 7.9a,b). The apolar domain is formed by coiling alkyl chains to maximize energy gained by dispersive interactions. In the polar domain, perchlorate anions are located close to the imidazolium ring and water molecules are present. At $U = 0.45$ V, both bands are slightly less intense than at $U = -0.05$ V, which may be due to a partial erection of chain fragments in order to make space for perchlorate ions moving into the film to screen the increased electrode surface charge. At negative potentials, both bands vanish, indicating and erection of both bands. As deduced for the $C_{18}Im^+$-film (Section 6.5), this may be required to screen the electrode charge by perchlorate ions flowing away from the electrode and potassium ions entering the film. However, after this ion transfer, the apolar domain could coil up again and would show visible signals then in PM IRRAS. As known from charge-oscillating nature of HTMS, neat ILs and IL-water solutions mentioned in section 3.3, at more extreme polarizations, a cationic surface layer is likely to be followed by an anionic second layer. The driving force of screening the cationic layer acts against the van der Waals energy gain of coiled alkyl chains. Due to the chaotropic nature of perchlorate ions, they can penetrate into the apolar segment without water and attach to the alkyl chains (Fig. 7.9c). Their interaction with alkyl chains partially compensates the energy which would be gained in a pure alkyl chain aggregate.

In the 0.1 M $KCl_{(aq)}$|[$C_{18}Im$-d_{37}][X]|Au(111) system, the spectra are similar to the 0.1 M $KClO_{4(aq)}$ electrolyte system at $U = -0.05$ V. Thus, also the structure of the monolayer may be similar. Alkyl chains in both polar and apolar domains are proposed to be tilted (Fig. 7.10b). Either the imidazolium ring, the chloride anions, or both of them are specifically adsorbed on the Au(111) surface. Upon polarization to negative potentials, chloride anions desorb form the Au surface and may leave the film, while hydrated potassium cations penetrate into the polar domain, causing the alkyl chains therein to erect and create space. In contrast to the perchlorate anions, chloride anions are more hydrated and kosmotropic. Chloride ions within the apolar segment are energetically unfavorable and their interaction with the alky chain may not yield enough energy to withstand the formation of an apolar coiled aggregate (Fig. 7.10c). Consequently, the anionic layer may be situated above the electrolyte|film interface, farther away from the electrode surface in comparison to perchlorate ions. Polarization to positive

potentials may lead to an inverse effect. Yet, the cohesive energy is too strong to desorb single $C_{18}Im$-d_{37}^+ cations. Instead, chloride ions penetrate into the film and find space in the polar chain segment close to the cationic headgroup, when all sites on the Au(111) surface for specific adsorption are occupied (Fig. 7.10a).
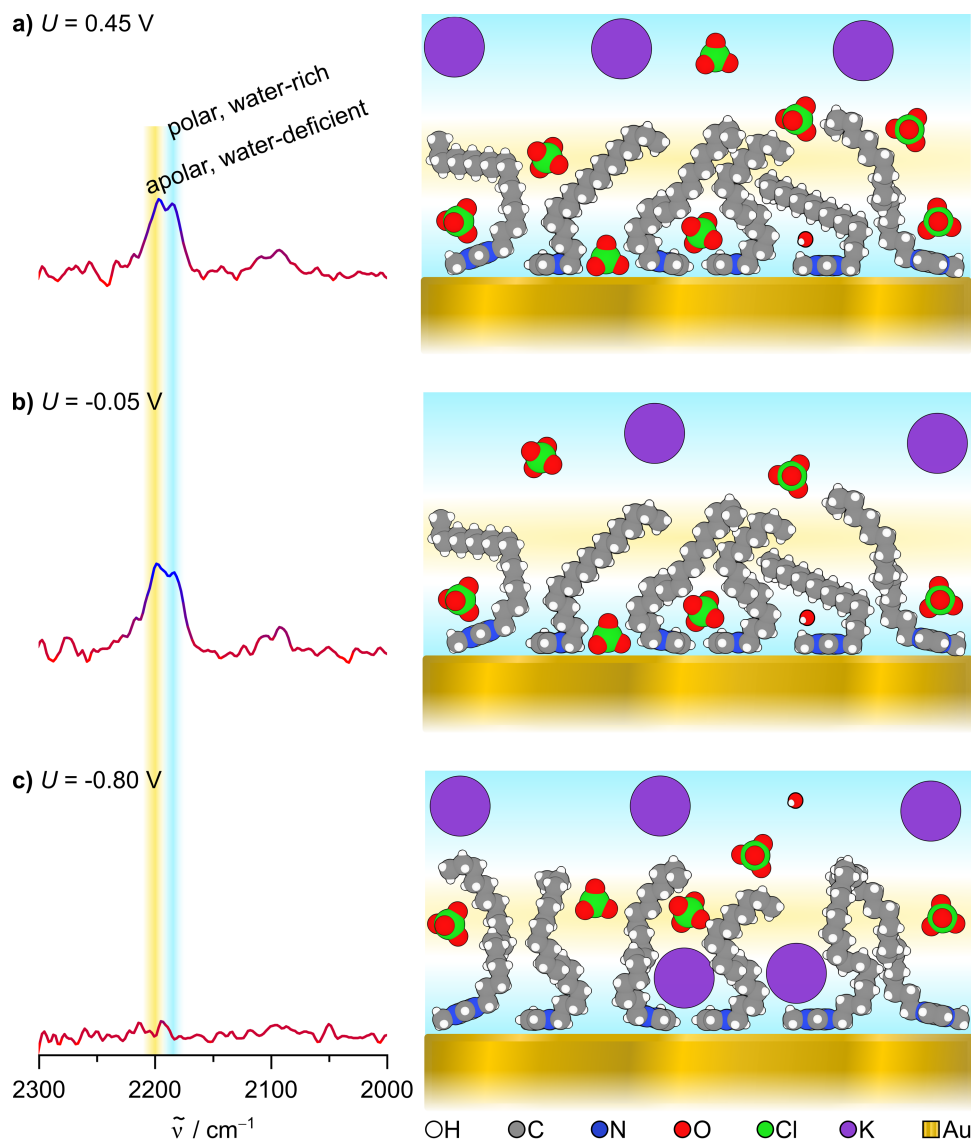
Figure 7.9: PM IRRA spectra (left) and molecular scale scheme (right) of the 0.1 M KClO$_{4(aq)}$|[C$_{18}$Im-d_{37}][X]|Au(111) system at different potentials: a) U = 0.45 V, b) U = -0.05 V, and c) U = -0.80 V. Note that van der Waals radii are used for the different atoms. The use of ionic radii would imply that no solvation shell is present, whereas hydrodynamic radii suggest a complete hydration shell. However, the hydration number of ions close to the electrode and in the organic film is unknown.
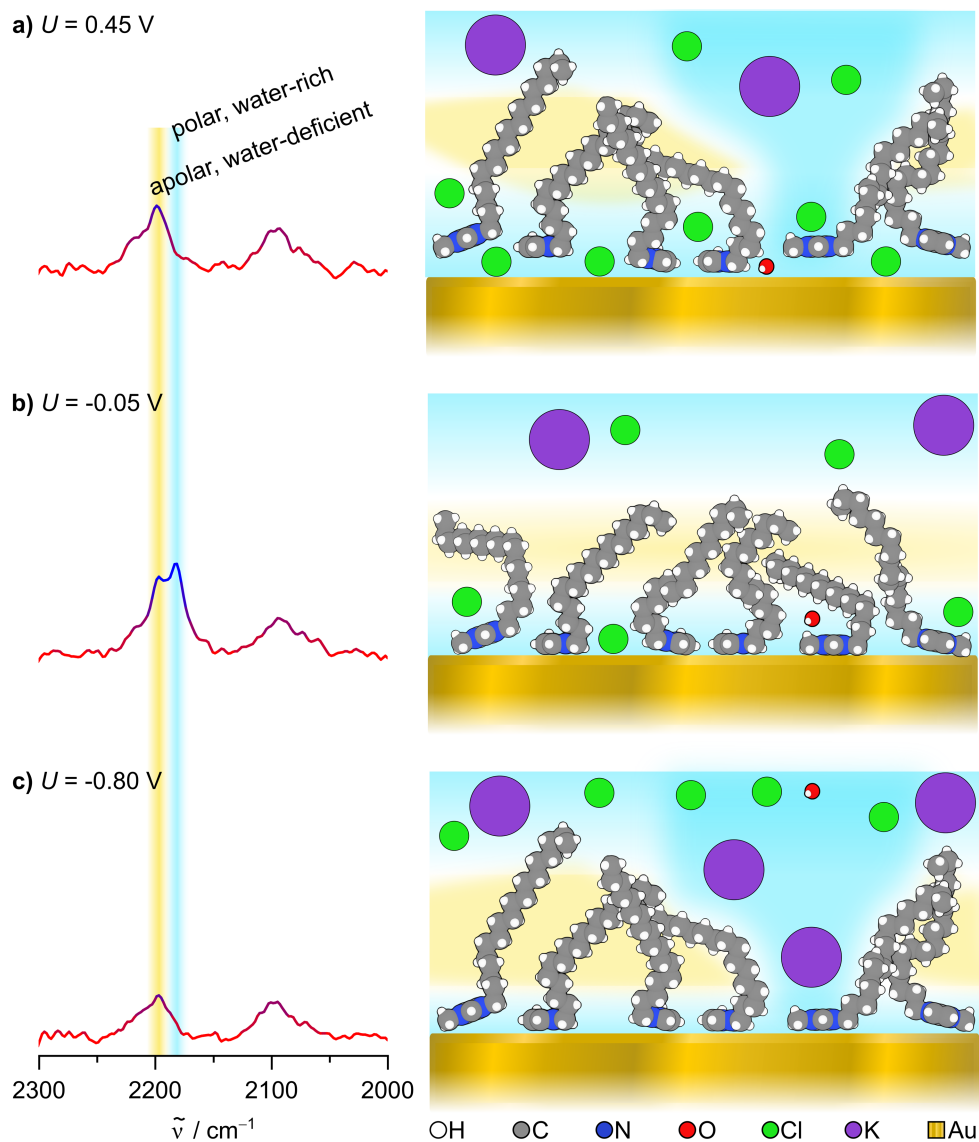
Figure 7.10: PM IRRA spectra (left) and molecular scale scheme (right) of the 0.1 M KCl$_{(aq)}$|[C$_{18}$Im-d_{37}][X]|Au(111) system at different potentials: a) $U = 0.45$ V, b) $U = -0.05$ V, and c) $U = -0.80$ V. Note that van der Waals radii are used for the different atoms. The use of ionic radii would imply that no solvation shell is present, whereas hydrodynamic radii suggest a complete hydration shell. However, the hydration number of ions close to the electrode and in the organic film is unknown.

8 Assignment of C-H Stretching Modes in 1-Ethyl-3-Methylimidazolium-Based Ionic Liquids

1-Ethyl-3-methylimidazolium-based ILs were subject to many vibrational spectroscopic studies and thus have a model character. Therefore, the 1-ethyl-3-methylimidazolium triflate [C_2Im][TfO] IL is used to the study the interactions of ILs in aqueous solutions in the following chapter 9. However, the detailed assignment of IR absorption bands in neat [C_2Im][TfO] as well as in its solutions is complicated and not straight-forward. Usually, the aromatic imidazolium ring CH stretching vibrations were focused on and debated with anharmonic frequency DFT calculations as well as experiments.[35, 151, 175-177, 212] Grondin et al. presented anharmonic frequency calculations for C_2Im$^+$ cations with different degrees of deuteration at the ring C-atoms. To explain spectral features for IR absorptions at $\tilde{\nu} > 3050$ cm^{-1}, they also calculated FR interaction with overtones and combinations of the in-plane ring modes R_1 and R_2. Unfortunately, no FR interactions were calculated for alkyl CH stretching vibrations. They were neglected in these studies, and sometimes assigned in a coarse and summarized manner to alkyl stretching.[27-28, 47, 213] Nevertheless, it should be noted that alkyl chains are an important structural motif that introduces asymmetry into ILs, leads to nanosegregation phenomena, and thus fundamentally distinguish ILs from classical molten salts.

8.1 Electronic Impact of the Imidazolium Ring on Aliphatic C-H Stretching Modes

Electronic effects of the imidazolium ring were proposed to severely affect the vibrations of the ethyl chain.[34] Experimental IR spectra of [C_2Im][TfO] deviate significantly from their longer chain homologues, which is illustrated in spectra by Kiefer et al. (Fig. 8.1A).[34] In spectra of [C_{4-8}Im][TfO] ILs, the alkyl CH stretching band positions and intensities

follow a clear trend and leave no doubts for their assignment. In contrast to its higher homologues, the intensity of the band at $\tilde{\nu}$ = 2990 cm^{-1} in the ethyl derivative is weak. Kiefer et al. assigned this bands to both ν_{as}(C-CH$_3$) and ν_{as}(N-CH$_3$) modes.[34] On the other hand, intensities of the IR absorption modes in the aromatic ν(CH) spectral region are significantly higher. Kiefer et al. compared the behavior of these *n*-alkyl-methylimidazolium triflates to *n*-alcohols of similar chain lengths.[34] Again, the IR spectrum of the ethyl-derivative deviates from the trend given by alcohols with longer alkyl chains (Fig. 8.1B). However, the ν_{as}(C-CH$_3$) mode intensity and resonance frequency is similar to the ones of longer alcohols and thus, the authors reasoned that just the prolongation of the alkyl chain cannot explain the anomalous behavior in [C$_2$Im][TfO]. Consequently, they concluded that the charge redistribution due to the positively charged imidazolium ring affects the terminal C-CH$_3$ group. This effect should be negligible in [C$_{4-8}$Im][TfO] ILs; because of the spatial separation by the methylene groups, the terminal methyl group should not be significantly affected by the ring moiety.
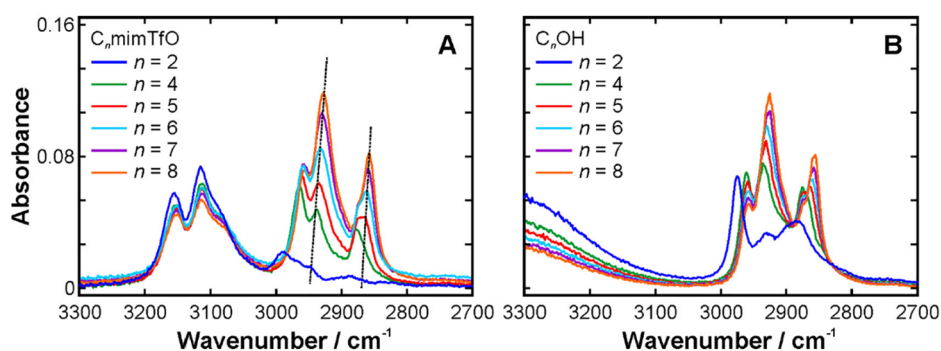
Figure 8.1: FTIR spectra of A – [C$_n$Im][TfO] and B – *n*-alcohol derivatives by Kiefer et al.[34] Copied with permission from Elsevier.

Ethyl groups in both [C$_2$Im][TfO] and ethanol are bound to a electronegative atom. IR spectra of both compounds hint for intriguingly different vibrational properties concerning the ν_{as}(C-CH$_3$) mode.[34] To elucidate this, harmonic frequency calculations were conducted for the C$_2$Im$^+$ and ethanol molecules. Unscaled harmonic frequencies, IR intensities (I_{IR}), force constants, and reduced masses are shown in table 8.1. Cartesian coordinates of the optimized ethanol and C$_2$Im$^+$ molecules are given in the appendix (Tabs 12.8 and 12.9, respectively).

Table 8.1: Properties of ν_{as}(ethyl) modes in harmonic frequency calculations of ethanol and C_2Im^+ molecules (B3LYP-D3BJ/6-311++G(d,p)).

Molecule	Mode	$\tilde{\nu}$ / cm^{-1}	I_{IR} / km mol^{-1}	k / N cm^{-1}	m / g mol^{-1}
Ethanol	$\nu_{as}(CH_3)$	3106	33.43	6.27	1.103
	$\nu_{as}(CH_3)$	3100	30.49	6.23	1.101
	$\nu_{as}(CH_2)$	3004	52.68	5.89	1.108
C_2Im^+	$\nu_{as}(CH_2CH_3)$	3135	8.01	6.41	1.108
	$\nu_{as}(C\text{-}CH_3)$	3124	6.14	6.34	1.102
	$\nu_{as}(CH_2CH_3)$	3110	2.67	6.30	1.105

Although both ethyl groups are bound to electronegative O or N atoms, their ν_{as}(CH) modes exhibit fundamentally different characteristics. Whereas separate $\nu_{as}(CH_3)$ and $\nu_{as}(CH_2)$ modes with significantly different force constants (Tab. 8.1) appear in ethanol, these modes are mixed in the C_2Im^+ cation. In this cation, one $\nu_{as}(C\text{-}CH_3)$ and two $\nu_{as}(CH_2CH_3)$ modes with similar force constants are present. The relative weights of deflected groups are almost equal in both out-of-phase and in-phase $\nu_{as}(CH_2CH_3)$ modes (Fig. 8.2). This behavior was also a result of calculations, e.g. by Heimer et al.[32] or Grondin et al.[151], but it has not been discussed in detail.

$\nu_{as}(CH_2CH_3)$ out of phase $\nu_{as}(CH_2CH_3)$ in phase
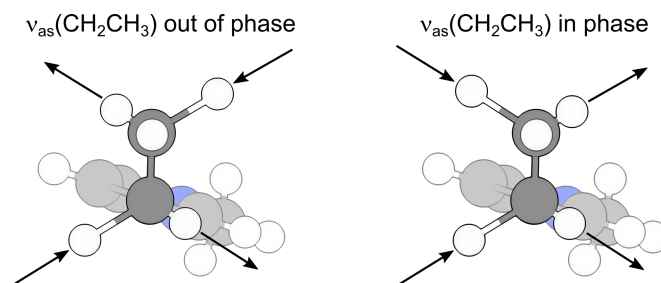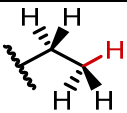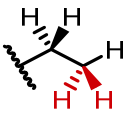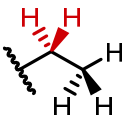
Figure 8.2: Mixed asymmetric stretching vibrations in the ethyl group of the C_2Im^+ cation.

Indeed, the electronic structure can be accounted for these spectral differences. C-H bond lengths and natural bond orbital (NBO) charges (Q) in both calculated ethyl groups are compared in table 8.2. In ethanol, the C-H bond lengths are around 109.2-190.3 pm in the CH_3 group and with 109.8 pm significantly larger in the CH_2 group. In contrast, all ethyl C-H bond lengths are close to 109.0-109.2 pm in the C_2Im^+ cation. The NBO analysis is used to characterize the charge distribution in molecules. In ethanol, the H atoms in the methylene group are less positively charged than in the methyl group

($\Delta Q_H \approx$ -0.05 e). However, in the C_2Im^+ cation the NBO charge of the methylene H atoms is more positive and lies in between the charges of the methyl H atoms ($Q_H \approx$ -0.22 e). This difference can be explained by the mesomeric effect with free lone pairs of the O atom, which donate charge density to the antibonding orbitals of the methylene C-H bonds and thus elongate them. In imidazolium rings, electrons forming (formal) π-Orbitals contribute to aromaticity and are not available for donation. Inductive effects of the electronegative N atom and the overall positively charged ring group withdraw electron density and shorten the C-H bond lengths of the methylene group. Similar bond lengths in C-H groups coincide with similar force constants. As reduced masses do not differ greatly (Tab. 8.1), single C-H vibrations of the CH_2 and CH_3 groups are degenerated and mix. Elongated alkyl chains may decouple methyl and $N-CH_2$ groups, and thus change the vibrational nature of the system, which is in line with the conclusion of Kiefer et al.[34]

Table 8.2: C-H bond lengths and NBO charges in the ethyl group of optimized ethanol and C_2Im^+ molecules (B3LYP-D3BJ/6-311++G(d,p)). The bond(s) and atoms of interest are marked red in the "Species" column.

Species	Bong length / pm		Q_H / e		Q_C / e	
	Ethanol	C_2Im^+	Ethanol	C_2Im^+	Ethanol	C_2Im^+
	109.340	109.133	0.200	0.236		
					-0.592	-0.588
	109.241	109.166*	0.203	0.214*		
	109.836	109.043*	0.148	0.219*	-0.023	-0.167

*Due to C_s symmetry, the H atoms out of the O-C-C plane exhibit the same distance in ethanol within the methylene or methyl group, respectively. Symmetry is broken in the nonplanar C_2Im^+ cation, and thus averaged values are reported for the H atoms out of the N-C-C plane.

Electronic effects of the electronegative imidazolium ring cause a mixed vibrational behavior. It is required to understand the vibrations of the C_2Im^+ cation, as these mixed modes may severely impact their coupling.

8.2 Experimental C-H Stretching Modes of N-CH$_3$ Groups in Alkyl-Methylimidazolium-Based Ionic Liquids

An overview of some literature attempts to assign certain modes in different C$_2$Im$^+$ ILs with weakly or not strongly coordinating anions is given in table 8.3. The IR and Raman spectra of these ILs are similar regardless of the used anions in the 2800 cm^{-1} < $\tilde{\nu}$ < 3050 cm^{-1} spectral region.[32-37] Despite the fact that all cited examples were aided by harmonic frequency calculations, the assignments differ strongly. In some cases, results of (scaled) harmonic frequency calculations were grossly neglected. For example, this lead to the doubtful assignment of the ν_{as}(C4,5-H$_2$) mode to the experimental IR/Raman absorption bands at $\tilde{\nu}$ = 2990/2997 cm^{-1} by Singh et al., while $\tilde{\nu}$ = 3105 cm^{-1} in their scaled harmonic calculation.[33]

Table 8.3: Literature assignments of aliphatic ν(CH) modes in C$_2$Im$^+$-based ILs, sorted according to anions[references].

Mode	Assigned $\tilde{\nu}$ / cm^{-1}					
	PF$_6^{-}$[36]	Tf$_2$N^{-}[35]	Tf$_2$N^{-}[37]	TfO^{-}[33]	TfO^{-}[34]	BF$_4^{-}$[32]
ν_s(C-CH$_3$)	2878	2950	3000	2837	2890**	2888-2890
ν_s(N-CH$_3$)	2917	2970	2970	2770		2938
ν_s(CH$_2$)	2942		2990	2890	2872	2950
ν_{as}(CH$_2$)	2970		3050 ± 30*	2956		2970, 2990***
ν_{as}(C-CH$_3$)	2952			2930	2990**	
ν_{as}(N-CH$_3$)	3115			2958, 2971		3112

* These ν_{as}(CH) bands are not observed. According to the authors, the bands are explicitly supposed to be masked by the ν(C2-H) band.[37]

** C-CH$_3$ and N-CH$_3$ groups were not distinguished.[34]

*** Of three vibrations denoted as "Ethyl HCH asym str" one is unassigned.[32]

In the following, a more detailed assignment of ν(CH) IR absorption bands in [C$_2$Im][TfO] is attempted. As found in the harmonic calculations of Grondin et al.[151] eight fundamentals for the CH alkyl stretching vibrations are expected for one C$_2$Im$^+$ conformer: two ν_{as}(N-CH$_3$) modes, two almost equally mixed ν_{as}(CH$_2$CH$_3$) modes (in phase and out of phase), and the following single modes, ν_{as}(CH$_3$), ν_s(CH$_2$), ν_s(C-CH$_3$), ν_s(N-CH$_3$). The assignment of ν(N-CH$_3$) bands can be aided by experiments and literature. The IR spectrum of [C$_2$Im][Tf$_O$] resembles the one of [C$_2$Im][Tf$_2$N] in the 2800 cm^{-1} < $\tilde{\nu}$ < 3000 cm^{-1} spectral region.[213] As shown by Höfft et al., the IR spectra of crystallized and frozen [C$_2$Im][Tf$_2$N] hint for much more bands in this region,

which merge in the liquid.[213] Unfortunately, they did not analyze the alkyl modes.

A comparison between ATR IR spectra of [C$_2$Im][TfO] (Fig. 8.3a) and [C$_{18}$Im-d_{37}][TfO] (Fig. 8.3b) facilitates the assignment from experimental side. As the octadecyl-d_{37} chain in [C$_{18}$Im-d_{37}][TfO] cannot contribute to the alkyl ν(CH) region, bands present there must originate from the non-deuterated N-CH$_3$ group. Two N-CH$_3$-related bands appear at $\tilde{\nu} \approx 2886$ cm^{-1} and $\tilde{\nu} \approx 2965$ cm^{-1} in the spectrum of [C$_{18}$Im-d_{37}][TfO] (Fig. 8.3b). For reference, the ν(CH$_3$) modes in elongated alkanes are observed at $\tilde{\nu}$ / cm^{-1} = 2870 – ν$_s$(CH$_3$), 2931 – ν$_{FR}$(CH$_3$), 2952 and 2962 – both ν$_{as}$(CH$_3$).[173] Higher C-H force constants may be the result of the electron withdrawing effect of the positively charged imidazolium ring and lead to a hypsochromic shift in resonance frequencies (Section 8.1).
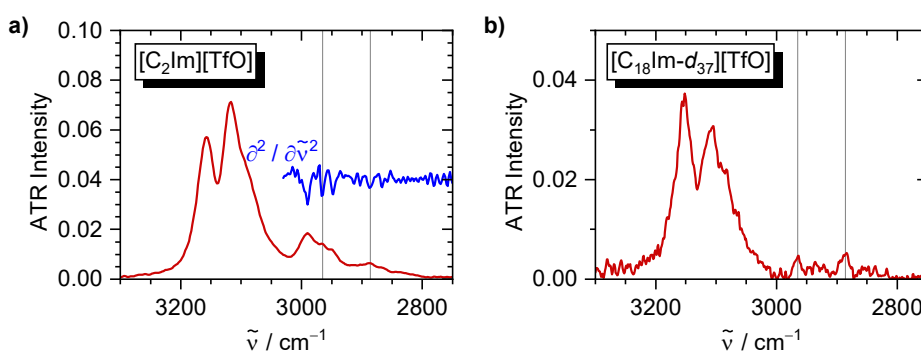
Figure 8.3: ATR IR spectra of neat a) [C$_2$Im][TfO] (red) with a magnified and offset second derivative (blue) in the alkyl ν(CH) region and b) [C$_{18}$Im-d_{37}][TfO].

In literature, the band around $\tilde{\nu} \approx 2970$ cm^{-1} is ascribed to symmetric stretching vibrations in aliphatic groups in helium nanodroplet isolated IR spectra of [C$_2$Im][Tf$_2$N] ion pairs by Obi et al.[47] Cooper et al. assigned this signal to the undistinguished ν$_s$(N/C-CH$_3$) band(s) in vapor-phase jet-cooled IR spectra of [C$_2$Im][Tf$_2$N] ion pairs.[37] Chatzipapadopolous et al. ascribed this band to the ν$_s$(N-CH$_3$) mode in time-resolved coherent anti-Stokes Raman scattering (CARS) spectra of methyl/ethyl/octyl-methylimidazolium Tf$_2$N$^-$ ILs.[35] These authors assume the corresponding asymmetric stretching vibrations to resonate in the 3000 cm^{-1} < $\tilde{\nu}$ < 3100 cm^{-1} spectral region. Following their assignment of the ν$_s$(N-CH$_3$) band, the band at $\tilde{\nu} \approx 2886$ cm^{-1} in the [C$_{18}$Im-d_{37}][TfO] IL is likely to originate from an overtone or binary combination of δ(N-CH$_3$) modes. Nevertheless, aliphatic stretching vibrations at wavenumbers this high are unusual.

1,3-dimethylimidazolium (C_1Im^+) ILs may yield further useful information (Tab. 8.4). Experimental IR or Raman bands around $\tilde{v}$ / cm^{-1} = 3035, 3001, 2971, 2940 and 2874 are reported in most listed cases. The number of bands hints for possible FR interactions, leading to enhanced overtone or combination modes in the CH stretching region. Endo et al. studied [C_1Im][PF_6] at different temperatures in liquid and two crystalline states.[214]. The C_1Im^+ cation itself exhibits no conformational isomerism, and thus packing of ions with respect to each other in α and β crystals must be different, which causes the difference in their Raman spectra (Tab. 8.4). Interestingly, the intensity and frequency pattern of the methyl bending modes matches well with the pattern of their stretching modes, which indicates that the environmental of the imidazolium cation influences stretching and bending modes in similar ways.

Table 8.4: Bands found in the aliphatic ν(CH) spectral region of 1,3-dimethylimidazolium compounds.

Anion[Reference]	$\tilde{v}$ / cm^{-1}						
TfO^{-}[215]			2968 s	2943 sh	2864 m		2770 w
Tf$_2$N^{-}[35]		3033 w		2969 vs	2939 sh		n.s.
PF$_6^{-}$, liquid, 373 K[214]		3039 br	3001 sh	2973 vs	2938 sh	2872 w	n.s.
PF$_6^{-}$, liquid, 313 K[214]		3035 br	3001 sh	2974 vs	2938 sh	2871 w	n.s.
PF$_6^{-}$, α crystal[214]		3035 w	2999 w	2974 vs		2867 w	n.s.
PF$_6^{-}$, β crystal[214]	3059 w	3034 w	3007 w	2977 s	2942 w	2888 w ~2850	n.s.

n.s. – spectral region not shown.

A study of Huang et al.[216] sheds light on methyl FR interactions. They used experimental and theoretical techniques to examine vibrational spectra of methylamine, dimethylamine, and trimethylamine as monomers and in small clusters. Methyl stretching/bending FR interactions in methylamines neither depend on the size of the cluster nor on coupling of individual methyl groups attached to the N atom. The resonance frequency of the ν_s(N-CH$_3$) mode was found to determine the complexity of the spectrum. In trimethylamine, the ν_s(N-CH$_3$) mode is shifted "outside the FR window".[216] The resonance frequency of the ν_s(N-CH$_3$) fundamental can probably be accounted to electronic effects, which depend on the substitution pattern of the N-atom. If the insignificant methyl-methyl coupling can be transferred to 1,3-dimethylimidazolium-based ILs, N-bound methyl groups in the latter may yield similar patterns in longer *n*-alkyl-methylimidazolium cations.

Concluding the discussion above, both bands at $\tilde{v} \approx 2965$ cm^{-1} and $\tilde{v} \approx 2886$ cm^{-1} must undoubtedly be assigned to the N-CH$_3$ group in [C$_{18}$Im-d_{37}][TfO], and therefore probably in [C$_2$Im][TfO], too.

8.3 Assignment of C-H Stretching Modes by Anharmonic Frequency Calculations of the C$_2$Im$^+$ Cation

Overtone and binary combination modes enhanced by FR interaction with fundamentals certainly influence the spectra of alkyl moieties.[171-173, 178, 217] They must be considered for vibrational assignment in experimental spectra. Vibrational modes are strongly affected by the molecular structure.

For a frequency calculation, a molecular geometry must be specified. Umebayashi et al. showed that two conformers of the 1-ethyl-3-methylimidazolium cation can be found in single crystals with different anions.[218] In the most abundant nonplanar C$_2$Im$^+$ conformer the ethyl chain is oriented in a C(2)-N(1)-C(6)-C(7) dihedral angle of 105 ° (C(6) and C(7) correspond to the methylene and methyl group of the ethyl chain, respectively). In contrast, the ethyl chain is only tilted by 15 ° out of the ring plane in the (almost) nonplanar conformer, which is less abundant. Their DFT and ab initio calculations indicate two local geometry minima for above mentioned dihedral angles of 0 ° and ca 110 ° for a C$_2$Im$^+$ cation in vacuo. Supported by harmonic frequency calculations, they could assign two distinct modes in the far IR region, each belonging to one conformer. Consequently, both planar and nonplanar C$_2$Im$^+$ conformers are present in the liquid phase, but the latter to much greater extent.

Therefore, an anharmonic frequency calculation including resonances was conducted using the generalized second-order vibrational perturbation theory (GVPT2) formalism for the most stable, nonplanar C$_2$Im$^+$ cation. For far less computational cost in comparison to electron correlation incorporating Møller-Plesset or coupled cluster post-HF methods,[147] DFT methods were shown to predict successfully ground- and excited-state equilibrium structures.[219] However, the choice of the density functional and basis set may strongly influence the results.[219] The B3LYP functional was shown to yield best anharmonic corrections in a benchmark study.[219] Furthermore, a proper description of electron correlation for dispersive interactions is required to achieve so-called chemical accuracy, which is

incorporated in DFT parametrically. The ωB97X-D functional exhibits long-range dispersion interaction corrections, and Singh et al. propagated the use of this functional for the description of the [C$_2$Im][TfO] IL.[33, 220] Furthermore, empirical dispersion correction may be used in conjunction with the B3LYP functional (D3BJ). A 6-311++G(d,p) triple-ζ basis set was used for all calculations. Cartesian coordinates of nonplanar and planar C$_2$Im$^+$ cations, optimized on the different levels of theory mentioned above, are given in the appendix (Tabs 12.9-12.12).

It must be emphasized that all calculations in this work and others[33, 35-36, 151] were executed for single ions, ion pairs, or small clusters in vacuo, and their comparison to experimental spectra is not always possible. For example, two asymmetric stretching vibrations are expected for methyl groups. For single molecules in gas phase and in crystals, these two modes can be identified separately in experiments.[173] However, chemical interactions and subtle rotations in liquid phase broaden the absorption bands and yield a single ν_{as}(CH$_3$) band convoluted by two individual ν_{as}(CH$_3$) modes.[172] In addition, intermolecular interactions in the liquid may substantially influence the geometry, and thus mode intensities and resonance frequencies. As aromatic ν(CH) modes were shown to be significantly affected by intermolecular interactions,[35, 151, 175-177, 212] and they will be discussed apart from the less sensitive aliphatic ν(CH) modes.[27-28, 220]

8.3.1 Assignment of Aliphatic C-H Stretching Modes in the C$_2$Im$^+$ Cation

Aliphatic ν(CH) modes are significantly weaker and less well resolved in IR spectra than in Raman spectra of liquid [C$_2$Im][TfO].[27-28] Thus, the latter are used for the primary band assignment and to judge the quality of the calculated resonance frequencies and intensities (Raman activities, I_{Raman}) (Fig. 8.4). Corresponding IR spectra are shown in figure 8.5. For the B3LYP-D3BJ/6-311++G(d,p) calculation of the nonplanar C$_2$Im$^+$ cation, harmonic and anharmonic modes as well as overtones and binary combinations in FR are shown in tables 8.5 and 8.6, respectively, in the ν(CH) spectral region.
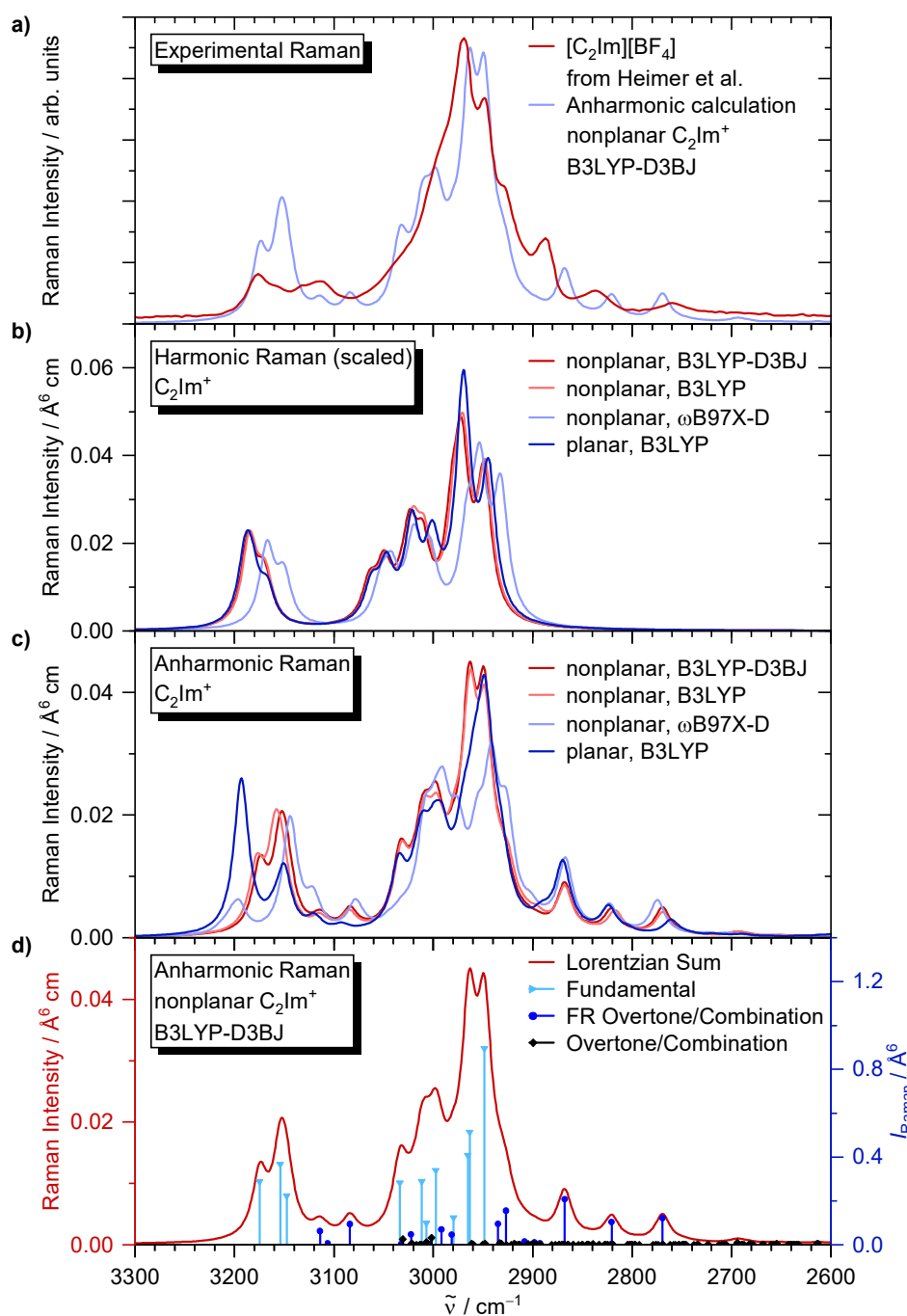
Figure 8.4: Raman spectra in the ν(CH) spectral region: a) Spectrum of [C₂Im][BF₄] (digitized from Heimer et al.,[32] copyright permission from Elsevier) and the calculation from d); b-d) frequency calculations (DFT/6-311++G(d,p)) of the C₂Im⁺ cation in vacuo. b) Harmonic spectra scaled by 0.95725[220] for ωB97X-D and 0.9679[221] for B3LYP and B3LYP-D3BJ functionals. c) Anharmonic spectra. d) Anharmonic spectrum (left axis) with line spectrum of individual modes (right axis). Curves in calculated spectra present the Lorentzian-distributed sum spectrum with fwhm = 18 cm⁻¹.
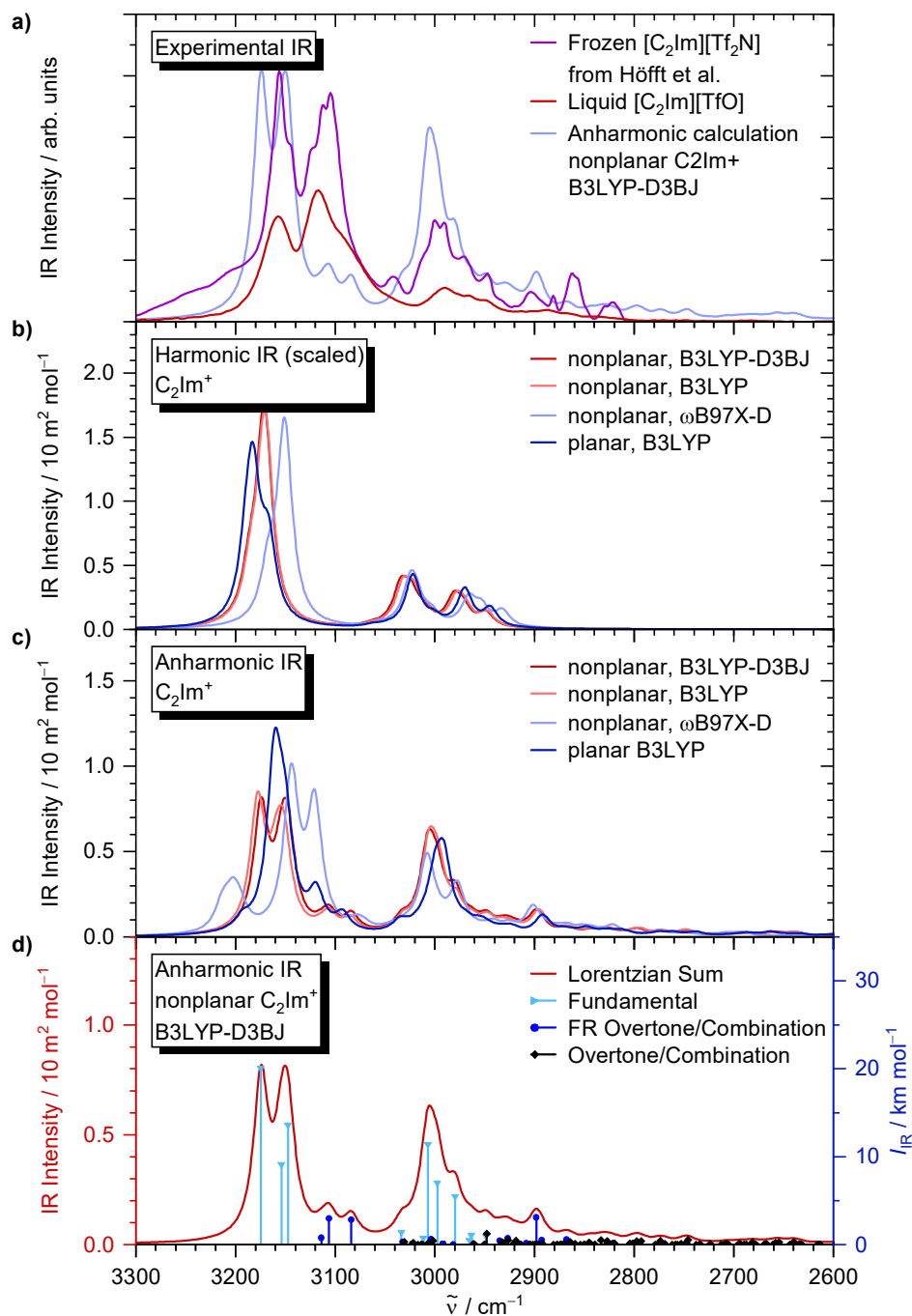
Figure 8.5: IR spectra in the ν(CH) spectral region: a) Spectra of frozen [C2Im][Tf2N] (digitized and adapted with permission from O. Höfft, S. Bahr, V. Kempter, *Langmuir* **2008**, *24*, 11562-11566.[213] Copyright 2008, American Chemical Society.), liquid [C2Im][TfO], and the calculation from d; b-d) frequency calculations (DFT/6-311++G(d,p)) of the C2Im+ cation in vacuo. b) Harmonic spectra scaled by 0.95725[220] for ωB97X-D and 0.9679[221] for B3LYP and B3LYP-D3BJ functionals. c) Anharmonic spectra. d) Anharmonic spectrum (left axis) with line spectrum of individual modes (right axis). Curves in calculated spectra present the Lorentzian-distributed sum spectrum with fwhm = 18 cm⁻¹.

Harmonic calculations have already been used to assign vibrational bands in C_2Im^+-based ILs,[32-37] and shall be featured briefly. The comparison of experimental spectra (Figs 8.4a,8.5a) with scaled harmonic frequency calculations (Figs 8.4b,8.5b) only yields a coarse agreement. In the Raman spectra, the most intense band at $\tilde{v} = 2970$ cm^{-1} can be correlated to the most intense calculated mode, v_s(N-CH$_3$) (Tab. 8.5). Similarly, the second most intense band at $\tilde{v} = 2950$ cm^{-1} may be assigned to the v_s(C-CH$_3$) mode. As discussed in section 8.2 and shown in table 8.3, harmonic calculations lead to a versatile and sometimes arbitrary band assignments. In general, the harmonic aliphatic v(CH) modes were predicted to be more intense than aromatic v(CH) modes in Raman spectra. This is reversed for IR spectra and in agreement with experimental results for both techniques (Figs 8.4a,b and 8.5a,b; Tab. 8.5). The employed density functional methods give slightly varying harmonic spectra, however none of them exhibits a significant advantage for band assignment. Similar harmonic spectra are obtained for the planar C_2Im^+ conformer (Figs 8.4b,8.5b).

Table 8.5: Fundamental modes in simulated vibrational spectra of the nonplanar C_2Im^+ cation in the v(CH) spectral region (B3LYP-D3BJ/6-311++G(d,p)).

Mode	Harmonic			Anharmonic		
	$\tilde{v}$ / cm^{-1}	I_{Raman} / Å^6	I_{IR} / km mol^{-1}	$\tilde{v}$ / cm^{-1}	I_{Raman} / Å^6	I_{IR} / km mol^{-1}
v_s(C4,5-H$_2$)	3292	0.55	8.99	3175	0.29	20.12
v(C2-H)	3278	0.12	32.58	3154	0.37	9.12
v_{as}(C4,5-H$_2$)	3274	0.20	16.38	3148	0.22	13.63
v_{as}(N-CH$_3$)	3166	0.24	0.41	3034	0.28	1.41
v_{as}(CH$_2$CH$_3$)	3151	0.33	0.22	3012	0.29	0.75
v_{as}(N-CH$_3$)	3135	0.06	8.01	3007	0.10	11.42
v_{as}(CH$_2$CH$_3$)	3124	0.52	6.15	2997	0.34	7.03
v_{as}(C-CH$_3$)	3110	0.41	2.67	2965	0.41	0.50
v_s(CH$_2$)	3080	0.48	5.61	2980	0.12	5.49
v_s(N-CH$_3$)	3070	0.98	3.60	2963	0.51	1.10
v_s(C-CH$_3$)	3047	0.90	3.06	2949	0.90	0.98

It is evident that many experimental features at $\tilde{v}$ / cm^{-1} = 3132, 3114, 2930, 2888, 2838, 2760 are not given by the harmonic calculations of Raman spectra, and neither in similar regions of IR spectra at $\tilde{v}$ / cm^{-1} = 3123, 3113, 3104, < 2920. FR interactions are sensitive to intramolecular as well as intermolecular interactions,[178, 222] and in the liquid phase the latter deviate strongly from the gas phase behavior. Nevertheless, anharmonic frequency calculations yield a far better description for the spectral modes for both

Raman and IR spectra (Figs 8.4a,c and 8.5a,c). The overlap of the calculated spectrum of the C_2Im^+ cation in gas phase with the experimental spectrum recorded for associated cations in liquid phase is surprisingly good.

Considering the strongest Raman modes at $\tilde{\nu}$ = 2970 and 2950 cm^{-1} (Fig. 8.4a,c), the B3LYP functional matches best, whereas the ωB97X-D functional describes a different intensity pattern. This functional also fails to predict the correct position of the FR interactions modes with the aromatic ν(CH) modes at $\tilde{\nu}$ > 3050 cm^{-1}, which is elaborated in section 8.3.3. The intensity shape in the Raman spectrum around $\tilde{\nu}$ = 2950 cm^{-1} is only given for the more stable nonplanar C_2Im^+ conformer (Fig. 8.4d). This is in agreement with results of Umebayashi et al.[218]

Table 8.6: FR interacting modes in simulated vibrational spectra of the nonplanar C_2Im^+ cation in the ν(CH) spectral region (B3LYP-D3BJ/6-311++G(d,p)).

Overtone or Combination	Fundamental(s) in FR	$\tilde{\nu}$ / cm^{-1}	I_{Raman} / Å^6	I_{IR} / km mol^{-1}
$2R_1$	ν_s(C4,5-H$_2$)	3114	0.06	0.78
$R_1 + R_2$	ν(C2-H)	3106	0.01	2.98
$2R_2$	ν(C2-H)	3084	0.09	2.83
δ(CH$_2$CH$_3$) + R_1	ν_{as}(CH$_2$CH$_3$)	3032	0.00	0.30
δ(CH$_2$CH$_3$) + R_2	ν_s(CH$_2$)	3022	0.05	0.15
δ(CH$_2$CH$_3$) + R_2	ν_s(CH$_2$)	3004	0.00	0.61
δ_s(N-CH$_3$) + R_1	ν_s(N-CH$_3$)	2992	0.07	0.15
δ_s(N-CH$_3$) + R_2	ν_s(N-CH$_3$)	2981	0.05	0.03
$2\delta_{as}$(N-CH$_3$)	ν_s(N-CH$_3$)	2935	0.10	0.45
2δ(CH$_2$CH$_3$)	ν_s(CH$_2$), ν_s(C-CH$_3$)	2927	0.16	0.70
2δ(CH$_2$CH$_3$)	ν_s(C-CH$_3$)	2908	0.02	0.16
δ(CH$_2$CH$_3$) + δ(CH$_2$CH$_3$)	ν_s(CH$_2$), ν_s(C-CH$_3$)	2898	0.01	3.10
$2\delta_{as}$(N-CH$_3$)	ν_s(N-CH$_3$)	2893	0.01	0.50
$2\delta_{as}$(C-CH$_3$)	ν_s(C-CH$_3$)	2868	0.21	0.56
$2\delta_s$(N-CH$_3$)	ν_s(N-CH$_3$)	2821	0.10	0.21
$2\delta_s$(C-CH$_3$)	ν_s(C-CH$_3$)	2769	0.12	0.08

The anharmonic spectrum of the nonplanar C_2Im^+ cation calculated on the B3LYP-D3BJ/6-311++G(d,p) level of theory is analyzed in detail (Figs 8.4d,8.5d; Tabs 8.5,8.6). By matching the spectra via their intensity patterns, three characteristic experimental Raman bands in the 2700 cm^{-1} < $\tilde{\nu}$ < 2900 cm^{-1} spectral region can be assigned to FR interaction bands (Fig. 8.4a,d), i.e. at $\tilde{\nu}$ / cm^{-1} = 2760 – $2\delta_s$(C-CH$_3$), 2838 – $2\delta_s$(N-CH$_3$), 2888 – $2\delta_{as}$(C-CH$_3$) (Tab. 8.6). The shoulder at $\tilde{\nu}$ = 2930 cm^{-1} may be assigned to the $2\delta_s$(CH$_2$CH$_3$) mode.

These assignments are in line with experimental Raman spectra of $[C_{2/3/4}Im][BF_4]$ ILs reported by Heimer et al.[32] (Fig. 8.6): The band at $\tilde{\nu} = 2760$ cm^{-1} shifts bathochromically upon prolongation of the alkyl chain from ethyl to butyl, whereas its intensity remains almost constant. Electron-withdrawing effects of the imidazolium ring affect the methyl group less in butyl than in ethyl substituents and thus slightly longer C-H bond lengths are expected, which in turn should lead to bathochromic shifts. Thus, it is reasonable that this mode is related to the C-CH$_3$ group. On the other hand, the mode at $\tilde{\nu} = 2838$ cm^{-1} changes neither its intensity nor resonance frequency and thus belongs to the N-CH$_3$ group.
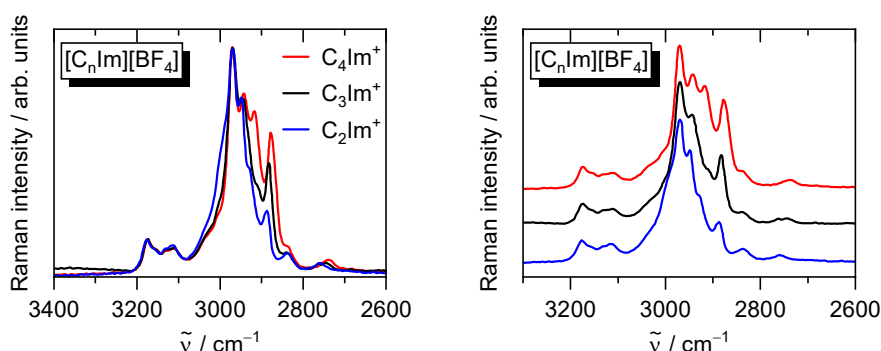
Figure 8.6: Raman spectra of $[C_2Im][BF_4]$, $[C_3Im][BF_4]$, and $[C_4Im][BF_4]$ in the ν(CH) spectral region (digitized from Heimer et al.,[32] copyright permission from Elsevier). Assuming that the prolongation of the alkyl chain does not significantly impact the aromatic ν(CH) modes, the intensities of the spectra were normalized to the maximum at $\tilde{\nu} = 3175$ cm^{-1} and minimum at $\tilde{\nu} = 3142$ cm^{-1}.

In the case of the bands at $\tilde{\nu} = 2888$ and 2930 cm^{-1}, the situation is more complex and experimental comparisons are difficult. When the alkyl chain is prolongated, additional methylene modes may influence this region, too. As mentioned above, the assignment by spectral intensity shape results in the ascription of the $2\delta_{as}$(C-CH$_3$) mode to the Raman band at $\tilde{\nu} = 2888$ cm^{-1}. However, in the discussion of N-CH$_3$ groups in the previous section 8.2, the IR band at $\tilde{\nu} = 2886$ cm^{-1} was ascribed to a FR of the N-CH$_3$ group. Experimental indications should be preferred over the simulation of an unassociated C$_2$Im$^+$ cation in vacuo. Of course, intensities in Raman spectra deviate from IR spectra. Nevertheless, resonance frequencies of single modes are equal and a band is found in both IR and Raman spectra at this position ($\Delta\tilde{\nu} = 2$ cm^{-1}, experimental spectra in figures 8.4a and 8.5a). Furthermore, the difference in calculated and experimental resonance frequencies is high for the discussed assignment ($\tilde{\nu} = 2888$ cm^{-1}, $\Delta\tilde{\nu} = 20$ cm^{-1} for the ascription to the theoretical $2\delta_{as}$(C-CH$_3$) mode). In comparison, the resonance frequency

differences in theoretical assignments for experimental bands at $\tilde{\nu} = 2838$ cm^{-1} ($\Delta\tilde{\nu} = 17$ cm^{-1} for the ascription to the theoretical $2\delta_s$(N-CH$_3$) mode) and at $\tilde{\nu} = 2760$ cm^{-1} ($\Delta\tilde{\nu} = 9$ cm^{-1} for the ascription to the theoretical $2\delta_s$(C-CH$_3$) mode) are little less. Another matching assignment for the band at $\tilde{\nu} = 2888$ cm^{-1} may be the $2\delta_{as}$(N-CH$_3$) overtone ($\Delta\tilde{\nu} = 5$ cm^{-1}), which however exhibits negligible calculated Raman intensity (Tab. 8.6). In this case the mode matching by the Raman intensity pattern may fail and the gas phase calculation may not reflect the liquid properly.

The most intense Raman feature in the calculated spectrum is double-peaked and fits to the experimental spectrum. The calculation reveals that the most intense experimental band at $\tilde{\nu} = 2970$ cm^{-1} is composed of two fundamentals, i.e. ν_s(N-CH$_3$) and ν_{as}(C-CH$_3$) modes, which are separated theoretically by $\Delta\tilde{\nu} = 2$ cm^{-1} only. Interestingly, the experimentally second strongest feature at $\tilde{\nu} = 2950$ cm^{-1} can be assigned to the ν_s(C-CH$_3$) mode, which exhibits the lowest resonance frequency among all fundamentals. In the 2950 cm$^{-1} < \tilde{\nu} < 3070$ cm^{-1} spectral region, broad Raman bands are recorded experimentally. According to the calculation, they are dominated by the ν_s(CH$_2$), ν_{as}(N-CH$_3$) and ν_{as}(CH$_2$CH$_3$) modes. Considering again the experimental results of Heimer et al.[32] (Fig. 8.6), it becomes evident that intensity in the shoulder at $\tilde{\nu} \approx 3000$ cm^{-1} vanishes upon prolongation of the ethyl chain. Consequently, it may indeed have CH$_2$CH$_3$-character. Prolongation of the alkyl chain should change electronic effects, C-H bond lengths, and thus mixing of the methyl group's ν_{as}(C-CH$_3$) with ν_{as}(CH$_2$) (Section 8.1). This is in line with the changes of the $2\delta_s$(C-CH$_3$) overtone described above.

In harmonic as well as in anharmonic calculations, the ν_{as}(N-CH$_3$) modes are split by $\Delta\tilde{\nu} \approx 30$ cm^{-1} (Tab. 8.5), which should in principle also be resolvable in spectra of liquids. In the Raman spectrum of [C$_2$Im][BF$_4$] (Figs 8.4 and 8.6), asymmetric C-CH$_3$-related modes should appear in the spectral region around $\tilde{\nu} \approx 3000$-3010 cm^{-1} according to the simulation. This is close the expected resonance frequency of ν_{as}(N-CH$_3$) modes, and in C$_2$Im$^+$-based ILs these modes may overlap (Tab. 8.5). As explained above, the Raman spectra of [C$_3$Im][BF$_4$] and [C$_4$Im][BF$_4$] ILs are not affected by the C-CH$_3$ in this spectral region. They exhibit two shoulders at $\tilde{\nu} \approx 3002$ cm^{-1} and $\tilde{\nu} \approx 3037$ cm^{-1} (Fig. 8.6), and the latter also appears in [C$_2$Im][BF$_4$]. Both wavenumbers match well with the anharmonic calculation (Tab. 8.5). Moreover, the IR spectrum of frozen [C$_2$Im][NTf$_2$] reported by Höfft et al.

(Fig. 8.5a) shows two bands close to these wavenumbers, too. They can be clearly assigned to the ν_{as}(N-CH$_3$) modes.

In general, the matching of predicted and experimental intensity patterns is more difficult in the case of IR spectra (Fig. 8.5a,d). In liquid [C$_2$Im][OTf], the strongest aliphatic ν(CH) band is located at $\tilde{\nu}$ = 2990 cm^{-1} and may be assigned to both ν_{as}(CH$_2$CH$_3$) and ν_{as}(N-CH$_3$) fundamentals (Tab. 8.5). Relative intensities of other fundamentals seem to be underestimated by the calculation. In agreement with the calculated resonance frequency and experimental findings discussed in section 8.2, the band at $\tilde{\nu}$ = 2966 cm^{-1} is assigned to the ν_s(N-CH$_3$) mode. By comparison to the Raman assignment, the band at $\tilde{\nu}$ = 2949 cm^{-1} is assigned to the ν_s(N-CH$_3$) fundamental (Tab. 8.5). IR Spectra of frozen [C$_2$Im][NTf$_2$] by Höfft et al. indicate a variety of bands at $\tilde{\nu}$ < 2949 cm^{-1}. These bands are proposed to originate from overtone and combination bands (Tab. 8.6), which are hard to distinguish due to similarly low intensities.

8.3.2 Impact of Fermi Resonance Effects on the Resonance Frequencies of CH Stretching Fundamentals

According to the calculation of the C$_2$Im$^+$ cation, aliphatic ν(CH) fundamentals are proposed to resonate at relatively high frequencies. The fundamental with the lowest wavenumber is located around $\tilde{\nu} \approx$ 2950 cm^{-1} (Tab. 8.5), which is in a harsh contrast to what is known for long-chain *n*-alkanes.[172-173] It is striking that aliphatic ν_s(CH) bands are proposed at $\tilde{\nu} \geq$ 2948 cm^{-1} (Tab. 8.5), whereas experimentalists may expect these modes at significantly lower wavenumbers (Tab. 8.3). This may explain the strongly differing band assignments in literature, which were carried out without use of anharmonic frequency calculations (Tab. 8.3 and references cited there). As elaborated in section 8.1, electronic effects of the imidazolium ring can be accounted for these high resonance frequencies. With change in the resonance frequencies, FR interactions change, too. Thus, the impact of electronics effects propagates in a hardly predictable manner.

As an example, the resonance frequency shifts due to FR coupling of ν_s(C-CH$_3$) modes in ethanol and the C$_2$Im$^+$ cation are compared (Fig. 8.7).
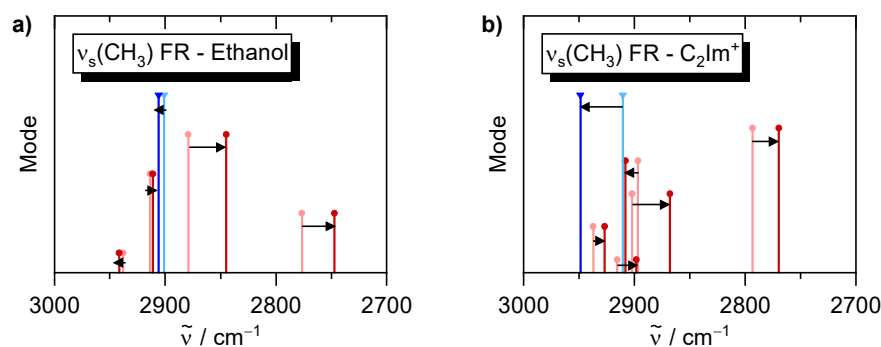
Figure 8.7: Resonance frequencies of the ν_s(C-CH$_3$) FR couples in a) ethanol and b) the C$_2$Im$^+$ cation (B3LYP-D3BJ/6-311++G(d,p)): Blue – ν_s(C-CH$_3$) fundamental, red – overtones or binary combinations. Lighter colors indicate deperturbed wavenumbers, whereas darker colors correspond to perturbed wavenumbers incorporating the FR effect. The change in resonance frequency is highlighted with arrows. Heights do not describe intensities but distinguish individual modes.

According to the anharmonic frequency calculation, the deperturbed ν_s(C-CH$_3$) fundamental at $\tilde{\nu} = 2901$ cm^{-1} resonates with four overtones and combinations in ethanol (Fig. 8.7a). The overall effect of FR coupling on the resonance frequency of the fundamental is subtle and leads to a $\Delta\tilde{\nu} = +5$ cm^{-1} shift. Although the deperturbed wavenumber of the ν_s(C-CH$_3$) mode in the C$_2$Im$^+$ cation (Fig. 8.7b) is close to the one in ethanol, $\tilde{\nu} = 2910$ cm^{-1}, FR effects perturb the resonance frequency to a greater extent and cause a shift of $\Delta\tilde{\nu} = +38$ cm^{-1}. As discussed in section 8.1, C-H bond lengths in the ethyl group attached to the methyl-imidazolium moiety are similar, and asymmetric stretching vibrations of methyl and methylene groups mix. The same was calculated for the corresponding bending modes. Mixing of one δ_{as}(CH$_3$) with the δ(CH$_2$) mode yields two δ(CH$_2$CH$_3$) modes. As a result, one more FR interacting mode is given for the ν_s(C-CH$_3$) in the C$_2$Im$^+$ cation, in contrast to ethanol. Note that these modes may not only resonate with ν_s(C-CH$_3$) but also with ν_s(CH$_2$) in a complex manner.

8.3.3 Impact of H-Bonding on the Aromatic C-H Stretching Modes

The interaction of aromatic ν(CH) modes was shown to greatly influence the 3000 cm^{-1} < $\tilde{\nu}$ < 3200 cm^{-1} spectral region of *n*-alkyl-methylimidazolium ILs. The ascription of bands in this region was discussed in literature and is summarized below. An overview of different assignments is given in table 8.7.

Even for weakly coordinating anions, more modes are observed experimentally than expected from the three aromatic ν(CH) fundamentals,

ν_s(C4,5-H$_2$), ν(C2-H), and ν_{as}(C4,5-H$_2$). Köddermann et al. reasoned that different types of H-bonded imidazolium species exist simultaneously, i.e. in ion pairs or H-bond networks.[223] However, this strongly disagrees with spectra of deuterated compounds, which reveal three bands only.[151, 175, 177] Lassègues et al. postulated with anharmonic calculations of the nonplanar C$_2$Im$^+$ cation and experimental deductions from selective deuteration the presence of overtones or the combination of the ring stretching modes R$_1$/R$_2$, which appear around $\tilde{\nu} \approx 1560$ cm^{-1}.[175] They argued that for weakly coordinating anions no considerations of H-bonds need to be invoked, which was strongly opposed by Wulf et al.[176-177] Indeed, the bathochromic shift of the ν(C2-H) band increases with increasing anion basicity/coordination strength.[151, 176] Whereas Lassègues et al. mostly considered reduced cubic constants, which reflect the mode coupling,[175] Roth et al. also focused on the frequency separation of potentially resonant modes.[212] With CARS and anharmonic simulations, the latter showed that hydrogen bonds matter even with the weakly coordinating Tf$_2$N$^-$ anion. They concluded that the C(2)-H group is mostly affected and thus experiences a considerable bathochromic shift, which allows for stronger resonance. Consequently, a ν(C2-H)-associated FR couple around was assigned to the two bands around $\tilde{\nu} \approx 3120$ cm^{-1}, whereas ν_s(C4,5-H$_2$) and ν_{as}(C4,5-H$_2$) bands were ascribed to the bands at $\tilde{\nu} \approx 3180$ cm^{-1} and $\tilde{\nu} \approx 3160$ cm^{-1}, respectively.

Table 8.7: Literature assignments of aromatic ν(CH) modes in C$_2$Im$^+$-based ILs, sorted according to anions[references].

Mode	Assigned $\tilde{\nu}$ / cm^{-1}					
	Tf$_2$N$^{-[175]}$	Tf$_2$N$^{-[212]}$	Tf$_2$N$^{-[223]}$	TfO$^{-[28]}$	TfO$^{-[33]}$	TfO$^{-[34]}$
ν_s(C4/5-H$_2$)		3174	3174 net	3190 net	3166/3171	
ν_{as}(C4/5-H$_2$)	3160	3153	3153 ip	3157 ip	2990/2997	3155
ν(C2-H)			3125 net / 3104 ip	3117 net / 3088 ip	3116	3116
R$_1$ + R$_2$	3120	3104, 3125*				
2R$_1$					3153, 3086	3088
2R$_2$	< 3100					

* one FR couple.

ip – in ion pairs; net – in H-bond networks.

In this section it shall be checked, how the vacuum phase calculations correspond to previous experimental and theoretical findings. In the case of the nonplanar C$_2$Im$^+$ conformer, the ωB97X-D functional predicted FRs ($\tilde{\nu}$ / cm^{-1} = 3195, 3202, 3202) to resonate at wavenumbers greater than the aromatic ν(CH) modes ($\tilde{\nu}$ / cm^{-1} = 3121, 3143, 3145) (Figs 8.4c and 8.5c).

This in in contrast to experimental findings of intensity gains or losses around $\tilde{\nu} \approx (3090 \pm 25)$ cm^{-1} for strongly and weakly coordinating anions, respectively.[35, 151, 175-177, 212] Thus, all calculations were conducted with the B3LYP functional and empirical dispersion correction (D3BJ) for associated molecules.

In addition to the unassociated nonplanar C_2Im^+ cation, two associates were simulated on the B3LYP-D3BJ/6-311++G(d,p) level of theory: The $[C_2Im][TfO]$ ion pair (Fig. 8.8a) and the twofold water associated $[C_2Im \cdot 2\,D_2O]^+$ complex (Fig. 8.8b).

O-H distances given in pm
○ H/D ● C ● N ● O ● F ● S
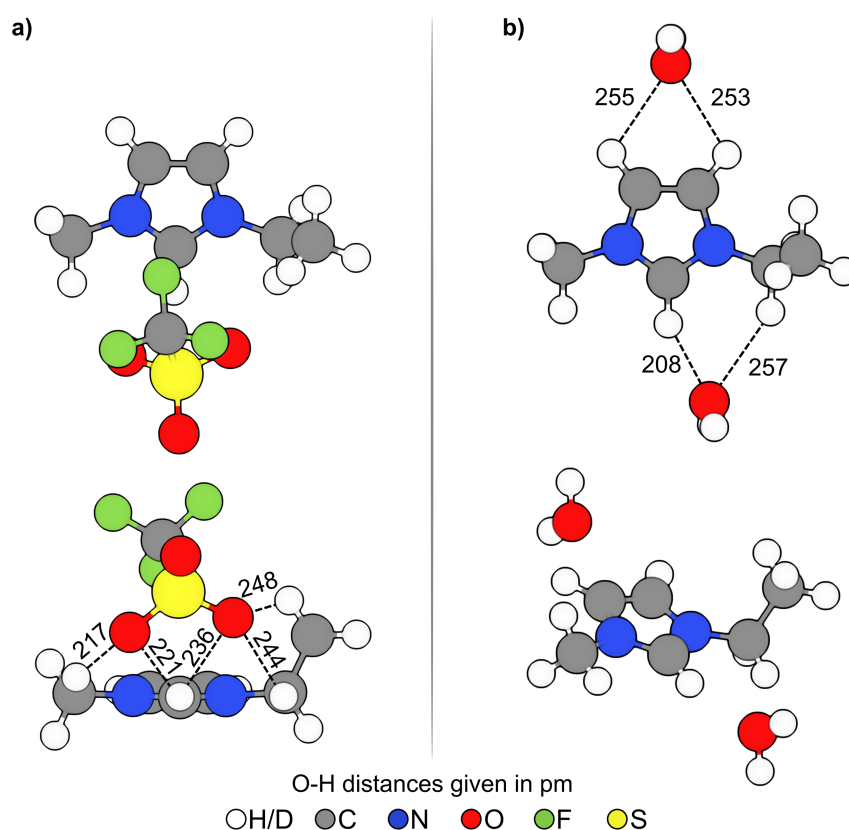
Figure 8.8: Geometries of associated C_2Im^+ cations for simulations of anharmonic spectra: a) the $[C_2Im][TfO]$ ion pair, and b) the $[C_2Im \cdot 2\,D_2O]^+$ cation.

The geometry of the $[C_2Im][TfO]$ ion pair was optimized starting from the lowest energy conformer (with and without BSSE correction) found by Singh et al. (ωB97X-D/6-311++G(d,p)).[33] In vacuo, H-bonding effects with an otherwise uncoordinated and unscreened anion may be overcompensated. Thus, water was chosen as a neutral and simple H-bond acceptor to both sides of the imidazolium ring. To dimmish unreasonable overtone effects of

the $\delta(OH_2)$ modes of the (apart from the imidazolium moiety) uncoordinated water molecules, D_2O was employed.

In the used GVPT2 formalism, FR interactions are identified by the Martin test.[219] An empirical threshold $\mathcal{K}$ is set to define a potential resonance as significant or insignificant (Eqs 8.1 and 8.2). For FRs, the value Λ to test versus that threshold is determined by the deperturbed frequency difference of the interacting fundamental ($\tilde{v}_f$) and overtone ($2\tilde{v}_i$) or combination modes ($\tilde{v}_i + \tilde{v}_j$) and their cubic force constants (k_{fii} or k_{fij}, respectively), which are the third derivative of the potential energy with respect to each of the dimensionless normal coordinates and reflect the coupling strength of modes. Following these equations, FR interactions become significant for high cubic force constants and low frequency differences, which lead to high values of Λ. During the calculations, $\mathcal{K}$ was set to relatively tolerable 0.1 cm⁻¹.

$$\text{Overtones:} \quad \Lambda = \frac{k_{fii}^4}{256(2\tilde{v}_i - 2\tilde{v}_f)^3} \geq \mathcal{K} \tag{8.1}$$

$$\text{Binary combinations:} \quad \Lambda = \frac{k_{fij}^4}{64(\tilde{v}_i + \tilde{v}_j - 2\tilde{v}_f)^3} \geq \mathcal{K} \tag{8.2}$$

The anharmonic frequency calculation of the unassociated nonplanar C_2Im^+ cation by Lassègues et al. did not include the calculation of IR or Raman intensities. Considering the calculation of the previous section 8.3.1, the intensities of $2R_1$, $2R_2$, and $R_1 + R_2$ modes (Tab. 8.6) are too low to accurately describe experimental spectra (Figs 8.4a,d and 8.5a,d). This supports that H-bond interactions need to be considered.
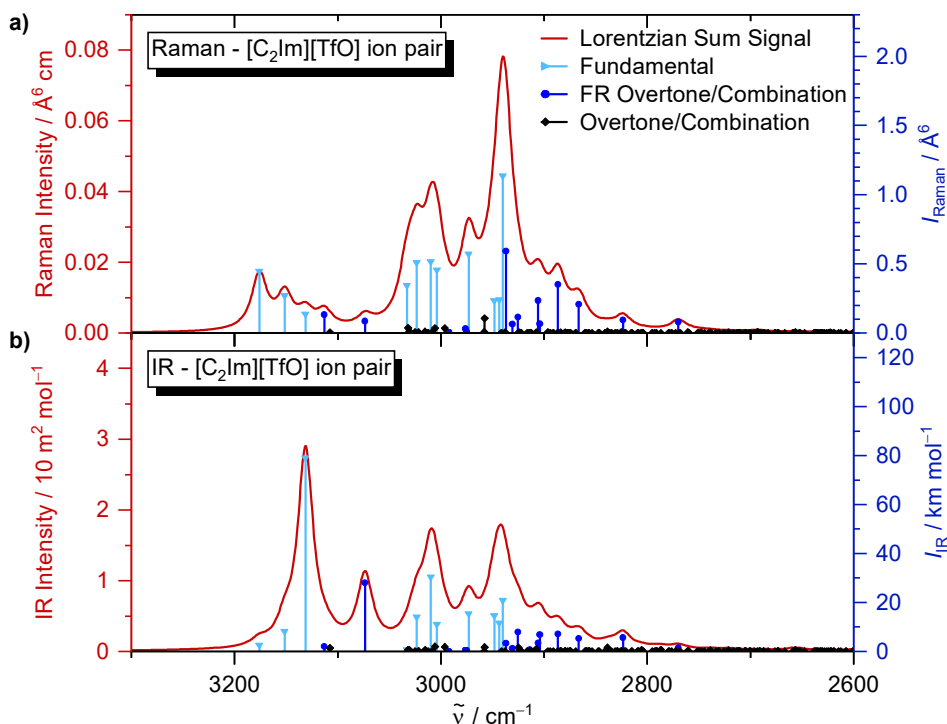
Figure 8.9: Simulated a) Raman and b) IR spectra of the [C₂Im][TfO] ion pair in the ν(CH) spectral region (B3LYP-D3BJ/6-311++G(d,p)): Anharmonic spectra (left axes) with line spectra of individual modes (right axes). Curves in calculated spectra present the Lorentzian-distributed sum spectrum with fwhm = 18 cm⁻¹.

Cartesian coordinates of the optimized [C₂Im][TfO] ion pair are given in the appendix (Tab. 12.13). In this structure, the H-accepting sulfonyl group is mainly associated with the C(2)-H group (Fig. 8.8a). In comparison to the calculation of the bare C₂Im⁺ cation (Figs 8.4d and 8.5d; Tab. 8.5), the ν(C4,5-H₂) modes are hypsochromically shifted by $\Delta\tilde{\nu}$ = 1-3 cm⁻¹ in the [C₂Im][TfO] ion pair (Fig. 8.9; Tab. 8.8), whereas the ν(C2-H) mode experiences a substantial bathochromic shift of $\Delta\tilde{\nu}$ = 20 cm⁻¹ to $\tilde{\nu}$ = 3131 cm⁻¹. This leads to a considerable FR with the 2R₂ overtone at $\tilde{\nu}$ = 3074 cm⁻¹. These findings are in a good (but not perfect) agreement with experimental resonance frequencies of the [C₂Im][TfO] and [C₂Im][Tf₂N] ILs mentioned in table 8.7. For the R₁ + R₂ combination, a FR interaction is unlikely, as it did not pass the Martin test (Tab. 8.8).

Table 8.8: Simulated anharmonic modes in the aromatic ν(CH) spectral region of the [C₂Im][TfO] ion pair (B3LYP-D3BJ/6-311++G(d,p)).

Mode	Fundamental(s) in FR	Λ / cm^{-1}	$\tilde{\nu}$ / cm^{-1}	I_{Raman} / Å^6	I_{IR} / km mol^{-1}
ν_s(C4,5-H₂)			3176	0.45	2.58
ν_{as}(C4,5-H₂)			3151	0.27	8.21
ν(C2-H)			3131	0.14	79.06
2R₁	ν_s(C4,5-H₂)	0.33	3113	0.13	2.04
2R₂	ν(C2-H)	1.73	3074	0.09	28.08
R₁ + R₂	−	< 0.1 ($\mathcal{K}$)	3108	0.00	1.34

In the [C₂Im · 2 D₂O]⁺ complex, water molecules are associated with both C(4,5)-H₂ and C(2)-H groups (Fig. 8.8b). Cartesian coordinates of the optimized [C₂Im · 2 D₂O]⁺ complex are given in the appendix (Tab. 12.14). In comparison to the calculation of the bare C₂Im⁺ cation (Figs 8.4d and 8.5d; Tab. 8.5), the ν(C4,5-H₂) modes are hypsochromically shifted by $\Delta\tilde{\nu}$ = 1-9 cm^{-1} in the water adduct (Fig. 8.10; Tab. 8.9), whereas the ν(C2-H) mode experiences huge bathochromic shift of $\Delta\tilde{\nu}$ = 107 cm^{-1} to $\tilde{\nu}$ = 3047 cm^{-1}. The FR is strong (Δ = 5-21 cm^{-1}) for both ring overtones and the combination ($\tilde{\nu}$ = 3099-3124 cm^{-1}), and their strengths vary in IR and Raman spectra (Tab. 8.5). In this case, the ν(C2-H) mode is located at lower resonance frequencies than its FR interaction modes. Indeed, strong H-bond acceptors, such as bromide, were shown to produce strong intensities around $\tilde{\nu}$ = 3050 cm^{-1}.[151, 177]

Table 8.9: Simulated anharmonic modes in the aromatic ν(CH) spectral region of the [C₂Im · 2 D₂O]⁺ complex (B3LYP-D3BJ/6-311++G(d,p)).

Mode	Fundamental(s) in FR	Λ / cm^{-1}	$\tilde{\nu}$ / cm^{-1}	I_{Raman} / Å^6	I_{IR} / km mol^{-1}
ν_s(C4,5-H₂)			3176	0.63	23.13
ν_{as}(C4,5-H₂)			3157	0.17	9.24
ν(C2-H)			3047	0.46	113.76
2R₁	ν(C2-H)	4.70	3124	0.06	5.36
2R₂	ν(C2-H)	12.16	3099	0.01	20.72
R₁ + R₂	ν(C2-H)	20.90	3122	0.11	41.52

It must be emphasized that the [C₂Im · 2 D₂O]⁺ complex was employed to simulate significant H-bond acceptors and not an aqueous environment. In fact, even dilute solutions of [C₂Im][TfO] in water show no shifts in resonance frequencies of the alkyl ν(CH) region and little changes in the aromatic ν(CH) region.[27-28, 220] However, coordinated water molecules as depicted in figure 8.8b have a pronounced effect on many modes (Figs 8.5d,

8.4d and 8.10), which shows that the $[C_2Im \cdot 2\,D_2O]^+$ complex is not suitable to describe experimental results of diluted $[C_2Im][TfO]$.
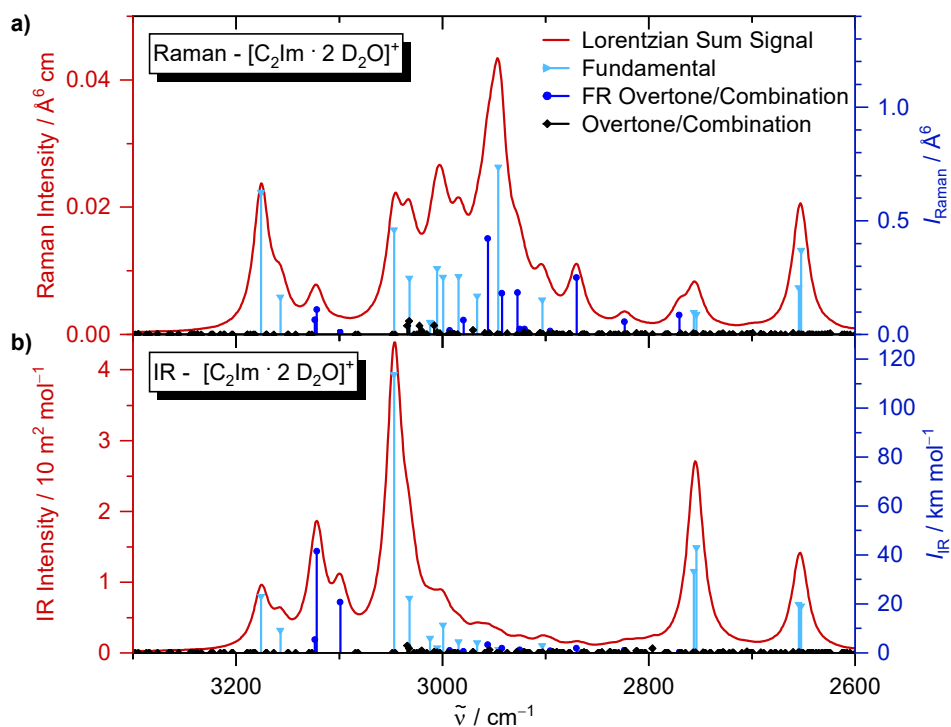
Figure 8.10: Simulated a) Raman and b) IR spectra of the $[C_2Im \cdot 2\,D_2O]^+$ complex in the $\nu(CH)$ spectral region (B3LYP-D3BJ/6-311++G(d,p)): Anharmonic spectra (left axes) with line spectra of individual modes (right axes). Curves in calculated spectra present the Lorentzian-distributed sum spectrum with fwhm = 18 cm^{-1}. Note that the bands at $\tilde{\nu} < 2800$ cm^{-1} originate from $\nu_{as}(OD_2)$ and $\nu_s(OD_2)$ fundamentals.

The quest to distinguish the ring FR couples remains difficult and experimentally not even be comprehensible, depending on the mixing and redistribution of involved modes.

8.4 Final Assignment

Based on sections 8.3.1 and 8.3.3, aliphatic and aromatic ν(CH) modes are finally assigned in table 8.10 and figure 8.11.

Table 8.10: Assignment of in the modes in the ν(CH) spectral region for [C$_2$Im][BF$_4$], frozen [C$_2$Im][Tf$_2$N], and liquid [C$_2$Im][TfO] aided by anharmonic frequency calculations.

Mode	$\tilde{\nu}$ /cm^{-1}			
	calculated	Raman [C$_2$Im][BF$_4$]	IR [C$_2$Im][Tf$_2$N]	IR [C$_2$Im][TfO]
ν_s(C4,5-H$_2$)	3176	3176	3156	3156
ν_{as}(C4,5-H$_2$)	3151	3156	3145	
ν(C2-H)	3131	3132	3122	
2R$_1$/2R$_2$/R$_1$ + R$_2$	3113/3074/3108	3114	3112/3104	3086/ }3117
ν_{as}(N-CH$_3$)	3034	3041	3042	3042
ν_{as}(CH$_2$CH$_3$)	3012		3012	
ν_{as}(N-CH$_3$)	3007	2997	3000	2990
ν_{as}(CH$_2$CH$_3$)	2997		2990	
ν_{as}(C-CH$_3$)/ν_s(N-CH$_3$)	2965/2963	2970	2970	2966
ν_s(C-CH$_3$)	2949	2950	2947	2948
2δ(CH$_2$CH$_3$)	2927	2930	2932	
δ(CH$_2$CH$_3$) + δ(CH$_2$CH$_3$)	2898		2903	2903
2δ_{as}(N-CH$_3$)/2δ_{as}(C-CH$_3$)	2893/2868	2888		2886
2δ_s(N-CH$_3$)	2821	2838		
2δ_s(C-CH$_3$)	2769	2760		

As the selected anions are moderately (TfO$^-$) or weakly (BF$_4^-$, Tf$_2$N$^-$) coordinating, the simulation of the [C$_2$Im][TfO] ion pair was used for assignment of aromatic ν(CH) modes. However, the model of the ion pair may not accurately represent chemical interactions (mostly H-bonding) in the liquid, and thus a detailed distinction of 2R$_1$, 2R$_2$, R$_1$ + R$_2$ modes was not attempted.
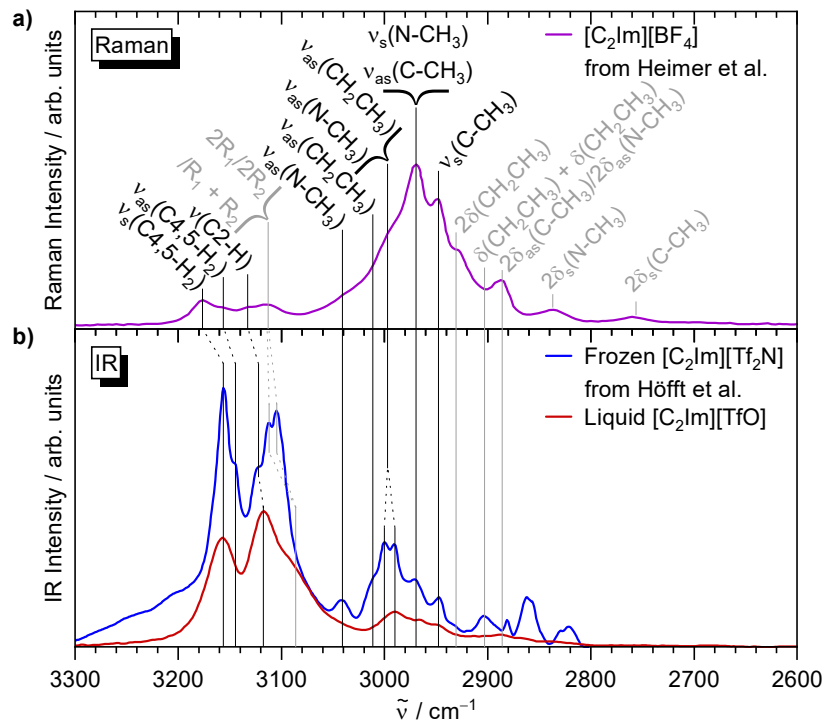
Figure 8.11: Reassigned vibrational spectra of C₂Im⁺-based ILs in the ν(CH) spectral region: a) Raman spectrum of [C₂Im][BF₄] (digitized from Heimer et al.,[32] copyright permission from Elsevier); b) IR spectra of frozen [C₂Im][Tf₂N] (digitized and adapted with permission from O. Höfft, S. Bahr, V. Kempter, *Langmuir* **2008**, *24*, 11562-11566.[213] Copyright 2008, American Chemical Society.) and liquid [C₂Im][TfO]. Fundamentals are colored black, overtones and combinations are colored grey.

This assignment is used in the following chapter to interpret complex spectroelectrochemical results.

9 Interfacial Interactions in Aqueous Solutions of Ionic Liquids

After analyzing the EDL model composed of a single IL monolayer on the Au(111) surface (chapters 6 and 7), the next step was to investigate interactions in the EDL formed by IL molecules originating from the bulk solution. As elaborated in the beginning of section 6.3, aqueous solutions are employed, due to decoupling of slow diffusion kinetics and molecular interactions occurring in ILs. Such experiments may fill a gap in theory and experiments between dilute inorganic electrolytes and highly concentrated ILs. In addition, aqueous solutions of ILs are of interest for electrocatalysis, e.g. the CO_2 reduction.[13-15, 224-225] Fundamental electrochemical studies on ILs in aqueous solutions are scarce, but they may likely gain in importance. In 2016, two interesting studies with aqueous solutions of 1-ethyl-3-methyl-imidazolium triflate $[C_2Im][TfO]$ were published:[27, 30]

Brummel et al. applied CV and in situ IRRAS to study the effect of the $[C_2Im][TfO]$ IL on the oxidation of methanol on Pt(111) in 0.1 M $HClO_{4(aq)}$.[30] With increasing IL concentration, the hydrogen as well as hydroxide adsorption were decreased steadily, but were never suppressed fully. Due to much stronger intensities of the corresponding IR absorption modes, their investigations were focused on the triflate anion. When C_2Im^+ cation desorbs at positive potentials, the TfO^- anion adsorbs, in a tilted geometry. The extent of absorption depends on time. The triflate adsorption is significantly slower than its desorption. Also, water molecules were found to reorient and be replaced on the electrode surface. Upon increasing the IL concentration, the IR adsorption bands of TfO^- sharpen and shift hypsochromically, indicating specific adsorption and/or interactions with water.

Cui et al. studied different $[C_2Im][TfO]$-water mixtures on Au(poly/111) electrode surfaces by means of cyclic voltammetry and AFM force-distance curves, as well as the impact on Zn electrodeposition.[27] Cyclic voltammetry reveal new processes upon water addition to the IL, which may be attributed to the adsorption of [IL-water] onto Au. AFM force-distance curves reveal solvation layers. Their number and rupture forces depend on both the applied potential and the IL volume fraction. They concluded, that at 30-40 vol-% water a transition occurs from the multilayer structure known for

neat ILs to a Stern layer structure with a diffuse layer as in aqueous solutions. Depending on the water fraction, dense or porous Zn structures are formed during electrodeposition.

For the study of this chapter, the model IL: [C₂Im][TfO] was also chosen. It mixes with water at any fraction and is commercially available in high purity. Two systems were used to investigate the electrochemical behavior of the [C₂Im][TfO] IL. In one approach, the experiments were carried out with a flame annealed Au(111) electrode. In this case, the structure of the first layer at the Au(111) surface is unknown in aqueous solutions. To aid the interpretation of results, a second system with a predefined first layer was employed. As described in chapters 6 and 7, the Au(111) surface was modified with a [C₁₈Im][X] monolayer. This approach incorporates a first layer, whose structure and behavior was studied before in absence of the [C₂Im][TfO] in the electrolyte.

However, studies on [C₁₈Im][X] monolayer covered Au(111) electrode surfaces in [C₂Im][TfO]$_{(aq)}$ solutions lacked sufficient reproducibility, despite similarities in the $C(U)$ curve shapes. The results did not allow to draw conclusions whether the monolayer was present on the electrode surface. Therefore, these results are not reported. Previous experiments (Chapters 6 and 7) had been carried out in 0.1 M KClO₄$_{(aq)}$ solutions and indicated no film desorption or dissolution. Followingly, low concentrations of [C₂Im][TfO] are analyzed in 0.1 M KClO₄$_{(aq)}$. The used concentrations lead to different volume and mole fractions, which are given in table 9.1.

Table 9.1: Properties of the [C₂Im][TfO] solutions in 0.1 M KClO₄$_{(aq)}$. The volume fraction of KClO₄ is constant and amounts to 0.55 %.

Concentration / M		Volume fraction / %		Mole fraction / %		
[C₂Im][TfO]	H₂O	[C₂Im][TfO]	H₂O	[C₂Im][TfO]	KClO₄	H₂O
0	55.20	0	99.45	0	0.181	99.82
0.005	55.15	0.09	99.36	0.009	0.181	99.81
0.010	55.10	0.19	99.26	0.018	0.181	99.80
0.025	54.94	0.47	98.98	0.045	0.182	99.77
0.050	54.68	0.94	98.51	0.091	0.182	99.73
0.100	54.16	1.87	97.58	0.184	0.184	99.63

[C₁₈Im][X] monolayers were fabricated according to conditions as described in section 6.1.[p2] For IR spectroscopic analyses, it is desirable to distinguish C-H stretching modes as well as in-plane ring stretching modes of the film from the same bands in the bulk electrolyte [C₂Im][TfO] species.

Therefore, the perdeuterated 1-(methyl-d_3)-3-(octadecyl-d_{42})-imidazolium-4,5-d_2 triflate [C$_{18}$Im-d_{42}][TfO] compound was employed. It was synthesized and provided by Torben Alpers from the working group of Jens Christoffers, University of Oldenburg.[195] Originally, the completely perdeuterated -d_{43} compound was aimed at, but during synthesis a D/H-exchange occurred at the C(2) atom of the imidazolium ring. This atom is the most acidic one and prone to this exchange.[151] As this compound was to be transferred from aqueous 0.1 M KClO$_{4(aq)}$ subphases and analyzed in H$_2$O and D$_2$O solutions, there was no need to prevent the exchange during the synthesis. With T_m = 64 °C,[195] it is an IL per definition.

9.1 Electrochemical Characterization of an Aqueous Ionic Liquid

Capacitance/potential curves of the flame annealed and [C$_{18}$Im][X] monolayer covered Au(111) surfaces in [C$_2$Im][TfO]$_{(aq)}$ + 0.1 M KClO$_{4(aq)}$ electrolytes are crucial to investigate the EDL structure. First, experimental $C(U)$ curves are described, and next, they are discussed within EDL theories.

9.1.1 Capacitance-Potential Curves

$C(U)$ curves of [C$_2$Im][TfO]$_{(aq)}$ at concentrations of 0, 5, 10, 25, 50, and 100 mM in 0.1 M KClO$_{4(aq)}$ are shown in figures 9.1 and 9.2. The measurement procedure was the same as described in section 6.3. Curves on the left side (a) were measured at flame annealed Au(111) electrode interfaces, whereas the right side (b) shows curves for [C$_{18}$Im][X] monolayer covered Au(111) surfaces. Plenty features appear in these curves and are marked exemplarily in figure 9.1a for c(IL) = 10 mM; in other figures they appear in similar potential regions but are omitted for clarity of presentation. Although the organic cation and anion have no amphiphilic character, shaking of the solutions lead to the appearance of some bubbles, which indicates surface activity of the IL.
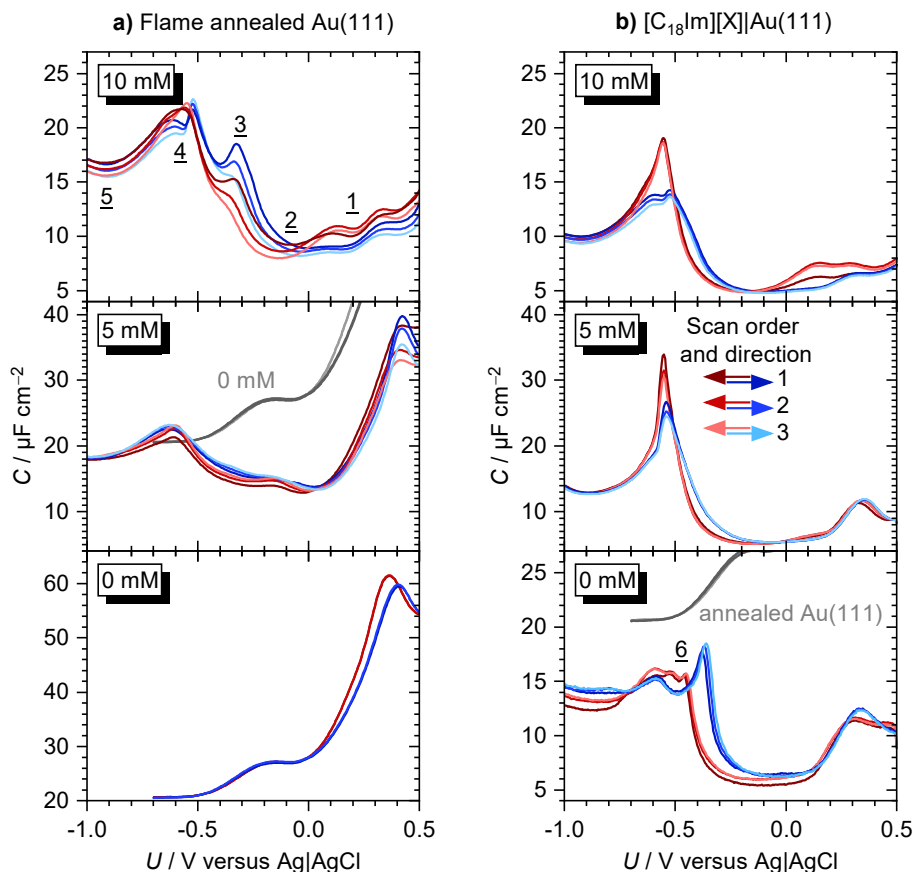
Figure 9.1: Differential capacitance versus potential curves of 0, 5, and 10 mM [C₂Im][TfO]$_{(aq)}$ in 0.1 M KClO$_{4(aq)}$ at the Au(111) electrode surface. a) Flame annealed Au(111) electrode. b) Au(111) electrode covered with the [C₁₈Im][X] LB monolayer. As marked in the figure, negatively (red lines) and positively (blue lines) going potential scans were recorded for three cycles (two for 0 mM of the flame annealed electrode). Please note that figures a) 10 mM, b) 0 mM and b) 10 mM are shown in the same capacitance magnitude as all graphs of figure 9.2.

Starting with the flame annealed Au(111) electrode, the addition of 5 mM [C₂Im][TfO]$_{(aq)}$ imposes large changes on the $C(U)$ curve with respect to the capacitive characteristic of the pure 0.1 M KClO$_{4(aq)}$ solution (Fig. 9.1a, 0 and 5 mM). Generally, the capacitance is lowered at -0.5 V < U < 0.5 V. The capacitance of the perchlorate and hydroxide adsorption peak[157] at U = 0.4 V is greatly reduced from C = 60 µF cm⁻² to $C \approx$ 36 µF cm⁻² (1). It indicates adsorption of the [C₂Im][TfO] IL from solution onto the Au(111) surface. This is consistent with literature; for example, Beattie et al. have shown self-assembly of an imidazolium-based IL onto the Au(poly) surface.[129]
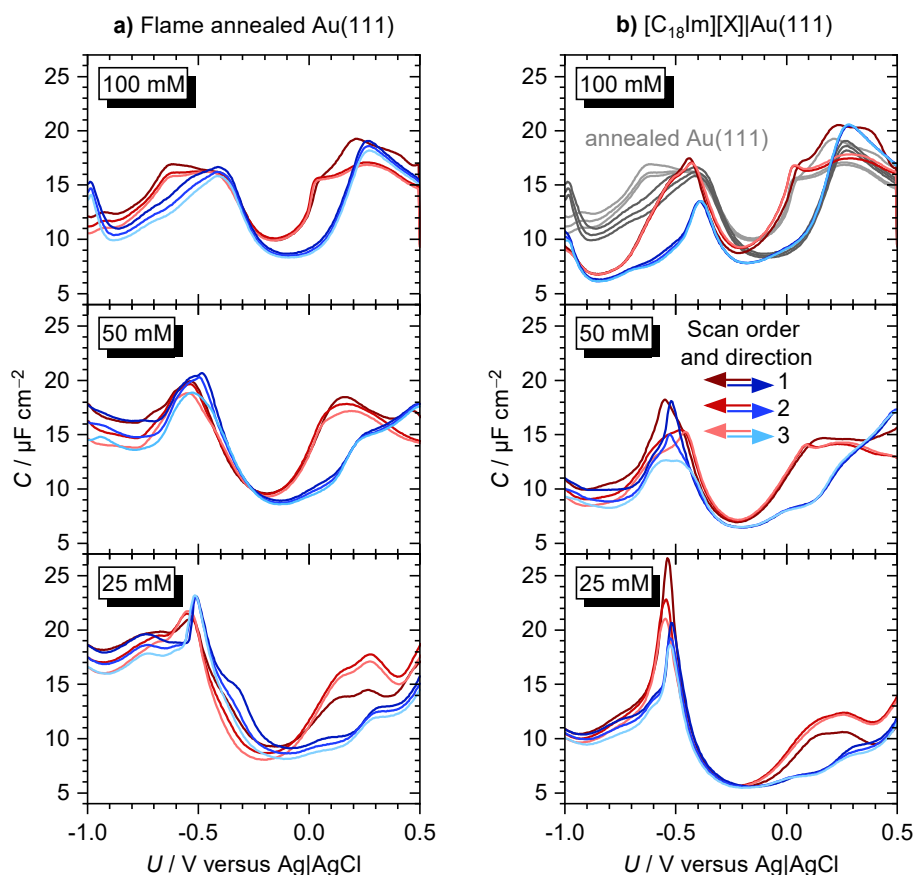
Figure 9.2: Differential capacitance versus potential curves of 25, 50, and 100 mM [C$_2$Im][TfO]$_{(aq)}$ in 0.1 M KClO$_{4(aq)}$ at the Au(111) electrode surface. a) Flame annealed Au(111) electrode. b) Au(111) electrode covered with the [C$_{18}$Im][X] LB monolayer. As marked in the figure, negatively (red lines) and positively (blue lines) going potential scans were recorded for three cycles. Please note that all graphs are shown in the same capacitance magnitude as graphs a) 10 mM, b) 0 mM and b) 10 mM of figure 9.1.

At $U \approx$ -0.6 V, a new feature (4) appears due to the addition of 5 mM [C$_2$Im][TfO]$_{(aq)}$. This feature resembles the pseudo-capacitive peak (6) found for the [C$_{18}$Im][X] monolayer covered systems (Figs 9.1b and 9.2b). In chapters 6 and 7 it was shown that this capacitive feature is accompanied by a huge structural change in the film. Thus, this potential region may represent a sate at which the electrode charge cannot be sufficiently screened by the surface charge density of a densely packed imidazolium-based film, which may be valid for the uncovered Au(111) electrode in [C$_2$Im][TfO]$_{(aq)}$ solution, too.

At concentrations $\geq$ 10 mM [C$_2$Im][TfO]$_{(aq)}$ in 0.1 M KClO$_{4(aq)}$ the electrochemical perchlorate characteristic vanishes completely at the flame

annealed Au(111) electrode surface. Broad features ($\underline{1}$) emerge at 0 V < U < 0.5 V (Fig. 9.1a, 10 mM), and strengthen with increasing electrolyte concentrations (Figs 9.1 and 9.2). The positive capacitance branches of the [C$_{18}$Im][X] monolayer covered Au(111) merge with the corresponding curves of the flame annealed electrode (Fig. 9.2b, 100 mM). However, the negative capacitance branches at -0.2 V < U < −1.0 V differ in these two systems.

Apart from hystereses between positive and negative scans, consecutive scans in the same direction reveal a general decrease in the capacitance, mostly in the negative region ($\underline{5}$). Exclusively for the 10 mM and 25 mM solutions at the flame annealed Au(111) electrode, a pronounced feature at $U \approx$ -0.3 V ($\underline{3}$) lowers and vanishes upon subsequent scans. These findings seem to depend on time or the number of scans rather than on the potential itself. They may tentatively be attributed to a segregation process in the electrolyte solution, in which organic ion rich and deficient phases are formed. In more concentrated IL$_{(aq)}$ solutions, this phenomenon was not observed.[27]

The pseudocapacitive peak ($\underline{6}$), which was attributed to the supramolecular phase transition in the [C$_{18}$Im][X] monolayer on the Au(111) surface (Section 6.5),[P2] changes upon addition of [C$_2$Im][TfO] (Figs 9.1b and 9.2b). The almost 100 mV capacitance hysteresis apparent in the pure 0.1 M KClO$_{4(aq)}$ solution (Fig. 9.1b, 0 mM) is lifted and the peak in the positive potential scan appears at ca ΔU = -0.1 V lower in [C$_2$Im][TfO] containing solutions. Thus, the transition to the ordered state of the monolayer[P2] is shifted to lower potentials. This indicates that the disordered state may be stabilized by the IL molecules from the electrolyte.

For both the flame annealed and [C$_{18}$Im][X] monolayer covered Au(111) surfaces, a camel shape emerges in the $C(U)$ curve with increasing concentrations of [C$_2$Im][TfO]$_{(aq)}$. A pronounced U-shaped valley is seen between the camel-humps ($\underline{2}$). The potentials at the capacitance minima U_{min} and the capacitances are summarized in table 9.2. With increasing c(IL), the minimum is shifted to more negative potentials for both positive (blue) and negative scans (red) for [C$_{18}$Im][X] monolayer covered as well as flame annealed Au(111) electrodes. However, this behavior is not monotonous, but reaches the most negative shift at c(IL) = 50 mM, where it is located at $U_{min} \approx$ -0.2 V for negative scans of both electrode systems and for the positive scan of the monolayer covered electrode. For the flame annealed Au(111) electrode, U_{min} is located ca 0.01 V higher in the positive scans.

Besides the potentials of the capacitance minima, also the capacitances at the minima differ for the two systems. $C(U_{min})$ decreases upon increase in $c(IL)$ at the flame annealed Au(111) electrode from 13 to 8 µF cm^{-2}, indicating surface adsorption of the IL and suppression of the weakly adsorbed perchlorate characteristic. In contrast, $C(U_{min})$ increases from 5 to 8 µF cm^{-2} at the monolayer covered electrode. The minimum capacitance of the film covered system converges with the one of the flame annealed Au(111) surface, which may indicate rearrangements or increasing disorder in the [C$_{18}$Im][X] monolayer.

Table 9.2: Potential and magnitude of capacitance minima in [C$_2$Im][TfO]$_{(aq)}$ + 0.1 M KClO$_{4(aq)}$ electrolytes at flame annealed and [C$_{18}$Im][X] monolayer covered Au(111) surfaces.

| | Flame annealed Au(111) | | [C$_{18}$Im][X] \| Au(111) | |
c(IL) / mM	U_{min} / V	$C(U_{min})$ / µF cm^{-2}	U_{min} / V	$C(U_{min})$ / µF cm^{-2}
		Negative scan		
100	-0.15	9.9	-0.22	8.7
50	-0.19	9.3	-0.23	6.9
25	-0.21	8.1	-0.19	5.6
10	-0.14	8.0	-0.18	4.8
5	-0.03	12.9	-0.13	5.1
		Positive scan		
100	-0.07	8.3	-0.18	7.8
50	-0.13	8.6	-0.20	6.4
25	-0.11	8.1	-0.18	5.5
10	-0.04	8.2	-0.08	4.8
5	0.05	13.4	-0.06	5.4

In general, the data suggest no desorption/dissolution of the [C$_{18}$Im][X] monolayer: The capacitance minima are slightly more negative for the [C$_{18}$Im][X] monolayer covered electrode than for the flame annealed one (Tab. 9.2). In addition, capacitances of the monolayer covered Au(111) surface are ca 5 µF cm^{-2} lower than for the flame annealed Au(111) surface at the most negative potentials (-1.0 V < U < -0.5 V, 5), independently on the [C$_2$Im][TfO]$_{(aq)}$ concentration (Figs. 9.1 and 9.2). If the film or a part of it would desorb, it is likely to be dissolved into the bulk solution and not be re-adsorbed to the electrode surface. Charge compensation at negative potentials could also be achieved by smaller ions from the electrolyte solution. As a result, the $C(U)$ curves of the hypothetically once monolayer covered Au(111) surface should merge completely with the flame annealed

one. Increasing capacitances would also be expected at negative potentials (5) during subsequent scans, which is not the case. Briefly, the electrochemical results suggest that the [C$_{18}$Im][X] monolayer remains adsorbed on the surface. Thus, potential regions of similar capacitive behavior in both systems, flame annealed and monolayer covered Au(111) surfaces, do not originate from the first layer but from layers in between the first layer and the bulk phase.

9.1.2 Discussion of Capacitances Within Electrical Double Layer Theories

According to the classic EDL theories (Section 3.3), the inner layer, and thus its capacitance, is unaffected by change of the electrolyte concentration. Effectively, the much lower diffuse layer capacitance is measured around the PZC at low electrolyte concentrations (Section 3.3.1, Fig. 3.2). At higher concentrations, the diffuse capacitance becomes large. Due to reciprocal addition of capacitances in series, the first layer capacitance dominates the measured capacitance then. Interestingly, the curves measured for the [C$_2$Im][TfO]$_{(aq)}$ + 0.1 M KClO$_{4(aq)}$ | Au(111) systems display a reverse behavior, i.e. an emerging camel-shape behavior with increasing IL concentration, whose explanation is not straight-forward. In the Gouy-Chapman perspective, the nature and size of the individual ions are neglected except for their charge, and the bulk concentration was raised from 0.1 M to 0.2 M. The Gouy-Chapman theory does not describe the apparent behavior. Clearly, in particular for ILs whose ions are generally voluminous, the finite ion size must be accounted for the description of the EDL.

The capacitance minimum is associated with the PZC and found for diluted electrolytes, HTMS, and ILs exhibiting lots of free volume and similar ion size (Section 3.3). Denoting the shape of the $C(U)$ curves with $c(\text{IL}) = 100$ mM as camel-shaped implies that the PZC is found at $C(U_{\min}) \approx$ -0.2 V. In the case of the pure 0.1 M KClO$_{4(aq)}$ solution, the PZC is found at ca 0.3 V.[188] The addition of specifically interacting [C$_2$Im][TfO] molecules may shift the PZC to negative potentials. For example, pyridine was proposed to shift the PZC to markedly more negative potentials.[164] Pyridine is not an IL but an organic and aromatic heterocycle, which is valid for imidazolium-moieties, too. Similarly to the well-known specific adsorption of sulfates on Au surfaces,[155] the sulfonyl group of the triflate anion may interact with the Au(111) surface.

Another reason for the non-Gouy-Chapman behavior of the IL solution system may be an accumulation of the IL beyond the physical laws of electrostatics and thermal randomization. Such phenomena are known from literature: Li et al. proposed a second adlayer for the adsorption of pyridine from 0.1 M NaClO$_{4(aq)}$ solution at the Au(111) interface. Pennathur et al. have shown via IRS that ILs in aqueous solutions strongly accumulate at organic-modified metal surfaces.[226] Results of Beattie et al. indicate a multilayered self-assembly of 1-hexyl-3-methylimidazolium Tf$_2$N onto Au(poly) surfaces from ethanol solution.[129] Time-dependent accumulation phenomena may also explain the decrease in subsequentially scanned capacitances in some potential ranges, which were mentioned above.

As the $C(U)$ curves of the [C$_{18}$Im][X] monolayer covered Au(111) surfaces match greatly at $U >$ -0.5 V with the flame annealed surfaces, these capacitances are most probably not dominated by the first layer on the Au(111) surface. Assuming that the first layer structure and capacitance remain unchanged when increasing the concentration of [C$_2$Im][TfO]$_{(aq)}$ in 0.1 M KClO$_{4(aq)}$, the diffuse capacitance must lower to become visible with its characteristic minimum. The Kornyshev theory incorporates size effects and should in principle be applicable for aqueous solutions, too.[45] For a pure IL, the concentration is strictly coupled to the density of the salt at a given temperature. Thus, it influences both the Debye capacitance (intensity of the central extremum) and the packing parameter (shape of the curve). Practically, both effects may be decoupled in an aqueous solution. Still, maximum ion packing density is responsible for the lattice saturation phenomenon and may not be exceed. However, interactions such as ion-ion correlations or dispersive forces may influence the local concentration close to the interface. The flame annealed Au(111) surfaces may be modified by self-assembly.[129] Next, the propensity of ILs for organic-modified surfaces may increase the local concentration.[226] Thus, the local concentration is not only determined by electrostatic interactions or thermal movement, but also by chemical interactions which are not incorporated into EDL theories. If the C$_2$Im$^+$ and TfO$^-$ ions accumulate at the interface, lattice saturation phenomena may occur differently than predicted by Kornyshev's theory.

The lowest capacitance dominates the general behavior of the system, as capacitances in series add reciprocally. In order to match the theoretical diffuse double layer with the emerging camel-shape in the experiments, its capacitance must lower upon increase in c(IL). Theoretical diffuse layer capacitances for the studied system are calculated in figure 9.3.
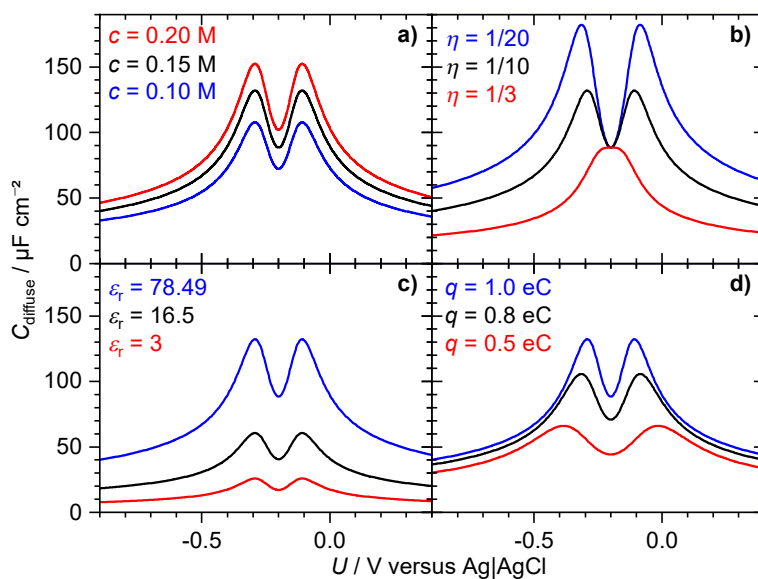
Figure 9.3: Differential capacitance versus potential curves calculated according to Kornyshev's[45] theory. An aqueous solution at room temperature was employed with the PZC at U = -0.2 V. Different parameters were varied: a) concentrations (x M [C$_2$Im][TfO] + 0.1 M KClO$_4$); b) camel-shape yielding packing parameters; c) permittivities (ε_r = 16.5 is the static permittivity of [C$_2$Im][TfO])[227]; d) charge numbers. When not varied, the parameters were: c = 0.15 M, η = 0.1, ε_r = 78.49, and q = 1.0 eC.

Increase in the ion concentration yields generally higher capacitances, when the packing parameter does not change significantly, and thus would not explain the occurrence of a capacitance minimum at higher concentrations (Fig. 9.3a). However, if the packing parameter at a constant concentration changes, the camel humps change with it (Fig. 9.3b). The less dilute the ions are, the more the camel flanks lower. This may lead to the appearance of the capacitance minimum. Moreover, the permittivity of the dielectric continuum was varied (Fig. 9.3c). Accumulation of ions and ordering of molecules severely influence the permittivity in the first and second layers of the EDL.[59] A lower permittivity in the diffuse layer causes tremendously lower capacitances, which also could lead to the appearance of the U-valley in the measured $C(U)$ curves (Figs 9.1 and 9.2). As the relative permittivity of ILs is significantly lower than for water,[43] this would be in line with the strong propensity of ILs for organic-modified metal surfaces mentioned above,[226] and thus the aggregation/accumulation of the IL in the vicinity of the electrode surface. Last, the effective ion charge in the 1:1 electrolyte was modified (Fig. 9.3d). Association, e.g. via H-bonds or dispersive forces, neutralizes a part of the formal charge, as reviewed by Kirchner et al. (Section 2.1).[23, 33] In aqueous solutions, the formal charge of

$q = 1$ eC for a singly charged ion may be reduced significantly. A result of lower effective charge numbers leads to a broader valley and broader camel-humps as well as generally lower capacitances, which are needed to corroborate the measured $C(U)$ curves with theory. Trends which may concur beneficially to describe the experimental curves were colored red in figure 9.3.

Attempts for fitting $C(U)$ curve of the flame annealed Au(111) electrode surface in 0.1 M [C$_2$Im][TfO]$_{(aq)}$ + 0.1 M KClO$_{4(aq)}$ were made in figure 9.4.

Results of the fit:

Full curve:	U_{PZC} =		(-0.148 ± 0.007) V
	η =		0.090 ± 0.006
	ε_r =		15.2 ± 1.5
	q =		(0.243 ± 0.008) eC
Valley only:	U_{PZC} =		(-0.1556 ± 0.0005) V
	η =		$3.6 \cdot 10^{-11} \pm 0.2 \cdot 10^{-11}$
	ε_r =		10.7 ± 0.3
	q =		(0.226 ± 0.003) eC
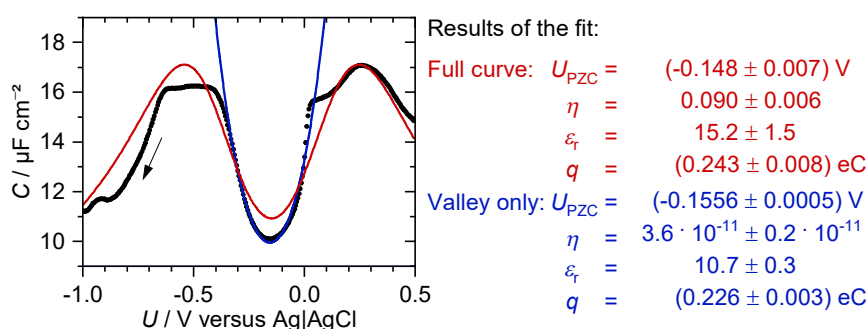
Figure 9.4: Differential capacitance versus potential curve of 0.1 M [C$_2$Im][TfO]$_{(aq)}$ + 0.1 M KClO$_{4(aq)}$ at the flame annealed Au(111) electrode surface (second negative scan from figure 9.2). The curve was fitted with Kornyshev's[45] theory over the whole range (red) and the U-shaped valley only (blue). Please note that these fits yield unphysical values and should not be taken seriously, as mentioned in the text.

This curve was fitted over its whole range (red) and for the U-shaped valley only (blue) with Kornyshev's theory of a 1:1 electrolyte at room temperature in water coarse agreement is only yielded for very low relative permittivities and effective ion charges. When fitting the U-shaped valley only, the packing parameter changes mostly and the overall curve converges with Gouy-Chapman theory. Nevertheless, unphysically low charges in the range of $q \approx 0.2$ eC are required due to the width of the valley for both fits. Also, the permittivities are too low for the dielectric continuum in the diffuse double layer, $\varepsilon_r \approx 11$-15. Note that the measured capacitances are probably not in equilibrium (cf. section 6.3), which may be a general problem for ILs (Section 3.3.3). Some conclusions can be drawn from these unrealistic results:

(i) The assumption that the composition, structure, and capacitance of the first layer do not change with increasing electrolyte concentrations is unlikely to be valid.

(ii) If a classical Stern-layered system is assumed, both diffuse and inner layer capacitances have values which do not diverge by huge

magnitudes. As a result, the measured capacitance reflects both layers.

(iii) The camel humps may originate from purely pseudo-capacitive features, which would impede any application of equilibrium EDL theories.

The deliberations mentioned above may be taken as tentative attempts to explain the unusual appearance of the camel shape with increasing IL concentrations.

9.2 Potential-Driven Reorientations in the Electrical Double Layer

To study the capacitive phenomena of the previous section, in situ PM IRRAS was applied to the [C_{18}Im-d_{42}][X] covered and flame annealed Au(111) electrodes and in 10 mM [C_2Im][TfO]$_{(aq)}$ + 0.1 M KClO$_{4(aq)}$. Different spectral regions elucidate the behavior of the anions, alkyl chains in the film, ring moieties of imidazolium molecules in electrolyte and film, and alkyl groups of the imidazolium molecules in the electrolyte.

9.2.1 Spectroelectrochemical Analysis of the Anions

Triflate, perchlorate, and hydroxide anions are present in the solution. First, the [C_{18}Im-d_{42}][X]|Au(111) system immersed in 10 mM [C_2Im][TfO]$_{(aq)}$ + 0.1 M KClO$_{4(aq)}$ is discussed, because the measurement in an H_2O solvent allows for the observation of important triflate bands. Both triflate and perchlorate anions give discreet signals (Fig. 9.5). Due to the comparably high concentration of KClO$_{4(aq)}$, the ν_{as}(ClO$_4$) band at $\tilde{\nu} \approx 1113$ cm^{-1} dominates the raw (Fig. 9.5a) and background corrected spectra (Fig. 9.5b).[228]

The C_{3v} symmetry of the triflate ion is broken due to chemical interactions (probably mono- or bidentate H-bonds at the sulfonyl group), and thus, the degeneracy of the asymmetric stretching modes is lifted.[229] As a result, two ν_{as}(SO$_3$) bands appear at $\tilde{\nu} \approx 1275$ cm^{-1} and $\tilde{\nu} \approx 1252$ cm^{-1} (Fig. 9.5a,b). In agreement with literature,[27-31] the corresponding ν_s(SO$_3$) band is found at $\tilde{\nu} \approx 1034$ cm^{-1}. The same reasons lead to split ν_{as}(CF$_3$) modes at $\tilde{\nu} \approx 1183$ cm^{-1} and $\tilde{\nu} \approx 1173$ cm^{-1}, leaving the mode at $\tilde{\nu} \approx 1228$ cm^{-1} to be assigned to ν_s(CF$_3$). These assignments confer with the modes in the ATR spectrum of neat

[C2Im][TfO], where corresponding bands are found at: $\tilde{v}$ / cm^{-1} = 1286 − v_{as}(SO$_3$), 1227 − v_s(CF$_3$), 1173 − v_{as}(CF$_3$), 1035 − v_s(SO$_3$).[28-29]
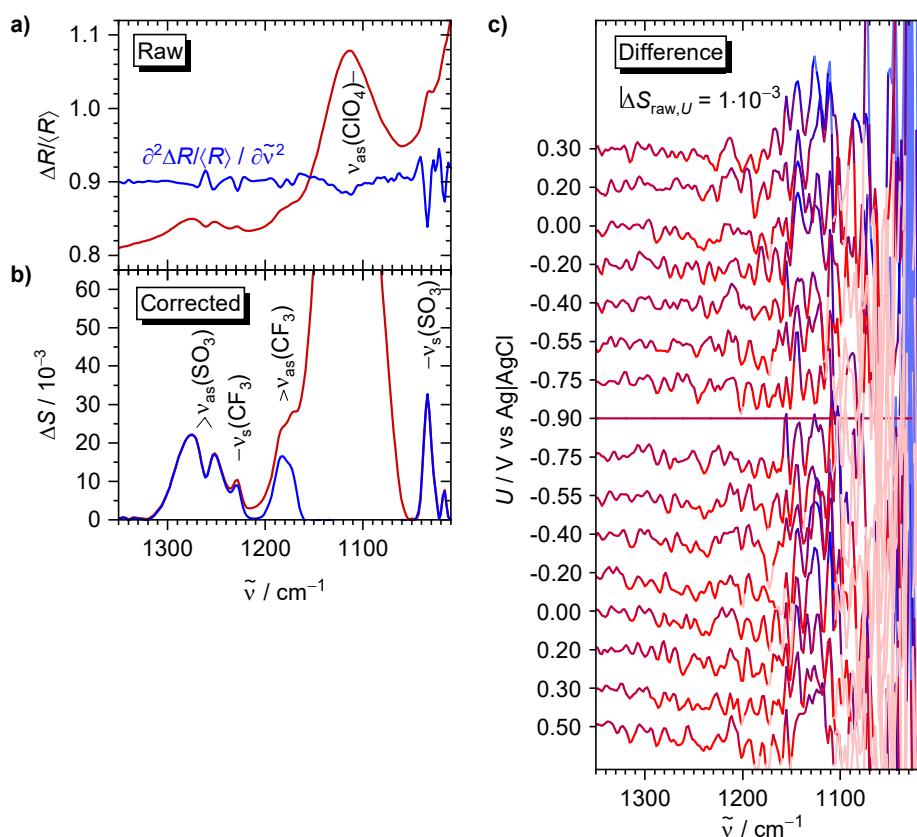
Figure 9.5: In situ PM IRRA spectra of the [C$_{18}$Im-d_{42}][X]|Au(111) system in 10 mM [C$_2$Im][TfO] + 0.1 M KClO$_4$ (H$_2$O) measured at $\tilde{v}_{HWR}$ = 2200 cm^{-1} in the 1350-1010 cm^{-1} spectral region: a) averaged raw spectrum (red) and its magnified and offset second derivative (blue); b) background corrected spectra – water and Bessel function background subtracted (red) and ClO$_4^-$ background subtracted additionally (blue); c) difference spectra referenced to U_{ref} = -0.9 V. Colors in c) correspond to higher (blue) or lower (red) intensities.

Note that some authors may assign the higher wavenumber mode generally to asymmetric stretching vibrations and the lower one to symmetric stretching vibrations.[33-34] Singh et al. assigned the mode at $\tilde{v}$ = 1223 cm^{-1} to the v_{as}(CF$_3$) mode and the band at $\tilde{v}$ = 1147 cm^{-1} to the v_s(CF$_3$) mode,[33] and this assignment was propagated by co-authors Kiefer et al. in a second paper.[34] This disagrees with early HF calculations, e.g. by Huang et al.[229] Besides calculations, the latter also deduced that a single and degenerate v_{as}(CF$_3$) mode cannot appear with two v_s(CF$_3$) modes, because the latter would require two differently coordinated triflate ions which in turn must lead to more than one v_{as}(CF$_3$) modes. I reproduced the harmonic

frequency calculation on the level of theory of Singh et al.[33] (ωB97x-D/6-311++G(d,p)) and found that the DFT calculation itself is consistent with HF calculations by Huang et al.[229] as well as the experimental observations of two ν_{as}(CF$_3$) modes resonating at lower wavenumbers than the single ν_s(CF$_3$) mode.

The ν_{as}(SO$_3$) band at $\tilde{\nu} \approx 1275$ cm^{-1} is to be broader than the second ν_{as}(SO$_3$) band at $\tilde{\nu} \approx 1252$ cm^{-1} (Fig. 9.5b), and therefore another mode may be convoluted there. Cui et al. investigated mixtures of water and [C$_2$Im][TfO] up to 70 vol% water.[27] Upon increase in the water volume fraction, the single ν_{as}(SO$_3$) band appearing at $\tilde{\nu} \approx 1250$ cm^{-1} started to split into at least two bands located at $\tilde{\nu} \approx 1252$ cm^{-1} and $\tilde{\nu} \approx 1276$ cm^{-1}, which is in agreement with the modes shown in figure 9.5a,b. Cui et al. reasoned that the band at $\tilde{\nu} \approx 1276$ cm^{-1} may appear due to the formation of triflic acid,[27] which can explain the broad feature around $\tilde{\nu} \approx 1275$ cm^{-1} found in this work, too. In addition, they showed that the mixture becomes more acidic upon increasing water fraction.[27]

Difference spectra in figure 9.5c show that potential-dependent changes in the anion intensities are negligible. The lack of potential-dependent changes suggests that the measured spectra are dominated by anions from the solution phase in comparison to anions which are possibly adsorbed at the Au(111) surface. Moreover, the spectral noise increases tremendously at $\tilde{\nu} < 1200$ cm^{-1} due to increasing IR absorption of the CaF$_2$ prism window of the in situ PM IRRAS cell.[230] Consequently, the ν_s(SO$_3$) band at $\tilde{\nu} \approx 1034$ cm^{-1} is only observed for averaged spectra but not for single potential scans.
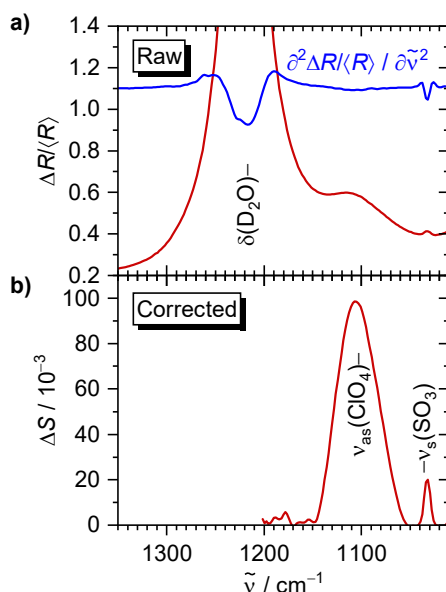
Figure 9.6: In situ PM IRRA spectra of the flame annealed Au(111) electrode in 10 mM [C₂Im][TfO] + 0.1 M KClO₄ (D₂O) measured at $\tilde{\nu}_{HWR} = 1600$ cm⁻¹ in the 1350-1010 cm⁻¹ spectral region: a) averaged raw spectrum (red) and its magnified and offset second derivative (blue); b) background corrected spectra.

The $\nu_s(SO_3)$ band at $\tilde{\nu} \approx 1032$ cm⁻¹ and $\nu_{as}(ClO_4)$ band at $\tilde{\nu} \approx 1106$ cm⁻¹ are also seen in spectra recorded from the flame annealed Au(111) electrode in in 10 mM [C₂Im][TfO]₍aq₎ + 0.1 M KClO₄₍aq₎ (Fig. 9.6). In contrast to the spectra discussed above, these spectra were recorded in D₂O and not in H₂O. The strong $\delta(D_2O)$ band at $\tilde{\nu} = 1219$ cm⁻¹ impedes the analysis of other modes in this region.

9.2.2 Spectroelectrochemical Analysis of the Alkyl Chains in the Monolayer

Potential-dependent PM IRRA spectra of the alkyl chains in the perdeuterated C₁₈Im-d_{42}⁺ cations on the Au(111) surface immersed in 10 mM [C₂Im][TfO]₍aq₎ + 0.1 M KClO₄₍aq₎ are shown in figure 9.7.

As for raw spectra in 0.1 M KClO₄₍aq₎ (cf. section 7.4), changes are hard to see in the measured spectra (Fig. 9.7a). The background-corrected spectra (Fig. 9.7b) reveal several bands, which are assigned based on the results described in chapter 7: $\tilde{\nu}$ / cm⁻¹ = 2217 – $\nu_{as}(CD_3)$, 2197 and 2181 – $\nu_{as}(CD_2)$, 2091 – $\nu_s(CD_2)$. Due to low intensities ($\Delta S \leq 2 \cdot 10^{-3}$) and a difficult background correction, difference spectra are shown for assurance (Fig. 9.7c).
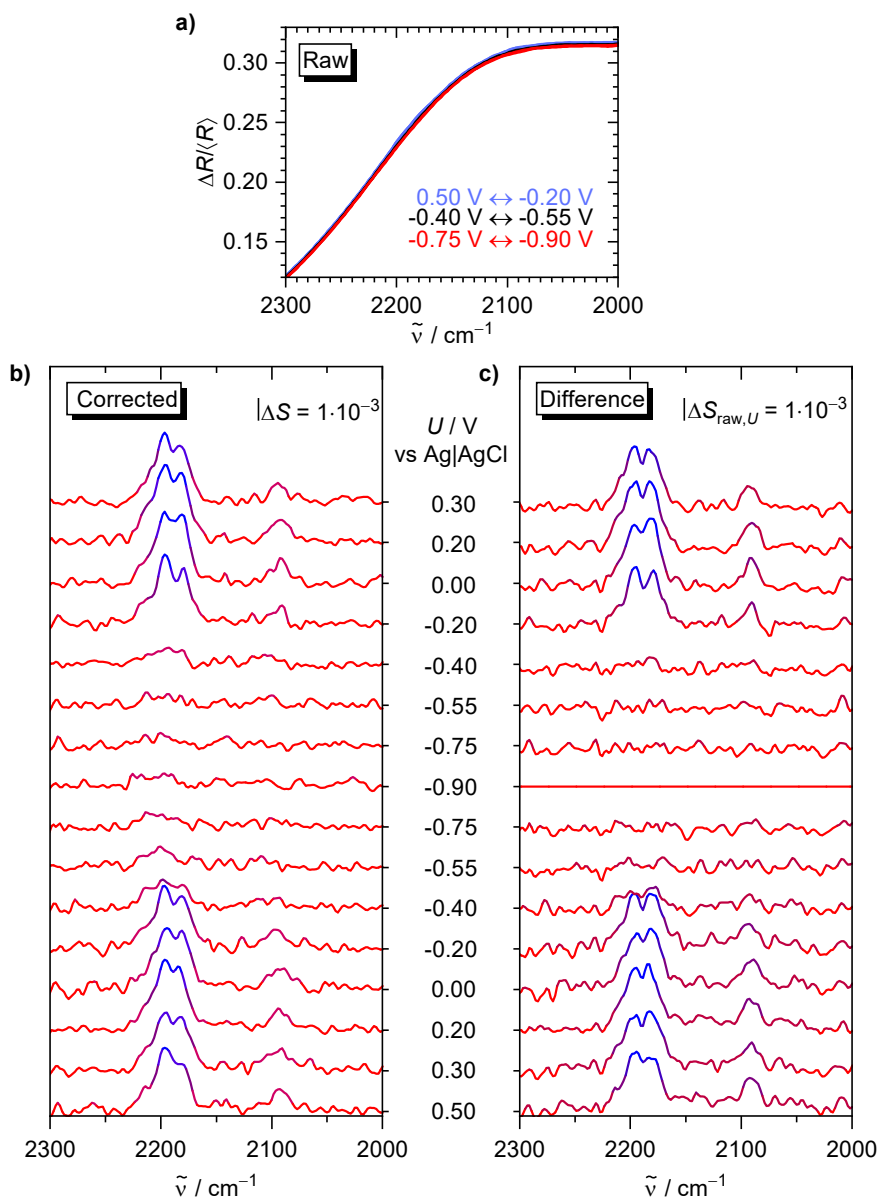
Figure 9.7: In situ PM IRRA spectra of the [C$_{18}$Im-d_{42}][X] monolayer on Au(111) in 10 mM [C$_2$Im][TfO] + 0.1 M KClO$_4$ (H$_2$O) measured at $\tilde{\nu}_{HWR}$ = 2200 cm^{-1}. a) Raw spectra with potential ranges applied to the Au(111) electrode as indicated in the figure. b) Background corrected spectra. c) Difference spectra of raw signals. Colors in b) and c) correspond to higher (blue) or lower (red) intensities.

When immersed in 10 mM [C$_2$Im][TfO]$_{(aq)}$ + 0.1 M KClO$_{4(aq)}$, the alkyl chains in the perdeuterated C$_{18}$Im-d_{42}^+ cations on the Au(111) surface show a similar behavior in absence of [C$_2$Im][TfO]$_{(aq)}$ in the electrolyte solution (cf. section 7.4): At positive and moderately negative potentials, both ν_{as}(CD$_2$) bands are strong, but at negative potentials they vanish. In the same matter

the $\nu_s(CD_2)$ band, which is weak at positive potentials, cannot be distinguished from the background noise at negative potentials.

Symmetric and asymmetric $\nu(C(4,5)-D_2)$ stretching modes of the imidazolium ring are expected to appear at $\tilde{\nu} \approx 2386$ cm^{-1} and $\tilde{\nu} \approx 2345$ cm^{-1}, respectively.[151, 175] In the spectra of this experiment, these modes could not be observed due to insufficient CO_2 compensation.

9.2.3 Spectroelectrochemical Analysis of the Imidazolium Ring Moieties

C_2Im^+ cations give rise to in-plane ring stretching modes.[151, 175] Due to less complexity, in situ PM IRRA spectra of the flame annealed Au(111) electrode in 10 mM [C_2Im][TfO]$_{(aq)}$ + 0.1 M KClO$_{4(aq)}$ are discussed first (Fig. 9.8a).
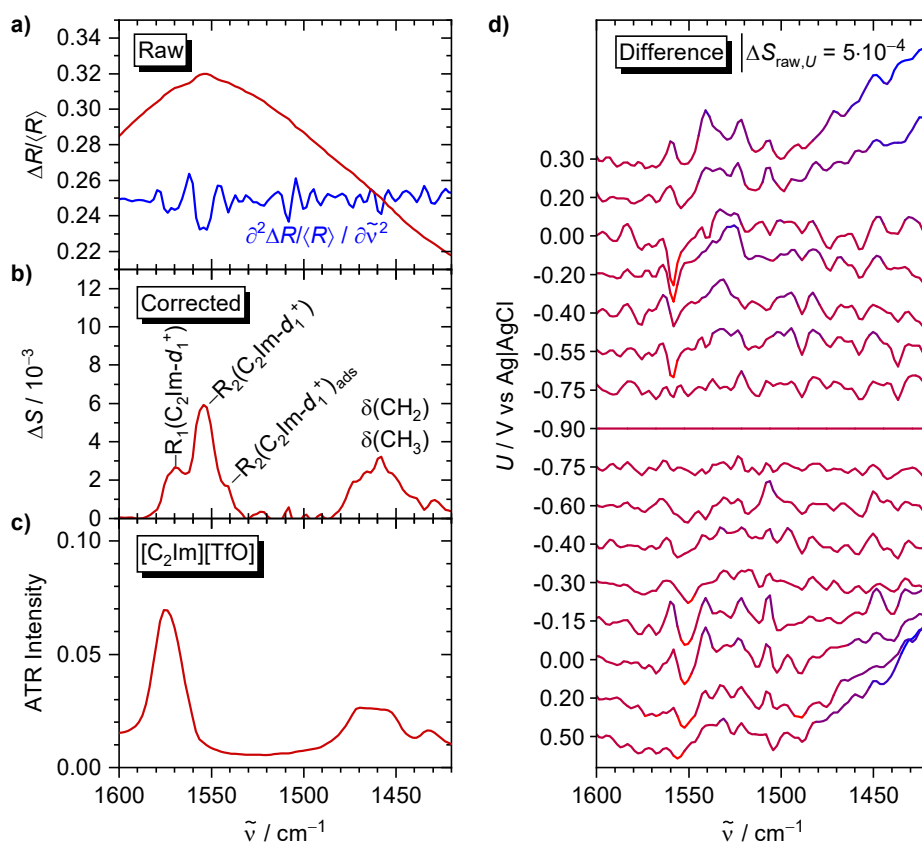
Figure 9.8: IR spectra of in-plane imidazolium ring modes and alkyl deformation modes in the 1600-1420 cm^{-1} spectral region. a,b,d) In situ PM IRRA spectra of the flame annealed Au(111) electrode in 10 mM [C_2Im][TfO] + 0.1 M KClO$_4$ (D$_2$O) measured at $\tilde{\nu}_{HWR} = 1600$ cm^{-1}: a) averaged raw spectrum (red) and its magnified and offset second derivative (blue); b) background corrected spectrum; d) difference spectra referenced to $U_{ref} = -0.9$ V. Colors in d) correspond to higher (blue) or lower (red) intensities. c) ATR spectrum of the neat [C_2Im][TfO] liquid.

The imidazolium ring stretching modes, R_1 and R_2, are clearly distinguished from the background in the raw spectrum (Fig. 9.8a). The background corrected spectra (Fig. 9.8b) reveal at least two modes at $\tilde{\nu}$ = 1571 cm^{-1} (medium) and $\tilde{\nu}$ = 1554 cm^{-1} (strong). In comparison to the ATR spectrum of neat [C$_2$Im][TfO] (Fig. 9.8c), these modes underwent a significant bathochromic shift ($\tilde{\nu} \approx 1575$ cm^{-1}).

In an H$_2$O solution of [C$_2$Im][TfO], Brummel et al. observe the stronger in plane ring stretching mode at $\tilde{\nu}$ = 1574 cm^{-1},[30] which is in contrast to the modes observed in this work. However, a D$_2$O solution was employed here. Depending on the degree of deuteration at the imidazolium ring, different resonance frequencies are expected for the concerning modes, as summarized in table 9.3. Clearly, the intensity ratio and wavenumber positions of the measured R_1 and R_2 modes indicate, that H/D exchange occurred at the C(2)-H group of the C$_2$Im$^+$ cation. This group is prone to H/D exchange and it may readily occur in diluted D$_2$O solutions within 20 min at room temperature, whereas the exchange at C(4,5)-H$_2$ groups requires more than a week at 100 °C.[151] Therefore, the C$_2$Im$^+$ cation in D$_2$O solutions is denoted as C$_2$Im-d_1^+ in the following.

Table 9.3: Imdazolium-related resonance frequencies of [C$_2$Im][Tf$_2$N] fundamentals according to Lassègues, Grondin, et al.[151, 175-177]

Mode	C$_2$Im$^+$	C$_2$Im-d_1^+ (C2)	C$_2$Im-d_2^+ (C4,C5)	C$_2$Im-d_3^+ (C2,C4,C5)
ν_s(C4,5-H$_2$)	3161*	3173 s		
ν_{as}(C4,5-H$_2$)	3161*	3151 s		
ν(C2-H)	3161*		3160 s	
ν_s(C4,5-D$_2$)			2386 w	2385 w
ν_{as}(C4,5-D$_2$)			2345 m	2354 s
ν(C2-D)		2350 s		2345 s
R_1	1576 m	1570 w	1568 w	1519 w
R_2	1568 m	1551 s	1524 s	1546 s

* unresolved band

A weak mode at $\tilde{\nu} \approx 1541$ cm^{-1} does certainly not originate from C$_2$Im-d_3^+ species, but may tentatively be assigned to a ring mode of C$_2$Im-d_1^+ adsorbed on Au(111) in a nonplanar orientation. On the other hand, it could originate from background noise (water vapor, cf. Fig. 6.7). Besides the in-plane ring modes, alkyl deformation modes are observed in the expectable range of 1480 cm$^{-1} < \tilde{\nu} < 1440$ cm^{-1}.[151] Difference spectra reveal no significant potential dependent changes in the observed bands, apart from a broad background variation at lower wavenumbers (Fig. 9.8d).

Assignments are similar for the $[C_{18}Im\text{-}d_{42}][X]$ monolayer covered Au(111) surface immersed in 10 mM $[C_2Im\text{-}d_1][TfO]_{(aq)}$ + 0.1 M $KClO_{4(aq)}$ (Fig. 9.9). The $C_2Im\text{-}d_1^+$ cation gives rise to the same modes as mentioned above: $\tilde{\nu}$ / cm^{-1} = 1571 – R$_1$, 1554 – R$_2$, 1480 < $\tilde{\nu}$ < 1440 – $\delta(CH_3)$ and $\delta(CH_2)$. The strikingly new feature is the band at $\tilde{\nu} \approx 1541$ cm^{-1}, which may have a shoulder on the lower wavenumber flank. In agreement with the experimental and theoretical results by Lassègues, Grondin, et al.,[151, 175-177] this mode originates from a completely deuterated imidazolium ring (Tab. 9.3). Under the experimental conditions, this may only be generated by substitution of the C(2)-H by D in the $C_{18}Im\text{-}d_{42}^+$ cation, leading to the formation of the completely perdeuterated $C_{18}Im\text{-}d_{43}^+$ molecule. The undoubted appearance of this band supports the weak spectral indication of the imidazolium rings in the $[C_{18}Im][X]$ film, which are supposedly non-flat oriented on the Au(111) surface (Section 6.4.1).
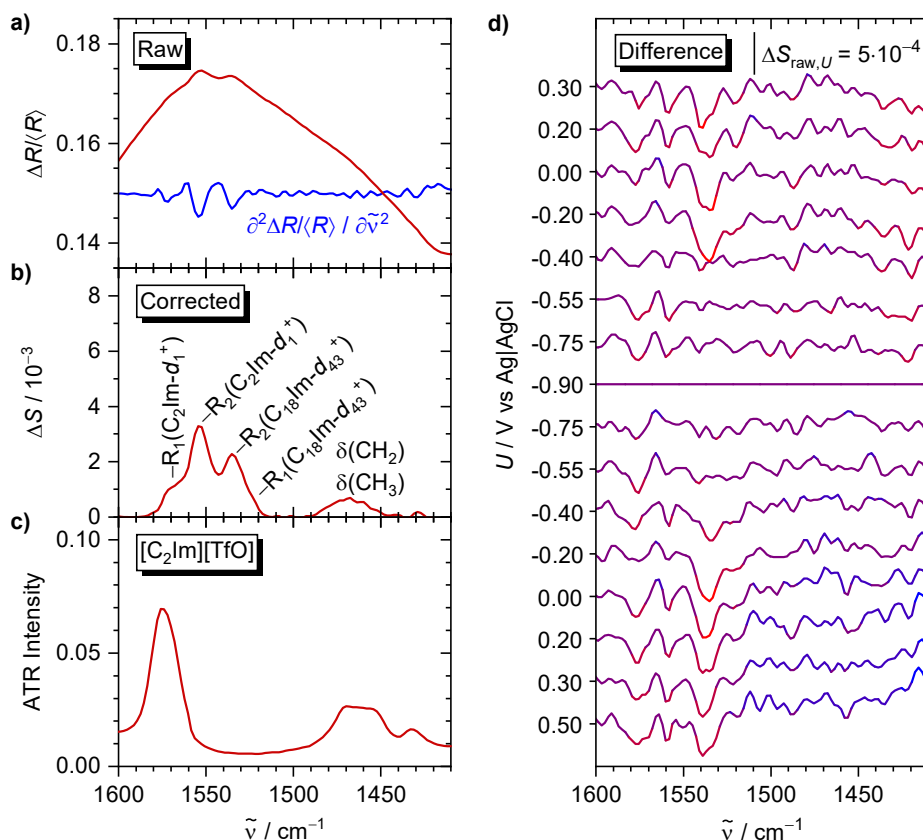
Figure 9.9: IR spectra of in-plane imidazolium ring modes and alkyl deformation modes in the 1600-1420 cm^{-1} spectral region. a,b,d) In situ PM IRRA spectra of the [C$_{18}$Im-d_{42}][X] monolayer on Au(111) in 10 mM [C$_2$Im-d_1][TfO] + 0.1 M KClO$_4$ (D$_2$O) measured at $\tilde{\nu}_{HWR}$ = 3000 cm^{-1}:§ a) averaged raw spectrum (red) and its magnified and offset second derivative (blue); b) background corrected spectrum; d) difference spectra referenced to U_{ref} = -0.9 V. Colors in d) correspond to higher (blue) or lower (red) intensities. c) ATR spectrum of the neat [C$_2$Im][TfO] liquid.

As in absence of the [C$_{18}$Im-d_{43}][X] monolayer, the difference spectra show no significant potential-dependent changes in this region. For both imidazolium compounds this means that neither the (surface) concentrations nor the orientation of the ring moieties change. This agrees with own studies (Section 6.4.1)[P2] as well as results from Motobayashi et al.[111] The scenario that variations in the orientation may compensate changing concentrations is unlikely.

---

§ This experiment was also conducted at $\tilde{\nu}_{HWR}$ = 1600 cm^{-1}, which is more suitable for the analysis of this region. Indeed, this experiment yielded larger intensities of the observed modes. However, the spectra were perturbed by noise of ill-compensated water vapor, which is why the spectra at $\tilde{\nu}_{HWR}$ = 3000 cm^{-1} are shown. Apart from intensities and noise, no further differences are noticeable.

9.2.4 Spectroelectrochemical Analysis of the CH Groups in the Electrolyte

Whereas no significant potential-dependent changes were observed for the anions or ring groups, the CH groups of the C_2Im-$d_1{}^+$ display interesting potential-driven changes, which differ in both the flame annealed and $[C_{18}Im$-$d_{43}][X]$ monolayer covered Au(111) electrode surfaces. Unfortunately, the background correction for the alkyl moieties was too difficult to be executed without major operator-imposed errors, due to the steep D_2O background in both systems. In theses cases, the second derivative spectra of the averaged spectra as well as the difference spectra become extraordinary useful.

First, the $[C_{18}Im$-$d_{43}][X]$ monolayer covered Au(111) electrode surface in 10 mM $[C_2Im$-$d_1][TfO]_{(aq)}$ + 0.1 M $KClO_{4(aq)}$ is analyzed (Fig. 9.10). No discreet mode can be observed in the averaged raw PM IRRA spectrum (Fig. 9.10a). Its second derivative reveals some modes. Symmetric and asymmetric $\nu(C4,5$-$H_2)$ modes of the C_2Im-$d_1{}^+$ cations are expected at $\tilde{\nu} \approx 3173$ cm^{-1} and $\tilde{\nu} \approx 3151$ cm^{-1}, respectively (Tab. 9.3). However, they were not observed (Fig. 9.10a). Cui et al. investigated mixtures of $[C_2Im][TfO]$ and water.[27] Evidently, the absorbance of the ring CH modes decrease greatly when increasing the water fraction. Consequently, these modes become weak and hard to detect in a dilute solution via IR and Raman spectroscopies. Furthermore, the resonance frequencies of modes in the 2700 cm^{-1} < $\tilde{\nu}$ < 3050 cm^{-1} spectral region were shown to be insensitive to dilution of $[C_2Im][TfO]$ in water,[27-28, 220] which facilitates the band assignment.

D/H-exchange of the aromatic C(2)-H group should not affect the aliphatic $\nu(CH)$ modes significantly.[174] Modes indicated by the second derivative (Fig. 9.10a) are assigned based on the anharmonic frequency calculations (Chapter 8) and located at: $\tilde{\nu}$ / cm^{-1} = 2960 – $\nu_s(N$-$CH_3)$ and $\nu_{as}(C$-$CH_3)$, 2924 – $2\delta(CH_2CH_3)$, 2904 – $\delta(CH_2CH_3)$ + $\delta(CH_2CH_3)$, 2873 – $2\delta_{as}(N$-$CH_3)$, 2854 – $2\delta_{as}(C$-$CH_3)$, and tentatively 2834 – $2\delta_s(N$-$CH_3)$. Interestingly, not all of these modes respond in the same manner to changing potentials. Whereas stretching fundamentals of the ethyl chain remain invariant, intensities of FR overtone and combination modes located at $\tilde{\nu}$ = 2924, 2904, and 2854 cm^{-1} decrease upon scanning from positive to negative potentials (Fig. 9.10c). No changes are observed for the $\nu_s(N$-$CH_3)$ and $2\delta_{as}(N$-$CH_3)$ modes at $\tilde{\nu}$ = 2960 and 2873 cm^{-1}, which are indicated by reference lines in the graph. Following, potential-driven changes affect the ethyl chain in the

$C_2Im\text{-}d_1^+$ cation, but not the CH groups of the ring or the $N\text{-}CH_3$ group. Background changes of D_2O in the lower wavenumber region complicate the studies ($\tilde{v} < 2900$ cm^{-1}). The difference spectra may indicate a potential or time dependence in the water background.
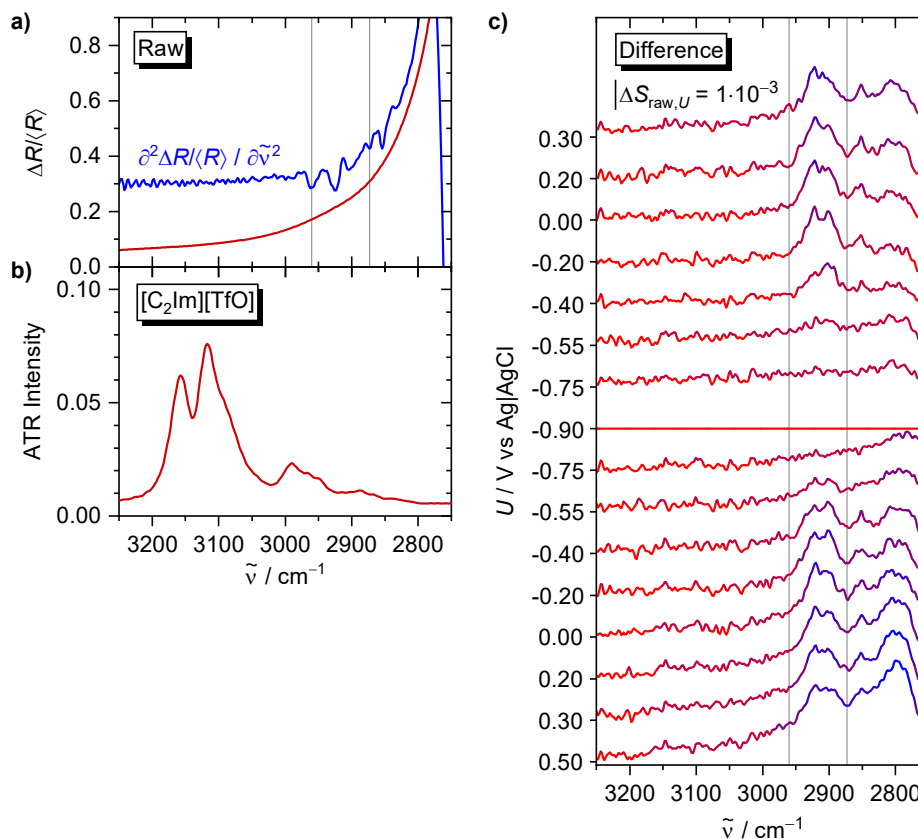
Figure 9.10: IR spectra of CH stretching modes in the 3250-2750 cm^{-1} spectral region. a,b,d) In situ PM IRRA spectra of the $[C_{18}Im\text{-}d_{43}][X]$ monolayer covered Au(111) in 10 mM $[C_2Im\text{-}d_1][TfO]$ + 0.1 M KClO$_4$ (D$_2$O) measured at $\tilde{v}_{HWR} = 3000$ cm^{-1}: a) averaged raw spectrum (red) and its magnified and offset second derivative (blue); c) difference spectra referenced to U_{ref} = -0.9 V. Colors in c) correspond to higher (blue) or lower (red) intensities. b) ATR spectrum of the neat $[C_2Im][TfO]$ liquid.

The flame annealed Au(111) electrode surface in 10 mM $[C_2Im\text{-}d_1][TfO]_{(aq)}$ + 0.1 M KClO$_{4(aq)}$ yields different results (Fig. 9.11). At $\tilde{v} \approx 3176$ cm^{-1} and $\tilde{v} \approx 3153$ cm^{-1} two bands appear (Fig. 9.11a,b), which can be assigned to symmetric and asymmetric $v(C4,5\text{-}H_2)$ modes of the $C_2Im\text{-}d_1^+$ cations (Table 9.3). The background correction was difficult and corrected spectra should not be interpreted quantitatively (Fig. 9.11b,c). Nevertheless, the difference spectra show interesting potential-dependent changes (Fig. 9.11d), and the background corrected spectra visualize them (Fig. 9.11c). Upon scanning to negative potentials, the most prominent

change is an intensity decrease of the $\delta(CH_2CH_3) + \delta(CH_2CH_3)$ combination band at $\tilde{\nu} \approx 2905$ cm^{-1}. In contrast, $2\delta(CH_2CH_3)$ and $2\delta_{as}(C\text{-}CH_3)$ overtone bands at $\tilde{\nu} \approx 2924$ cm^{-1} and $\tilde{\nu} \approx 2854$ cm^{-1}, respectively, increase slightly in intensity.
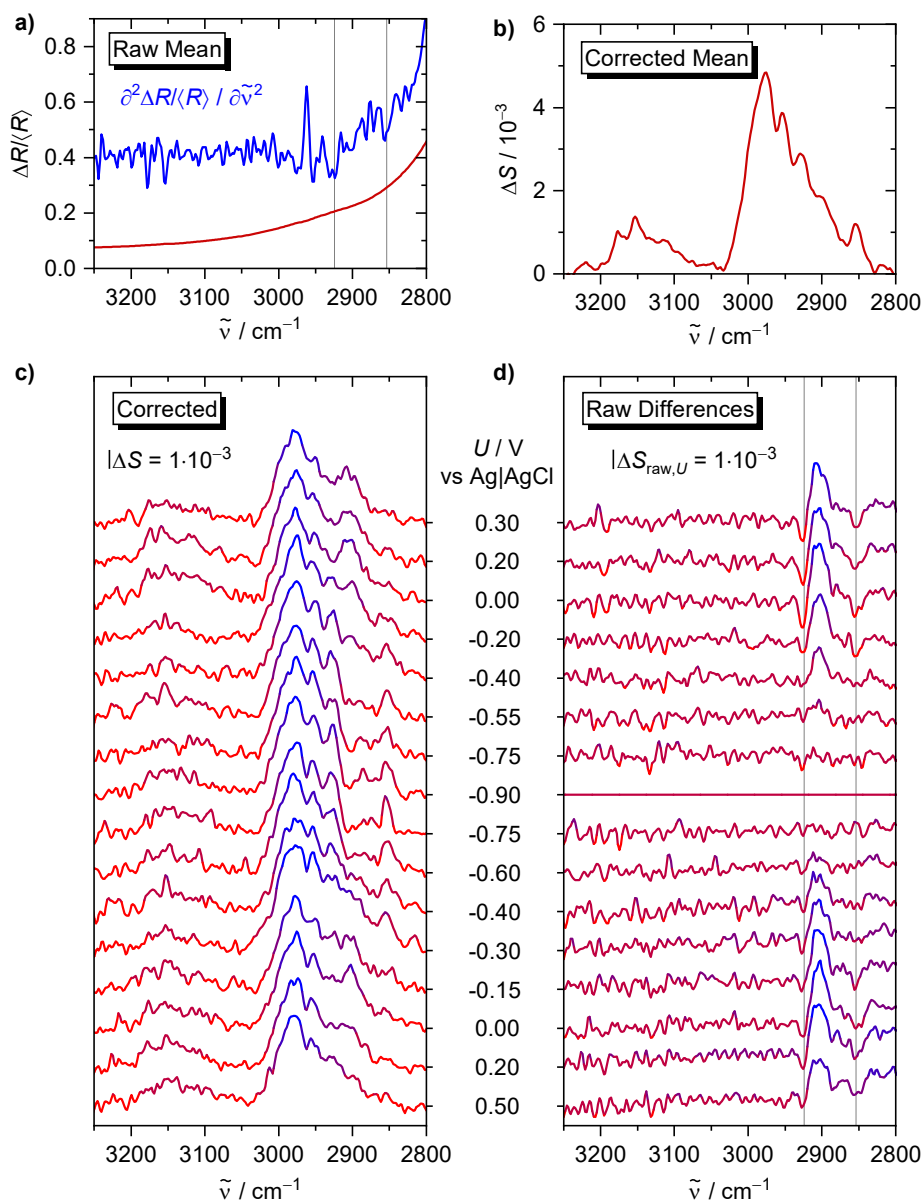
Figure 9.11: In situ PM IRRA spectra of the flame annealed Au(111) electrode surface in 10 mM [C$_2$Im-d_1][TfO] + 0.1 M KClO$_4$ (D$_2$O) measured at $\tilde{\nu}_{HWR} = 3000$ cm^{-1}: a) averaged raw spectrum (red) and its magnified and offset second derivative (blue); b) background corrected mean signal; c) background corrected spectra; d) raw difference spectra referenced to $U_{ref} = -0.9$ V. Colors in d) correspond to higher (blue) or lower (red) intensities. Due to the difficult and uncertain background correction, spectra in b) and c) may not be interpreted quantitatively.

All of these changing FR modes involve the C-CH$_3$ group, suggesting that particularly this sub-molecular segment is prone to potential-dependent changes.

9.3 Deductions for the Electrical Double Layer in Aqueous Ionic Liquid Solutions

Previous potential-dependent investigations indicate a complex EDL structure for [C$_2$Im][TfO]$_{(aq)}$ + 0.1 M KClO$_{4(aq)}$ solutions at flame annealed and [C$_{18}$Im][X] monolayer covered Au(111) electrode surfaces.

In capacitance-potential curves a minimum is formed in between two camel humps upon increase in [C$_2$Im][TfO]$_{(aq)}$ concentration in 0.1 M KClO$_{4(aq)}$. This behavior is found for uncovered and monolayer covered Au(111) surfaces and contrasts with classical aqueous electrolytes, whose capacitance minimum at the PZC is formed upon decrease of ionic strength. Attempts to explain this non-Gouy-Chapman behavior of the aqueous IL solution with Kornyshev's theory resulted in unphysical values of the continuum permittivity or ionic charge. Consequently, the shape of the $C(U)$-curves cannot be explained by considering merely electrostatic interactions, thermal randomization, or ion size (lattice saturation) effects. Time-dependent features hint for a slow segregation process within the solution. $C(U)$-curves of flame annealed and monolayer covered Au(111) surfaces merge at positive potentials with in increasing IL concentrations, which indicates that not the closest layer to the electrode surface dominates the measured capacitance.

In situ PM IRRAS studies reveal that the addition of 10 mM [C$_2$Im][TfO]$_{(aq)}$ to 0.1 M KClO$_{4(aq)}$ does not affect the [C$_{18}$Im-d_{43}][X] monolayer on the Au(111) electrode surface significantly. Similarly to the perchlorate anion, the triflate anion is chaotropic.[211, 231-233] Band characteristics and potential-dependent changes as found and interpreted in chapters 6 and 7 match. Moreover, in situ spectra confirm the presence of characteristic anion modes. Their signals were independent of the applied potential, and thus indicate neither reorientations nor concentration changes within the sensitivity of measurement. The same is valid for imidazolium ring stretching vibrations in the cations. For both uncovered and [C$_{18}$Im-d_{43}][X] monolayer covered Au(111) electrode surfaces, the resonance frequencies of the ring stretching

modes revealed a H/D-exchange in D_2O at the C(2) position, which agrees with literature.[151] In accordance with the ring modes, CH stretching fundamentals of both aromatic and aliphatic groups do not change as a function of the applied potential in the cation. This indicates a stiff, potential-independent orientation of C_2Im-d_1^+ cations in the vicinity of the electrode surface. Note that changes in (surface) concentrations or molecular orientations still may occur beyond the limits of noise and PM IRRAS sensitivity.

Despite that the ethyl chain in the C_2Im-d_1^+ cation is very short, and thus not prone to aggregation or segregation phenomena known for $C_{n>3}Im^+$-based ILs,[21-22] interesting spectral changes are observed for its FR modes. Bending overtone and combination bands related to the methyl group of the ethyl moiety clearly respond to the electric potential. These responses cannot originate from a nonplanar to planar conformation change (chapter 8), molecular reorientation, or concentration changes, as these causes must affect much more modes. Nevertheless, FR modes are sensitive to intra- and intermolecular interactions.[178, 222] Without conformational changes, intramolecular effects remain invariant. On the other hand, intermolecular interactions may change along with the EDL structure depending on the potential. In a combined theoretical and experimental study, Singh et al. suggested that C_2Im^+ and TfO^- ions form small clusters with a water-free domain even in highly diluted $[C_2Im][TfO]_{(aq)}$ solutions.[220] Variations in the electric field at the Au(111) surface may perturb local concentrations of different species. In the present study, cations (C_2Im-d_1^+, K^+, H_3O^+), anions (ClO_4^-, TfO^-, HO^-), or neutral water molecules may enrich or deplete, interact stronger or weaker with each other, or reorient in the EDL as a response to potential changes. As a result, C_2Im-d_1^+ cations present in the EDL may perceive different chemical environments with changing electrode potentials, which is observed by the methyl FR modes. The FR band alterations occur for the same modes in both uncovered and $[C_{18}Im$-$d_{43}][X]$ monolayer covered Au(111) electrode surfaces, but differ with respect to intensity gain and losses in both systems. This indicates a pronounced effect of the interfacial layer, and that primary C_2Im-d_1^+ cations in it (flame annealed surface) or close to it ($[C_{18}Im$-$d_{43}][X]$ monolayer covered surface) are affected. Hitherto, no further explanations for molecular scale causes of the FR band changes can be given and additional studies are required.

An attempt to describe the coarse structure of the EDL at the x mM $[C_2Im][TfO]_{(aq)}$ + 0.1 M $KClO_{4(aq)}$ | Au(111) interface is given in figure 9.12.
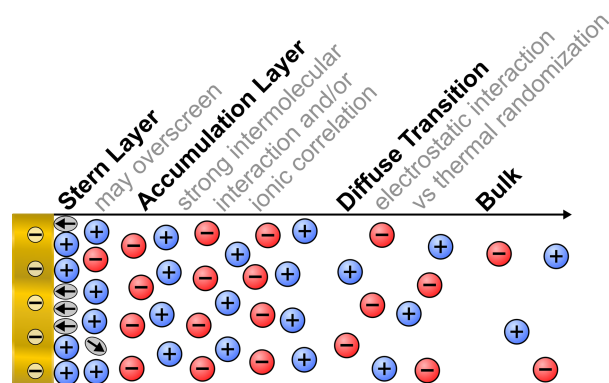
Figure 9.12: Proposed three layer model to describe the EDL of diluted ILs. White space may be occupied by solvation shells, unoriented solvent dipoles, or voids.

Ions may adsorb specifically and nonspecifically in the Stern layer along with oriented solvent molecules. Multilayering and charge oscillations are not incorporated into Kornyshev's theory,[45] but are clearly present in both pure and diluted ILs.[27, 76, 81] On the other hand, water was found to weaken interactions of cations and anions in ILs, and less (or less strongly associated layers with undetectable rupture forces) are found.[27, 81] Nevertheless, ILs exhibit a "strong propensity […] in their aqueous solutions for an organic-modified surface"[226] and may self-assemble in multilayers on gold.[129] The in situ PM IRRA spectra show that intermolecular interactions may significantly affect the first and closely following layers. Thus, after the Stern layer the formation of an accumulation layer is proposed. Here, the ion distribution may depend on many factors, e.g. ion-ion correlations or, intermolecular interactions of so far unspecified nature. If the accumulation layer does not screen the electrode charge completely, it may be followed by a diffuse layer transition into the bulk, which is governed by the classical Gouy-Chapman behavior in terms of electrostatic interaction and thermal randomization, only.

10 Conclusion and Outlook

Different methods were applied to study the structure and potential-driven changes of amphiphilic ionic liquids at various interfaces. Structure, order, and composition of IL monolayers were shown to affect their interfacial properties.

First, films of ILs with short, more environmentally friendly, perfluorinated alkyl chain segments were studied.[P1] Monolayers of fluorinated ionic liquids (bis(1*H*,1*H*,2*H*,2*H*-perfluorooctyl)- imidazolium, 1,2,3-triazolium, and 1,2,4-triazolium triflates) were formed by the LB technique. These FILs were examined on both pure water and 1 M NaCl$_{(aq)}$ subphases. Whereas compression isotherms on the water subphase were ill-defined and badly reproducible, the addition of NaCl electrolyte lead to reproducible and well-defined results. Some of the above-mentioned compounds melt at $T_m > 100\,°C$, and thus cannot be strictly defined as ILs.[8] However, inverse compressibility moduli of all studied amphiphilic ILs revealed a wide 2D liquid-like state when spread in (sub-)monolayer coverages at the air∣aqueous solution interface. Upon compression, Im^{F+}- and 1,2,4-Tria$^+$-based films reach the monolayer collapse in the liquid-like state. In contrast, the 1,2,3-Tria$^+$-based monolayer exhibits a phase transition to a solid-like structure, in which it finally collapses. This interesting difference within the studied azolium-based ILs is attributed to H-bonding interactions with the CH group located in α-position with respect to two neighboring and substituted N atoms, which is absent in the 1,2,3-Tria$^+$ cation. For further analysis, the FIL monolayers were transferred from pure water and 1 M NaCl$_{(aq)}$ subphases onto polycrystalline gold substrates. Next, the deposited monolayers were characterized by XPS. The analysis revealed that triflate anions were exchanged by chloride and maybe hydroxide anions from the 1 M NaCl$_{(aq)}$ subphase during LB transfer of the Im^{F+}-based film.[P1] At least two Cl 2p doublets indicate the presence of two different chloride species, which are specifically adsorbed on the gold surface or present in the following layer. Furthermore, the imidazolium ring is also proposed to directly interact with the Au surface, because the according N 1s line is downshifted in contrast to the bulk ILs.[127, 129] The same is valid for the transfer from an aqueous subphase. In this case, triflate was deposited together with the FIL cation, and no or a partial anion exchange by hydroxide anions took place. Conformation and order of the FILs were studied by PM

IRRAS at the Air|Au(poly) interface. Aided by optical constants, a density functional theory frequency calculation, and literature of the imidazolium FIL cation, bands in experimental spectra were assigned and quantitatively evaluated. As expected, the perfluorinated hydrocarbon segment adopted a helical conformation. Upon transfer from the aqueous subphase, a low order of helical CF stretching modes was found. In contrast, the fluorinated chains adopted a well-defined tilt of $\theta = (43 \pm 3)$ °, when transferred from the 1 M NaCl$_{(aq)}$ subphase. The chain order was reflected in the water repellency of the films: Monolayers transferred from pure water gave a contact angle of $\vartheta = (94 \pm 2)$ °, whereas $\vartheta = (109 \pm 2)$ ° was measured for those transferred from 1 M NaCl$_{(aq)}$. In macroscopically thick films of [Im^F][TfO] smeared on to glass, much less water repellency was found, $\vartheta = (70 \pm 1)$ °.[10] Clearly, the molecular scale order affects macroscopic properties of the material.

For studies of a model Helmholtz layer in the EDL, aliphatic ILs (1-methyl-3-octadecylimidazolium chloride or triflate) were transferred onto single crystalline Au(111) electrode surfaces.[P2] Due to solubility in pure water, they were studied on an 0.1 M KClO$_{4(aq)}$ subphase. The C$_{18}$Im$^+$-monolayer collapses (or transforms to a multilayer according to Filipe et al.)[25] within liquid-like compressibility moduli. A liquid-like monolayer state was chosen for transfer, enabling molecular mobility and the possibility to respond to potential changes during following investigations. As for the studied FILs, XPS showed that LB transfers from 0.1 M KClO$_{4(aq)}$ or 0.1 M KCl$_{(aq)}$ solutions lead to exchange of anions depending on the respective subphases. Also, lowering of the N 1s binding energy indicated interaction of the imidazolium moiety and the Au surface. Capacitance-potential curves of flame annealed and film covered Au(111) electrodes in 0.1 M KClO$_{4(aq)}$ revealed that the C$_{18}$Im$^+$-monolayer had modified the surfaces fundamentally. In the latter, two capacitive plateaus appeared and were separated by transition peaks. The low capacitance (6-7 µF cm^{-2}) state was located at moderately negative potentials (-0.3 V $< U <$ 0.1 V vs Ag|AgCl), and the high capacitance (13-15 µF cm^{-2}) state at more negative potentials (-1.0 V $< U <$ -0.7 V). The pseudocapacitive peaks in between those states exhibited a ca 0.1 V hysteresis for positive and negative scans, indicating a slow rearrangement. At $U \approx$ -0.8 V, an electrochemical impedance spectroscopy study hinted for ionic permeability in the monolayer. The in situ polarization modulation infrared reflection absorption spectroscopy investigation of this system indicated that imidazolium ring moieties were rigid and did not respond to changes in the electric field of the electrode. On

the other hand, profound potential responses were found for the octadecyl-chain, i.e. intensity changes for the asymmetric CH stretching vibration at $\tilde{v} = (2926 \pm 1)$ cm^{-1} and a Fermi resonance band at $\tilde{v} \approx 2900$ cm^{-1}. This FR band is sensitive to intermolecular interactions,[178] and thus indicates potential-driven changes in them. The overall chain order was evaluated from the average tilt of the methylene groups. In the low capacitance state, it equaled $S = 0.25 \pm 0.1$, whereas it increased to $S = 0.60 \pm 0.05$ in the high capacitance state at more negative potentials. Judged by the non-changing position of the resonance frequencies in CH stretching modes, the liquid physical state and the number of gauche conformations were constant. The increase in chain order is in line with a general erection of alkyl chains, probably to let co- and counter-ions pass in order to screen the strongly negative electrode charge. This corroborates well with results by Fedorov et al.[83] They showed that alkyl chains act as latent voids in neat ILs, i.e. that free lattice sites can be redistributed by molecular reorientation of uncharged alkyl segments.

Next, the impact of the anion and the behavior of the octadecyl chains in the $C_{18}Im^+$-monolayer was studied in detail by perdeuteration. Whereas the original bulk compound [$C_{18}Im$-d_{37}][TfO] exhibits one asymmetric CD stretching band, $C_{18}Im$-d_{37}^+-monolayers transferred from the 0.1 M KClO$_{4(aq)}$ subphase gave rise to two bands in the according spectral region ($\tilde{v} \approx 2197$ cm^{-1} and $\tilde{v} \approx 2183$ cm^{-1}). The appearance of two prominent bands in the $v_{as}(CD_2)$ region is unusual and was found ex situ at the air|Au(111) interface as well as in situ at the 0.1 M KClO$_{4(aq)}$|Au(111) interface. Isotopic dilution of the deuterated compound in its perhydro-analogue still showed two bands, and thus eliminated intermolecular interactions as a cause for the appearance of the second band. Aided by DFT calculations with the polarizable continuum solvent model, it is proposed that both bands originate from $v_{as}(CD_2)$ modes in alkyl chain segments with polar (water) or apolar (alkyl) environments. In situ PM IRRA spectra of the [$C_{18}Im$-d_{37}][X]|Au(111) system were recorded in 0.1 M KClO$_{4(aq)}$ and 0.1 M KCl$_{(aq)}$ electrolytes after LB-transfer from the respective subphase. Depending on the anion., the two $v_{as}(CD_2)$ bands responded differently to potential changes. An explanation may be given by the Hofmeister series.[211] Perchlorate anions are chaotropic and may interact with both water and alkyl chains, whereas chloride anions are more kosmotropic and preferably interact with water. Altogether, perchlorate anions are proposed to stay within the erected alkyl chain region to screen the positive imidazolium ring layer at negative potentials. In contrast, chloride anions should move out of

the alkyl chain region, leading to the formation of an apolar, aggregated, and coiled chain structure.

The assignment of the two bands at $\tilde{\nu} \approx 2197$ cm^{-1} and $\tilde{\nu} \approx 2183$ cm^{-1} in [C$_{18}$Im-d_{37}][X] film may be revisited and must be debated with the perhydro-analogue ([C$_{18}$Im][X]). In the latter, similar potential-dependent responses were found for modes located at $\tilde{\nu} = (2926 \pm 1)$ cm^{-1} and band at $\tilde{\nu} \approx 2900$ cm^{-1}. Based on literature,[172-173, 178, 217] these modes were assigned to the ν_{as}(CH$_2$) band and a FR band, respectively. In contrast the bands at $\tilde{\nu} \approx 2197$ cm^{-1} and $\tilde{\nu} \approx 2183$ cm^{-1} were both assigned to ν_{as}(CD$_2$) modes, which implies a profound difference in ν(CH) and ν(CD) spectra apart from a bathochromic shift. The CH-related band at $\tilde{\nu} \approx 2900$ cm^{-1} may actually be a convolution of two bands, i.e. a literature-consistent FR band and an additional ν_{as}(CH$_2$) bands with exceptionally low resonance frequency due to environmental effects as proposed above. As the nature of the anion exhibits a strong influence on the behavior of the film, different anions along the Hofmeister series, e.g. sulfate, nitrate, thiocyanate, or tetrafluoroborate, may be employed. Parallel studies of perhydro- and perdeutero-films may allow for a potential differentiation of FR effects in the $\tilde{\nu} \approx 2900$ cm^{-1} in future studies. An anharmonic frequency calculation of both monolayers on Au(111) surfaces would facilitate the final band assignment.

To study the interactions of the C$_{18}$Im$^+$-monolayer with IL molecules from the solution phase vibrational spectroscopy, the modes of the chosen solute IL, 1-ethyl-3-methylimidazolium triflate, must be assigned. Especially in the aliphatic CH stretching region, literature presents contrary assignments, which were aided by harmonic frequency calculations.[32-37] Therefore, anharmonic frequency calculations were conducted on DFT level. The analysis of the most stable, nonplanar C$_2$Im$^+$-cation in vacuo allowed for a complete assignment in the ν(CH) region. These spectra were consistent with experimental spectra from literature and changes upon elongation of the alkyl chain. As previously proposed,[34] electronic effects of the electronegative imidazolium ring were found to exhibit a profound impact on the CH stretching modes of the ethyl chain. Due to the charge distribution, resonance frequencies become hypsochromically shifted and CH bond lengths are similar. Thus, symmetric ethyl-CH stretching and bending modes mix to give new in-phase and out-of-phase vibrations. The mixed modes enable complicated Fermi resonance interactions. Charge distribution and FR effects lead to a spectrum in which the ν(CH)

fundamentals resonate at unexpectedly high frequencies, $\tilde{\nu} \geq 2948\ \text{cm}^{-1}$, which explains previous difficulties in the mode assignment.

Finally, the EDL of 0-100 mM $[C_2Im][TfO]_{(aq)}$ + 0.1 M $KClO_{4(aq)}$ solutions with flame annealed and $C_{18}Im^+$-monolayer covered Au(111) electrode surfaces were investigated. Their capacitance-potential curves exhibited an anomalous behavior and contrasted classical studies of diluted electrolytes, e.g. $NaF_{(aq)}|Ag(100)$,[55] which agree with the Gouy-Chapman theory. According to the latter, an increase of electrolyte concentration leads to higher capacitances in the diffuse layer. Due to reciprocal addition of capacitances in series, the inner layer capacitance should dominate the measured $C(U)$-curve at high concentrations. However, with increasing concentrations of $[C_2Im][TfO]$ in 0.1 M $KClO_{4(aq)}$, a camel-shaped $C(U)$-curve emerged for both flame annealed and $C_{18}Im^+$-monolayer covered Au(111) electrodes. This shape is expected according to Kornyshev's theory, which incorporates ion size effects and lattice saturation;[45] in this diffuse double layer, ions can be diluted by voids or solvent molecules. Considering the anomalous capacitive behavior, the Stern model[58] of an inner and diffuse layer cannot explain the observed results. In situ vibrational studies in 10 mM $[C_2Im][TfO]_{(aq)}$ + 0.1 M $KClO_{4(aq)}$ solution showed that the $[C_{18}Im-d_{43}][X]$-monolayer responded to potential changes as in pure 0.1 M $KClO_{4(aq)}$ solution. This was related to the chaotropy of the triflate anions, which is similar to perchlorate.[231-233] Apart from the alkyl chains of the $C_{18}Im^+$-film, no potential-driven reorientations were found among anions, ring moieties in both C_2Im^+ and $C_{18}Im^+$ cations, or the alkyl groups of the C_2Im^+ cations. The same was valid for the uncovered Au(111) surface. Interestingly, Fermi resonance enhanced overtone and combination bands of deformation modes in the ethyl group in the C_2Im^+ molecules responded to potential changes. The same three FR bands were affected in both electrode systems, but their intensity changes deviated for flame annealed and $C_{18}Im^+$-monolayer covered Au(111) surfaces. FR interactions are sensitive to intermolecular interactions.[178, 222] If these are proposed to cause the observed intensity changes, the interaction of C_2Im^+ must vary significantly upon potential changes. More detailed experimental and theoretical studies are required to understand the nature of these changes. Literature results of ILs or heteroaromatic molecules show for the formation of adlayers next to the first layer at the electrode surface, even in highly diluted solutions.[27, 129, 164, 226] In these layers, the molecules are accumulated with respect to the bulk phase. A more complicated EDL model is proposed: The Stern layer next to the

metal surface may overscreen the electrode charge. It may be followed by an accumulation layer of IL molecules. In this layer, forces beyond electrostatic interactions and thermal randomization govern the structure. As known for molten salts, strong ion-ion correlations lead to a multilayered and charge-oscillating structure.[20, 63, 76] On the other hand, the extent should be small in diluted systems.[27] Nevertheless, the observed FR interaction changes indicated interesting and potential-dependent association. Last, the accumulation layer may be screened with a diffuse layer into the bulk phase.

EDL models are crude and only account for thermal motion, electrostatic interactions, and, with Kornyshev, ionic size.[20] Properties such as polarizability, ionic correlation, dispersive interactions, or H-bonding are relevant, but hard to incorporate into a general theory. These weak interactions also affect time-consuming molecular rearrangements or reorientations, hampering the analysis by dynamic methods as conveniently used EIS. Studies of this thesis show that ILs at interfaces are strongly subjected to the above-mentioned effects. The LB-monolayer model approach facilitates the decoupling of different interactions, serving as a good model for both experimental and theoretical studies of the EDL in ILs.

11 Methodological Details

All experiments were conducted at room temperature.

11.1 Chemicals

Deionized water with a resistivity $\geq 18.2\ \text{M}\Omega$ cm was obtained from a Pure-Lab Classic system (Elga LabWater, UK). All commercially obtained chemicals were used as received and are listed in table 11.1.

Table 11.1: Commercially obtained chemicals.

Product	Sum Formula	Supplier	Grade
Argon	Ar	Air Liquide	5 N
Chloroform	$CHCl_3$	Sigma-Aldrich	$\geq 99\ \%$, contains 0.5-1.0 % ethanol as stabilizer
Chloroform-d	$CDCl_3$	Eurisotop	99.96 % D
Deuterium oxide	D_2O	Eurisotop, Deutero	99.90 % D, 99.9 %
Ethanol	C_2H_6O	Fisher Scientific	$\geq 99.8\ \%$, a.r.g.
1-Ethyl-2-methyl-imidazolium triflate	$C_7H_{11}F_3N_2O_3S$	IoLiTec	99.5 %
Hydrogen peroxide	H_2O_2	Merck	30 %, puriss, p.a., reag. ISO, reag. Ph. Eur.
Methanol	CH_4O	Fisher Scientific	$\geq 99.99\ \%$, a.r.g.
Methanol-d_4	CD_4O	Eurisotop	99.96 % D
1-Methy-3-octadecyl-imidazolium chloride	$C_{22}H_{43}ClN_2$	IoLiTec	$\geq 98\ \%$
2-Propanol	C_3H_8O	Merck	$\geq 99.8\ \%$, ACS reagent, reag. ISO, reag. Ph. Eur.
Potassium bromide	KBr	Fisher Scientific	Spectroscopy grade
Potassium chloride	KCl	Carl Roth	$\geq 99.5\ \%$, p.a., ACS ISO
Potassium perchlorate	$KClO_4$	Merck, Acros	99.5 %, EMSURE®, ACS; $\geq 99\ \%$ for analysis
Sodium chloride	NaCl	Carl Roth	$\geq 99.5\ \%$, p.a., ACS ISO
Sulfuric acid	H_2SO_4	Sigma-Aldrich	95-97 %, puriss, p.a., ACS reagent, reag. ISO, reag. Ph. Eur.

The compounds in table 11.2 were synthesized and provided by Torben Alpers, working group of Jens Christoffers (University of Oldenburg) according to procedures given in the references.

Table 11.2: Compounds obtained from the Christoffers group.

Compound	Sum formula
1,3-Bis(1H,1H,2H,2H-perfluorooctyl)-imidazolium iodide[10]	$C_{19}H_{11}F_{26}IN_2$
1,3-Bis(1H,1H,2H,2H-perfluorooctyl)-imidazolium triflate[10]	$C_{20}H_{11}F_{29}N_2O_3S$
1,3-Bis(1H,1H,2H,2H-perfluorooctyl)-1,2,3-triazolium triflate[11]	$C_{19}H_{10}F_{29}N_3O_3S$
1,4-Bis(1H,1H,2H,2H-perfluorooctyl)-1,2,4-triazolium triflate[11]	$C_{19}H_{10}F_{29}N_3O_3S$
1-Methyl-3-(octadecyl-d_{37})-imidazolium triflate[195]	$C_{23}H_6D_{37}F_3N_2O_3S$
1-(Methyl-d_3)-3-(octadecyl-d_{37})-imidazolium-4,5-d_2 triflate[195]	$C_{23}H_1D_{42}F_3N_2O_3S$

11.2 Electrode Materials

The substrates for LB transfer were Au(111) disc electrodes (3 mm and 12 mm diameter, polished with an orientation accuracy < 1°, MaTeck, Germany) or a gold film evaporated onto a glass slide. Prior to use, Au(111) electrodes were flame annealed in a Bunsen burner and gently cooled in an argon atmosphere. Microscope glass slides (VWR International, Belgium) were cut in pieces of 1.0×2.5 cm^2 and rinsed with water and 2-propanol. Afterward, the glass slides were dried in a stream of argon. On the cleaned glass surface 0.7 nm of adhesive Cr (99.7 %, Goodfellow) and 200 nm Au (99.999 %, Goodfellow) layers were evaporated using a Tectra MiniCoater instrument (Tectra, Germany). Before each LB transfer, the slides were rinsed with water and ethanol, dried with Ar and placed in an UV/ozone cleaner (Bioforce Nanoscience Inc., USA) for 10 min. These slides are denoted as Au(poly) in this thesis.

11.3 Langmuir-Blodgett Method

Surface pressure versus mean molecular area isotherms were recorded using a KSV LB Mini Trough (KSV, Finland) equipped with two hydrophilic barriers and a Wilhelmy balance with a paper Wilhelmy plate. Prior to use, it was cleaned with copious amounts of water, ethanol, wiped with chloroform, and rinsed with ethanol and water again. After each rinse, the surface was dried with delicate task wipes (Kimtech). To protect the experimental setup from dust, it was placed in a laminar flow hood. Fresh

solutions of ILs in organic solvents (typically 2 mL) were prepared daily: FILs [Im^F][TfO], [1,2,3-Tria][TfO], and [1,2,4-Tria][TfO] in CHCl$_3$: MeOH = 2 : 1 (v/v), 1 g L^{-1}; aliphatic ILs [C$_{18}$Im][Cl], [C$_{18}$Im-d_{37}][TfO], and [C$_{18}$Im-d_{42}][TfO] in CHCl$_3$ ([C$_{18}$Im-d_{37}][TfO] in CDCl$_3$ once), 2-3 mM. For the isotopic dilution experiment of [C$_{18}$Im][Cl]:[C$_{18}$Im-d_{37}][TfO] = 1:10 molar ratio, a solution of 12.8 mg [C$_{18}$Im][Cl] + 1.8 mg [C$_{18}$Im-d_{37}][TfO] in 20 mL CHCl$_3$ was prepared, yielding an averaged mass concentration of 0.73 g L^{-1}. Using a microsyringe (Hamilton, USA), a few microliters of the IL solution were placed on the aqueous subphase and left for solvent evaporation: 10 min for CHCl$_3$: MeOH solutions and 5 min for CHCl$_3$/CDCl$_3$ solutions. Compression and expansion isotherms were conducted at a barrier speed of 15 mm s^{-1}. The accuracy of measurements was ± 0.02 nm^2 for A_{molec} and ± 0.1 mN m^{-1} for Π. Transfer conditions are described in the according chapters. If not stated differently, the substrates were dried and kept in argon atmosphere overnight after transfer.

11.4 X-Ray Photoelectron Spectroscopy

X-ray photoelectron spectra were measured from the LB monolayer transferred onto an Au(poly) substrate, using an ESCALAB 250 Xi spectrometer (Thermo Fisher Scientific, UK). The instrument was operated using a monochromatic Al K$_\alpha$ X-ray radiation source (hν_{photon} = 1486.6 eV). Samples were grounded by connecting carbon tape to the surface and the sample holder. It has been shown that ILs|Au degrade upon irradiation with X-rays.[127] Thus, the acquisition time was kept rather low to avoid sample damage. Due to different sensitivities and concentrations, the pass energy, step size, and dwell time were varied for different photoelectron lines (Tab. 11.3). The binding energy scale was referenced to the Au 4f$_{7/2}$ line at E_b = 84.0 eV. The spectra were fitted using Avantage v5.982 software (Thermo Fisher Scientific, UK) by employing Gaussian-Lorentzian functions with a fixed ratio within each spectral region after Shirley-type background subtraction. For the fit of Cl 2p and S 2p lines the doublet splitting was fixed to 1.60 eV and 1.2 eV,[143] respectively, and the fwhms were constrained to be the same.

Table 11.3: XPS acquisition parameters.

Figure	Spectrum type	Pass energy / eV	Step size / eV	Dwell time / ms
5.3a	Survey	100	0.5	50
5.3b	N 1s	30	0.05	1000
5.3c	F 1s	30	0.05	200
5.3d	C 1s	30	0.05	1000
5.4a	S 2p	100	0.1	500
5.4b	O 1s	30	0.05	1000
5.4c	Cl 2p	30	0.05	1000
5.4d	Na 1s	70	0.1	500
5.5a	Survey	100	0.5	25
5.5b	N 1s	30	0.05	500
5.5c	S 2p	70	0.1	1000
6.2	Survey	200	1.0	10
6.3a	C 1s	70	0.1	250
6.3b	N 1s	70	0.1	500
6.3c	Cl 2p	70	0.1	500
6.3d	O 1s	20	0.05	500
7.1	Survey	100	0.5	30
7.2a	Na 1s	20	0.5	250
7.2b	C 1s	20	0.05	250
7.2c	N 1s	20	0.05	1000
7.2d	O 1s	50	0.1	250
7.2e	Cl 2p	20	0.05	1000

11.5 Infrared Spectroscopy

All IR spectra were recorded with a Vertex 70 spectrometer (Bruker, Germany). Acquisition and processing of spectra was executed with OPUS v5.5 software (Bruker, Germany). The spectrometer and measurement chambers are purged with dry air.

11.5.1 Attenuated Total Reflection

ATR IR spectra were recorded by co-adding 64 scans with a nominal resolution of 2 cm^{-1} of the pure [C$_{18}$Im-d_{37}][TfO] powder on a single reflection silicon prism using a MVP-Pro ATR unit (Harrick Scientific Products, USA). The spectrum of neat [C$_2$Im][TfO] was measured with 256 scans and 4 cm^{-1} resolution.

11.5.2 Polarization Modulation Reflection Absorption

PM IRRA spectra were measured with the Vertex 70 spectrometer and an external reflection setup (Bruker, Germany) containing a photoelastic modulator with the frequency of 50 kHz and a demodulator PMA 50 (Hinds Instruments, USA). The nominal resolution for all PM IRRA spectra was 4 cm^{-1}. Further experimental parameters are given in table 11.4. The spectral background was corrected by spline interpolation. Spectra are either given in differential reflectivity or converted to absorbance.

In situ were recorded in a three-electrode spectroelectrochemical cell[234] at various potentials applied to the Au(111) electrode (12 mm diameter), which simultaneously served as a mirror for the IR light. All glass and Teflon ware were cleaned with copious amounts of water, ethanol, and water for experiments given in sections 6.4 and 7.4. For investigations in section 9.2, glass and Teflon ware were cleaned in self-heating Caroic acid (96 % H_2SO_4 : 30 % H_2O_2 = 3:1 v/v. Caution, Caroic acid may react explosively with organic compounds!), followed by rinsing with copious amounts of water and boiling in water (at least two times). Next, these parts were dried in an oven over night. A CaF_2 equilateral prism (Bioxin Photoelectric, China) was used as an optical window for the IR radiation. Before assembly of the spectroelectrochemical cell, the prism was washed with water and ethanol and cleaned for 10 min in the UV/ozone chamber. The spectroelectro-chemical cell has a built-in platinum counter electrode. The reference electrode was Ag|AgCl in 3 M KCl$_{(aq)}$ (CH Instruments, USA). The electrolyte was purged with argon for 1 h to remove oxygen, and afterwards an Ar blanket was maintained above the electrolyte. The potential was stepped and hold for 20 s before starting the collection spectral scans. In each experiment, four to six negatively going and positively going potential scans were recorded. Each potential scan was analyzed separately and averaged. The thickness of the electrolyte layer between the CaF_2 prism and the Au electrode was evaluated from the shape of the water reflectivity curve.[235]

Table 11.4: PM IRRAS acquisition parameters. Φ – Angle of incidence for the IR beam.

Fig.	Sample film	Medium	Φ / °	$\tilde{\nu}_{HWR}$ / cm^{-1}	Total number of Scans (Spectral sets to average)
5.9b	[Im^F][X]	Air	80	1300	500 (1)
5.9c	[1,2,4-Tria][X]	Air	80	1300	500 (1), 1500 (3)
5.9d	[1,2,3-Tria][X]	Air	80	1300	500 (1), 3000 (6), 1500 (3)
6.7	[C$_{18}$Im][X]	0.1 M KClO$_{4(aq)}$	54	1600	3000 (5)
6.10	[C$_{18}$Im][X]	0.1 M KClO$_{4(aq)}$	55	2900	3000 (5)
7.3b	[C$_{18}$Im-d_{37}][X]	Air	80	2200	36096 (71)*
7.3c	[C$_{18}$Im-d_{37}][X]	Air	80	2200	512 (1)
7.3d	[C$_{18}$Im-d_{37}][X]	Air	80	2200	1536 (3)
7.3e	[C$_{18}$Im-d_{37}][X]	Air	80	2200	400 (1)
7.7	[C$_{18}$Im-d_{37}][X]	0.1 M KClO$_{4(aq)}$	58	2200	2000 (4)
7.8	[C$_{18}$Im-d_{37}][X]	0.1 M KCl$_{(aq)}$	58	2200	2500 (5)
9.5; 9.7	[C$_{18}$Im-d_{42}][X]	10 mM [C$_2$Im][TfO] + 0.1 M KClO$_{4(aq)}$	58	2200	3600 (6)
9.6; 9.8a,b,d	None	10 mM [C$_2$Im][TfO] + 0.1 M KClO$_{4(aq)}$	54	1600	2000 (5)
9.9a,b,d; 9.10a,c	[C$_{18}$Im-d_{42}][X]	10 mM [C$_2$Im][TfO] + 0.1 M KClO$_{4(aq)}$	54	3000	2400 (6)
9.11	None	10 mM [C$_2$Im][TfO] + 0.1 M KClO$_{4(aq)}$	54	3000	2400 (4)

*This experiment originally should track time-dependent changes directly after LB transfer. However, no significant changes occurred over 24 h, and the average of these spectra, weighted by the number of scans, was used for its extraordinary signal-to-noise ratio.

11.5.3 Extraction of Isotropic Optical Constants and Simulation of Polarization Modulation Infrared Reflection Absorption Spectra

Isotropic optical constants of [Im^F][I] were obtained from a transmission measurement in a KBr pellet (1 % analyte). After background correction with the spectrum of a pure KBr pellet, the attenuation coefficient was extracted with Lambert-Beer's law and Kramers-Kronig transformation was used to determine the refractive index.

For the determination of isotropic optical constants of [C$_{18}$Im][Cl], the compound was dissolved in methanol-d_4 and measured using a thin layer cell (Sigma-Aldrich, Germany) with ZnSe windows (Sigma-Aldrich, Germany) for transmission. A 50 µm Teflon spacer was introduced between

two ZnSe windows and the transmission spectra of the pure solvent and the 3.9 vol-% analyte solution were measured. The isotropic optical constants were calculated according to the procedure described by Zamlynny.[183]

Fresnel1 (Vlad Zamlynny, Arcadia University, Canada) was used for the simulation of PM IRRA spectra. Reflectivities were calculated for a stratified system utilizing the Abeles-matrix notation of the Fresnel-equations. The angles of incidence were set according to the experimental conditions (Section 11.5.2). Details for estimation of surface coverages and monolayer thicknesses are given in the according descriptions (Sections 5.1, 0, 6.1, and 6.4.1). Isotropic optical constants of air, Au, CaF_2, methanol-d_4, and water were required for the simulations and provided by the program.

11.6 Electrochemical Characterization

Electrochemical measurements were performed in a three-electrode glass cell with the Au(111) disc electrode (3 mm diameter) as the working electrode. All glass and Teflon ware were cleaned in self-heating Caroic acid (96 % H_2SO_4 : 30 % H_2O_2 = 3:1 v/v. Caution, Caroic acid may react explosively with organic compounds!), followed by rinsing with copious amounts of water and boiling in water. A gold wire spiral served as the counter electrode and a silver|silver chloride electrode (Ag|AgCl|sat. KCl; CH Instruments, USA), abbreviated as Ag|AgCl, as the reference electrode. All potentials are referred versus this electrode. The reference electrode was separated from the electrolyte solution via a salt bridge. Prior to the experiment, the cell was purged with argon for 1 h, and afterwards an Ar blanket was maintained above the electrolyte. An Autolab PGSTAT302N potentiostat (Metrohm, Netherlands) with the corresponding software Nova 2.1.3 (Metrohm, Netherlands) was used to perform electrochemical measurements. The single frequency electrochemical impedance spectra were recorded in negative and positive directions with a scan rate of 5 mV s^{-1} and a perturbation of $U_0 = 10$ mV peak-to-peak amplitude at $f = 20$ Hz. The differential capacitance versus potential curves were calculated for an R-C-circuit as described in section 4.3.4. Frequency-dependent EIS was performed versus a Pt-wire quasi-reference electrode (QRE) at selected potentials. Multiple $C(U)$ sweeps were recorded to ensure the stability of the Pt-QRE and used for potential calibration. A $U_0 = 10$ mV RMS amplitude was

applied with ten points per decade being measured within a range of $f = 10^5 - 10^{-1}$ Hz.

11.7 Water Contact Angle Measurement

The static water contact angle was measured with the sessile drop method using 9 μL drops with the contact angle system OCA 15plus (Dataphysics, Germany) equipped with a CCD camera and SCA20 software (v1.0.0). The denoted values are the average of eight measurements.

11.8 Computational Chemistry

Calculations were performed using the Gaussian 16[236] program on the High-Performance Computing Cluster Carl, University of Oldenburg. Geometry optimizations were followed by frequency calculations on the same level of theory. No imaginary harmonic frequencies were found for the optimized molecule geometries.

For B3LYP[237]/6-31+G*[238], B3LYP/def2-TZVPD[239-240], and B3LYP/def2-TZVP[239-240] calculations of the Im^{F+} cation, Gaussian 16 Rev. A.03 (Gaussian Inc., USA) was employed. Orca 4.0.0 (Max Planck Institute for Chemical Energy Conversion, Germany) was used for RI-MP2[241]/def2-TZVPD calculation with the def2-TZVPD/C[242] auxiliary basis set.

The solvent model calculation in section 7.3 was executed as follows by Thorben Petersen, working group of Thorsten Klüner: Calculations were performed with Gaussian 16 Rev. A.03. Throughout the calculations, density functional theory on the PBE0[243]/def2-TZVP[239] level of theory in conjunction with Grimme's D3 dispersion correction[148] with Becke-Johnson damping[244] was employed. The harmonic frequencies were obtained after full structural optimization of the respective geometry and afterwards scaled by a factor of 0.9575.[210] For solvation, the Polarizable Continuum Model[208] of water, $\varepsilon_r = 78.3553$, and heptane, $\varepsilon_r = 1.9113$, was applied.

NBO[245] analyses, harmonic and anharmonic frequency calculations for the C$_2$Im$^+$ cation, ethanol molecule, [C$_2$Im-d_1-D$_2$O]$^+$ associate, and [C$_2$Im][TfO] ion pair were executed with Gaussian 16 Rev C.01. As denoted in according tables and figures, B3LYP, B3LYP-D3BJ, or ωB97X-D[246] density

functionals and the 6-311++G(d,p)[247-248] basis set were employed. Prior to frequency calculations, the geometries of the molecules were optimized to tight convergence criteria. For the anharmonic frequency calculation, the GVPT2[219, 249] method was used and the Martin test[250] threshold was set to $\mathcal{K} = 0.1$ cm^{-1}. In some cases low wavenumber modes were found to yield unreasonably high intensities or imaginary frequencies after anharmonic corrections and would perturb the whole spectrum with it. Thus, the lowest 10 modes in the C_2Im^+ cation, 20 modes in the $[C_2Im\text{-}d_1\text{-}D_2O]^+$ associate and 20 modes in the $[C_2Im][TfO]$ ion pair were excluded from anharmonic frequency calculations.

12 Appendix

Table 12.1: Cartesian coordinates of the minimum energy conformer V of the Im^{F+} cation (E_{sp} = -3437.249259 hartree, B3LYP/def2-TZVP).

Symbol	x / Å	y / Å	z / Å	Symbol	x / Å	y / Å	z / Å
C	-0.07638	4.80982	0.66999	C	3.48015	1.21986	-0.33188
H	-0.00435	4.40414	1.66435	C	3.33526	-0.12687	0.46228
N	0.9524	5.10308	-0.12443	C	3.75756	-1.39051	-0.37208
N	-1.21144	5.0763	0.02458	C	4.03847	-2.65539	0.51089
C	0.45574	5.56913	-1.32489	C	4.06932	-4.00353	-0.28427
C	-0.89711	5.55228	-1.23194	F	-1.56299	2.20984	-0.50589
C	2.37996	4.96613	0.22184	F	-2.30724	2.29624	1.55481
H	2.45107	4.9409	1.30752	F	-4.19249	1.38509	-1.2716
H	2.87261	5.87605	-0.11706	F	-4.63947	1.20575	0.86845
C	-2.56954	4.88714	0.56762	F	-2.28697	-0.38617	-1.19581
H	-2.46963	4.77368	1.64459	F	-2.12738	-0.326	0.98872
H	-3.12264	5.80665	0.38093	F	-5.07606	-1.1575	-0.7155
C	-3.33315	3.7074	-0.03517	F	-4.42677	-1.50256	1.34915
H	-4.33296	3.71629	0.40208	F	-3.35599	-2.86243	-1.70137
H	-3.45194	3.81433	-1.11274	F	-2.18979	-2.95823	0.15349
C	-2.69039	2.3545	0.24924	F	-4.19078	-4.2112	1.42942
C	-3.6526	1.16286	-0.05208	F	-5.5555	-3.89575	-0.23225
C	-2.98207	-0.2566	-0.04941	F	-3.79915	-5.14695	-0.48388
H	-1.64935	5.84789	-1.94131	F	1.3658	2.21337	0.1296
H	1.09641	5.88514	-2.12888	F	2.95975	2.51025	1.60307
C	-4.01609	-1.43454	0.06891	F	3.03545	1.05614	-1.59839
C	-3.42967	-2.82409	-0.35967	F	4.78774	1.55505	-0.37657
C	-4.27557	-4.0547	0.11004	F	2.05003	-0.26991	0.83892
C	3.07577	3.75318	-0.4002	F	4.10478	-0.03966	1.56294
H	4.14988	3.89886	-0.28717	F	2.76553	-1.66753	-1.24027
H	2.86833	3.679	-1.46823	F	4.87409	-1.09674	-1.06631
C	2.70496	2.43549	0.26794	F	3.08038	-2.75776	1.45427
C	3.48015	1.21986	-0.33188	F	5.23143	-2.50285	1.1102
C	3.33526	-0.12687	0.46228	F	2.84917	-4.33256	-0.70501
C	3.75756	-1.39051	-0.37208	F	4.88383	-3.90373	-1.33669
C	4.03847	-2.65539	0.51089	F	4.51793	-4.96175	0.5234

Table 12.2: Cartesian coordinates of the [C₁₈Im-*d₃₇*][ClO₄] ion pair in vacuo (E_{sp} = -1733.515394 hartree, PBE0-D3BJ/def2-TZVP).

Symbol	x / Å	y / Å	z / Å	Symbol	x / Å	y / Å	z / Å
C	-7.775663	0.923799	-1.30422	C	2.624664	-1.21133	-0.01354
C	-7.838711	-0.26591	-0.65833	D	2.561782	-0.86872	1.026647
C	-6.375262	0.997203	0.385907	D	2.484566	-0.31593	-0.63118
N	-6.859397	1.694431	-0.63375	C	4.004921	-1.79106	-0.27023
H	-8.293051	1.281207	-2.17741	D	4.06909	-2.12756	-1.31283
H	-8.420863	-1.14843	-0.85785	D	4.141296	-2.69015	0.344197
H	-5.582737	1.307391	1.06141	C	5.134507	-0.81547	0.012164
N	-6.962475	-0.1952	0.395137	D	5.07165	-0.48095	1.055201
C	-6.416661	3.02201	-1.02311	D	4.997473	0.084615	-0.59992
H	-5.558782	3.30355	-0.41365	C	6.514587	-1.39458	-0.24715
H	-6.096414	2.994047	-2.06344	D	6.579781	-1.72196	-1.29251
H	-7.233988	3.73252	-0.89836	D	6.64849	-2.29918	0.359464
C	-6.639769	-1.27663	1.327153	C	7.64499	-0.4227	0.045214
D	-7.359391	-2.07284	1.127205	D	7.587222	-0.1039	1.093985
D	-6.819649	-0.90907	2.339092	D	7.499843	0.482948	-0.5539
C	-5.213361	-1.76915	1.170522	C	9.021931	-1.00936	-0.22309
D	-5.06134	-2.54361	1.930588	D	9.099459	-1.27717	-1.28455
D	-4.527357	-0.95298	1.411349	D	9.117057	-1.94928	0.333017
C	-4.908113	-2.32783	-0.20948	C	10.180008	-0.09403	0.150569
D	-5.665593	-3.07775	-0.47331	D	11.122119	-0.64315	0.032785
D	-4.982129	-1.5231	-0.94927	D	10.104768	0.155525	1.214992
C	-3.522652	-2.95436	-0.30793	C	10.255748	1.181415	-0.67643
D	-3.413975	-3.4046	-1.30113	D	9.367079	1.7965	-0.49523
D	-3.446414	-3.78217	0.409129	D	10.227531	0.911468	-1.73899
C	-2.384702	-1.97185	-0.08246	C	11.498565	2.020975	-0.41013
D	-2.509783	-1.11326	-0.74931	D	11.527844	2.846992	-1.12842
D	-2.433202	-1.56021	0.931167	D	12.390757	1.414886	-0.60794
C	-1.012745	-2.5858	-0.2967	C	11.571125	2.585919	0.999467
D	-0.939438	-2.96395	-1.32482	D	11.637594	1.795588	1.750454
D	-0.892307	-3.46124	0.355343	D	12.444832	3.229837	1.123787
C	0.117166	-1.60367	-0.03861	D	10.683052	3.18312	1.226885
D	-0.026234	-0.71513	-0.66332	Cl	-3.134554	1.825589	0.318744
D	0.052899	-1.2434	0.99489	O	-3.80355	1.154163	-0.78101
C	1.495602	-2.19002	-0.28724	O	-3.446756	3.231606	0.26198
D	1.561628	-2.53693	-1.32659	O	-1.729403	1.608692	0.253167
D	1.631814	-3.08322	0.336418	O	-3.66573	1.284845	1.563793

Table 12.3: Cartesian coordinates of the [C₁₈Im-*d₃₇*][ClO₄] ion pair in heptane (E_sp = -1733.526935 hartree, PBE0-D3BJ/def2-TZVP).

Symbol	x / Å	y / Å	z / Å	Symbol	x / Å	y / Å	z / Å
C	-7.94528	0.800038	-1.16587	C	2.651555	-1.21444	-0.02602
C	-7.95476	-0.37432	-0.48903	D	2.610723	-0.93984	1.035332
C	-6.40575	0.907067	0.396918	D	2.500582	-0.28141	-0.58242
N	-6.97251	1.581517	-0.59525	C	4.025636	-1.77658	-0.34739
H	-8.53607	1.140548	-1.99832	D	4.071469	-2.03552	-1.41283
H	-8.55472	-1.25827	-0.617	D	4.169263	-2.71827	0.197688
H	-5.56937	1.240252	1.001613	C	5.162364	-0.8262	-0.01247
N	-6.99079	-0.28329	0.482776	D	5.119828	-0.57359	1.054419
C	-6.59237	2.914731	-1.02882	D	5.015795	0.118378	-0.55087
H	-5.68007	3.21014	-0.51418	C	6.53638	-1.38403	-0.34158
H	-6.39686	2.895115	-2.09958	D	6.58395	-1.62226	-1.41172
H	-7.39896	3.613966	-0.80976	D	6.677374	-2.3363	0.185281
C	-6.60845	-1.33689	1.423911	C	7.673559	-0.44131	0.013435
D	-7.30436	-2.1601	1.255628	D	7.635775	-0.21591	1.087071
D	-6.77357	-0.95967	2.434582	D	7.518623	0.513222	-0.50142
C	-5.17196	-1.7866	1.235407	C	9.044571	-1.00164	-0.33097
D	-4.97808	-2.54971	1.996933	D	9.103282	-1.17093	-1.41373
D	-4.50197	-0.9509	1.453519	D	9.147636	-1.98833	0.135552
C	-4.88657	-2.34782	-0.14813	C	10.21031	-0.1241	0.104789
D	-5.64047	-3.10695	-0.39214	D	11.14964	-0.65781	-0.08433
D	-4.98898	-1.54944	-0.89147	D	10.15684	0.022659	1.189474
C	-3.49755	-2.96002	-0.27489	C	10.26898	1.224585	-0.5979
D	-3.39875	-3.3941	-1.27628	D	9.384882	1.818317	-0.33952
D	-3.40423	-3.79705	0.428993	D	10.21806	1.057453	-1.68058
C	-2.3622	-1.97436	-0.04934	C	11.51769	2.036745	-0.2788
D	-2.50908	-1.09878	-0.68992	D	11.53116	2.928652	-0.91394
D	-2.39017	-1.59382	0.977438	D	12.40512	1.45417	-0.55372
C	-0.99194	-2.57316	-0.31311	C	11.62119	2.462465	1.177151
D	-0.93613	-2.90572	-1.35775	D	11.70403	1.602982	1.84617
D	-0.85962	-3.47566	0.298275	D	12.49756	3.093122	1.343983
C	0.142496	-1.6029	-0.03138	D	10.73817	3.032921	1.480514
D	-0.01338	-0.68572	-0.61035	Cl	-3.11773	1.948824	0.215585
D	0.101394	-1.29612	1.020722	O	-3.7518	1.236435	-0.87329
C	1.515914	-2.17378	-0.33825	O	-3.48343	3.34187	0.140261
D	1.562592	-2.45781	-1.39743	O	-1.69965	1.796168	0.151181
D	1.660834	-3.10243	0.229031	O	-3.61614	1.405262	1.469781

Table 12.4: Cartesian coordinates of the [C$_{18}$Im-d_{37}][ClO$_4$] ion pair in water (E_{sp} = -1733.549094 hartree, PBE0-D3BJ/def2-TZVP).

Symbol	x / Å	y / Å	z / Å	Symbol	x / Å	y / Å	z / Å
C	-7.87177	0.844612	-1.39194	C	2.575246	-1.26941	-0.02331
C	-7.9497	-0.33619	-0.72999	D	2.487674	-0.81959	0.973704
C	-6.39155	0.875878	0.230095	D	2.454484	-0.44608	-0.73855
N	-6.8935	1.582347	-0.77488	C	3.960851	-1.87166	-0.18122
H	-8.42161	1.218397	-2.23791	D	4.050011	-2.31844	-1.17948
H	-8.58048	-1.19354	-0.88748	D	4.080244	-2.69692	0.532065
H	-5.58629	1.185853	0.880524	C	5.083356	-0.86829	0.021176
N	-7.0207	-0.29354	0.277498	D	4.994105	-0.42231	1.019785
C	-6.4733	2.918117	-1.15701	D	4.963537	-0.0424	-0.69126
H	-5.64093	3.220876	-0.52693	C	6.469481	-1.46932	-0.13686
H	-6.15273	2.909442	-2.19722	D	6.560577	-1.9107	-1.13741
H	-7.30594	3.608849	-1.03359	D	6.587988	-2.29854	0.572004
C	-6.73805	-1.36183	1.236406	C	7.591317	-0.4664	0.072242
D	-7.44566	-2.16147	1.017874	D	7.50726	-0.03251	1.077045
D	-6.95716	-0.98221	2.235049	D	7.460792	0.364813	-0.62951
C	-5.30739	-1.85653	1.14053	C	8.975182	-1.07464	-0.09348
D	-5.18024	-2.61094	1.923516	D	9.077747	-1.46449	-1.11428
D	-4.62681	-1.03711	1.388264	D	9.058681	-1.94125	0.572766
C	-4.96075	-2.45452	-0.21334	C	10.12217	-0.11552	0.195686
D	-5.69911	-3.22632	-0.45827	D	11.0677	-0.67052	0.168403
D	-5.04932	-1.68569	-0.9899	D	10.01925	0.261004	1.219714
C	-3.56443	-3.05899	-0.27196	C	10.21737	1.049874	-0.77871
D	-3.43805	-3.55357	-1.24151	D	9.320634	1.675207	-0.70163
D	-3.47952	-3.84767	0.485912	D	10.2247	0.65079	-1.80019
C	-2.43864	-2.0545	-0.08388	C	11.44706	1.926687	-0.57901
D	-2.56236	-1.23325	-0.79969	D	11.49766	2.655709	-1.39458
D	-2.50431	-1.59715	0.909479	D	12.3477	1.307396	-0.66734
C	-1.05914	-2.66783	-0.25078	C	11.46763	2.666483	0.749306
D	-0.98	-3.11845	-1.24818	D	11.50732	1.977777	1.596371
D	-0.938	-3.49109	0.464675	D	12.3357	3.326078	0.821423
C	0.067827	-1.66737	-0.06021	D	10.57053	3.28218	0.865803
D	-0.05351	-0.84549	-0.77673	Cl	-2.91991	2.113397	0.44953
D	-0.01645	-1.2138	0.935276	O	-3.36809	1.508749	-0.78014
C	1.451625	-2.27269	-0.21992	O	-3.26965	3.512435	0.449722
D	1.537893	-2.72268	-1.217	O	-1.49579	1.965696	0.579289
D	1.571979	-3.09576	0.49575	O	-3.57576	1.461907	1.564875

Table 12.5: Harmonic CD stretching vibrations of the [C_{18}Im-d_{37}][ClO_4] ion pair in vacuum.

$\tilde{\nu}$ / cm^{-1}	I_{IR} / km mol^{-1}	Stretching vibration: participating group position in the alkyl chain (1 – α-CH$_2$ to 18 – terminal CH$_3$) (relative weight in %)
2188.1	2.43	ν_s(CD$_2$): 6 (25.5), 8 (14.7), 4 (5.1)
2188.9	11.82	ν_s(CD$_3$) 18 (62.0); ν_s(CD$_2$): 17 (5.4)
2191.7	4.41	ν_s(CD$_2$): 8 (13.8), 10 (13.0), 6 (8.6), 12 (5.0)
2193.5	7.67	ν_s(CD$_2$): 12 (11.0), 3 (10.6), 4 (8.2), 10 (6.8)
2194.0	14.78	ν_s(CD$_2$): 3 (11.1), 12 (9.1), 4 (6.4), 6 (5.3), 8 (5.3)
2195.8	4.01	ν_s(CD$_2$): 14 (8.6), 11 (8.4), 8 (7.5), 13 (7.3), 10 (7.4)
2198.0	1.62	ν_s(CD$_2$): 11 (15.2), 14 (11.3), 9 (9.4), 15 (7.1)
2198.5	12.94	ν_s(CD$_2$): 10 (9.9), 12 (9.9), 13 (8.4)
2201.7	34.46	ν_s(CD$_2$): 4 (21.4), 3 (15.1)
2202.0	3.61	ν_s(CD$_2$): 9 (15.0), 13 (12.3), 14 (6.0), 15 (5.7)
2202.8	17.16	ν_s(CD$_2$): 16 (17.3), 17 (10.3), 14 (8.5)
2204.3	48.32	ν_s(CD$_2$): 13 (11.0), 11 (10.9), 9 (10.4), 15 (8.8)
2206.0	41.82	ν_s(CD$_2$): 15 (17.6), 14 (11.0), 13 (6.5), 16 (8.0), 12 (5.0)
2209.5	14.56	ν_s(CD$_2$): 17 (27.2), 16 (15.3)
2211.6	16.99	ν_s(CD$_2$): 7 (32.5), 9 (7.2), 5 (5.4)
2221.7	12.57	ν_s(CD$_2$): 5 (26.1), 2 (14.7)
2223.7	5.27	ν_s(CD$_2$): 2 (26.7), 5 (15.3)
2242.2	17.31	ν_s(CD$_2$): 1 (42.7), 2 (6.3)
2249.6	4.25	ν_{as}(CD$_2$): 8 (9.6), 9 (8.1), 10 (8.7), 11 (6.1)
2250.8	4.47	ν_{as}(CD$_2$): 6 (10.5), 11 (6.6), 12 (6.9), 7 (5.2), 10 (5.2), 8 (5.1)
2252.5	2.67	ν_{as}(CD$_2$): 6 (10.3), 8 (6.8), 12 (7.3)
2256.6	0.41	ν_{as}(CD$_2$): 10 (8.1), 13 (7.8), 8 (7.1), 12 (6.6), 14 (6.0)
2261.8	4.54	ν_{as}(CD$_2$): 14 (10.1), 15 (8.7), 16 (5.8)
2264.2	6.46	ν_{as}(CD$_2$): 4 (13.6), 3 (6.6)
2264.6	2.98	ν_{as}(CD$_2$): 16 (7.9), 15 (6.0), 4 (5.5)
2272.4	1.58	ν_{as}(CD$_2$): 17 (7.6), 11 (7.7), 9 (7.6), 14 (5.1)
2274.0	4.73	ν_{as}(CD$_2$): 17 (13.6), 15 (6.3), 9 (5.0)
2275.1	15.73	ν_{as}(CD$_2$): 3 (18.6), 4 (8.4)
2280.2	2.80	ν_{as}(CD$_2$): 10 (9.8), 9 (9.7), 7 (7.7), 11 (7.4), 13 (6.8), 14 (5.9)
2284.7	30.93	ν_{as}(CD$_2$): 16 (18.7), 15 (16.2), 17 (8.8)
2285.2	22.13	ν_{as}(CD$_2$): 13 (12.4), 7 (9.4), 12 (8.8), 14 (8.2), 11 (6.1)
2286.6	83.34	ν_{as}(CD$_2$): 7 (13.4), 9 (7.9), 8 (7.7), 10 (5.5), 13 (5.5), 11 (5.3)
2298.1	25.53	ν_{as}(CD$_2$): 5 (26.7), 4 (8.5), 6 (7.1)
2305.4	1.64	ν_{as}(CD$_2$): 2 (28.4), 3 (6.5), 1 (6.3)
2306.5	19.56	ν_{as}(CD$_3$): 18 (50.0); ν_s(CD$_2$): 17 (9.1)
2313.4	18.75	ν_{as}(CD$_3$): 18 (48.5); ν_s(CD$_2$): 17 (7.1)
2327.0	3.62	ν_{as}(CD$_2$): 1 (49.0), 2 (7.9)

Table 12.6: Harmonic CD stretching vibrations of the [C_{18}Im-d_{37}][ClO_4] ion pair in heptane.

$\tilde{\nu}$ / cm⁻¹	I_{IR} / km mol⁻¹	Stretching vibration: participating group position in the alkyl chain (1 – α-CH₂ to 18 – terminal CH₃) (relative weight in %)
2188.0	14.48	$\nu_s(CD_3)$: 18 (62.3); $\nu_s(CD_2)$: 17 (5.9)
2189.0	2.01	$\nu_s(CD_2)$: 6 (23.8), 8 (16.2)
2191.8	4.64	$\nu_s(CD_2)$: 10 (14.5), 8 (11.2), 6 (9.9), 12 (7.0)
2193.5	4.41	$\nu_s(CD_2)$: 12 (14.2), 8 (8.1), 14 (6.6), 11 (6.3), 6 (5.0)
2195.4	1.03	$\nu_s(CD_2)$: 14 (8.4), 8 (7.6), 11 (7.5), 10 (6.9), 13 (6.9)
2196.9	21.14	$\nu_s(CD_2)$: 4 (15.3), 3 (14.0)
2197.3	1.38	$\nu_s(CD_2)$: 11 (14.7), 9 (10.5), 14 (10.3), 15 (5.9)
2198.1	29.33	$\nu_s(CD_2)$: 10 (8.9), 12 (8.7), 13 (6.3)
2200.9	3.85	$\nu_s(CD_2)$: 9 (15.9), 13 (11.7), 14 (5.9), 10 (5.2)
2202.2	33.35	$\nu_s(CD_2)$: 16 (16.7), 17 (9.7), 14 (8.0)
2203.2	46.07	$\nu_s(CD_2)$: 13 (12.6), 11 (9.8), 9 (7.2), 15 (7.0)
2203.8	38.95	$\nu_s(CD_2)$: 3 (21.8), 4 (18.9)
2205.4	43.04	$\nu_s(CD_2)$: 15 (20.8), 14 (11.9), 16 (8.5)
2208.3	26.71	$\nu_s(CD_2)$: 7 (20.1), 9 (8.1)
2209.0	16.86	$\nu_s(CD_2)$: 17 (26.0), 16 (14.9)
2223.4	12.67	$\nu_s(CD_2)$: 5 (28.3), 2 (15.5)
2225.6	6.81	$\nu_s(CD_2)$: 2 (28.0), 5 (15.6)
2246.5	17.08	$\nu_s(CD_2)$: 1 (42.5), 2 (5.5)
2249.3	3.17	$\nu_{as}(CD_2)$: 10 (9.3), 9 (9.1), 8 (8.4), 11 (7.1)
2250.9	3.66	$\nu_{as}(CD_2)$: 6 (8.0), 8 (7.2), 7 (5.4), 12 (6.7), 11 (6.3)
2253.1	4.96	$\nu_{as}(CD_2)$: 6 (11.4), 12 (6.5)
2256.7	0.42	$\nu_{as}(CD_2)$: 13 (7.3), 10 (7.4), 8 (7.3), 14 (6.2), 12 (5.3)
2261.4	5.75	$\nu_{as}(CD_2)$: 14 (9.6), 15 (8.5), 16 (6.0)
2264.2	0.45	$\nu_{as}(CD_2)$: 16 (8.7), 15 (6.6)
2265.0	9.45	$\nu_{as}(CD_2)$: 4 (15.8), 3 (7.6)
2271.8	1.37	$\nu_{as}(CD_2)$: 9 (8.0), 11 (7.8), 17 (6.7), 12 (5.3), 14 (5.2)
2273.6	7.10	$\nu_{as}(CD_2)$: 17 (15.2), 15 (6.9)
2275.8	16.35	$\nu_{as}(CD_2)$: 3 (19.3), 4 (8.2), 2 (5.3)
2279.1	3.67	$\nu_{as}(CD_2)$: 10 (9.6), 9 (8.8), 7 (8.0), 11 (7.6), 13 (6.2), 14 (5.6)
2283.8	3.85	$\nu_{as}(CD_2)$: 7 (11.5), 13 (10.8), 12 (7.0), 14 (6.5), 8 (6.0)
2284.0	42.61	$\nu_{as}(CD_2)$: 16 (21.5), 15 (19.5), 17 (10.1)
2285.0	128.02	$\nu_{as}(CD_2)$: 7 (9.9),13 (8.3), 9 (7.3), 12 (6.6), 8 (6.5), 11 (6.5), 10 (5.8)
2297.6	33.86	$\nu_{as}(CD_2)$: 5 (27.2), 4 (8.9), 6 (7.1)
2305.1	2.91	$\nu_{as}(CD_2)$: 2 (19.0), 3 (7.2), 5 (6.1), 1 (5.0)
2305.5	23.23	$\nu_{as}(CD_3)$: 18 (49.9); $\nu_{as}(CD_2)$: (9.2)
2312.3	21.96	$\nu_{as}(CD_3)$: 18 (48.5); $\nu_{as}(CD_2)$: (7.0)
2331.8	4.44	$\nu_{as}(CD_2)$: 1 (39.9), 2 (6.3)

Table 12.7: Harmonic CD stretching vibrations of the [C_{18}Im-d_{37}][ClO_4] ion pair in water.

$\tilde{\nu}$ / cm^{-1}	I_{IR} / km mol^{-1}	Stretching vibration: participating group position in the alkyl chain (1 – α-CH$_2$ to 18 – terminal CH$_3$) (relative weight in %)
2186.2	22.05	ν_s(CD$_3$): 18 (62.3); ν_s(CD$_2$): 17 (6.7)
2192.3	0.30	ν_s(CD$_2$): 8 (10.2), 6 (10.0), 9 (10.0), 11 (9.2), 12 (6.1)
2192.6	0.17	ν_s(CD$_2$): 10 (15.4), 12 (12.9), 8 (9.6), 9 (5.4)
2193.8	6.70	ν_s(CD$_2$): 6 (11.6), 11 (9.2), 14 (7.4), 10 (5.0)
2195.0	0.74	ν_s(CD$_2$): 9 (11.0), 12 (10.0), 11 (7.8), 7 (7.3), 14 (6.5), 8 (6.4)
2195.8	2.01	ν_s(CD$_2$): 14 (9.3), 6 (6.9), 8 (6.8), 13 (5.9), 15 (5.7), 12 (5.1)
2197.3	1.48	ν_s(CD$_2$): 11 (11.2), 9 (8.0), 7 (7.5), 6 (6.6), 14 (6.2), 10 (5.9)
2198.0	36.00	ν_s(CD$_2$): 10 (11.0), 12 (7.7), 8 (6.8), 7 (5.5)
2199.1	100.04	ν_s(CD$_2$): 7 (14.8), 9 (10.6), 8 (9.1)
2200.0	121.21	ν_s(CD$_2$): 13 (13.9), 16 (10.5), 14 (7.3), 11 (6.4), 12 (5.8), 17 (5.0)
2201.1	35.53	ν_s(CD$_2$): 4 (15.1), 3 (8.6), 16 (6.1)
2201.4	12.46	ν_s(CD$_2$): 16 (10.5), 13 (9.4), 17 (7.3), 4 (6.0)
2204.5	47.56	ν_s(CD$_2$): 15 (25.1), 14 (12.6), 16 (7.1)
2207.6	26.40	ν_s(CD$_2$): 3 (17.8), 4 (14.7)
2208.1	23.72	ν_s(CD$_2$): 17 (24.1), 16 (13.5)
2208.3	39.15	ν_s(CD$_2$): 5 (33.3)
2226.8	10.42	ν_s(CD$_2$): 2 (42.4)
2248.5	0.27	ν_{as}(CD$_2$): 10 (8.5), 9 (8.3), 11 (7.2), 8 (7.0), 12 (5.0)
2250.6	0.12	ν_{as}(CD$_2$): 7 (7.1), 12 (6.8), 8 (6.5), 11 (6.5), 6 (6.0)
2253.8	3.94	ν_{as}(CD$_2$): 6 (7.7), 12 (6.3), 9 (5.8), 13 (5.1)
2254.2	17.80	ν_s(CD$_2$): 1 (36.2)
2257.8	0.99	ν_{as}(CD$_2$): 14 (7.4), 13 (6.3), 6 (6.0), 8 (5.8), 11 (5.0)
2261.3	10.90	ν_{as}(CD$_2$): 15 (7.7), 14 (6.6), 16 (6.5)
2263.4	0.31	ν_{as}(CD$_2$): 16 (7.4), 15 (5.5)
2266.4	6.68	ν_{as}(CD$_2$): 4 (9.7)
2270.1	1.95	ν_{as}(CD$_2$): 9 (6.3), 11 (5.4), 4 (5.2), 12 (5.0)
2272.4	11.33	ν_{as}(CD$_2$): 17 (18.1), 15 (7.7)
2274.6	14.40	ν_{as}(CD$_2$): 3 (11.6), 11 (5.6), 8 (5.0)
2276.5	4.92	ν_{as}(CD$_2$): 3 (8.7), 10 (7.0), 11 (6.2), 7 (6.1), 6 (5.2), 4 (5.0)
2279.3	70.58	ν_{as}(CD$_2$): 8 (10.6), 9 (10.2), 7 (9.3), 10 (7.6)
2281.4	175.05	ν_{as}(CD$_2$): 13 (14.1), 14 (10.3), 12 (9.7), 15 (7.8), 11 (6.6), 16 (5.5)
2282.2	61.81	ν_{as}(CD$_2$): 16 (16.2), 15 (13.2), 13 (8.7), 17 (7.4), 12 (5.7)
2286.5	101.49	ν_{as}(CD$_2$): 5 (23.9), 4 (15.1), 6 (10.5), 3 (5.8)
2302.5	14.94	ν_{as}(CD$_2$): 2 (32.5), 3 (9.3)
2303.4	33.22	ν_{as}(CD$_3$): 18 (50.3); ν_{as}(CD$_2$): 17 (9.1)
2310.6	29.33	ν_{as}(CD$_3$): 18 (48.9); ν_{as}(CD$_2$): 17 (6.6)
2341.0	5.96	ν_{as}(CD$_2$): 1 (41.5)

Table 12.8: Cartesian coordinates of the ethanol molecule (E_{sp} = -155.102132 hartree, B3LYP-D3BJ/6-311++G(d,p)).

Symbol	x / Å	y / Å	z / Å	Symbol	x / Å	y / Å	z / Å
C	-1.222833	-0.223717	0.000004	H	0.13903	1.19436	0.887668
H	-2.074074	0.462519	0.00002	H	0.139021	1.194379	-0.887642
H	-1.289432	-0.859863	0.885585	O	1.154315	-0.396175	-0.000009
H	-1.289444	-0.85984	-0.885592	H	1.989865	0.079731	-0.00003
C	0.081252	0.550069	0.000006				

Table 12.9: Cartesian coordinates of the nonplanar C_2Im^+ cation (E_{sp} = -344.664785 hartree, B3LYP-D3BJ/6-311++G(d,p)).

Symbol	x / Å	y / Å	z / Å	Symbol	x / Å	y / Å	z / Å
C	1.177381	1.227004	0.079278	H	3.52653	-0.270328	-0.55112
C	-0.162436	1.304196	-0.149044	H	3.243746	-0.36657	1.209915
C	0.413171	-0.825787	-0.20329	C	-2.03035	-0.380261	-0.555428
N	1.51803	-0.112595	0.042026	H	-2.40407	0.244376	-1.367674
H	1.907849	1.997622	0.256653	H	-2.013709	-1.410432	-0.911706
H	-0.817612	2.156301	-0.204476	C	-2.873258	-0.235753	0.705351
H	0.365214	-1.898216	-0.290505	H	-2.897878	0.79815	1.054774
N	-0.620477	0.012205	-0.325861	H	-3.898275	-0.540256	0.487135
C	2.870622	-0.655909	0.228402	H	-2.492484	-0.868002	1.50975
H	2.827032	-1.740858	0.162487				

Table 12.10: Cartesian coordinates of the nonplanar C_2Im^+ cation (E_{sp} = -344.637191 hartree, B3LYP/6-311++G(d,p)).

Symbol	x / Å	y / Å	z / Å	Symbol	x / Å	y / Å	z / Å
C	-2.032026	-0.369958	-0.55725	C	-2.032026	-0.369958	-0.55725
C	-2.890951	-0.246668	0.69687	H	-2.890951	-0.246668	0.69687
N	-0.619959	0.019947	-0.317638	H	-0.619959	0.019947	-0.317638
C	1.185796	1.225656	0.083274	H	1.185796	1.225656	0.083274
C	-0.154188	1.308564	-0.140135	H	-0.154188	1.308564	-0.140135
C	0.412857	-0.819874	-0.201292	H	0.412857	-0.819874	-0.201292
N	1.522378	-0.113998	0.041866	H	1.522378	-0.113998	0.041866
H	1.917924	1.995411	0.259827	H	1.917924	1.995411	0.259827
H	-0.803155	2.166143	-0.192093	H	-0.803155	2.166143	-0.192093
H	0.361328	-1.892278	-0.292467				

Table 12.11: Cartesian coordinates of the nonplanar C_2Im^+ cation (E_{sp} = -344.522424 hartree, ωB97X-D/6-311++G(d,p)).

Symbol	x / Å	y / Å	z / Å	Symbol	x / Å	y / Å	z / Å
C	1.16982	1.222342	0.073129	H	3.516094	-0.265014	-0.552942
C	-0.165484	1.293979	-0.153767	H	3.234972	-0.350966	1.209544
C	0.41481	-0.822594	-0.197641	C	-2.020081	-0.390416	-0.550849
N	1.513373	-0.110364	0.042155	H	-2.392153	0.218237	-1.376163
H	1.897937	1.996873	0.246585	H	-2.003608	-1.427676	-0.887346
H	-0.823727	2.144371	-0.213	C	-2.865149	-0.222808	0.701513
H	0.369918	-1.896666	-0.279378	H	-2.891461	0.817923	1.030476
N	-0.617868	0.005458	-0.32326	H	-3.889026	-0.531817	0.486017
C	2.862167	-0.646942	0.229947	H	-2.486276	-0.839453	1.51887
H	2.822299	-1.732838	0.171083				

Table 12.12: Cartesian coordinates of the planar C_2Im^+ cation (E_{sp} = -344.636279 hartree, B3LYP/6-311++G(d,p)).

Symbol	x / Å	y / Å	z / Å	Symbol	x / Å	y / Å	z / Å
C	-2.127285	0.396511	0.000007	C	2.641338	-1.081201	0
C	-2.726963	-1.00021	-0.000004	H	2.331429	-2.12421	0.000004
N	-0.63878	0.404662	-0.000003	H	3.23183	-0.878898	-0.893023
C	1.439419	1.154708	0.000003	H	3.231839	-0.878893	0.893014
C	0.137593	1.548865	-0.000005	H	-2.44004	0.954889	0.884178
C	0.176282	-0.65439	-0.000001	H	-2.44005	0.954908	-0.884148
N	1.444064	-0.226802	0.000003	H	-2.451779	-1.567113	0.892423
H	2.348622	1.731838	-0.000009	H	-3.813855	-0.904397	-0.000005
H	-0.296576	2.534363	-0.000005	H	-2.45178	-1.567098	-0.892441
H	-0.128936	-1.686105	0.000006				

Table 12.13: Cartesian coordinates of the [C₂Im][TfO] ion pair (E_{sp} = -1306.547878 hartree, B3LYP-D3BJ/6-311++G(d,p)).

Symbol	x / Å	y / Å	z / Å	Symbol	x / Å	y / Å	z / Å
C	-2.787816	-1.292178	0.779231	H	-1.516954	2.034974	-1.525709
C	-3.058495	0.039821	0.723096	C	-1.6138	2.812316	0.479808
C	-1.588815	-0.421978	-0.861389	H	-2.250168	2.771074	1.367312
N	-1.867944	-1.559448	-0.218499	H	-1.538668	3.855674	0.166707
H	-3.154824	-2.059854	1.437203	H	-0.613831	2.455664	0.723325
H	-3.706096	0.651464	1.32521	S	1.730047	0.188277	-0.84951
H	-0.848572	-0.315881	-1.635046	C	1.7089	-0.103199	1.012672
N	-2.300788	0.563328	-0.309944	F	2.070099	0.994669	1.689105
C	-1.221671	-2.848655	-0.488061	F	0.451806	-0.432535	1.423293
H	-0.273058	-2.645725	-0.983102	F	2.518282	-1.10659	1.370213
H	-1.869273	-3.468343	-1.109209	O	0.750761	1.294511	-0.99513
H	-1.03105	-3.343741	0.462769	O	3.120595	0.49705	-1.156867
C	-2.185363	1.991855	-0.668703	O	1.203954	-1.101245	-1.36993
H	-3.178935	2.334769	-0.966202				

Table 12.14: Cartesian coordinates of the [C₂Im · 2 D₂O]⁺ complex (E_{sp} = -497.616029 hartree, B3LYP-D3BJ/6-311++G(d,p)).

Symbol	x / Å	y / Å	z / Å	Symbol	x / Å	y / Å	z / Å
C	1.11677	-1.749505	-0.430745	H	-0.706937	3.196947	1.299363
C	1.048046	-2.682155	0.772286	H	0.773353	-2.24293	-1.341319
N	0.275037	-0.548845	-0.242885	H	2.131444	-1.388936	-0.597531
C	-1.474	0.768791	0.02333	H	0.032641	-3.044496	0.944232
C	-1.107358	-0.521831	-0.200691	H	1.687316	-3.548612	0.593501
C	0.73861	0.689986	-0.046159	H	1.39643	-2.180263	1.677244
N	-0.30797	1.509163	0.117472	O	-4.148463	-0.687395	-0.162815
H	-2.456143	1.197527	0.114953	D	-4.704611	-0.963059	0.574201
H	-1.722986	-1.39347	-0.332644	D	-4.726409	-0.721561	-0.933098
H	1.785745	0.959855	-0.03364	O	3.813509	0.527326	-0.246375
C	-0.231044	2.95462	0.349768	D	4.345225	0.749436	-1.019421
H	0.815325	3.250566	0.383092	D	4.445479	0.445791	0.477166
H	-0.73184	3.4821	-0.461427				

13 Abbreviations and Symbols

Table 13.1: Acronyms.

Acronym	Meaning
ACV	Alternating current voltammetry
AOT	1,4-bis(2-ethylhexoxy)-1,4-dioxobutane-2-sulfonate
ATR	Attenuated total reflection
BSSE	Basis set superposition error
CARS	Coherent anti-Stokes Raman scattering
EDL	Electrical double layer
EIS	Electrochemical impedance spectroscopy
FT	Fourier transformed
GC	Glassy carbon
GVPT2	Generalized second-order vibrational perturbation theory
HF	Hartree-Fock
HTMS	High temperature molten salt
HOPG	Highly oriented pyrolytic graphite
HWR	Half-wave retardation
IHP	Inner Helmholtz plane
Im	Imdiazolium
IRRAS	Infrared reflection absorption spectroscopy
IRS	Infrared spectroscopy
MSSR	Metal surface selection rule
NBO	Natural bond orbital
OHP	Outer Helmholtz plane
PB	Poisson-Boltzmann
PCM	Polarizable continuum model
PFC	Polyfluorinated compound
PM	Polarization modulation
PZC	Point of zero charge
PZTC	Point of zero total charge
Tf	Triflyl
WE	Working electrode
XPS	X-ray photoelectron spectroscopy
fwhm	Full width at half maximum

Table 13.2: Latin symbols.

Symbol	Property/Meaning	Indices
$\mathcal{A}$	Absorbance	
A	Interfacial area	molec – mean molecular area
		molec,0 – lift-off mean molecular area
		molec,lim – limiting mean molecular area
		molec,t – mean molecular area at transfer
B	Excess charge factor	
C	Differential capacitance per unit area (real)	complex – complex capacitance
		diffuse – diffuse or Gouy-Chapman layer
		inner – inner or Helmholtz layer
		min – minimum
$\tilde{C}$	Integral capacitance	
D	$= (d_1 + a)/d_1$	
E	Energy	b – binding energy of an electron
		kin – kinetic energy of an electron
		N – system with N electrons
		pot – potential energy
		sp – single point energy
		sp, min – sp energy of the minimum energy conformer
$\vec{E}$	Electric field vector	z – in z-direction
F	Force	
G	Free enthalpy	
I	Intensity (without index for XPS)	IR – calculated integrated IR absorption coefficient
		Raman – calculated integrated Raman scattering activity
J_τ	Bessel function	τ – integer order of the function
K^{-1}	Inverse compressibility modulus	
$\mathcal{K}$	Threshold fort he Martin test	
$\vec{M}$	Transition dipole moment vector	
$\mathcal{N}$	Particle number	
N	Number of electrons	
Q	Atomic charge by NBO analysis	Indices for H and C elements
R	Reflectivity	d – detected
		s – perpendicularly polarized
		p – parallelly polarized
$\mathcal{R}$	Residuals	

S	PM IRRAS signal	background – uncovered surface raw – uncorrected spectrum
$\mathcal{S}$	Segmental order parameter	
T	Temperature	m – melting point
U	Electrode potential with respect to a reference electrode	
W	Electrical work for ion transfer	
Z	Complex impedance	
Z'	Real impedance	
Z''	Imaginary impedance	
a	Distance between ionic layers following the first layer in a molten salt	
c	Molar volume concentration	
$\tilde{c}$	Bulk number concentration	
d	Screening length	1 – to the first ionic layer sol – solvation shell
exp	In equations: Euler's number In indices: experimental	
h	Planck constant	
f	Frequency of alternating voltage or current	
i	Current	
j	Imaginary unit	
k	Attenuation coefficient	
$\mathbb{k}$	Force constant of an oscillator	f – fundamental mode in FR i, j – combination or overtone in FR Three indices indicate cubic force constants.
k_B	Boltzmann constant	
l	Circumference of the Wilhelmy plate	
m	Reduced mass	
n	Refractive index	
n	Amount of substance at the interface	i – for a given species
p	Pressure	
p	Polarization parallel to the plane of incidence	
q	Ionic charge	
r	Internuclear distance	

s	Polarization perpendicular to the plane of incidence	
t	time	
v	Vibrational quantum number	
x	Space coordinate along the surface	
y	Space coordinate along the surface	
z	Space coordinate along the surface normal	

Table 13.3: Greek symbols.

Symbol	Property/Meaning	Indices
Γ	Surface excess / concentration	lim – at limiting mean molecular area t – at transfer
Θ	Surface coverage	
Λ	Fermi resonance probability	
Π	Surface pressure	
Φ	Angle of incidence for the IR beam	
α	Polarizability	
β	An effective screening length in the model of Sotnikov and Esin	
γ	Surface tension	0 – uncovered subphase L – liquid G – gaseous S – solid
δ	An effective screening length in the model of Sotnikov and Esin	
ε	Permittivity	
ϵ	Molar extinction coefficient	
ζ	Natural number	$\tilde{v}$ – added to $\tilde{v}_{HWR}$ ω – added to ω_m
θ	Tilt angle of the index vector with respect to the electric field vector	as – asymmetrical methylene stretching $\vec{M}$ backbone – methylene backbone axis sym – symmetrical methylene stretching $\vec{M}$

ϑ	Water contact angle	
κ	Inverse Debye length	
λ	Inverse ionic correlation radius	
μ	Chemical potential	
ν	Frequency	osc – oscillator
		photon – idem
$\tilde{\nu}$	Wavenumber	HWR – wavenumber at the HWR
ξ	Effective coordination number	
π	Archimedes constant	
ρ	Space charge density	
φ	Phase shift of alternating current with respect to alternating voltage	
ϕ	Work function of the X-ray photoelectron spectrometer	
σ	Surface charge density per unit area	
τ	Order of a Bessel function (integer)	
ψ	Potential at a plane within the electrical double layer	
ω	Angular frequency	AC – alternating current or voltage
		m – photoelastic modulator

Table 13.4: Vibrational nomenclature according to Schrader.[149] Ring modes are named as proposed by Lassègues, Grondin et al.[151, 175]

Symbol	Meaning
Vibrations:	
ν	Stretching
δ	Deformation / Scissoring
ϱ	Rocking
ω	Wagging
τ	Twisting
R	Ring modes composed of several vibrations
FR	Overtone or combination band enhanced by Fermi resonance
With indices: as – asymmetric and s – symmetric	
Intensities:	
vs	Very strong
s	Strong
m	Medium
w	Weak
vw	Very weak
sh	shoulder

14 References

[1]   W. Demtröder, *Experimentalphysik 1: Mechanik und Wärme*, Vierte, neu bearbeitete und aktualisierte Auflage, Springer, Berlin, Heidelberg, **2006**.

[2]   A. Behr, J. Gmehling, M. Baerns, A. Brehm, K.-O. Hinrichsen, H. Hofmann, U. Onken, R. Palkovits, A. Renken, *Technische Chemie*, John Wiley & Sons, Inc., Weinheim, **2013**.

[3]   A. J. Bard, L. R. Faulkner, *Electrochemical methods: Fundamentals and Applications*, 2nd ed., Wiley, Hoboken, **2001**.

[4]   K. Cammann, *Instrumentelle analytische Chemie: Verfahren, Anwendungen und Qualitätssicherung*, Spektrum, Akademischer Verlag, Heidelberg, **2001**.

[5]   C. Reichardt, T. Welton, *Solvents and solvent effects in organic chemistry*, 4th, updated and enl., Wiley-VCH, Weinheim, Germany, **2011**.

[6]   A. B. Lindstrom, M. J. Strynar, E. L. Libelo, *Environ. Sci. Technol.* **2011**, *45*, 7954-7961.

[7]   P. Domínguez de María, in *The Application of Green Solvents in Separation Processes* (Eds.: F. Pena-Pereira, M. Tobiszewski), Elsevier, **2017**, pp. 139-154.

[8]   N. V. Plechkova, K. R. Seddon, *Chem. Soc. Rev.* **2008**, *37*, 123-150.

[9]   T. J. S. Schubert, in *Ionic Liquids: Current State and Future Directions, Vol. 1250* (Eds.: M. B. Shifflet, A. M. Scurto), American Chemical Society, Washington, DC, **2017**, pp. 35-65.

[10]   T. Alpers, M. Schmidtmann, T. W. T. Muesmann, O. Temme, J. Christoffers, *Eur. J. Org. Chem.* **2017**, *2017*, 4283-4290.

[11]   T. Alpers, T. W. T. Muesmann, O. Temme, J. Christoffers, *Eur. J. Org. Chem.* **2018**, *2018*, 4331-4337.

[12]   M. P. Krafft, J. G. Riess, *Chem. Rev.* **2009**, *109*, 1714-1792.

[13]   N. G. Rey, D. D. Dlott, *J. Phys. Chem. C* **2015**, *119*, 20892-20899.

[14]   B. A. Rosen, J. L. Haan, P. Mukherjee, B. Braunschweig, W. Zhu, A. Salehi-Khojin, D. D. Dlott, R. I. Masel, *J. Phys. Chem. C* **2012**, *116*, 15307-15312.

[15]   B. A. Rosen, A. Salehi-Khojin, M. R. Thorson, W. Zhu, D. T. Whipple, P. J. A. Kenis, R. I. Masel, *Science* **2011**, *334*, 643-644.

[16]   D. C. Grahame, *Chem. Rev.* **1947**, *41*, 441-501.

[17]   R. Parsons, *Chem. Rev.* **1990**, *90*, 813-826.

[18]   A. D. Graves, *J. Electroanal. Chem. Interfacial Electrochem.* **1970**, *25*, 349-356.

[19] A. D. Graves, D. Inman, *J. Electroanal. Chem. Interfacial Electrochem.* **1970**, *25*, 357-372.

[20] M. V. Fedorov, A. A. Kornyshev, *Chem. Rev.* **2014**, *114*, 2978-3036.

[21] J. N. A. C. Lopes, A. A. H. Padua, *J. Phys. Chem. B* **2006**, *110*, 3330-3335.

[22] A. Triolo, O. Russina, H. J. Bleif, E. Di Cola, *J. Phys. Chem. B* **2007**, *111*, 4641-4644.

[23] B. Kirchner, F. Malberg, D. S. Firaha, O. Hollóczki, *J. Phys.: Condens. Matter* **2015**, *27*, 463002.

[24] X. Mao, P. Brown, C. Červinka, G. Hazell, H. Li, Y. Ren, D. Chen, R. Atkin, J. Eastoe, I. Grillo, A. A. H. Padua, M. F. Costa Gomes, T. A. Hatton, *Nat. Mater.* **2019**, *18*, 1350-1357.

[25] E. J. M. Filipe, P. Morgado, M. Teixeira, K. Shimizu, N. Bonatout, M. Goldmann, J. N. C. Lopes, *Chem. Commun.* **2016**, *52*, 5585-5588.

[26] H. P. Steinrück, J. Libuda, P. Wasserscheid, T. Cremer, C. Kolbeck, M. Laurin, F. Maier, M. Sobota, P. S. Schulz, M. Stark, *Adv. Mater.* **2011**, *23*, 2571-2587.

[27] T. Cui, A. Lahiri, T. Carstens, N. Borisenko, G. Pulletikurthi, C. Kuhl, F. Endres, *J. Phys. Chem. C* **2016**, *120*, 9341-9349.

[28] Z. Liu, S. Z. El Abedin, F. Endres, *ChemPhysChem* **2015**, *16*, 970-977.

[29] S. Schernich, D. Kostyshyn, V. Wagner, N. Taccardi, M. Laurin, P. Wasserscheid, J. Libuda, *J. Phys. Chem. C* **2014**, *118*, 3188-3193.

[30] O. Brummel, F. Faisal, T. Bauer, K. Pohako-Esko, P. Wasserscheid, J. Libuda, *Electrochim. Acta* **2016**, *188*, 825-836.

[31] T. Bauer, S. Mehl, O. Brummel, K. Pohako-Esko, P. Wasserscheid, J. Libuda, *J. Phys. Chem. C* **2016**, *120*, 4453-4465.

[32] N. E. Heimer, R. E. Del Sesto, Z. Z. Meng, J. S. Wilkes, W. R. Carper, *J. Mol. Liq.* **2006**, *124*, 84-95.

[33] D. K. Singh, B. Rathke, J. Kiefer, A. Materny, *J. Phys. Chem. A* **2016**, *120*, 6274-6286.

[34] J. Kiefer, M. Stuckenholz, B. Rathke, *J. Mol. Liq.* **2018**, *255*, 413-418.

[35] S. Chatzipapadopoulos, T. Zentel, R. Ludwig, M. Lütgens, S. Lochbrunner, O. Kühn, *ChemPhysChem* **2015**, *16*, 2519-2523.

[36] E. R. Talaty, S. Raja, V. J. Storhaug, A. Dölle, W. R. Carper, *J. Phys. Chem. B* **2004**, *108*, 13177-13184.

[37] R. Cooper, A. M. Zolot, J. A. Boatz, D. P. Sporleder, J. A. Stearns, *J. Phys. Chem. A* **2013**, *117*, 12419-12428.

[38] Y. Wang, R. Jarošová, G. M. Swain, G. J. Blanchard, *Langmuir* **2020**, *36*, 3038-3045.

[39] P. Walden, *Bull. Acad. Impér. Sci. St. Pétersbourg* **1914**, *8*, 405-422.

[40] P. Wasserscheid, *Chem. unserer Zeit* **2003**, *37*, 52-63.

[41] J. S. Wilkes, M. J. Zaworotko, *J. Chem. Soc., Chem. Commun.* **1992**, 965-967.

[42] M. A. Gebbie, H. A. Dobbs, M. Valtiner, J. N. Israelachvili, *Proceedings of the National Academy of Sciences* **2015**, *112*, 7432.

[43] Y. Marcus, *Ionic Liquid Properties: From Molten Salts to RTILs*, Springer Berlin Heidelberg, New York, USA, **2016**.

[44] P. Hapiot, C. Lagrost, *Chem. Rev.* **2008**, *108*, 2238-2264.

[45] A. A. Kornyshev, *J. Phys. Chem. B* **2007**, *111*, 5545-5557.

[46] S. Fletcher, V. J. Black, I. Kirkpatrick, T. S. Varley, *J. Solid State Electrochem.* **2013**, *17*, 327-337.

[47] E. I. Obi, C. M. Leavitt, P. L. Raston, C. P. Moradi, S. D. Flynn, G. L. Vaghjiani, J. A. Boatz, S. D. Chambreau, G. E. Douberly, *J. Phys. Chem. A* **2013**, *117*, 9047-9056.

[48] M. Haumann, P. Wasserscheid, in *Catalysis in Ionic Liquids: From Catalyst Synthesis to Application*, The Royal Society of Chemistry, **2014**, pp. 410-432.

[49] C. Graenacher (Society of Chemical Industry in Basle), Patent: US-A 1943176, **1934**.

[50] G. Wedler, H.-J. Freund, *Lehrbuch der physikalischen Chemie*, 6., vollst. überarb. und aktualisierte Aufl., Wiley-VCH, Weinheim, **2012**.

[51] D. M. Kolb, J. Schneider, *Electrochim. Acta* **1986**, *31*, 929-936.

[52] H. Helmholtz, *Ann. Phys.* **1879**, *243*, 337-382.

[53] G. Valette, A. Hamelin, R. Parsons, *Z. Phys. Chem.* **1978**, *113*, 71-89.

[54] G. Valette, *J. Electroanal. Chem.* **1989**, *269*, 191-203.

[55] G. Valette, *J. Electroanal. Chem.* **1982**, *138*, 37-54.

[56] M. Gouy, *J. Phys. Theor. Appl.* **1910**, *9*, 457-468.

[57] D. L. Chapman, *The London, Edinburgh, and Dublin Philosophical Magazine and Journal of Science* **1913**, *25*, 475-481.

[58] O. Stern, *Zeitschrift für Elektrochemie und angewandte physikalische Chemie* **1924**, *30*, 508-516.

[59] J. O. M. Bockris, M. A. V. Devanathan, K. Müller, *Proceedings of the Royal Society of London. Series A. Mathematical and Physical Sciences* **1963**, *274*, 55-79.

[60] W. Schmickler, *Chem. Rev.* **1996**, *96*, 3177-3200.

[61] J. J. Lopez-Garcia, J. Horno, C. Grosse, *J. Colloid Interface Sci.* **2017**, *496*, 531-539.

[62] E. A. Ukshe, N. G. Bukun, D. I. Leikis, A. N. Frumkin, *Electrochim. Acta* **1964**, *9*, 431-439.

[63] R. R. Dogonadze, Y. A. Chizmadzhev, *Dokl. Akad. Nauk SSSR* **1964**, *157*, 4.

[64]   A. I. Sotnikov, O. A. Esin, in *Physical Chemistry and Electrochemistry of Molten Salts and Slags (Proceedings 3rd All-Soviet Conference, 1966)*, Khimiya, **1968**, pp. 209-214.

[65]   A. Kisza, *Electrochim. Acta* **2006**, *51*, 2315-2321.

[66]   M. V. Fedorov, A. A. Kornyshev, *Chemical Reviews* **2014**, *114*, 2978-3036.

[67]   C. Nanjundiah, S. F. McDevitt, V. R. Koch, *J. Electrochem. Soc.* **1997**, *144*, 3392-3397.

[68]   R. J. Gale, R. A. Osteryoung, *Electrochim. Acta* **1980**, *25*, 1527-1529.

[69]   S. Baldelli, *J. Phys. Chem. B* **2005**, *109*, 13049-13051.

[70]   H. N. Wang, L. Pilon, *Electrochim. Acta* **2012**, *63*, 55-63.

[71]   B. Roling, M. Druschler, *Electrochim. Acta* **2012**, *76*, 526-528.

[72]   H. N. Wang, L. Pilon, *Electrochim. Acta* **2012**, *76*, 529-531.

[73]   K. B. Oldham, *J. Electroanal. Chem.* **2008**, *613*, 131-138.

[74]   M. V. Fedorov, A. A. Kornyshev, *J. Phys. Chem. B* **2008**, *112*, 11868-11872.

[75]   K. Kirchner, T. Kirchner, V. Ivanistsev, M. V. Fedorov, *Electrochim. Acta* **2013**, *110*, 762-771.

[76]   R. G. Horn, D. F. Evans, B. W. Ninham, *J. Phys. Chem.* **1988**, *92*, 3531-3537.

[77]   R. Atkin, G. G. Warr, *J. Phys. Chem. C* **2007**, *111*, 5162-5168.

[78]   R. Hayes, S. Z. El Abedin, R. Atkin, *J. Phys. Chem. B* **2009**, *113*, 7049-7052.

[79]   X. Zhang, Y. X. Zhong, J. W. Yan, Y. Z. Su, M. Zhang, B. W. Mao, *Chem. Commun.* **2012**, *48*, 582-584.

[80]   Y. X. Zhong, J. W. Yan, M. G. Li, X. Zhang, D. W. He, B. W. Mao, *J. Am. Chem. Soc.* **2014**, *136*, 14682-14685.

[81]   Y. X. Zhong, J. W. Yan, M. G. Li, L. Chen, B. W. Mao, *Chemelectrochem* **2016**, *3*, 2221-2226.

[82]   S. Perkin, L. Crowhurst, H. Niedermeyer, T. Welton, A. M. Smith, N. N. Gosvami, *Chem. Commun.* **2011**, *47*, 6572-6574.

[83]   M. V. Fedorov, N. Georgi, A. A. Kornyshev, *Electrochem. Commun.* **2010**, *12*, 296-299.

[84]   N. Nishi, A. Hashimoto, E. Minami, T. Sakka, *Phys. Chem. Chem. Phys.* **2015**, *17*, 5219-5226.

[85]   N. Nishi, S. Yasui, A. Hashimoto, T. Sakka, *J. Electroanal. Chem.* **2017**, *789*, 108-113.

[86]   M. T. Alam, M. M. Islam, T. Okajima, T. Ohsaka, *J. Phys. Chem. C* **2008**, *112*, 16600-16608.

[87]   M. T. Alam, J. Masud, M. M. Islam, T. Okajima, T. Ohsaka, *J. Phys. Chem. C* **2011**, *115*, 19797-19804.

[88]   C. Gomes, R. Costa, C. M. Pereira, A. F. Silva, *RSC Advances* **2014**, *4*, 28914-28921.

[89]   T. R. Gore, T. Bond, W. B. Zhang, R. W. J. Scott, I. J. Burgess, *Electrochem. Commun.* **2010**, *12*, 1340-1343.

[90]   M. Gnahm, T. Pajkossy, D. M. Kolb, *Electrochim. Acta* **2010**, *55*, 6212-6217.

[91]   M. Gnahm, C. Müller, R. Répánszki, T. Pajkossy, D. M. Kolb, *Phys. Chem. Chem. Phys.* **2011**, *13*, 11627-11633.

[92]   C. Muller, S. Vesztergom, T. Pajkossy, T. Jacob, *J. Electroanal. Chem.* **2015**, *737*, 218-225.

[93]   T. Pajkossy, C. Muller, T. Jacob, *Phys Chem Chem Phys* **2018**, *20*, 21241-21250.

[94]   A. J. Lucio, S. K. Shaw, J. Zhang, A. M. Bond, *J. Phys. Chem. C* **2017**, *121*, 12136-12147.

[95]   N. M. Vargas-Barbosa, B. Roling, *J. Chem. Phys.* **2018**, *148*.

[96]   M. M. Islam, M. T. Alam, T. Ohsaka, *J. Phys. Chem. C* **2008**, *112*, 16568-16574.

[97]   V. Lockett, M. Horne, R. Sedev, T. Rodopoulos, J. Ralston, *Phys. Chem. Chem. Phys.* **2010**, *12*, 12499-12512.

[98]   L. J. Small, D. R. Wheeler, *J. Electrochem. Soc.* **2014**, *161*, H260-H263.

[99]   C. Aliaga, S. Baldelli, *J. Phys. Chem. B* **2006**, *110*, 18481-18491.

[100]   B. Roling, M. Drüschler, B. Huber, *Faraday Discuss.* **2012**, *154*, 303-311.

[101]   V. Lockett, R. Sedev, J. Ralston, M. Horne, T. Rodopoulos, *J. Phys. Chem. C* **2008**, *112*, 7486-7495.

[102]   C. Muller, K. Nemeth, S. Vesztergom, T. Pajkossy, T. Jacob, *Phys. Chem. Chem. Phys.* **2016**, *18*, 916-925.

[103]   M. Druschler, B. Roling, *Electrochim. Acta* **2011**, *56*, 7243-7245.

[104]   T. Pajkossy, *Electrochim. Acta* **2011**, *56*, 7246-7247.

[105]   T. Pajkossy, R. Jurczakowski, *Curr. Opin. Electrochem.* **2017**, *1*, 53-58.

[106]   C. Muller, S. Vesztergom, T. Pajkossy, T. Jacob, *Electrochim. Acta* **2016**, *188*, 512-515.

[107]   S. Makino, Y. Kitazumi, N. Nishi, T. Kakiuchi, *Electrochem. Commun.* **2011**, *13*, 1365-1368.

[108]   R. S. Anaredy, S. K. Shaw, *Langmuir* **2016**, *32*, 5147-5154.

[109]   J. Lindner, F. Weick, F. Endres, R. Schuster, *J. Phys. Chem. C* **2020**, *124*, 693-700.

[110]   K. Motobayashi, K. Minami, N. Nishi, T. Sakka, M. Osawa, *J. Phys. Chem. Lett.* **2013**, *4*, 3110-3114.

[111]   K. Motobayashi, N. Nishi, Y. Inoue, K. Minami, T. Sakka, M. Osawa, *J. Electroanal. Chem.* **2017**, *800*, 126-133.

[112]   S. Rivera-Rubero, S. Baldelli, *J. Phys. Chem. B* **2004**, *108*, 15133-15140.

[113] A. V. Rudnev, M. R. Ehrenburg, E. B. Molodkina, A. Abdelrahman, M. Arenz, P. Broekmann, T. Jacob, *ChemElectroChem* **2020**, *7*, 501-508.

[114] R. Wen, B. Rahn, O. M. Magnussen, *Angew. Chem. Int. Ed.* **2015**, *54*, 6062-6066.

[115] G. G. Roberts, *Langmuir-Blodgett films*, Plenum Press, New York, **1990**.

[116] D. Briggs, J. T. Grant, *Surface analysis by Auger and x-ray photoelectron spectroscopy*, IM Publications, Chichester, West Sussex, **2003**.

[117] B. D. Ratner, D. G. Castner, in *Surface Analysis: The Principal Techniques* 2nd Ed. ed. (Eds.: J. C. Vickerman, I. S. Gilmore), Wiley, Chichester, U.K., **2009**.

[118] M. Hesse, H. Meier, B. Zeeh, *Spektroskopische Methoden in der organischen Chemie*, 7., überarb. Aufl., Thieme, Stuttgart, New York, **2005**.

[119] F. M. Mirabella, *Modern Techniques in Applied Molecular Spectroscopy*, John Wiley & Sons, Inc., New York, NY, **1998**.

[120] I. Brand, *Application of Polarization Modulation Infrared Reflection Absorption Spectroscopy in Electrochemistry*, 1st ed. 2020., Cham Springer International Publishing, **2020**.

[121] A. Lasia, *Electrochemical Impedance Spectroscopy and its Applications*, Springer, New York, **2014**.

[122] E. Rogalska, R. Bilewicz, T. Brigaud, C. El Moujahid, G. Foulard, C. Portella, M. J. Stebe, *Chem. Phys. Lipids* **2000**, *105*, 71-91.

[123] D. B. Cordes, M. Smiglak, C. C. Hines, N. J. Bridges, M. Dilip, G. Srinivasan, A. Metlen, R. D. Rogers, *Chem. Eur. J.* **2009**, *15*, 13441-13448.

[124] A. Bondi, *J. Phys. Chem.* **1964**, *68*, 441-451.

[125] E. Blanco, Á. Piñeiro, R. Miller, J. M. Ruso, G. Prieto, F. Sarmiento, *Langmuir* **2009**, *25*, 8075-8082.

[126] A. Yokozeki, D. J. Kasprzak, M. B. Shiflett, *Phys. Chem. Chem. Phys.* **2007**, *9*, 5018-5026.

[127] T. Cremer, M. Stark, A. Deyko, H. P. Steinruck, F. Maier, *Langmuir* **2011**, *27*, 3662-3671.

[128] T. Cremer, L. Wibmer, S. K. Calderon, A. Deyko, F. Maier, H. P. Steinruck, *Phys. Chem. Chem. Phys.* **2012**, *14*, 5153-5163.

[129] D. A. Beattie, S. L. Harmer-Bassell, T. T. M. Ho, M. Krasowska, J. Ralston, P. M. F. Sellapperumage, P. Wasik, *Phys. Chem. Chem. Phys.* **2015**, *17*, 4199-4209.

[130] I. J. Villar-Garcia, E. F. Smith, A. W. Taylor, F. Qiu, K. R. J. Lovelock, R. G. Jones, P. Licence, *Phys. Chem. Chem. Phys.* **2011**, *13*, 2797-2808.

[131]   K. Ford, B. J. Battersby, B. J. Wood, I. R. Gentle, *J. Colloid Interface Sci.* **2012**, *370*, 162-169.

[132]   S. Frey, K. Heister, M. Zharnikov, M. Grunze, K. Tamada, R. Colorado Jr, M. Graupe, O. E. Shmakova, T. R. Lee, *Isr. J. Chem.* **2000**, *40*, 81-97.

[133]   A. Shaporenko, P. Cyganik, M. Buck, A. Ulman, M. Zharnikov, *Langmuir* **2005**, *21*, 8204-8213.

[134]   H. Lu, D. Zeysing, M. Kind, A. Terfort, M. Zharnikov, *J. Phys. Chem. C* **2013**, *117*, 18967-18979.

[135]   A. Downard, M. J. Earle, C. Hardacre, S. E. J. McMath, M. Nieuwenhuyzen, S. J. Teat, *Chem. Mater.* **2004**, *16*, 43-48.

[136]   B. Koslowski, H. G. Boyen, C. Wilderotter, G. Kästle, P. Ziemann, R. Wahrenberg, P. Oelhafen, *Surf. Sci.* **2001**, *475*, 1-10.

[137]   A. I. Stadnichenko, S. V. Koshcheev, A. I. Boronin, *Moscow Univ. Chem. Bull. (Engl. Transl.)* **2007**, *62*, 343-349.

[138]   Z. Zheng, M. Yang, B. Zhang, *J. Phys. Chem. C* **2008**, *112*, 6597-6604.

[139]   R. F. Tabor, A. J. Morfa, F. Grieser, D. Y. C. Chan, R. R. Dagastine, *Langmuir* **2011**, *27*, 6026-6030.

[140]   G. N. Kastanas, B. E. Koel, *Appl. Surf. Sci.* **1993**, *64*, 235-249.

[141]   W. Gao, T. A. Baker, L. Zhou, D. S. Pinnaduwage, E. Kaxiras, C. M. Friend, *J. Am. Chem. Soc.* **2008**, *130*, 3560-3565.

[142]   J. H. Scofield, *J. Electron. Spectrosc. Relat. Phenom.* **1976**, *8*, 129-137.

[143]   J. F. Moulder, W. F. Stickle, P. E. Sobol, K. D. Bomben, *Handbook of X-ray Photoelectron Spectroscopy: A Reference Book of Standard Spectra for Identification and Interpretation of XPS Data*, Physical Electronics Inc., Eden Prairie, USA, **1995**.

[144]   D. Martin-Vosshage, B. V. R. Chowdari, *J. Electrochem. Soc.* **1993**, *140*, 3531-3536.

[145]   S. L. Hsu, N. Reynolds, S. P. Bohan, H. L. Strauss, R. G. Snyder, *Macromolecules* **1990**, *23*, 4565-4575.

[146]   T. J. Lenk, V. M. Hallmark, C. L. Hoffmann, J. F. Rabolt, D. G. Castner, C. Erdelen, H. Ringsdorf, *Langmuir* **1994**, *10*, 4610-4617.

[147]   F. Jensen, *Introduction to computational chemistry*, 2nd Ed., John Wiley & Sons, Chichester, England; Hoboken, USA, **2007**.

[148]   S. Grimme, J. Antony, S. Ehrlich, H. Krieg, *J. Chem. Phys.* **2010**, *132*, 154104.

[149]   B. Schrader, *Infrared and Raman Spectroscopy: Methods and Applications*, John Wiley & Sons Inc., Berlin, **1995**.

[150]   T. Yamada, Y. Tominari, S. Tanaka, M. Mizuno, *J. Phys. Chem. B* **2017**, *121*, 3121-3129.

[151]   J. Grondin, J. C. Lassegues, D. Cavagnat, T. Buffeteau, P. Johansson, R. Holomb, *J. Raman Spectrosc.* **2011**, *42*, 733-743.

[152] S. Sadhu, K. Aqueche, T. Buffeteau, J. M. Vincent, L. Hirsch, D. M. Bassani, *Mater. Horiz.* **2019**, *6*, 192-197.

[153] IoLiTec Ionic Liquids Technologies, 1-Methyl-3-octadecylimidazolium chloride, https://iolitec.de/products/ionic_liquids/catalogue/imidazolium-based/il-0160-hp, accessed on 05.01.21.

[154] J. Clavilier, N. Vanhuong, *J. Electroanal. Chem.* **1973**, *41*, 193-199.

[155] J. Lipkowski, Z. C. Shi, A. C. Chen, B. Pettinger, C. Bilger, *Electrochim. Acta* **1998**, *43*, 2875-2888.

[156] C. Jungnickel, J. Luczak, J. Ranke, J. F. Fernandez, A. Muller, J. Thoming, *Colloids Surf., A* **2008**, *316*, 278-284.

[157] T. Pajkossy, T. Wandlowski, D. M. Kolb, *J. Electroanal. Chem.* **1996**, *414*, 209-220.

[158] D. M. Small, *J. Lipid Res.* **1984**, *25*, 1490-1500.

[159] M. A. Amin, *Electrochim. Acta* **2009**, *54*, 1857-1863.

[160] F. P. Coenen, M. Kastner, G. Pirug, H. P. Bonzel, U. Stimming, *J. Phys. Chem.* **1994**, *98*, 7885-7890.

[161] R. J. Thorn, K. D. Carlson, G. W. Crabtree, H. H. Wang, *J. Phys. C: Solid State Phys.* **1985**, *18*, 5501-5510.

[162] U. E. Zhumaev, A. S. Lai, I. V. Pobelov, A. Kuzume, A. V. Rudnev, T. Wandlowski, *Electrochim. Acta* **2014**, *146*, 112-118.

[163] U. E. Zhumaev, I. V. Pobelov, A. V. Rudnev, A. Kuzume, T. Wandlowski, *Electrochem. Commun.* **2014**, *44*, 31-33.

[164] J.-F. Li, Y.-J. Zhang, A. V. Rudnev, J. R. Anema, S.-B. Li, W.-J. Hong, P. Rajapandiyan, J. Lipkowski, T. Wandlowski, Z.-Q. Tian, *J. Am. Chem. Soc.* **2015**, *137*, 2400-2408.

[165] L. Stolberg, S. Morin, J. Lipkowski, D. E. Irish, *J. Electroanal. Chem. Interfacial Electrochem.* **1991**, *307*, 241-262.

[166] T. Laredo, J. Leitch, M. H. Chen, I. J. Burgess, J. R. Dutcher, J. Lipkowski, *Langmuir* **2007**, *23*, 6205-6211.

[167] G. Valincius, M. Mickevicius, in *Advances in Planar Lipid Bilayers and Liposomes, Vol. 21* (Eds.: A. Iglič, C. V. Kulkarni, M. Rappolt), Academic Press, **2015**, pp. 27-61.

[168] G. Valincius, T. Meškauskas, F. Ivanauskas, *Langmuir* **2012**, *28*, 977-990.

[169] Z. Su, M. Shodiev, J. J. Leitch, F. Abbasi, J. Lipkowski, *Langmuir* **2018**, *34*, 6249-6260.

[170] S. A. Katsyuba, P. J. Dyson, E. E. Vandyukova, A. V. Chernova, A. Vidiš, *Helv. Chim. Acta* **2004**, *87*, 2556-2565.

[171] R. G. Snyder, S. L. Hsu, S. Krimm, *Spectrochim. Acta, Part A* **1978**, *34*, 395-406.

[172]   R. G. Snyder, H. L. Strauss, C. A. Elliger, *J. Phys. Chem.* **1982**, *86*, 5145-5150.

[173]   R. A. Macphail, H. L. Strauss, R. G. Snyder, C. A. Elliger, *J. Phys. Chem.* **1984**, *88*, 334-341.

[174]   Y. Jeon, J. Sung, C. Seo, H. Lim, H. Cheong, M. Kang, B. Moon, Y. Ouchi, D. Kim, *J. Phys. Chem. B* **2008**, *112*, 4735-4740.

[175]   J. C. Lassegues, J. Grondin, D. Cavagnat, P. Johansson, *J. Phys. Chem. A* **2009**, *113*, 6419-6421.

[176]   A. Wulf, K. Fumino, R. Ludwig, *J. Phys. Chem. A* **2010**, *114*, 685-686.

[177]   J. C. Lassegues, J. Grondin, D. Cavagnat, P. Johansson, *J. Phys. Chem. A* **2010**, *114*, 687-688.

[178]   P. T. T. Wong, T. E. Chagwedera, H. H. Mantsch, *J. Chem. Phys.* **1987**, *87*, 4487-4497.

[179]   B. Jordanov, D. Tsankov, E. H. Korte, *J. Mol. Struct.* **2003**, *651-653*, 101-107.

[180]   S. A. Kirsch, R. A. Böckmann, *Biophys. J.* **2019**, *116*, 2131-2148.

[181]   S. L. Horswell, V. Zamlynny, H. Q. Li, A. R. Merrill, J. Lipkowski, *Faraday Discuss.* **2002**, *121*, 405-422.

[182]   W. Liptay, *Angew. Chem., Int. Ed. Engl.* **1969**, *8*, 177-188.

[183]   N. H. Li, V. Zamlynny, J. Lipkowski, F. Henglein, B. Pettinger, *J. Electroanal. Chem.* **2002**, *524*, 43-53.

[184]   R. Wang, M. A. S. Aquino, *IUCrData* **2019**, *4*, x190494.

[185]   R. S. Crees, M. L. Cole, L. R. Hanton, C. J. Sumby, *Inorg. Chem.* **2010**, *49*, 1712-1719.

[186]   J. Pesch, K. Harms, T. Bach, *Eur. J. Org. Chem.* **2004**, *2004*, 2025-2035.

[187]   S. Cha, M. Ao, W. Sung, B. Moon, B. Ahlstrom, P. Johansson, Y. Ouchi, D. Kim, *Phys. Chem. Chem. Phys.* **2014**, *16*, 9591-9601.

[188]   Z. Su, J. Leitch, J. Lipkowski, *Z. Phys. Chem.* **2012**, *226*, 995-1009.

[189]   M. V. Fedorov, A. A. Kornyshev, *Electrochim. Acta* **2008**, *53*, 6835-6840.

[190]   K. C. Jha, H. Liu, M. R. Bockstaller, H. Heinz, *J. Phys. Chem. C* **2013**, *117*, 25969-25981.

[191]   R. Bartucci, S. Belsito, L. Sportelli, *Chem. Phys. Lipids* **1996**, *79*, 171-180.

[192]   S. Sunder, D. Cameron, H. H. Mantsch, H. J. Bernstein, *Can. J. Chem.* **1978**, *56*, 2121-2126.

[193]   E. Tyrode, J. Hedberg, *J. Phys. Chem. C* **2012**, *116*, 1080-1091.

[194]   D. G. Cameron, H. L. Casal, H. H. Mantsch, Y. Boulanger, I. C. P. Smith, *Biophys. J.* **1981**, *35*, 1-16.

[195]   T. Alpers, Dissertation: Synthese neuartiger fluorhaltiger Spezialwachse, University of Oldenburg, **2018**.

[196]   R. A. Dluhy, R. Mendelsohn, H. L. Casal, H. H. Mantsch, *Biochemistry* **1983**, *22*, 1170-1177.

[197]   C. L. Brosseau, J. Leitch, X. Bin, M. Chen, S. G. Roscoe, J. Lipkowski, *Langmuir* **2008**, *24*, 13058-13067.

[198]   D. Matyszewska, R. Bilewicz, Z. Su, F. Abbasi, J. J. Leitch, J. Lipkowski, *Langmuir* **2016**, *32*, 1791-1798.

[199]   D. C. Lee, A. A. Durrani, D. Chapman, *Biochim. Biophys. Acta* **1984**, *769*, 49-56.

[200]   V. R. Kodati, R. Eljastimi, M. Lafleur, *J. Phys. Chem.* **1994**, *98*, 12191-12197.

[201]   X. Bin, S. L. Horswell, J. Lipkowski, *Biophys. J.* **2005**, *89*, 592-604.

[202]   M. Mašát, J. Wen, Z. Sofer, J. Michl, *Langmuir* **2017**, *33*, 5613-5616.

[203]   S. C. Hsi, A. P. Tulloch, H. H. Mantsch, D. G. Cameron, *Chem. Phys. Lipids* **1982**, *31*, 97-103.

[204]   M. V. Fraile, B. Patrón-Gallardo, G. López-Rodríguez, P. Carmona, *Chem. Phys. Lipids* **1999**, *97*, 119-128.

[205]   J. J. Leitch, C. L. Brosseau, S. G. Roscoe, K. Bessonov, J. R. Dutcher, J. Lipkowski, *Langmuir* **2013**, *29*, 965-976.

[206]   W. R. Fawcett, G. Liu, T. E. Kessler, *J. Phys. Chem.* **1993**, *97*, 9293-9298.

[207]   P. L. Yeagle, in *The Membranes of Cells (Third Edition)* (Ed.: P. L. Yeagle), Academic Press, Boston, **2016**, pp. 155-188.

[208]   J. Tomasi, B. Mennucci, R. Cammi, *Chem. Rev.* **2005**, *105*, 2999-3094.

[209]   A. Seelig, J. Seelig, *Biochemistry* **1974**, *13*, 4839-4845.

[210]   M. K. Kesharwani, B. Brauer, J. M. L. Martin, *J. Phys. Chem. A* **2015**, *119*, 1701-1714.

[211]   K. I. Assaf, W. M. Nau, *Angew. Chem. Int. Ed.* **2018**, *57*, 13968-13981.

[212]   C. Roth, S. Chatzipapadopoulos, D. Kerlé, F. Friedriszik, M. Lütgens, S. Lochbrunner, O. Kühn, R. Ludwig, *New J. Phys.* **2012**, *14*, 105026.

[213]   O. Höfft, S. Bahr, V. Kempter, *Langmuir* **2008**, *24*, 11562-11566.

[214]   T. Endo, T. Morita, K. Nishikawa, *Chem. Phys. Lett.* **2011**, *517*, 162-165.

[215]   W. Wu, W. Li, B. Han, Z. Zhang, T. Jiang, Z. Liu, *Green Chemistry* **2005**, *7*, 701-704.

[216]   Q.-R. Huang, T. Endo, S. Mishra, B. Zhang, L.-W. Chen, A. Fujii, L. Jiang, G. N. Patwari, Y. Matsuda, J.-L. Kuo, *Phys. Chem. Chem. Phys.* **2021**, *23*, 3739-3747.

[217]   R. G. Snyder, J. R. Scherer, *J. Chem. Phys.* **1979**, *71*, 3221-3228.

[218]   Y. Umebayashi, T. Fujimori, T. Sukizaki, M. Asada, K. Fujii, R. Kanzaki, S.-i. Ishiguro, *J. Phys. Chem. A* **2005**, *109*, 8976-8982.

[219] V. Barone, M. Biczysko, J. Bloino, *Phys. Chem. Chem. Phys.* **2014**, *16*, 1759-1787.

[220] D. K. Singh, P. Donfack, B. Rathke, J. Kiefer, A. Materny, *J. Phys. Chem. B* **2019**, *123*, 4004-4016.

[221] M. P. Andersson, P. Uvdal, *J. Phys. Chem. A* **2005**, *109*, 2937-2941.

[222] A. Arencibia, M. Taravillo, M. Cáceres, J. Núñez, V. G. Baonza, *J. Chem. Phys.* **2005**, *123*, 214502.

[223] T. Köddermann, C. Wertz, A. Heintz, R. Ludwig, *ChemPhysChem* **2006**, *7*, 1944-1949.

[224] A. Hailu, S. K. Shaw, *Energy Fuels* **2018**, *32*, 12695-12702.

[225] A. Hailu, A. A. Tamijani, S. E. Mason, S. K. Shaw, *Energy Fuels* **2020**, *34*, 3467-3476.

[226] A. K. Pennathur, M. J. Voegtle, S. Menachekanian, J. M. Dawlaty, *J. Phys. Chem. B* **2020**, *124*, 7500-7507.

[227] M.-M. Huang, Y. Jiang, P. Sasisanker, G. W. Driver, H. Weingärtner, *J. Chem. Eng. Data* **2011**, *56*, 1494-1499.

[228] J. L. Bishop, R. Quinn, M. D. Dyar, *Am. Mineral.* **2014**, *99*, 1580-1592.

[229] W. Huang, R. Frech, R. A. Wheeler, *J. Phys. Chem.* **1994**, *98*, 100-110.

[230] D. F. Bezuidenhout, in *Handbook of Optical Constants of Solids* (Ed.: E. D. Palik), Academic Press, Burlington, **1997**, pp. 815-835.

[231] D. Constantinescu, H. Weingärtner, C. Herrmann, *Angew. Chem. Int. Ed.* **2007**, *46*, 8887-8889.

[232] C. Schröder, *Top. Curr. Chem.* **2017**, *375*, 25.

[233] E. Loeser, S. Babiak, M. DelaCruz, P. Karpinski, *J. Chromatogr. Sci.* **2011**, *49*, 57-62.

[234] I. Brand, *Z. Phys. Chem.* **2016**, *230*, 133-183.

[235] V. Zamlynny, J. Lipkowski, in *Advances in Electrochemical Science and Engineering*, Wiley-VCH Verlag GmbH, **2008**, pp. 315-376.

[236] M. J. Frisch, G. W. Trucks, H. B. Schlegel, G. E. Scuseria, M. A. Robb, J. R. Cheeseman, G. Scalmani, V. Barone, G. A. Petersson, H. Nakatsuji, X. Li, M. Caricato, A. V. Marenich, J. Bloino, B. G. Janesko, R. Gomperts, B. Mennucci, H. P. Hratchian, J. V. Ortiz, A. F. Izmaylov, J. L. Sonnenberg, D. Williams-Young, F. Ding, F. Lipparini, F. Egidi, J. Goings, B. Peng, A. Petrone, T. Henderson, D. Ranasinghe, V. G. Zakrzewski, J. Gao, N. Rega, G. Zheng, W. Liang, M. Hada, M. Ehara, K. Toyota, R. Fukuda, J. Hasegawa, M. Ishida, T. Nakajima, Y. Honda, O. Kitao, H. Nakai, T. Vreven, K. Throssell, J. A. Montgomery, Jr., J. E. Peralta, F. Ogliaro, M. J. Bearpark, J. J. Heyd, E. N. Brothers, K. N. Kudin, V. N. Staroverov, T. A. Keith, R. Kobayashi, J. Normand, K. Raghavachari, A. P. Rendell, J. C. Burant, S. S. Iyengar, J. Tomasi, M. Cossi, J. M. Millam, M. Klene, C. Adamo, R. Cammi, J. W. Ochterski, R. L. Martin, K. Morokuma, O.

Farkas, J. B. Foresman, D. J. Fox, Gaussian 16, Gaussian Inc.,
Wallingford, USA, **2016**.

[237]   A. D. Becke, *J. Chem. Phys.* **1993**, *98*, 5648-5652.

[238]   V. A. Rassolov, M. A. Ratner, J. A. Pople, P. C. Redfern, L. A.
Curtiss, *J. Comput. Chem.* **2001**, *22*, 976-984.

[239]   F. Weigend, R. Ahlrichs, *Phys. Chem. Chem. Phys.* **2005**, *7*, 3297-3305.

[240]   D. Rappoport, F. Furche, *J. Chem. Phys.* **2010**, *133*, 134105.

[241]   F. Weigend, M. Häser, *Theor. Chem. Acc.* **1997**, *97*, 331-340.

[242]   A. Hellweg, C. Hättig, S. Höfener, W. Klopper, *Theor. Chem. Acc.*
2007, *117*, 587-597.

[243]   C. Adamo, V. Barone, *J. Chem. Phys.* **1999**, *110*, 6158-6170.

[244]   S. Grimme, S. Ehrlich, L. Goerigk, *J. Comput. Chem.* **2011**, *32*, 1456-
1465.

[245]   E. D. Glendening, A. E. Reed, J. E. Carpenter, F. Weinhold, NBO
Version 3.1, University of Wisconsin, Madison, USA,

[246]   J.-D. Chai, M. Head-Gordon, *Phys. Chem. Chem. Phys.* **2008**, *10*, 6615-
6620.

[247]   R. Krishnan, J. S. Binkley, R. Seeger, J. A. Pople, *J. Chem. Phys.* **1980**,
72, 650-654.

[248]   A. D. McLean, G. S. Chandler, *J. Chem. Phys.* **1980**, *72*, 5639-5648.

[249]   V. Barone, *J. Chem. Phys.* **2004**, *122*, 014108.

[250]   J. M. L. Martin, T. J. Lee, P. R. Taylor, J. P. François, *J. Chem. Phys.*
1995, *103*, 2589-2602.

15 Publications and Conference Participations

Peer-reviewed Journal Articles

[p1]   T. Sieling, J. Christoffers, I. Brand, *ACS Sustainable Chem. Eng.* **2019**, *7*, 11593-11602.

[p2]   T. Sieling, I. Brand, *ChemElectroChem* **2020**, *7*, 3233-3243.

[p3]   T. Sieling, T. Petersen, T. Alpers, J. Christoffers, T. Klüner, I. Brand, *Chem. Eur. J.* **2021**, submitted, under review.

[p4]   N. Kordts, S. Künzler, S. Rathjen, T. Sieling, H. Großekappenberg, M. Schmidtmann, T. Müller, *Chem. Eur. J.* **2017**, *23*, 10068-10079.

[p5]   J. Wittmar, S. Meyer, T. Sieling, J. Kunte, J. Smiatek, I. Brand, *J. Phys. Chem. B* **2020**, *124*, 7999-8011.

Poster Presentations

EuCheMSIL – 2018 27th Conference on Molten Salts and Ionic Liquids, October 7-12, 2018 in Lisbon (Portugal). Title: In situ Spectroelectrochemical Studies of the Electrical Double Layer at the Ionic Liquid|Electrode Interface

Bunsentagung 2019 – 118th General Assembly of the German Bunsen Society for Physical Chemistry, May 30 - June 1, 2019 in Jena (Germany). Title: Interfacial Behaviour of Surfaces Modified with 2D-Ionic Liquid Films

Oral Presentations

69th Annual Meeting of the International Society of Electrochemistry, September 2-7, 2018 in Bologna (Italy). Title: In situ Spectroelectrochemical Studies of the Electrical Double Layer at the Ionic Liquid|Electrode Interface

Electrochemistry 2018 – Electrochemical Surface Science: From Fundamentals to Applications, September 24-26, 2018 in Ulm (Germany). Title: In situ Spectroelectrochemical Studies of the Electrical Double Layer at the Ionic Liquid|Electrode Interface

Eidesstattliche Erklärung

Ich versichere hiermit, dass ich die vorliegende Arbeit selbstständig verfasst habe und nur die angegeben Quellen und Hilfsmittel benutzt habe. Aus der Dissertation sind die zuvor genannten Publikationen hervorgegangen. Die Dissertation hat weder in Teilen noch in ihrer Gesamtheit einer anderen wissenschaftlichen Hochschule zur Begutachtung in einem Promotionsverfahren vorgelegen.

Die Leitlinien guter wissenschaftlicher Praxis der Carl von Ossietzky Universität Oldenburg sind befolgt worden. Im Zusammenhang mit dem Promotionsvorhaben wurden keine kommerziellen Vermittlungs- oder Beratungsdienste (Promotionsberatung) in Anspruch genommen.

Oldenburg, 18. Juni 2021

_____